Jianxun Zhu

Cavity flows and wake behind an elliptic cylinder translating above a wall

Doctoral thesis

Jianxun Zhu

Doctoral theses at NTNU, 2020:312

NTNU
Norwegian University of
Science and Technology
Thesis for the degree of
Philosophiae Doctor
Faculty of Engineering
Department of Marine Technology

□ NTNU
Norwegian University of
Science and Technology

Jianxun Zhu

Cavity flows and wake behind an elliptic cylinder translating above a wall

Thesis for the degree of Philosophiae Doctor

Trondheim, Oct 2020

Norwegian University of Science and Technology
Faculty of Engineering
Department of Marine Technology

NTNU
Norwegian University of
Science and Technology

Abstract

Vortex formation is one of the fundamental modes in fluid mechanics and it can develop in almost every realization of fluid motion. Studying its fundamental dynamics and interactions is of great interest for engineering applications; the vortex shedding behind slender cylindrical structures with various cross sections like pipelines, risers, bridges, buildings and wind turbine blades, can cause fluctuating drag and lift forces, which lead to the vortex-induced vibration (VIV), causing the material subjected to periodic bending stresses, which eventually can lead to fracture; the vortex shedding behind the offshore pipeline placed on/close to the seabed determines the gentle slope of the downstream scour hole. In order to understand the complex physics underpinning the vortex dynamics, some classical flow problems, i.e. oscillatory lid-driven cavity flows, cavity flows with an inserted cylinder and wake behind an elliptic cylinder translating above a wall, which are dominated by the vortex flow have been investigated numerically in the present thesis.

Flow in a two-dimensional oscillatory lid-driven rectangular cavity with a depth-to-width ratio 1:2 is investigated, covering a wide range of Reynolds numbers (based on the velocity amplitude and the cavity depth) and Stokes numbers (based on the lid oscillation angular frequency and the cavity depth) where this flow is known to be in the two-dimensional regime. Effects of these two parameters on vortex dynamics, vertical and horizontal centerline velocities and the drag force on the lid are presented and discussed. Four different flow patterns are classified based on the vortex dynamics. Moreover, the corner singularity effect on the flow patterns is also presented and discussed.

Effects of an inserted circular cylinder on a steady lid-driven cavity flow are investigated and discussed for different Reynolds numbers (based on the lid motion velocity and the cavity depth), depth-to-width ratios, cylinder radii and locations. An immersed boundary method is applied to treat the circular cylinder surface. Numerical results concerning the vortex structures and pressure distribution around the cylinder are presented and discussed. For the depth-to-width ratio of 1:2, seven flow patterns have been classified based on the vortex structures and their distributions are presented as a function of the Reynolds numbers and the cylinder radii for a given cylinder location.

Wake behind an elliptic cylinder translating above a plane wall is investigated numerically for Reynolds numbers less than 150 and gap ratios from 0.1 to 5 (i.e., the ratio between the gap and semi-major axis length of the elliptic cylinder). Numerical results concerning the steady and unsteady wake structures (Kármán vortex street, the two-layered wake and the secondary vortex street), the hydrodynamic forces and the onset location of the two-layered wake are presented and discussed. Four flow patterns are classified based on the wake structure and their distributions are given in the space of the Reynolds number and the gap ratio.

Numerical simulations of the oscillating boundary layer on a plane wall have been conducted for $Re_\delta = 500$ and 1120 (based on the boundary layer thickness and the amplitude of the oscillation velocity), and the present results for the wall shear stress and instantaneous vorticity contours are in a good agreement with previous numerical and experimental results.

Preface

This thesis is submitted to the Norwegian University of Science and Technology (NTNU) for partial fulfilment of the requirements for the degree of philosophiae doctor. This doctoral work has been performed at Department of Marine Technology, NTNU, Trondheim, with Professor Lars Erik Holmedal as main supervisor and with co-supervisors Professor Dag Myrhaug, Dr. Hong Wang and Asst. Professor Mohammad Saud Afzal.

Acknowledgement

I would like to express my deepest gratitude to my supervisor Professor Lars Erik Holmedal, for his patient guidance, encouragement and advice throughout my PhD research studies. He guided me to become an independent researcher with rigorous thinking. His perspectives have always provided valuable input to the work as it progressed. I gained a lot from many fruitful discussions with him both on career and life.

Sincere thanks are extended to my co-supervisor Professor Dag Myrhaug, for his comments and suggestions of all the scientific paper during my PhD study. I would greatly appreciate many insightful discussions with him. He was and remain my best role model for a scientist, mentor, and teacher. My gratitude also goes to my co-supervisors Dr. Hong Wang and Asst. Professor Mohammad Saud Afzal, for their help and support to my research work and life in Norway.

I want to give a sincere thank you to Professor Jiping Zhang at Zhejiang Ocean University for helping me prepare the documents for the PhD application, Professor Liping Sun for her patient guidance for my master study and her support on my PhD application at Harbin Engineering University, Professor Heather Peng at Memorial University of Newfoundland for her support on my decision to start my PhD study at NTNU, as well as Professor Muk Chen Ong at University of Stavanger for his care and help during my stay here.

Many thanks to Fengjian Jiang, for the valuable discussions related to bluff body wakes and vortex dynamics. Special thanks go to Ping Fu, Yuan Tian, Joar Gunnarsjaa Harkestad and Anna Duong for every happy moment at Trondheim. I would also like to express my appreciation to Xiaolong Lin, Chai Tian, Shi Deng and Zhengru Ren, for helping me adjust to a new life in Norway, as well as Sondre, Marte and Mariell for helping me learn about Norwegian culture. Furthermore, I am thankful to all my good friends and colleagues at NTNU for providing a pleasant life and work environment.

Finally, I am truly grateful to my parents and my big brother for their immeasurable love and care. They have always encouraged me to explore my potential and pursue my dreams. They helped me a lot to reach this stage in my life.

Nomenclature

Abbreviation

2D	Two-dimensional
3D	Three-dimensional
APV	Anti-clockwise primary vortex
BLCV	Bottom left corner vortex
BRCV	Bottom right corner vortex
BV	Bottom vortex
CPV	Clockwise primary vortex
LWV	Left wall vortex
ULCV	Upper left corner vortex
URCV	Upper right corner vortex

Greek letters

β	Coefficient for the Lagrange interpolation
Δt	Dimensionless simulation time-step
Δx	Dimensionless grid size in the streamwise direction
Δy	Dimensionless grid size in the crossflow direction
Δz	Dimensionless grid size in the spanwise direction
δ	Wall boundary layer thickness
δ/D	Wall boundary layer thickness to cylinder diameter ratio

Γ	Immersed boundary
λ	Weighting factors for the interpolation in different directions.
ν	Kinematic viscosity of fluid
Ω	Lid oscillation frequency
ω	Vorticity
ψ	Stream function
ρ	Fluid density

Roman letters

Re	Reynolds number
St	Stokes number or Strouhal number
G/D	Gap-to-diameter ratio
$(G/D)_c$	Critical gap-to-diameter ratio
H	Cavity depth
D	Cylinder diameter or semi-major axis length of the elliptic cylinder
S	Surface area of the cylinder
F_D	Drag force
C_D	Instantaneous drag coefficient
$\overline{C}_D$	Time-averaged drag coefficient
F_L	Lift force
C_L	Instantaneous lift coefficient
$\overline{C}_L$	Time-averaged lift coefficient
C_p	Instantaneous pressure coefficient
$\overline{C}_p$	Time-averaged pressure coefficient

U Free-stream velocity

U_{lid} Steady lid motion velocity

U_a Velocity amplitude of the lid oscillation

f Vortex shedding frequency

p_0 Static pressure in the freestream

l Distance between the inactive velocity point and the immersed boundary

Subscripts

x Streamwise direction

y Crossflow direction

z Spanwise direction

Contents

Chapter 1

Introduction

1.1 Background & motivation

Vortex formation is one of the fundamental modes in fluid mechanics and it can develop in almost every realization of fluid motion (Lugt 1983). Studying its fundamental dynamics and interactions is of great interest for engineering applications; the vortex shedding behind slender cylindrical structures with various cross sections like pipelines, risers, bridges, buildings and wind turbine blades, can cause fluctuating drag and lift forces, which lead to the vortex-induced vibration (VIV), causing the material subjected to periodic bending stresses, which eventually can lead to fracture (Blevins 1977, Williamson & Govardhan 2004); the vortex shedding behind the offshore pipeline placed on/close to the seabed determines the gentle slope of the downstream scour hole (Li & Cheng 2001, Liang et al. 2005); the primary horseshoe vortex formed in front of a pier plays a key role for scour over the entire process of scouring (Muzzammil & Gangadhariah 2003, Zhao et al. 2010); the upward velocity associated with Görtler vortices can be a significant mechanism for the sediment transport over ripples (Zedler & Street 2001). Fundamental understanding the vortex formation is also of vital importance in understanding the turbulence; in turbulent boundary layers, the buffer layer is dominated by the quasi-streamwise vortices, which induce the low-speed streak while the outer layer is occupied by hairpin-like vortices, which contain a spanwise-extending head and one or two streamwise-inclined legs Robinson (1991), Adrian (2007); the energy cascade in homogeneous isotropic turbulence can be caused by the successive formation of smaller-scale tubular vortices in the larger-scale straining regions existing between pairs of larger-scale tubular vortices (Goto 2008), while the physical mechanism for the inverse energy cascade in two-dimensional turbulence is at-

tributed to the stretching of small-scale vorticity, i.e. the so-called vortex thinning (Xiao et al. 2009); a vortex interaction mechanism was proposed by Yasuda et al. (2019), for generating the energy and enstrophy fluctuations in high-symmetric turbulence; based on the vortex dynamics, various models have been developed to predict or postdict high Reynolds number turbulences (Pullin & Saffman 1998).

Identification of the vortex is the first step to study its fundamental mechanisms in different types of flows. A widely acceptable definition of a vortex was given by Robinson et al. (1989): *a vortex exists when instantaneous streamlines mapped onto a plane normal to the vortex core exhibit a roughly circular or spiral pattern, when viewed from a reference frame moving with the center of the vortex core.* This gives rise to a problem for identifications of the vortex since the motion of the vortex core can not be priorly obtained. Various detection algorithms have been implemented to identify the vortices. The closed or spiral streamlines, as a Galilean variant, was widely used to identify vortices in steady flows (Dennis & Chang 1970, Cheng & Hung 2006) but with a poor ability to capture those in unsteady flows. The vorticity magnitude was used in early studies (Metcalfe et al. 1987, Hussain & Hayakawa 1987). However, it can not identify the vortex in a shear flow, especially when the vorticity magnitude in the shear layer is comparable to that within the vortex. Thereafter, some Galilean-invariant identifications of a vortex like the Q method (Hunt et al. 1988) 1988, Δ method (Chong et al. 1990) and λ_2 method (Jeong & Hussain 1995) have been proposed using invariants of the velocity gradient tensor. These methods have been verified in various numerical and experimental studies. Recently, Zhu et al. (2020) investigated the vortex structures in a two-dimensional steady lid-driven cavity. The λ_2 criterion identified the primary vortex and the bottom corner vortices, which are also visualized by closed streamlines. However, the flow at the upper-left corner was also identified as a vortex by the λ_2-criterion whereas the streamlines were not closed, thus demonstrating the complexity of vortex identification.

1.2   Outline of the present study

In order to understand the complex physics underpinning the vortex dynamics, some classical flow problems, i.e. oscillatory lid-driven cavity flows, cavity flows with an inserted cylinder and wake behind an elliptic cylinder translating above a wall, which are dominated by the vortex flow have been studied in the present thesis.

A brief description of each chapter is provided as follow:

Chapter 2:
This chapter provides the theoretical background about the Stokes boundary layer, steady and oscillatory lid-driven cavity flows, flow around a free and a near-wall cylinder in steady current, and flow around the free elliptic cylinder.

Chapter 3:
This chapter introduces the present numerical method. A non-iterative projection method is used to solve the incompressible Navier-Stokes equations; the Adams-Bashforth and Crank-Nicolson schemes are used for the convective and viscous terms, respectively. The spatial derivatives are evaluated by means of second-order, central finite-difference operators on a staggered grid arrangement. The solid surface is treated by an immersed boundary method. Moreover, some classical immersed boundary methods introduced in the literature are described and discussed.

Chapter 4:
This chapter presents numerical investigations of flow in an oscillatory lid-driven rectangular cavity with depth-to-width ratio 1:2. The Reynolds number and the Stokes number cover a wide range of values where the flow is known to be two-dimensional. It is observed that the flow can be classified into four different flow patterns based on the vortex dynamics. The distribution of these flow patterns is given in the Stokes number and Reynolds number space. For the flow pattern with lowest Reynolds number, there is no transfer of vortices between two successive oscillation half-cycles while for the three other patterns, vortices are transferred from one oscillation half-cycle to the next.

Chapter 5:
This chapter presents comprehensive numerical investigations of flow in a steady lid-driven cavity of depth to width ratio 1:2 containing a circular cylinder. Three different Reynolds numbers of 100, 500 and 1000 as well as four different cylinder radius to cavity depth ratios (0.1, 0.2, 0.3 and 0.4) located at three different positions along the horizontal centerline of the cavity, are considered. It appears that these flows can be classified into seven different flow patterns. These flow patterns are given for different cylinder radii and positions as well as Reynolds numbers.

Chapter 6:
This chapter presents numerical investigations of the flow over an elliptic

cylinder near a moving wall for Reynolds numbers less than 150. Here the ratio between the gap (i.e., the distance between the cylinder and the wall) and the length of the semi-major axis of the elliptic cylinder varies from 0.1 to 5. This ratio is hereafter denoted the gap ratio. The resulting Kármán vortex street, the two-layered wake and the secondary vortex street have been investigated and visualized.

Chapter 7:
This chapter presents numerical investigations of oscillatory boundary layer flow over a plane wall for Reynolds numbers of 500 and 1120 (based on the boundary layer thickness and the amplitude of the oscillation velocity). The wall shear stress and the vorticity contours are plotted and compared with previous numerical and experimental results.

Chapter 8:
This chapter presents a summary of the findings of the present numerical study and recommendations for the future work.

References

Adrian, R. J. (2007), 'Hairpin vortex organization in wall turbulence', *Physics of Fluids* **19**, 041301.

Blevins, R. D. (1977), Flow-induced vibration, Technical report, Van Nostrand Reinhold Company.

Cheng, M. & Hung, K. C. (2006), 'Vortex structure of steady flow in a rectangular cavity', *Computers & Fluids* **35**, 1046–1062.

Chong, M. S., Perry, A. E. & Cantwell, B. J. (1990), 'A general classification of three-dimensional flow fields', *Physics of Fluids A: Fluid Dynamics* **2**, 765–777.

Dennis, S. C. R. & Chang, G.-Z. (1970), 'Numerical solutions for steady flow past a circular cylinder at reynolds numbers up to 100', *Journal of Fluid Mechanics* **42**, 471–489.

Goto, S. (2008), 'A physical mechanism of the energy cascade in homogeneous isotropic turbulence', *Journal of Fluid Mechanics* **605**, 355–366.

Hunt, J. C. R., Wray, A. A. & Moin, P. (1988), 'Eddies, streams, and convergence zones in turbulent flows', *Center for Turbulence Research Report CTR-S88* pp. 193–229.

Hussain, A. K. M. F. & Hayakawa, M. (1987), 'Eduction of large-scale organized structures in a turbulent plane wake', *Journal of Fluid Mechanics* **180**, 193–229.

Jeong, J. & Hussain, F. (1995), 'On the identification of a vortex', *Journal of Fluid Mechanics* **285**, 69–94.

Li, F. & Cheng, L. (2001), 'Prediction of lee-wake scouring of pipelines in currents', *Journal of Waterway, Port, Coastal, and Ocean Engineering* **127**, 106–112.

Liang, D., Cheng, L. & Li, F. (2005), 'Numerical modeling of flow and scour below a pipeline in currents: Part ii. scour simulation', *Coastal Engineering* **52**, 43–62.

Lugt, H. J. (1983), *Vortex flow in nature and technology*, Wiley.

Metcalfe, R. W., Hussain, A. K. M. F., Menon, S. & Hayakawa, M. (1987), 'Coherent structures in a turbulent mixing layer: a comparison between direct numerical simulations and experiments', *Turbulent Shear Flows 5* pp. 110–123.

Muzzammil, M. & Gangadhariah, T. (2003), 'The mean characteristics of horseshoe vortex at a cylindrical pier', *Journal of Hydraulic Research* **41**, 285–297.

Pullin, D. & Saffman, P. (1998), 'Vortex dynamics in turbulence', *Annual Review of Fluid Mechanics* **30**, 31–51.

Robinson, S. K. (1991), 'Coherent motions in the turbulent boundary layer', *Annual Review of Fluid Mechanics* **23**, 601–639.

Robinson, S. K., Kline, S. J. & Spalart, P. R. (1989), 'A review of quasi-coherent structures in a numerically simulated turbulent boundary layer', *NASA Technical Memorandum* **1021**, 91.

Williamson, C. & Govardhan, R. (2004), 'Vortex-induced vibrations', *Annual Review of Fluid Mechanics* **36**, 413–455.

Xiao, Z., Wan, M., Chen, S. & Eyink, G. L. (2009), 'Physical mechanism of the inverse energy cascade of two-dimensional turbulence: a numerical investigation', *Journal of Fluid Mechanics* **619**, 1–44.

Yasuda, T., Kawahara, G., van Veen, L. & Kida, S. (2019), 'A vortex interaction mechanism for generating energy and enstrophy fluctuations in high-symmetric turbulence', *Journal of Fluid Mechanics* **874**, 639–676.

Zedler, E. A. & Street, R. L. (2001), 'Large-eddy simulation of sediment transport: currents over ripples', *Journal of Hydraulic Engineering* **127**, 444–452.

Zhao, M., Cheng, L. & Zang, Z. (2010), 'Experimental and numerical investigation of local scour around a submerged vertical circular cylinder in steady currents', *Coastal Engineering* **57**(8), 709–721.

Zhu, J., Holmedal, L. E., Wang, H. & Myrhaug, D. (2020), 'Vortex dynamics and flow patterns in a two-dimensional oscillatory lid-driven rectangular cavity', *European Journal of Mechanics-B/Fluids* **79**, 255–269.

Chapter 2

Theoretical background

2.1 Stokes boundary layer

The Stokes boundary layer, also known as Stokes second problem or Rayleigh problem (Schlichting & Gersten 2016), refers to determining the flow driven by an infinitely long plate, which is oscillating horizontally with a velocity $U_0 cos(nt)$. Here t, U_0 and n are the physical time, the velocity amplitude and frequency of the plate oscillation, respectively. This plate is considered to be located at $y = 0$ and oscillate in the x direction, such that the flow is described by the incompressible Navier-Stokes equations given as follows:

$$\frac{\partial u}{\partial t} = \nu \frac{\partial^2 u}{\partial y^2} \tag{2.1}$$

where u is the velocity in the x direction, ν denotes the kinematic viscosity and y is the vertical coordinate. The initial and no-slip conditions on the plate as well as the boundary condition for u far away from the plate are given by

$$u(0,0) = 1 \tag{2.2}$$

$$u(0,t) = U_0 cos(nt) \tag{2.3}$$

$$u(\infty, t) = 0 \tag{2.4}$$

The velocity u can be written as the real part of the complex function

$$u(y,t) = U_0 \mathcal{R}[e^{int} f(y)] \tag{2.5}$$

which substituted into Eq.(2.1) yields

$$f'' - \frac{in}{\nu} f = 0 \tag{2.6}$$

with boundary conditions $f(0) = 1$ and $f(\infty) = 0$. The solution of Eq.(2.1)
is

$$f(y) = exp\left[-\frac{1+i}{\sqrt{2}}\sqrt{\frac{n}{\nu}}\,y\right] \tag{2.7}$$

Consequently, substituting Eq.(2.7) into Eq.(2.5) yields the velocity solution
for the oscillatory boundary layer as follows:

$$u(y,t) = U_0 e^{-\sqrt{\frac{n}{2\nu}}y}cos\left(nt - \sqrt{\frac{n}{2\nu}}\,y\right) \tag{2.8}$$

Figure 2.1 shows the velocity distribution for different times. The velocity
u is highly damped away from the plate by the exponential factor $\sqrt{n/2\nu}$,
of which the reciprocal is defined as the Stokes boundary layer thickness.
This thickness decreases as n increases and increases as ν increases.
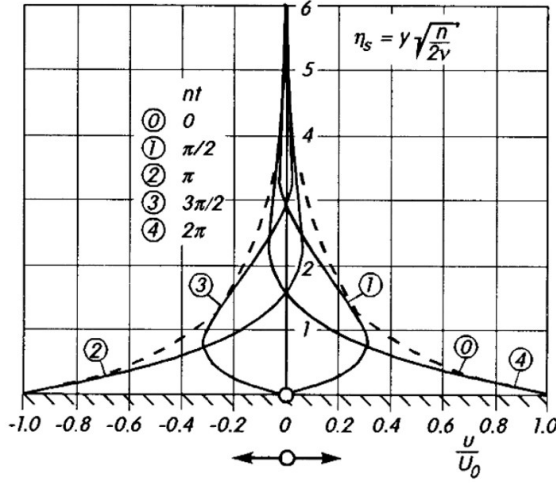
Figure 2.1: Velocity distribution close to an oscillating wall (from Schlicht-
ing & Gersten 2016).

2.2 Lid-driven cavity flow

2.2.1 Steady lid-driven cavity flow

Steady lid-driven cavity flow is one of the most studied fluid problems in
computational fluid dynamics. The simplicity of its geometry makes the
problem easy to code and apply boundary conditions. Despite its simple
geometry involved, Shankar & Deshpande (2000) reported the importance

of this flow in the study of basic fluid mechanics since complex phenomena such as counter-rotating vortices, instability and transition to turbulence occur naturally in this flow. The vortices within the cavity provide insight about such structures in applications like protrusions on the cylinder surface (Demartino & Ricciardelli 2017), drag-reducing riblets and mixing cavities (Zumbrunnen et al. 1996). Flow in the between armour blocks in marine civil engineering applications is similar to that in cavities only to have a constant exchange of water between the cavity and the main body of the flow, in contrast to the lid-driven cavity flow studied in the present work where no such exchange is allowed. Suction of sediment from between armour blocks is an important problem in river and marine civil engineering (Sumer et al. 2001, Dixen et al. 2008, Nielsen et al. 2012).
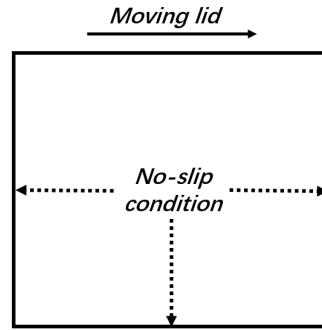
Figure 2.2: Sketch of a two-dimensional steady lid-driven cavity.

A large amount of researches have been conducted on the two-dimensional steady lid-driven square cavity flow, which is determined by the Reynolds number given by

$$Re = \frac{U_{lid}H}{\nu} \tag{2.9}$$

where ν is the kinematic viscosity whilst U_{lid} and H denote the lid motion velocity and the cavity height.

Figure 2.2 shows a sketch of the two-dimensional lid-driven square cavity consisting of the three rigid walls with no-slip conditions and a lid moving with a tangential unit velocity (U_{lid}). Typical flow patterns within the cavity are given in figure 2.3 taken from Erturk & Gökçöl (2006) and Shukla et al. (2007); as the lid moves towards the right (top images of figure 2.3), the cavity contains a primary vortex and two bottom corner vortices for Reynolds number of 1000 while an additional left-wall vortex is formed for Reynolds number of 5000; as the lid moves towards the left (bottom images

of figure 2.3), the flow pattern varies for different instants a, b and c for Reynolds number of 10000 due to Hopf bifurcation.

Kawaguti (1961) conducted the first numerical investigation of flow in the steady lid-driven square cavity for Reynolds numbers up to 128, and found that flow driven by the lid circulates within the cavity, forming a large primary vortex. Later, Burggraf (1966) conducted a more extensive theoretical and numerical study for Reynolds numbers up to 400, and found that two secondary vortices, counter-rotating with the primary vortex, were formed at the bottom left and right corners, respectively. Ghia et al. (1982) investigated the cavity flow for Reynolds numbers up to 10000 using a coupled strongly multigrid method with fine grid resolutions. Additional small corner vortices, counter-rotating with their adjacent vortices, were observed when the Reynolds number was larger than 1000. These corner vortices are also called Moffatt eddies, proposed by Moffatt (1964), who used the asymptotic approach to study a viscous fluid near a sharp corner between two plates. Ghia et al. (1982) also found that a small left wall vortex was formed near the right-moving wall for Reynolds numbers larger than 3200, and it was counter-rotating with the primary vortex (qualitatively shown in the top-right image of figure 2.3). Auteri et al. (2002) reported that the steady lid-driven cavity flow exhibits a transition to unsteady periodic flow for a critical Reynolds number between 8017.6 and 8018.8 due to Hopf bifurcation, and more complex time-depend flow patterns were visualized by Shukla et al. (2007) using streamline contours for the Reynolds number of 10000 (bottom images of figure 2.3). In addition to the Reynolds number, the steady lid-driven cavity flow depends strongly on the height to width ratio of the cavity. Cheng & Hung (2006) conducted a comprehensive study on the vortex structures for aspect ratios ranging from 0.1 to 7 and for Reynolds numbers up to 5000, and suggested that for aspect ratios less than 1, the cavity contains a large primary vortex and more complex secondary vortices as the Reynolds number increases, while for aspect ratios larger than 1 the flow is characterized by counter-rotating large vortices, of which the number increases as the aspect ratio and the Reynolds number increase. Comprehensive reviews of lid-driven cavity flow are given by Shankar & Deshpande (2000) and Kuhlmann & Romanò (2019).

Corner singularity, i.e. the infinity vorticity at the upper corners, is one of the important issues present in the cavity since this singularity can cause numerical challenges, making it more difficult to obtain an accurate numerical solution in the close vicinity of the upper corners. For spectral methods, the global nature of the trial function in conjunction with the upper corner singularities leads to spurious oscillations (Botella & Peyret
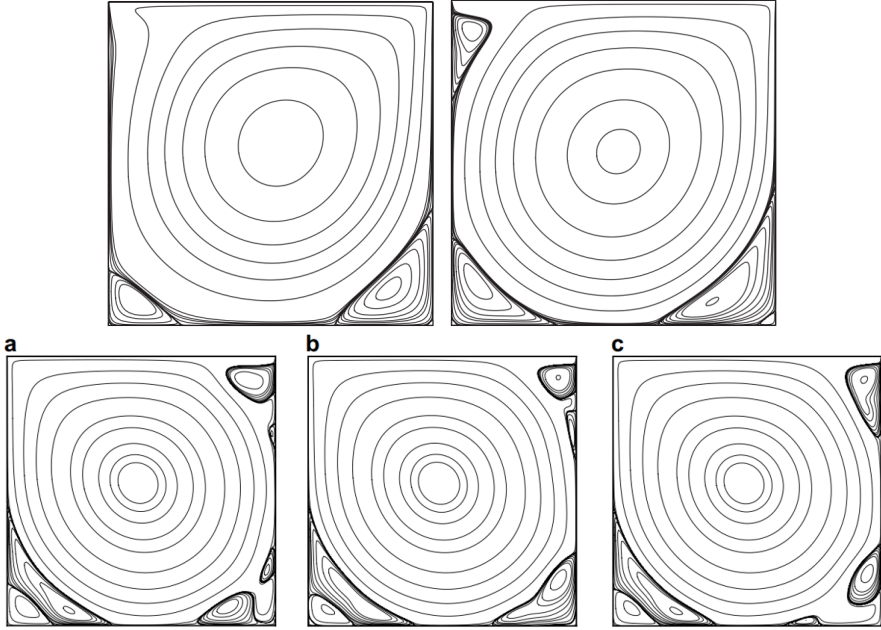
Figure 2.3: Top images (lid moves towards the right): streamline contours for steady lid-driven cavity flow for the Reynolds number of 1000 and 5000; bottom images (lid moves towards the left): streamline contours for steady lid-driven cavity flow for the Reynolds number of 10000 at dimensionless time scaled by H/U_{lid} equal to (a) 2003.5; (b) 2008.75; (c) 2014.0. The top and bottom images are taken from Erturk & Gökçöl (2006) and Shukla et al. (2007), respectively.

1998, Botella et al. 2001). This is overcome by combining the trial functions with local analytic solutions based on asymptotic series expansions in terms of the local Reynolds number, which is small due to the small flow velocity near the upper corner. Figure 2.4 shows a comparison of the stream function (ψ) and vorticity contour lines (ω) of the creeping flow in a two-dimensional lid-driven square cavity using a pseudospectral method without (a) and with (b) the subtraction of the corner singularity (Schultz et al. 1989). Spurious eddies are evident in (a), but largely suppressed in (b). For finite difference, finite volume and finite element methods, the corner singularities can also result in numerical inaccuracies. Bruneau & Saad (2006) investigated a steady lid-driven square cavity flow using finite difference methods for Reynolds numbers of 1000 and 5000, showing that grid convergence was obtained for the total kinetic energy $E = \frac{1}{2} \oint_S ||U_c||^2 dS$

(where S is the computation domain, and U_c is the velocity evaluated at the cell center), whilst grid convergence could not be obtained for neither the enstrophy $Z = \frac{1}{2} \oint_S ||\omega||^2 dS$ nor the palinstrophy $P = \frac{1}{2} \oint_S ||\nabla\omega||^2 dS$ (where ω is the vorticity evaluated at the cell center). As pointed out by Bruneau & Saad (2006), this is caused by the infinite velocity gradients in the corners, causing the enstrophy and the palinstrophy to approach infinity as the grid cell size approaches zero.
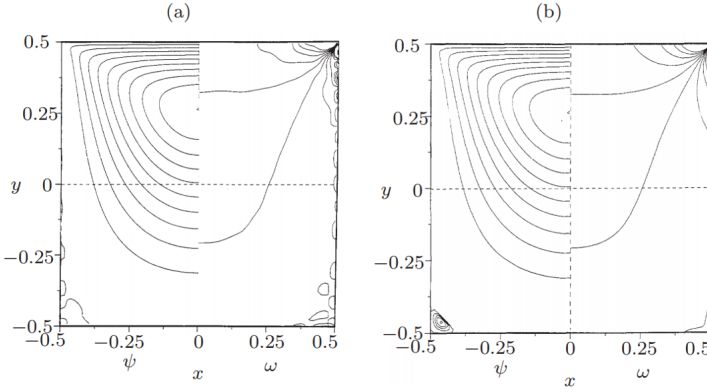
Figure 2.4: A comparison of the streamline function (ψ, left half) and vorticity contour lines (ω, right half) of the creeping flow in a two-dimensional lid-driven square cavity using a pseudospectral method without (a) and with (b) the subtraction of the corner singularity. The figure is taken from Schultz et al. (1989)
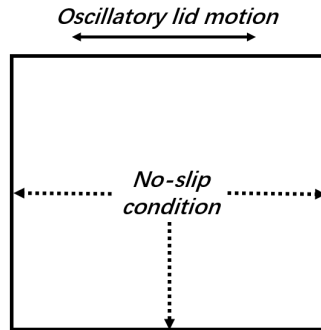
Figure 2.5: Sketch of a two-dimensional oscillatory lid-driven cavity.

2.2.2 Oscillatory lid-driven cavity flow

Although not gaining the attention as much as the steady lid-driven flow, oscillatory lid-driven cavity flow (figure 2.5) has been investigated over the years because of its relevance to industrial flows (Karniadakis et al. 2006). This flow is determined by the Reynolds number based on the lid motion velocity amplitude (U_a) and the cavity height, and the Stokes number based the lid oscillation angular frequency and the cavity height to width ratio given by

$$Re_{osc} = \frac{U_a H}{\nu} \tag{2.10}$$

$$St_{osc} = \frac{\Omega H^2}{\nu} \tag{2.11}$$

where Ω is the oscillation angular frequency of the lid.
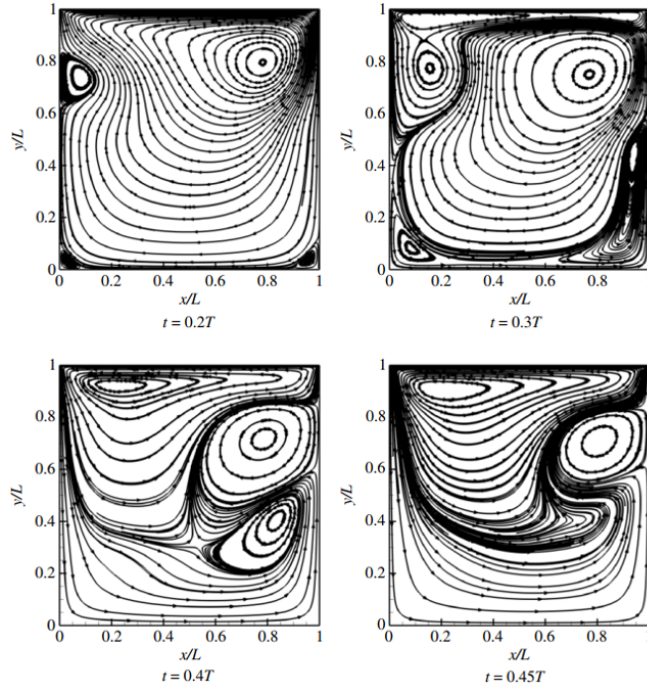
Figure 2.6: Streamline contours of the oscillatory lid-driven square cavity flow during the first half cycle for the Reynolds number of 400 and Stokes number of 419 by Mendu & Das (2013).

Iwatsu et al. (1992), Soh & Goodrich (1988) and Mendu & Das (2013) used numerical simulations to investigate the flow in an oscillatory lid-driven

square cavity for different ratios of the Reynolds number to the Stokes number. They found complex vortex dynamics including the merging of the co-rotating vortices and the counteraction of the counter-rotating vortices, resulting in the growth and decay of vortices within the cavity during the oscillation cycle as shown in figure 2.6 taken from Mendu & Das (2013) for the Reynolds number of 400 and the Stokes number of 419.

The generation mechanism of the corner vortices is attributed to the flow separation, which is qualitatively similar to the steady lid-driven cavity flow, but with time-dependent movement of the separation points. The generation mechanisms of the primary vortex have been attributed to two aspects; *i*) vorticity produced by the shear motion induced by the oscillating walls, and *ii*) roll-up of vortex sheets as the wall-induced flow changes direction when the fluid meets the vertical walls, proposed by Ovando et al. (2009), who investigated the flow in a rectangular cavity driven by a simultaneous oscillatory motion of the vertical walls, relevant to a piston moving inside a circular cylinder in combustion engines.

Lopez & Hirsa (2001) reported the possible application of the oscillatory lid-driven cavity flow as a viable viscometer, which spurred further investigations for the stability of the oscillatory lid-driven rectangular cavity flow, including the experimental work by Vogel et al. (2003) and Leung et al. (2005) as well as the stability analysis by Blackburn & Lopez (2003). Their work provided stability regions based on the Reynolds number and Stokes number. Three different flow states were found: *i*) a basic two-dimensional time-periodic flow, *ii*) a three-dimensional time-periodic flow with a cellular structure in the spanwise direction, *iii*) a three-dimensional irregular flow.

2.3 Flow around a circular cylinder in steady current

2.3.1 Boundary layer and separation

Flow around a circular cylinder has been studied extensively because of its vital importance in understanding vortex shedding in engineering applications such as marine risers and pipelines. The Reynolds number is a governing parameter for this flow and defined by (Sumer & Fredsøe 2006)

$$Re = \frac{DU}{\nu} \tag{2.12}$$

where D, U and ν denote the cylinder diameter, free-stream velocity and the kinematic viscosity of the fluid, respectively.
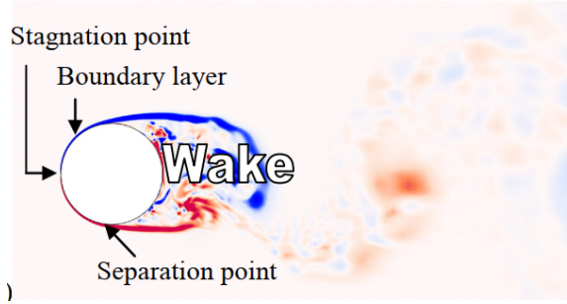
Figure 2.7: Definition of the boundary layer and wake region. This figure is taken from Prsic (2016).

The presence of the fluid viscosity slows down the fluid particles close to the cylinder surface, forming a thin slow-moving fluid layer called a boundary layer. High vorticity is present inside the boundary layer. This layer remains attached to the cylinder surface until the occurrence of flow separation, which is caused by the development of the adverse pressure gradient. Consequently, the boundary layer detaches from the cylinder surface, forming a free shear layer over the cylinder. An area bounded by the shear layers from top and bottom of the cylinder is called the wake. The detached shear layers roll up, forming the vortices, which may remain attached to the cylinder or shed downstream. The boundary layer and wake region are visualized by vorticity contours for $Re = 13100$ as shown in figure 2.7.
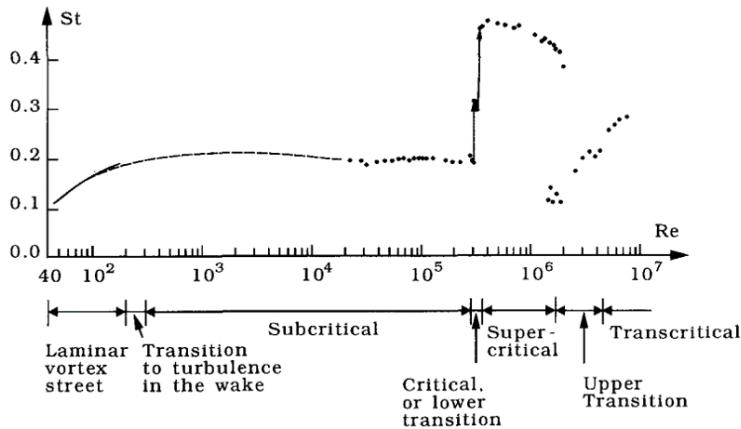
Figure 2.8: Strouhal number (St) for a circular cylinder, presented as a function of Re. This figure is taken from Sumer & Fredsøe (2006).
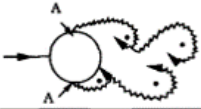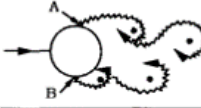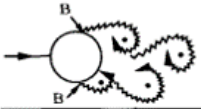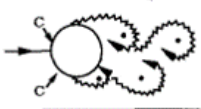
a)	No separation. Creeping flow	Re < 5
b)	A fixed pair of symmetric vortices	5 < Re < 40
c)	Laminar vortex street	40 < Re < 200
d)	Transition to turbulence in the wake	200 < Re < 300
e)	Wake completely turbulent. A:Laminar boundary layer separation	$300 < Re < 3 \times 10^5$ Subcritical
f)	A:Laminar boundary layer separation B:Turbulent boundary layer separation;but boundary layer laminar	$3 \times 10^5 < Re < 3.5 \times 10^5$ Critical (Lower transition)
g)	B: Turbulent boundary layer separation;the boundary layer partly laminar partly turbulent	$3.5 \times 10^5 < Re < 1.5 \times 10^6$ Supercritical
h)	C: Boundary layer completely turbulent at one side	$1.5 \times 10^6 < Re < 4 \times 10^6$ Upper transition
i)	C: Boundary layer completely turbulent at two sides	$4 \times 10^6 < Re$ Transcritical

Figure 2.9: Flow regimes in the cylinder wake (from Sumer & Fredsøe 2006)

Vortex shedding is the dominant flow feature for $Re > 40$. The vortices are shed alternately from the top and bottom of the cylinder, forming a recognizable vortex street, which is often called the Kármán - Bernard vortex street. The vortex shedding frequency is commonly studied through a dimensionless parameter, i.e. the Strouhal number defined by

$$St = \frac{fD}{U} \tag{2.13}$$

where f is the vortex shedding frequency. Figure 2.8 shows the Strouhal

number over different flow regimes which will be introduced in the next section. In the laminar vortex street regime (of interest in the present study), St increases to about 0.2 as Re increases.

2.3.2 Near-wake flow regimes

Although the dominant characteristics of the vortex shedding are present, the flow undergoes tremendous changes as Re increases from zero. Different flow regimes are identified by Sumer & Fredsøe (2006) and summarized in figure 2.9.

For $Re < 5$ (figure 2.9a), no separation occurs, such that no recirculation vortices are formed in the wake. For $5 < Re < 40$, a pair of counter-rotating vortices are formed symmetrically about the center-line of the wake (figure 2.9b), and the wake length increases with increasing Re. As Re increases further, the flow becomes unstable, forming the phenomenon called vortex shedding, in which vortices are shed alternately at either side of the cylinder at a certain frequency (see figures 2.9c-h). For $40 < Re < 200$, the vortex street is laminar and uniform in the cylinder span (figure 2.9c).

Figure 2.10: Time-averaged drag coefficient $\overline{C}_D$ for a circular cylinder, presented as a function of the Reynolds number (from Sumer & Fredsøe 2006).

The wake experiences a transition to turbulence as the Reynolds number increases up to 300 (figure 2.9d), and the transition region moves towards the cylinder as Re increases. When $Re \approx 400$, the vortices, once formed, are turbulent. The wake is completely turbulent while the boundary layer

separation on the cylinder remains laminar for $300 < Re < 3 \times 10^5$. This regime is known as the subcritical flow regime (figure 2.9e).

The boundary layer has a transition to turbulence with a further increase of Re. This transition firstly occurs at the boundary layer separation point on one side of the cylinder for $3 \times 10^5 < Re < 3.5 \times 10^5$ (figure 2.9f). This flow regime is called the critical flow regime, which is accompanied with a discontinuous drop in the time-averaged drag force coefficient $\overline{C}_D$ (figure 2.10) and with a non-zero time-averaged lift force coefficient $\overline{C}_L$ (figure 2.11). Here $C_D = 2F_D/(\rho U^2 D)$ where F_D denotes the drag force, $C_L = 2F_L/(\rho U^2 D)$ where F_L is the lift force and ρ is the fluid density. The boundary layer separation becomes turbulent on both sides of the cylinder for $3.5 \times 10^5 < Re < 1.5 \times 10^6$ (figure 2.9g). However, transition to turbulence in the boundary layer has not been completed yet; the region of the transition is located somewhere between the stagnation point and the separation point. This flow is the so-called supercritical flow regime.

The boundary layer becomes fully turbulent on one side of the cylinder and intermittently turbulent on the other side of the cylinder for $1.5 \times 10^6 < Re < 4.5 \times 10^6$ (figure 2.9h). This flow regime is called the upper-transition flow regime. For $Re > 4.5 \times 10^6$, the boundary layer becomes fully turbulent over the cylinder surface (figure 2.9i). This flow regime is called the transcritical flow regime. Varaitions of $\overline{C}_D$ over different flow regimes are presented in figure 2.10. Values of $\overline{C}_D$ decrease as Re increases in the laminar flow regimes, i.e. for $Re < 200$ (of interest in the present study).

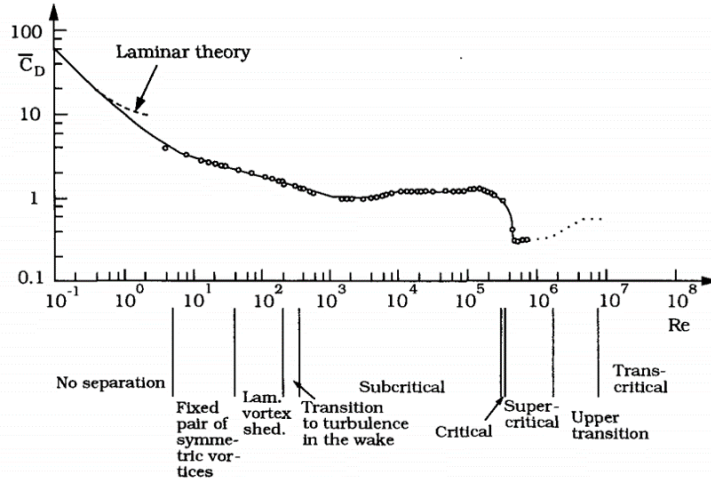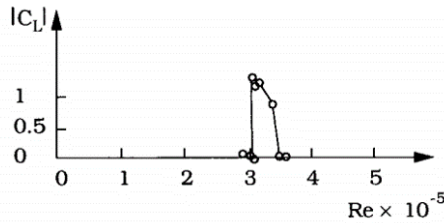*Figure 2.11: Time-averaged lift coefficient $\overline{C}_L$ for a circular cylinder, presented as a function of the Reynolds number (from Sumer & Fredsøe 2006).*

2.3.3   Far-wake flow regimes

The Kármán vortex street in the near-wake region described in the last section has a transition to a two-layered wake further downstream, followed by a second transition to a secondary vortex street with larger spatial scale

than the primary ones. These three wake structures are visualized by vorticity contours in figure 2.12 for $Re = 600$, presented by Jiang & Cheng (2019) using two-dimensional numerical simulations.

Durgin & Karlsson (1971) and Karasudani & Funakoshi (1994) conducted experiments to investigate the physical mechanism underpinning the formation of the two-layered wake. They measured the vertical distance (h) between the upper and lower wake vortices and the horizontal distance (l) between two successive co-rotating vortices along the wake, and found that the ratio (h/l) between these vertical and horizontal distances increases downstream. At a given downstream location, this ratio reaches a critical value where two successive vortices shed from the upper part of the cylinder impose convection of vorticity within the vortex shed from the lower part of the cylinder. This vortex is located horizontally in between the two upper vortices (and vice versa if the two successive vortices shed from the lower part of the cylinder). As a result, this vortex starts to distort and rotate to align with the stream-wise direction, forming the two-layered wake.

Figure 2.12: Wake behind an isolated circular cylinder for Re = 600. This figure is taken from Jiang & Cheng (2019).

Two different theories were proposed for the physical mechanism resulting in the formation of the secondary vortex street. Experiments conducted by Cimbala et al. (1988) showed a broad-band frequency spectra of the cross-stream velocity fluctuation in the far wake. For Reynolds numbers between 100 and 160, the broad-band spectra contains several prominent frequencies considerably lower than the Kármán shedding frequency. These low frequencies are related to the presence of the secondary vortex street with vortical structures of different sizes. In the view of this, Cimbala et al. (1988) attributed the physical mechanism for the secondary vortex street to the hydrodynamic instability of the mean wake. Karasudani & Funakoshi (1994) further identified the mechanism as the convective instability of the time-averaged wake flow.

The second theory explains the formation of the secondary vortex street

in terms of the merging of two-layered vortices. This theory was reported in the experiments conducted by Matsui & Okude (1983) for Reynolds numbers less than 160. Their conclusion was questioned by Cimbala et al. (1988). They argued that the vortex merging observed by Matsui & Okude (1983) may be the merging of the residual smoke patterns since the smoke diffuses downstream at much lower rate than the vortex decays. Matsui & Okude (1983) also conducted experiments for forced (uniform inlet velocity with perturbations) cylinder wakes, and found that two or three vortices merge regularly (depending on the forcing frequency), forming the secondary vortex street. Qualitatively similar behaviors were found by Inoue & Yamazaki (1999) using two-dimensional numerical simulations for forced wakes with Reynolds numbers between 140 and 1000. The explanation of these behaviors, as demonstrated experimentally by Williamson & Prasad (1993) for Reynolds numbers less than 170, is that the far wake flow is sensitive to the free-stream perturbation, which leads to spectral peaks in the wake at the perturbation frequency and at the difference between the Kármán shedding and the perturbation frequencies. Recently, Jiang & Cheng (2019) investigated unforced (uniform inlet velocity without perturbations) cylinder wakes using two-dimensional numerical simulations and found two formation processes for the secondary vortex street; i) the merging of two co-rotating vortices for Reynolds numbers ranging from 200 to 300; ii) the pairing of two counter-rotating vortices, followed by the merging of the paired vortices for Reynolds numbers ranging from 400 to 1000.

2.3.4   Effect of elliptic cross section on the wake

Wakes behind isolated elliptic cylinders have been the focus of some researches due to some practical scenario like the wing and the rotor blade. Figure 2.13 shows a sketch of flow around an elliptic cylinder in a steady current. The aspect ratio (AR) of the elliptic cylinder is defined by a/D, and the Reynolds number (Re) is based on the semi-major axis length D of the cylinder and the free-stream velocity U. Here the flow direction is normal to the semi-major axis of the cylinder.

Figure 2.14 shows the vorticity contours of flow behind an elliptic cylinder of different AR for $Re = 150$ (Thompson et al. 2014). A decrease of AR appears to destabilize the flow, resulting in the formation and irregularity of the secondary vortex street. Moreover, the transition locations for the two-layered wake and secondary vortex street move closer to the cylinder with decreasing AR. They also found that the transition to two-layered wake occurs at a spacing ratio of Kármán vortices larger than the theoretical critical criterion (0.365) obtained by Durgin & Karlsson (1971) and
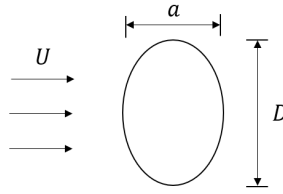
Figure 2.13: Sketch of flow around an elliptic cylinder in a steady current.

Karasudani & Funakoshi (1994) using inviscid methods.

2.4 Effect of wall proximity

This topic is closely related to pipelines placed on an erodible sea bed. Scour may occur below the pipe due to flow action, resulting in suspended spans of the pipeline where the pipe is suspended above the bed with a small gap, usually in the range from $O(0.1D)$ to $O(1D)$. Therefore, it is important to understand the effect of wall proximity on the flow around the pipe.

The key parameters influencing this flow are the Reynolds number (Re), the gap-to-diameter ratio (G/D) and the wall boundary layer thickness to diameter ratio (δ/D) as sketched in figure 2.15. Here the wall boundary layer thickness (δ) at the cylinder's location in the absence of the cylinder is commonly used.

The presence of the wall leads to asymmetry of the flow around the cylinder as shown in figure 2.16. The front stagnation point on the near-wall cylinder shifts towards the gap, and the separation point on the upper part of the near-wall cylinder moves upstream while the separation point on the lower half of the near-wall cylinder moves downstream (figure 2.16b). This causes an asymmetry in the development of vortices shed from the upper and lower parts of the cylinder. The upper vortex grows larger and stronger than the lower vortex. The strength difference between these two vortices reduces their interaction, weakening or completely suppressing the regular, periodic vortex shedding.

Bearman & Zdravkovich (1978) investigated flow around a near-wall cylinder using smoke tunnel measurements, showing that the regular, periodic vortex shedding is completely suppressed at $G/D < 0.3$ for $2.4{\times}10^4 < Re < 4.8{\times}10^4$. Figure 2.17 shows flow patterns visualized by smoke filaments for $G/D = 1.2$ and 0.2, indicating the wide regime (where the vortex shedding exists) and the narrow regime (where the vortex shedding is completely suppressed and the flow is dominated by a strong asymmetric,
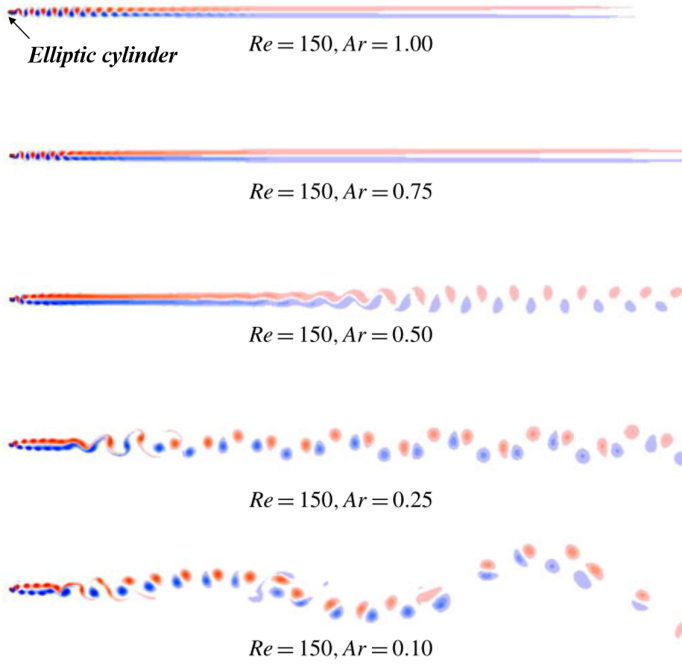
Figure 2.14: Wake behind an isolated elliptic cylinder for the Reynolds number of 150 and for different aspect ratios (AR). This figure is taken from Thompson et al. (2014).

upwards deflected wake), respectively, for $Re = 2.5 \times 10^4$. Many numerical (Sarkar & Sarkar 2010, Ong et al. 2010, Prsic et al. 2016) and experimental (Bearman & Zdravkovich 1978, Buresti & Lanciotti 1992, Lei et al. 1999, He et al. 2017) investigations have been conducted in the subcritical regime, i.e. for values of Re between O(10^3) and O(10^5), showing that the critical gap-to-diameter ratio $(G/D)_c$ for the vortex shedding suppression is about 0.2 to 0.3. Moreover, this critical value was found to be affected by the wall boundary layer thickness at the cylinder location in the absence of the cylinder; some researches show that $(G/D)_c$ decreases as the wall boundary thickness increases (Bearman & Zdravkovich 1978, Buresti & Lanciotti 1992, Lei et al. 1999) while the opposite tendency was reported in some other works (Taniguchi & Miyakoshi 1990, Lei et al. 2000). The reason for this discrepancy is not completely clear. Recently, He et al. (2017) used particle image velocimetry to investigate vortex dynamics at $0 \leq G/D \leq 3$ for $Re = 1047$. Five distinct regions corresponding to different ranges of G/D were identified based on the formation of wake vortices and the secondary
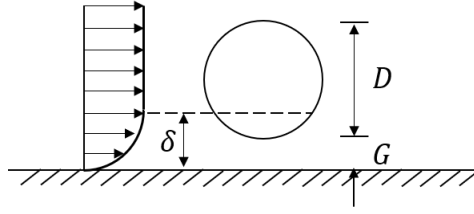
Figure 2.15: Sketch of the flow around a circular cylinder near a plane wall.
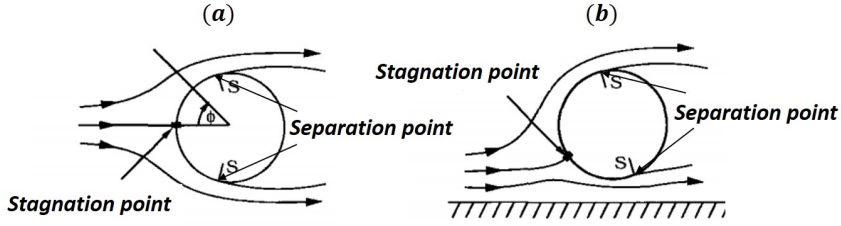
Figure 2.16: Flow around a free (a) and near-wall (b) circular cylinder (from Sumer & Fredsøe 2006).

vortex on the wall as well as the interactions among these vortices.

Regarding the effect of wall proximity on the vortex shedding frequency (St) for the range of G/D where the vortex shedding exists, measurements of Angrilli et al. (1982) show that the vortex shedding frequency tends to increase slightly as G/D decreases. Here G/D ranges from 0.5 to 6 and values of Re are 2860, 3820 and 7460. Similar results was also reported in the experiments conducted by He et al. (2017) for a lower Re of 1072. He et al. (2017) suggested that the defection of the gap flow away from the wall and its following interaction with the upper shear layer may be the cause of the higher vortex shedding frequency. For $Re > 10^4$, the vortex shedding frequency is almost independent of G/D (Bearman & Zdravkovich 1978, Zdravkovich 1985a, Taniguchi & Miyakoshi 1990).

Forces on the cylinder is of direct relevance to the pressure distribution around the cylinder. A dimensionless pressure coefficient (C_p) is commonly used to study the pressure distribution around a cylinder. Here $C_p = 2(p - p_0)/(\rho U^2)$ where p_0 the static pressure in the freestream. Figure 2.18 shows the time-averaged pressure distribution ($\overline{C}_p$) around the cylinder for $Re = 4.8 \times 10^4$ at $G/D = 1$ and 0.1 (Bearman & Zdravkovich 1978). For $G/D = 1$, the distribution of $\overline{C}_p$ is almost symmetric about the horizontal centerline of the cylinder, similar as that for a free cylinder. As G/D decreases to 0.1, the distribution of $\overline{C}_p$ becomes asymmetric (resulting in a non-zero

(**a**)   (**b**)
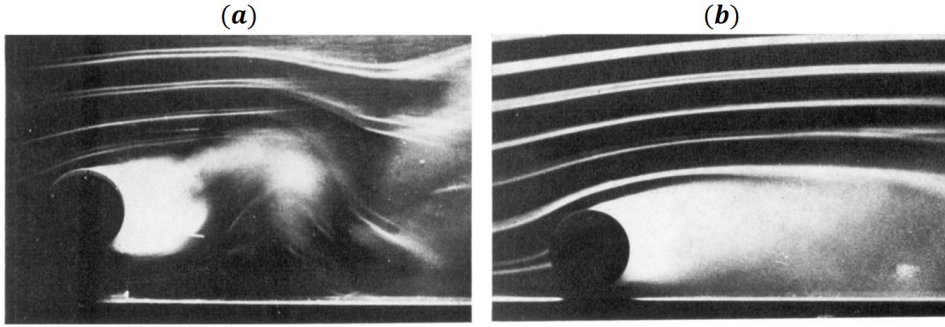
Figure 2.17: Flow patterns of cylinder near a plate for the Reynolds number of 2.5×10⁴ at gap-to-diameter ratios of 1.2 (a) and 0.2 (b). This figure is taken from Bearman & Zdravkovich (1978).

mean lift force discussed further in the next section) and the base pressure becomes less negative than for $G/D = 1$, resulting in a smaller time-averaged drag coefficient. Similar behaviors were observed by Jensen et al. (1990), Zdravkovich (1985a) and Lei et al. (1999) as shown in figure 2.19(a). The differences between various experiments may be attributed to the different values of Re.

The effect of the boundary layer thickness on the mean drag force was investigated experimentally and numerically by Lei et al. (1999) and Kazem-inezhad et al. (2010), respectively. They reported that for a given Re and a given G/D, the base pressure becomes less negative as δ/D increases, forming a smaller $\overline{C}_D$. Zdravkovich (1985a) introduced a new parameter, namely the gap-to-thickness ratio (G/δ). As shown in figure 2.19(b) for different values of Re, $\overline{C}_D$ start to decrease with decreasing G/δ once the cylinder is immersed within the wall boundary layer ($G/\delta \leq 1$). The asymmetry of the pressure distribution around the cylinder at small G/D (figure 2.18b) leads to a non-zero mean lift force. Figure 2.20(a) shows experimental results of $\overline{C}_L$ as a function of G/D for different values of Re (Thomschke 1971, Jones 1971, Fredsøe et al. 1987). As G/D decreases, $\overline{C}_L$ increases due to an increase of suction pressure on the free-stream side of the cylinder and the downward movement of the front stagnation point. At small G/D, $\overline{C}_L$ undergoes a substantial drop. Fredsøe & Hansen (1987) reported that this drop is caused by a decrease of the stagnation pressure (figure 2.20b) due to a small far-field flow velocity (U_s) associated with the stagnation streamline. However, as the cylinder moves extremely close to the wall, more fluid will pass over the top of the cylinder, causing a larger suction pressure on the top half of the cylinder.
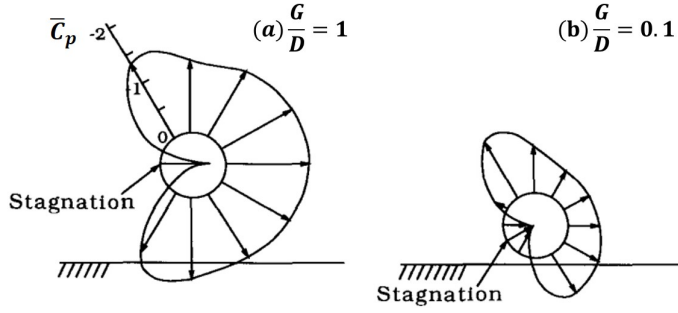
Figure 2.18: Time-averaged pressure coefficients ($\overline{C}_p$) around a cylinder near a wall for G/D=1 and 0.1 (from Sumer & Fredsøe 2006).
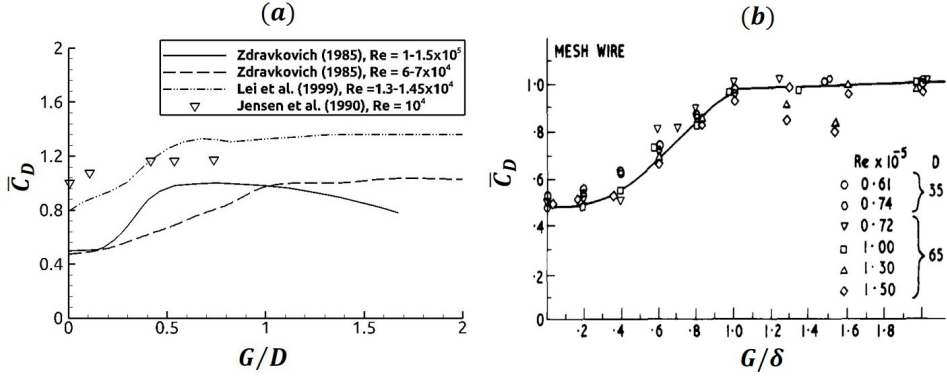
Figure 2.19: Time-averaged drag coefficient ($\overline{C}_D$) around a cylinder near a wall as a function of (a) G/D and (b) G/δ (from Zdravkovich 1985a).

Buresti & Lanciotti (1992) and Lei et al. (1999) investigated the effect of δ/D on the time-averaged lift coefficient $\overline{C}_L$ in their experiments. They reported that as G/D increases $\overline{C}_L$ decreases more rapidly for a larger δ/D. This behavior was explained by Lei et al. (1999); the presence of thick wall boundary layers displaces the positive pressure area in front of the cylinder away from the gap side, generating a downward force. This force contributes to the reduction of the upward lift force.

2.5 Effect of moving wall proximity

Understanding the flow around a cylinder translating above a plane wall is of fundamental importance due to its engineering applications such as a
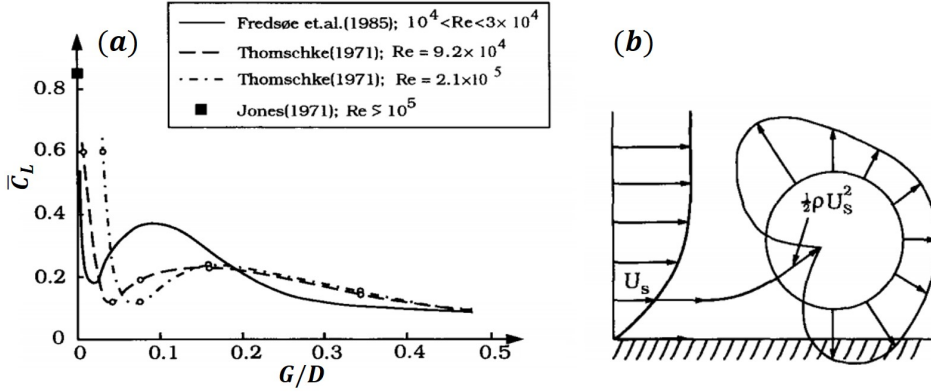
Figure 2.20: (a) time-averaged lift coefficient ($\overline{C}_L$) as a function of G/D; (b) sketch of the stagnation pressure $\frac{1}{2}\rho U_s^2$ (from Sumer & Fredsøe 2006).

submarine moving near a wall in still water. Figure 2.21 shows a sketch of this flow; the cylinder is moving towards the left at a velocity U with a gap G from a plane wall. This flow equals the flow around a fixed cylinder in still water near a wall moving rightwards with a velocity U.
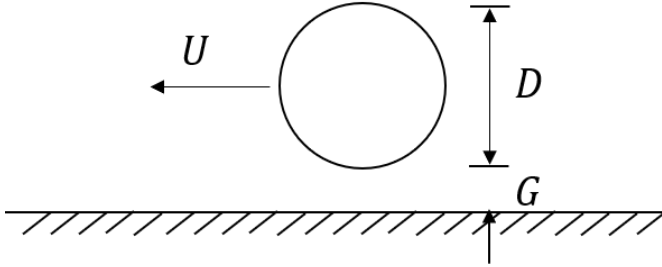
Figure 2.21: Sketch of a circular cylinder translating above a wall.

Taneda (1959) towed a circular cylinder near a plane wall for a Reynolds number of 170 and found that the vortices are alternately shed from the cylinder for the gap-to-diameter ratio of 0.6. As the gap-to-diameter ratio decreases to 0.1, only one single row of vortices was shed from the top of the cylinder. Qualitatively similar behaviors were observed in the experimental work by Zdravkovich (1985b) for the Reynolds number of 3350. Nishino et al. (2007) conducted experiments for two upper-subcritical Reynolds numbers of 0.4×10^5 and 1.0×10^5, classifying three flow regimes: i) the large gap regime (gap ratios larger than 0.5), where the Kármán vortex shedding exists; ii) the intermediate-gap regime (gap-to-diameter ratios larger than

0.35), where the Kármán vortex street becomes intermittent, leading to a rapid decrease of the mean drag coefficient; *iii*) the small-gap regime (gap-to-diameter ratios smaller than 0.35), where the vortex shedding totally ceases, forming two nearly parallel shear layers containing small vortices. Of particular interest, the mean drag coefficient in the small-gap regime is almost constant, suggesting that if the wall boundary layer thickness is sufficiently small the drag reduction is directly related to the vortex shedding suppression.

Huang & Sung (2007) conducted two-dimensional numerical simulations and found that for a Reynolds number of 300 the flow exhibits: *i*) a Kármán vortex shedding at a gap-to-diameter ratio of 0.6; *ii*) a pair-wise vortex shedding where the lift and drag forces fluctuate with a same frequency at a gap-to-diameter ratio of 0.2; *iii*) a single row of vortex shedding from the upper part of the cylinder at a gap-to-diameter ratio of 0.1. They also found that for a given Reynolds number the time-averaged drag coefficient increases to a maximum value as the gap-to-diameter ratio decreases to a critical value (where alternating vortex shedding does not exist) and then decreases as the gap-to-diameter ratio decreases further, coincide with the variation of the base pressure. Jiang et al. (2017) investigated the two- and three-dimensional instabilities for Reynolds numbers up to 300 for gap-to-diameter ratios between 0.1 to 19.5 using numerical simulations, showing that the critical Reynolds number for the onset of the vortex shedding increases with decreasing gap-to-diameter ratios.

References

Angrilli, F., Bergamaschi, S. & Cossalter, V. (1982), 'Investigation of wall induced modifications to vortex shedding from a circular cylinder', *ASME Transactions Journal of Fluids Engineering* **104**, 518–522.

Auteri, F., Parolini, N. & Quartapelle, L. (2002), 'Numerical investigation on the stability of singular driven cavity flow', *Journal of Computational Physics* **183**(1), 1–25.

Bearman, P. W. & Zdravkovich, M. M. (1978), 'Flow around a circular cylinder near a plane boundary', *Journal of Fluid Mechanics* **89**(1), 33–47.

Blackburn, H. M. & Lopez, J. M. (2003), 'The onset of three-dimensional standing and modulated travelling waves in a periodically driven cavity flow', *Journal of Fluid Mechanics* **497**, 289–317.

Botella, O., Forestier, M. Y., Pasquetti, R., Peyret, R. & Sabbah, C. (2001), 'Chebyshev methods for the Navier–Stokes equations: Algorithms and applications', *Nonlinear Analysis: Theory, Methods & Applications* **47**(6), 4157–4168.

Botella, O. & Peyret, R. (1998), 'Benchmark spectral results on the lid-driven cavity flow', *Computers & Fluids* **27**(4), 421–433.

Bruneau, C. H. & Saad, M. (2006), 'The 2D lid-driven cavity problem revisited', *Computers & Fluids* **35**(3), 326–348.

Buresti, G. & Lanciotti, A. (1992), 'Mean and fluctuating forces on a circular cylinder in cross-flow near a plane surface', *Journal of Wind Engineering and Industrial Aerodynamics* **41**(1-3), 639–650.

Burggraf, O. R. (1966), 'Analytical and numerical studies of the structure of steady separated flows', *Journal of Fluid Mechanics* **24**(1), 113–151.

Cheng, M. & Hung, K. C. (2006), 'Vortex structure of steady flow in a rectangular cavity', *Computers & Fluids* **35**(10), 1046–1062.

Cimbala, J. M., Nagib, H. M. & Roshko, A. (1988), 'Large structure in the far wakes of two-dimensional bluff bodies', *Journal of Fluid Mechanics* **190**, 265–298.

Demartino, C. & Ricciardelli, F. (2017), 'Aerodynamics of nominally circular cylinders: A review of experimental results for civil engineering applications', *Engineering Structures* **137**, 76–114.

Dixen, F. H., Sumer, B. M. & Fredsøe, J. (2008), 'Suction removal of sediment from between armor blocks. ii: waves', *Journal of Hydraulic Engineering* **134**(10), 1405–1420.

Durgin, W. W. & Karlsson, S. K. (1971), 'On the phenomenon of vortex street breakdown', *Journal of Fluid Mechanics* **48**(3), 507–527.

Erturk, E. & Gökçöl, C. (2006), 'Fourth-order compact formulation of Navier–Stokes equations and driven cavity flow at high reynolds numbers', *International Journal for Numerical Methods in Fluids* **50**(4), 421–436.

Fredsøe, J. & Hansen, E. A. (1987), 'Lift forces on pipelines in steady flow', *Journal of Waterway, Port, Coastal, and Ocean Engineering* **113**(2), 139–155.

Fredsøe, J., Sumer, B. M., Andersen, J. & Hansen, E. A. (1987), 'Transverse vibrations of a cylinder very close to a plane wall', *Journal of Offshore Mechanics and Arctic Engineering* **109**(1), 52–60.

Ghia, U., Ghia, K. N. & Shin, C. T. (1982), 'High-Re solutions for incompressible flow using the Navier-Stokes equations and a multigrid method', *Journal of Computational Physics* **48**(3), 387–411.

He, G., Wang, J., Pan, C., Feng, L., Gao, Q. & Rinoshika, A. (2017), 'Vortex dynamics for flow over a circular cylinder in proximity to a wall', *Journal of Fluid Mechanics* **812**, 698–720.

Huang, W. & Sung, H. J. (2007), 'Vortex shedding from a circular cylinder near a moving wall', *Journal of Fluids and Structures* **23**(7), 1064–1076.

Inoue, O. & Yamazaki, T. (1999), 'Secondary vortex streets in two-dimensional cylinder wakes', *Fluid Dynamics Research* **25**(1), 1.

Iwatsu, R., Hyun, J. M. & Kuwahara, K. (1992), 'Numerical simulation of flows driven by a torsionally oscillating lid in a square cavity', *Journal of Fluids Engineering* **114**(2).

Jensen, B. L., Sumer, B. M., Jensen, H. R. & Fredsøe, J. (1990), 'Flow around and forces on a pipeline near a scoured bed in steady current', *Journal of Offshore Mechanics and Arctic Engineering* **112**(3), 206–213.

Jiang, H. & Cheng, L. (2019), 'Transition to the secondary vortex street in the wake of a circular cylinder', *Journal of Fluid Mechanics* **867**, 691–722.

Jiang, H., Cheng, L., Draper, S. & An, H. (2017), 'Two- and three-dimensional instabilities in the wake of a circular cylinder near a moving wall', *Journal of Fluid Mechanics* **812**, 435–462.

Jones, W. T. (1971), Forces on submarine pipelines from steady currents, Technical report.

Karasudani, T. & Funakoshi, M. (1994), 'Evolution of a vortex street in the far wake of a cylinder', *Fluid Dynamics Research* **14**(6), 331.

Karniadakis, G., Beskok, A. & Aluru, N. (2006), *Microflows and nanoflows: fundamentals and simulation*, Vol. 29, Springer Science & Business Media.

Kawaguti, M. (1961), 'Numerical solution of the Navier-Stokes equations for the flow in a two-dimensional cavity', *Journal of the Physical Society of Japan* **16**(11), 2307–2315.

Kazeminezhad, M. H., Yeganeh-Bakhtiary, A. & Etemad-Shahidi, A. (2010), 'Numerical investigation of boundary layer effects on vortex shedding frequency and forces acting upon marine pipeline', *Applied Ocean Research* **32**(4), 460–470.

Kuhlmann, H. C. & Romanò, F. (2019), The lid-driven cavity, *in* 'Computational Modelling of Bifurcations and Instabilities in Fluid Dynamics', Springer, pp. 233–309.

Lei, C., Cheng, L., Armfield, S. W. & Kavanagh, K. (2000), 'Vortex shedding suppression for flow over a circular cylinder near a plane boundary', *Ocean Engineering* **27**(10), 1109–1127.

Lei, C., Cheng, L. & Kavanagh, K. (1999), 'Re-examination of the effect of a plane boundary on force and vortex shedding of a circular cylinder', *Journal of Wind Engineering and Industrial Aerodynamics* **80**(3), 263–286.

Leung, J. J. F., Hirsa, A. H., Blackburn, H. M., Marques, F. & Lopez, J. M. (2005), 'Three-dimensional modes in a periodically driven elongated cavity', *Physical Review E* **71**(2), 026305.

Lopez, J. M. & Hirsa, A. H. (2001), 'Oscillatory driven cavity with an air/water interface and an insoluble monolayer: Surface viscosity effects', *Journal of Colloid and Interface Science* **242**(1), 1–5.

Matsui, T. & Okude, M. (1983), Formation of the secondary vortex street in the wake of a circular cylinder, *in* 'Structure of complex turbulent shear flow', Springer, pp. 156–164.

Mendu, S. S. & Das, P. K. (2013), 'Fluid flow in a cavity driven by an oscillating lid - a simulation by Lattice Boltzmann method', *European Journal of Mechanics-B/Fluids* **39**, 59–70.

Moffatt, H. K. (1964), 'Viscous and resistive eddies near a sharp corner', *Journal of Fluid Mechanics* **18**(1), 1–18.

Nielsen, A. W., Sumer, B. M. & Fredsøe, J. (2012), 'Suction removal of sediment from between armor blocks. iii: Breaking waves', *Journal of Hydraulic Engineering* **138**(9), 803–811.

Nishino, T., Roberts, G. T. & Zhang, X. (2007), 'Vortex shedding from a circular cylinder near a moving ground', *Physics of Fluids* **19**(2), 025103.

Ong, M. C., Utnes, T., Holmedal, L. E., Myrhaug, D. & Pettersen, B. (2010), 'Numerical simulation of flow around a circular cylinder close to a flat seabed at high reynolds numbers using a k–ε model', *Coastal Engineering* **57**(10), 931–947.

Ovando, G., Juarez, H., Huelsz, G. & Ramos, E. (2009), 'Vortex formation in a cavity with oscillating walls', *Physics of Fluids* **21**(2), 024101.

Prsic, M. A. (2016), Numerical simulations of the flow around single and tandem circular cylinders close to a plane wall, PhD thesis, Norwegian University of Science and Technology.

Prsic, M. A., Ong, M. C., Pettersen, B. & Myrhaug, D. (2016), 'Large Eddy Simulations of flow around a circular cylinder close to a flat seabed', *Marine Structures* **46**, 127–148.

Sarkar, S. & Sarkar, S. (2010), 'Vortex dynamics of a cylinder wake in proximity to a wall', *Journal of Fluids and Structures* **26**(1), 19–40.

Schlichting, H. & Gersten, K. (2016), *Boundary-layer theory*, Springer.

Schultz, W. W., Lee, N. Y. & Boyd, J. P. (1989), 'Chebyshev pseudospectral method of viscous flows with corner singularities', *Journal of Scientific Computing* **4**(1), 1–24.

Shankar, P. N. & Deshpande, M. D. (2000), 'Fluid mechanics in the driven cavity', *Annual Review of Fluid Mechanics* **32**(1), 93–136.

Shukla, R. K., Tatineni, M. & Zhong, X. (2007), 'Very high-order compact finite difference schemes on non-uniform grids for incompressible Navier–Stokes equations', *Journal of Computational Physics* **224**(2), 1064–1094.

Soh, W. Y. & Goodrich, J. W. (1988), 'Unsteady solution of incompressible Navier-Stokes equations', *Journal of Computational Physics* **79**(1), 113–134.

Sumer, B. M., Cokgor, S. & Fredsøe, J. (2001), 'Suction removal of sediment from between armor blocks', *Journal of Hydraulic Engineering* **127**(4), 293–306.

Sumer, B. M. & Fredsøe, J. (2006), *Hydrodynamics around cylindrical strucures*, World Scientific.

Taneda, S. (1959), 'Downstream development of the wakes behind cylinders', *Journal of the Physical Society of Japan* **14**(6), 843–848.

Taniguchi, S. & Miyakoshi, K. (1990), 'Fluctuating fluid forces acting on a circular cylinder and interference with a plane wall', *Experiments in Fluids* **9**(4), 197–204.

Thompson, M. C., Radi, A., Rao, A., Sheridan, J. & Hourigan, K. (2014), 'Low-Reynolds-number wakes of elliptical cylinders: from the circular cylinder to the normal flat plate', *Journal of Fluid Mechanics* **751**, 570–600.

Thomschke, H. (1971), 'Experimentelle untersuchung der stationären umströmung von kugel und zylinder in wandnähe.', *Fakultät für Mashchinenbau der Universität Karlsruhe, Karlsruhe, West Germany* .

Vogel, M. J., Hirsa, A. H. & Lopez, J. M. (2003), 'Spatio-temporal dynamics of a periodically driven cavity flow', *Journal of Fluid Mechanics* **478**, 197–226.

Williamson, C. H. K. & Prasad, A. (1993), 'A new mechanism for oblique wave resonance in the 'natural'far wake', *Journal of Fluid Mechanics* **256**, 269–313.

Zdravkovich, M. M. (1985*a*), 'Forces on a circular cylinder near a plane wall', *Applied Ocean Research* **7**(4), 197–201.

Zdravkovich, M. M. (1985*b*), Observation of vortex shedding behind a towed circular cylinder near a wall, *in* 'Flow Visualization III', pp. 423–427.

Zumbrunnen, D. A., Miles, K. C. & Liu, Y. H. (1996), 'Auto-processing of very fine-scale composite materials by chaotic mixing of melts', *Composites Part A: Applied Science and Manufacturing* **27**(1), 37–47.

Chapter 3

Numerical method

3.1 Governing equation

Incompressible flow with a constant density ρ and kinematic viscosity ν is governed by the Navier-Stokes equations described as follows

$$\frac{\partial u_i}{\partial x_i} = 0 \tag{3.1}$$

$$\frac{\partial u_i}{\partial t} + \frac{\partial u_i u_j}{\partial x_j} = -\frac{1}{\rho}\frac{\partial p}{\partial x_i} + \nu\frac{\partial^2 u_i}{\partial x_j \partial x_j} \tag{3.2}$$

where the Einstein notation using repeated indices is applied. Here $u_i = (u,\ v,\ w)$ and $x_i = (x,\ y,\ z)$ for $i = 1,\ 2$ and 3 indicate the velocity and Cartesian coordinates, respectively, whilst t and p denote the time and pressure, respectively.

3.2 Non-iterative projection method

A non-iterative projection method, proposed by Armfield & Street (2002), is applied to solve Eqs.(3.1) and (3.2). This method is identical to the iterative method but with only a single iteration carried out at each time step. The Adams–Bashforth and Crank-Nicolson schemes are used for the convective and viscous terms, respectively. The spatial derivatives are evaluated by means of second-order, central finite-difference operators on a staggered grid arrangement. The intermediate velocity u_i^* is obtained as

$$u_i^* = u_i^n + \Delta t[\frac{1}{2}(3H_i^n - H_i^{n-1}) + \frac{1}{2}(F_i^n + F_i^*) - \frac{1}{\rho}\frac{\delta}{\delta x_i}(p^{n-1/2})] \tag{3.3}$$

where $\delta/\delta x_i$ represents the numerical spatial gradient operator; the convective and diffusive terms are denoted by $H_i = \delta(u_i u_j)/\delta x_j$ and $F_i = \nu\delta^2(u_i)/(\delta x_j \delta x_j)$, respectively; the superscript n denotes the time step, and $p^{n-1/2}$ indicates the pressure obtained at the previous time-step. This intermediate velocity will not initially satisfy the continuity, i.e. Eq.(3.1). A correction of the velocity is then given by

$$u_i^{n+1} = u_i^* - \Delta t \frac{\delta}{\delta x_j}(\phi^{n+1}) \tag{3.4}$$

where $\phi^{n+1} = p^{n+1/2} - p^{n-1/2}$ is determined such that the resulting velocity field u_i^{n+1} satisfies the continuity condition. Substitution of Eq.(3.4) into the continuity equation $\delta u_i/\delta x_i = 0$ yields a Poisson equation for the pressure correction

$$\frac{\delta^2}{\delta x_j^2}(\phi^{n+1}) = -\frac{1}{\Delta t}\frac{\delta u_i^*}{\delta x_i} \tag{3.5}$$

As the pressure correction $p^{n+1/2} = p^{n-1/2} + \phi^{n+1}$ is only solved once each time-step, it is necessary to obtain an accurate solution ϕ^{n+1} of the Poisson equation. Hence a Jacobi preconditioned biconjugate gradient stabilized method is used to solve Eq.(3.5).

3.3   Immersed boundary method

The immersed boundary method (IBM) has been studied and applied extensively due to its great advantage in mesh generation, memory and CPU saving and parallelization. This method was firstly introduced by Peskin (1972) and has been considerably extended since then Iaccarino & Verzicco (2003) and Mittal & Iaccarino (2005). The underlying physics of IBM is to add an additional body-force term f_i to the Eq.(3.2), thus yielding

$$\frac{\partial u_i}{\partial t} + \frac{\partial u_i u_j}{\partial x_j} = -\frac{1}{\rho}\frac{\partial p}{\partial x_i} + \nu\frac{\partial^2 u_i}{\partial x_j \partial x_j} + f_i \tag{3.6}$$

The IBM can be categorized as continuous forcing approach or discrete forcing approach. In the continuous forcing approach, Eq.(3.6) is discretized on a Cartesian grid and solved in the entire domain. This method is used successfully for problems with elastic bodies such as cardiac mechanics (Peskin 1982), bubble dynamics (Unverdi & Tryggvason 1992), aquatic animal locomotion (Fauci & McDonald 1995) and flow past flexible filaments (Zhu & Peskin 2003). However, this method is not suitable for problems with rigid
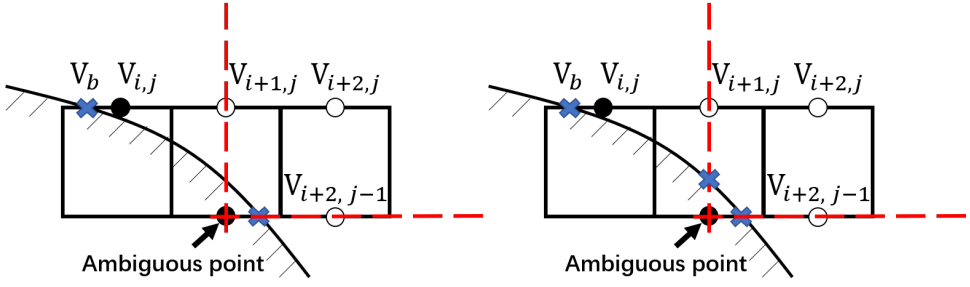
Figure 3.1: Treatment of the immersed boundary by Fadlun et al. (2000) (left) and Peller et al. (2006) (right).
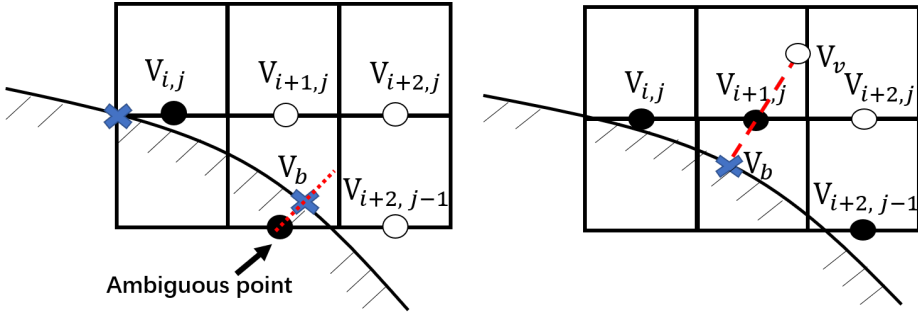
Figure 3.2: Treatment of the immersed boundary by Kim et al. (2001) (left) and Balaras (2004) (right).

bodies due to the rigid limit and numerical stability constraint (Stockie & Wetton 1999, Lai & Peskin 2000).

In the discrete forcing approach, Eq.(3.6) is firstly discretized on a Cartisian grid disregarding the immersed boundary, i.e. $f_i = 0$. Then, the boundary condition is imposed implicitly or explicitly on the immersed boundary. Mohd-Yusof (1997) firstly proposed this method by reversing the tangential velocities across the immersed boundary and preserving the normal velocities. Fadlun et al. (2000) further developed this method in conjunction with a finite difference method. As shown in the left image of figure 3.1, the forcing term is imposed on the velocity point ($V_{i,j}$) closest to the immersed boundary. The value of this velocity point is linearly interpolated using its adjacent grid velocity ($V_{i+1,j}$) and the boundary value (V_b). However, an ambiguity of the interpolation direction can arise when the enforced velocity point can be interpolated in two directions (marked by the red dashed line in the left image of figure 3.1). To eliminate this ambiguity, several different methods have been introduced. Peller et al. (2006) (right
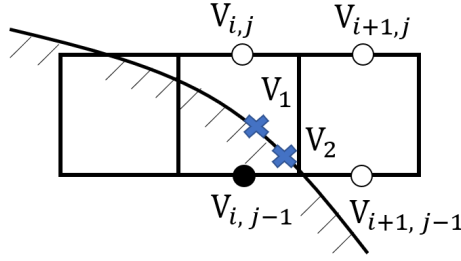
Figure 3.3: Treatment of the immersed boundary by Zhang & Zheng (2007).

image of figure 3.1) obtained the value at the ambiguous point from a sum of values interpolated in each direction where a weighted factor is multiplied based on the horizontal and vertical distances between the ambiguous point and the immersed boundary. Kim et al. (2001) (left image of figure 3.2) calculated the value at the ambiguous point by a bilinear extrapolation using the intersection point (V_b) between the immersed boundary and the wall-normal line through the ambiguous point and three surrounding velocities ($V_{i+1,j}$, $V_{i+2,j}$ and $V_{i+2,j-1}$). They also introduced a mass source/sink for the grid containing the immersed boundary to satisfy the mass conservation. Balaras (2004) (right image of figure 3.2) introduced a virtual point V_v on the line normal to the boundary. The enforced point ($V_{i+1,j}$) can be obtained from a linear interpolation using V_b and V_v which can be interpolated using its surrounding points in the fluid. Later on, Gilmanov & Sotiropoulos (2005) introduced a quadratic interpolation method which improves the accuracy in problems with moving boundaries. Zhang & Zheng (2007) proposed a method, in which (figure 3.3) V_1 on the immersed boundary is firstly calculated by a bilinear interpolation method using its surrounding four points ($V_{i,j}$, $V_{i+1,j}$, $V_{i+2,j}$ and $V_{i+2,j-1}$). Then, the difference between the desired boundary value and the calculated boundary value, i.e. V_b-V_1, is extrapolated to the internal layer grid point $V_{i,j}$ using the same bilinear weighting functions. Moreover, more boundary points like V_2 surrounded by the same grid points can be interpolated and extrapolated in the similar way, and then $V_{i,j}$ can by obtained by averaging the values extrapolated from different boundary differences, e.g. V_b-V_1 and V_b-V_2. In this way, the immersed boundary resolution can be improved by increasing the number of boundary points instead of increasing the grid resolution (Fadlun et al. 2000, Kim et al. 2001, Gilmanov et al. 2003).

The concept of ghost cells introduces an alternative way of imposing the boundary conditions. The variables (velocity and pressure) located within the immersed boundary are identified as ghost points, which are
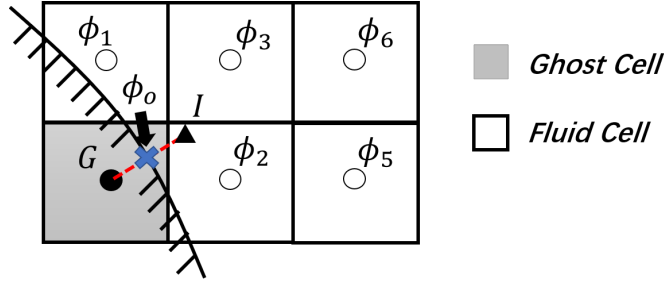
Figure 3.4: Definition of the ghost cell.

extrapolated using values from the flow field and the boundary. On a non-staggered grid arrangement, the ghost values for velocities and pressure are obtained on the same grid while on a staggered grid arrangement, each velocity component and pressure need to be calculated at different grids. Here the boundary conditions are implicitly incorporated through the ghost cells while the numerical operators do not need to be reformulated near the boundary. Majumdar et al. (2001) and Tseng & Ferziger (2003) use two-dimensional linear and quadratic interpolation involving boundary points and fluid points near the boundary to construct the local polynomial as shown in figure 3.4. A ghost cell method using a two-dimensional linear interpolation is described briefly here. The linear interpolation in a two-dimensional space is given by

$$\phi = a_0 + a_1 x + a_2 y \qquad (3.7)$$

where ϕ denotes the variable value and (x, y) is the coordinate of the variable. The value at the ghost point (ϕ_G) is a weighted combination of ϕ_0, ϕ_1 and ϕ_2 where ϕ_0 denotes the boundary value on the wall normal line through the ghost point, ϕ_1 and ϕ_2 are the two nearest fluid points. These three coefficients can be obtained by

$$a_n = B^{-1}\phi_n \quad n = 0, 1 \text{ and } 2 \qquad (3.8)$$

$$B = \begin{bmatrix} 1 & x_0 & y_0 \\ 1 & x_1 & y_1 \\ 1 & x_2 & y_2 \end{bmatrix} \qquad (3.9)$$

where (x_0, y_0), (x_1, y_1) and (x_2, y_2) denote the coordinates of the corresponding three points. In this approach, ϕ_G is obtained by an extrapolation which may have large and negative weighting coefficients, resulting in severe numerical instability. To eliminate this drawback, an image point I is
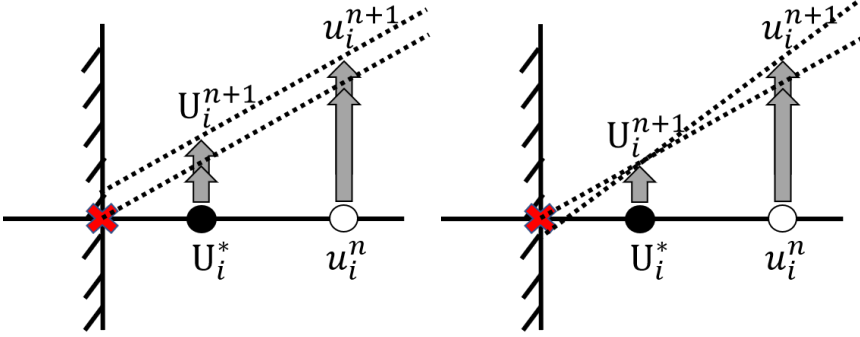
Figure 3.5: Example of inconsistent wall condition for pressure. Left image: no wall condition; right image: Neumann condition for pressure correction imposed at enforcing points.

identified in the fluid, along the wall normal line through G. It lies at the same distance as G away from the boundary point (figure 3.4). The value at the image point (ϕ_I) can be interpolated using its nearby fluid values (e.g. ϕ_2 and ϕ_3) and the boundary value (ϕ_0), such that the weighting coefficient are guaranteed to be positive and less than unity. Then the values at the ghost point can be given by

$$\phi_G = 2\phi_0 - \phi_I \tag{3.10}$$

$$\phi_G = \phi_I \tag{3.11}$$

where Eqs.(3.10) and (3.11) denote the enforcement of the Dirichlet velocity condition and Nuemann pressure condition on the wall, respectively.

It should be noted that in the above immersed boundary method, the wall condition for pressure and velocity is inconsistent. Left image of figure 3.5 shows the method of, e.g. Mohd-Yusof (1997), Fadlun et al. (2000) and Balaras (2004), in which no wall condition for the pressure is imposed. The intermediate enforcing velocity (U_i^*) is interpolated using the grid velocity (u_i^*) and the wall velocity. After the pressure correction, the updated velocity U_i^{n+1} and u_i^{n+1} do not meet the wall condition. Figure 3.5 shows the method of, e.g. Tseng & Ferziger (2003) and Peller et al. (2006), in which the Neumann condition for the pressure correction is imposed at the enforcing point (U_i^*), which remains the same at the new time step (U_i^{n+1}). However, the grid velocity (u_i^{n+1}) is updated, resulting in the inconsistency with the wall condition. To eliminate this inconsistency, Ikeno & Kajishima (2007) and Berthelsen & Faltinsen (2008) introduced an enforcing pressure gradient, which is interpolated by the Neumann pressure condition at the
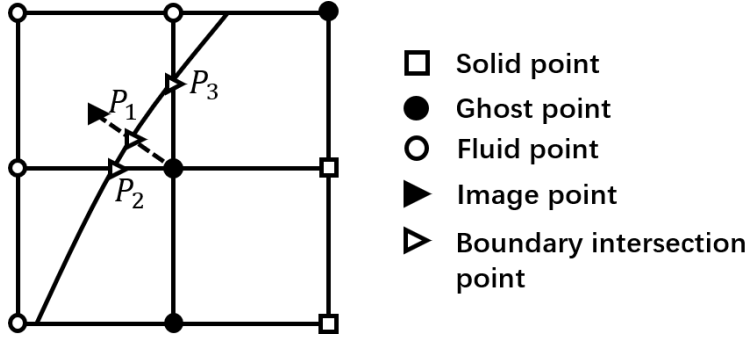
Figure 3.6: Conventional ghost-cell method: sketch for a two-dimensional case.

immersed boundary and pressure gradients at adjacent grid points. For instance, using an quadratic Lagrange polynominal (Berthelsen & Faltinsen 2008) in x-direction gives

$$\left(\frac{\partial p}{\partial x}\right)_g = \frac{2}{a(a+1)}\left(\frac{\partial p}{\partial x}\right)_\Gamma + \frac{2(a-1)}{a}\left(\frac{\partial p}{\partial x}\right)_{i-1} - \frac{a-1}{a+1}\left(\frac{\partial p}{\partial x}\right)_{i-2} \quad (3.12)$$

where the suffixes g, Γ, $i-1$ and $i-2$ denote the values obtained at the forcing point, immersed boundary, the first and second nearest grid points, respectively, while a is the horizontal distance between the enforcing point and the immersed boundary.

In a recent work, Chi et al. (2019) reported the main bottlenecks of the conventional ghost-cell method; *i*) the convergence rate of the truncation error is fluctuating and not persistent since the error term based on the distance between the ghost cell and the boundary does not necessarily converge as the grid size; *ii*) for multi-directional simulations, as explained in figure 3.6, the intersection point P_1 between the boundary and the wall-normal line through the ghost point is implicitly enforced by extrapolating the values at the ghost point, while the boundary intersection points P_2 and P_3 relevant to the numerical discretization stencil are not; *iii*) when considering high-order spatial discretization schemes, multiple layers of ghost points are required, resulting in more complex problems relevant to the first bottleneck and also leads to a complex implementation such as the parallelization and accurate predictions of the boundary layer at sharp corners. To eliminate second drawback, they employed two different sets of independent ghost values at the same ghost cell, accounting for the presence of the two boundary points P_2 and P_3. To eliminate the third drawback, the order of the discretization scheme is reduced progressively as the interpolation

points move closer to the immersed boundary, such that only one layer of ghost points is required to reconstruct the boundary forces.

The above discrete immersed boundary methods can also be classified as sharp-interface direct-forcing methods, in which the forcing term (f_i) is directly imposed on the Eulerian grid which is not coincide with the body surface. These methods are particularly attractive for simulating the flow around complex rigid geometries due to its simplicity of implementation into existing finite-difference or finite-volume methods. However, in these methods, the boundary motion/deformation can lead to spurious oscillations of hydrodynamic forces (Lee & You 2013), which are also potential sources of the numerical instability. In order to suppress the force oscillations, a family of discrete immersed boundary methods are introduced and classified as smooth-interface direct forcing formulations, in which the forcing terms are calculated on a set of Lagrangian points representing the body surface in conjunction with spreading operations of these forces towards the nearby Eulerian grids.

Silva et al. (2003) proposed a smooth-interface direct forcing formulation, named "Physical Virtual Model". The Lagrangian forces are calculated using second-order Lagrange polynomials. Then, the computed forces are distributed to Eulerian grids using a Dirac delta function. A drawback of this method is that the polynomials approximations are not necessarily consistent with the discretization of the momentum equations from which the forces are derived. Uhlmann (2005) introduced an improved method, in which the Peskin's regularized delta function approach (Peskin 2002) is used for the force transfer between Lagrangian and Eulerian locations. The basic computational algorithm steps for this force transfer are briefly described here. Firstly, the intermediate velocity on the Lagrangian points can be obtained from surrounding Eurlerian grids as follows:

$$u_k^* = \sum_{x \in \Gamma} u_E^* \cdot \delta_h(x_k - x_E) \cdot h^2 \tag{3.13}$$

where x_k and x_E denote the locations of the Lagrangian points and Eulerian points, respectively, and $\delta_h(x_k - x_E)$ and u_E^* represent the delta function as well as the intermediate velocity on the Eulerian grids, respectively. Then, the Lagrangian forces can be obtained by

$$F_k(x_k) = \frac{u_L - u_k^*}{\Delta t} \tag{3.14}$$

where u_L is the desired velocity at the Lagrangian points. The effect of the

Lagrangian forces then spreads into the Eulerian grids by

$$f(x_E) = \sum_{k=1}^{N} F_k(x_k) \cdot \delta_h(x_E - x_k) \cdot \Delta V_k \tag{3.15}$$

where N is the number of Lagrangian points, and ΔV_k denotes the discrete volume for each Lagrangian point.

However, this method can violate the no-slip condition in simulations where the Reynolds number is low and the CFL number is large (Kempe & Fröhlich 2012, Park et al. 2016). A concept of multi-direct forcing (Yu & Shao 2007, Wang et al. 2008, Kempe & Fröhlich 2012, Breugem 2012) is introduced to improve the enforcement of the no-slip condition. In their methods, the Lagrangian forces within the predictor step are corrected iteratively before solving the equation for pressure correction. In recent years, the smooth-interface direct forcing formulations gain much attention and have been further improved; e.g. Luo et al. (2019) proposed an improved multi-direct forcing method to dynamically correct effective hydrodynamic diameters of the particles, which affects the prediction accuracy for both drag and flow field, in the particle-laden flow; Azis et al. (2019) implemented the smooth-interface direct forcing method on non-conforming, unstructured grids.

Cut-cell methods (Ye et al. 1999, Muralidharan & Menon 2016) have also drawn a lot of attention because the conservation of mass and momentum is strictly enforced by the body-fitted cut-cells, avoiding the spurious force fluctuations observed in the ghost cell methods (Lee et al. 2011). However, there are two main problems arising in the cut-cell method; i) the presence of very small cut-cells, leading to an extremely small simulation time-step and stiffness of the resulting system of linear equations; ii) the presence of irregularities in the stencil spacing of the grid point adjacent to the boundaries, causing the numerical oscillations. Several methods have been introduced for solving the first issue such as (a) the cell-merging approach (Ye et al. 1999, Chung 2006), in which the small cell is merged with its adjacent cell to create a larger cell, (b) the cell linking approach (Kirkpatrick et al. 2003), where two cells are linked as a "master/slave" pair in which the pressure gradient and velocity correction calculated at the master node are used for the slave node, (c) cell mixing/redistribution (Meyer et al. 2010, Seo & Mittal 2011), where the numerical fluxes from the small cells are mixed with the surrounding cells in a conservative manner.
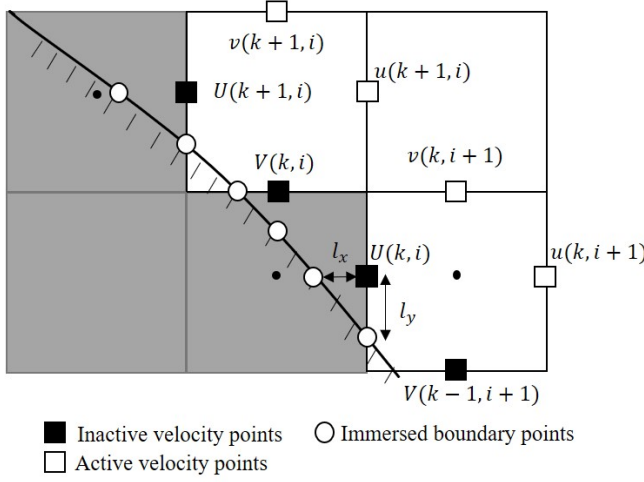
Figure 3.7: Definition of the inactive velocity points (■), immersed bound-
ary points (○), and active velocity points (□).

3.4   Present immersed boundary method

In the present work, an immersed boundary method based on the ideas of
Peller et al. (2006) is used to treat the solid surface. Figure 3.7 shows the
treatment of the relationship between the Cartesian grid and the immersed
boundary. A grid cell is blocked out of the simulation if its corresponding
variable (velocity or pressure) lies within the immersed boundary. Then,
the velocity point at the cell face between a blocked cell and an unblocked
cell is set as an inactive velocity (■), which are updated by interpolation
using boundary condition at the immersed boundary points (○) and ac-
tive velocity points (□) within the fluids. Here, a one-dimensional, cubic
Lagrange interpolation scheme is applied according to the following stencil
formulation.

$$f(x) = \sum_{k=1}^{3} \beta_k(x) f_k + \beta(x_\Gamma) f_\Gamma \tag{3.16}$$

where $f(x)$, f_k and f_Γ represent the velocity values at the inactive points,
the active velocity points and the immersed boundary, respectively, and the

Lagrange coefficients $\beta_k(x)$ and $\beta(x_\Gamma)$ can be obtained by

$$\beta_k(x) = \left(\prod_{j=1, j \neq k}^{3} \frac{(x - x_j)}{(x_k - x_j)} \right) \frac{x - x_\Gamma}{x_k - x_\Gamma} \qquad (3.17)$$

$$\beta(x_\Gamma) = \left(\prod_{j=1}^{3} \frac{(x - x_j)}{(x_\Gamma - x_j)} \right) \qquad (3.18)$$

If an inactive velocity point can be interpolated from two directions, each direction is multiplied by a weighting factor as follows

$$f(x) = \lambda_x f^x + \lambda_y f^y \qquad (3.19)$$

where the superscript x and y denotes the interpolation in x and y-directions, respectively, and the weighting factors λ_x and λ_y are given as

$$\lambda_x = \frac{1}{1 + (\frac{l_x}{l_y})^2} \quad and \quad \lambda_y = \frac{1}{1 + (\frac{l_y}{l_x})^2} \qquad (3.20)$$

where l_x and l_y is the distance between the inactive velocity point and the immersed boundary in x and y-directions, respectively, as shown in figure 3.7. Moreover, a Neumann condition for pressure correction is applied at the inactive velocity points.

References

Armfield, S. & Street, R. (2002), 'The pressure accuracy of fractional-step methods for the navier-stokes equations on staggered grids', *ANZIAM Journal* **44**, 20–39.

Azis, M. H. A., Evrard, F. & van Wachem, B. (2019), 'An immersed boundary method for incompressible flows in complex domains', *Journal of Computational Physics* **378**, 770–795.

Balaras, E. (2004), 'Modeling complex boundaries using an external force field on fixed cartesian grids in large-eddy simulations', *Computers & Fluids* **33**(3), 375–404.

Berthelsen, P. A. & Faltinsen, O. M. (2008), 'A local directional ghost cell approach for incompressible viscous flow problems with irregular boundaries', *Journal of Computational Physics* **227**(9), 4354–4397.

Breugem, W.-P. (2012), 'A second-order accurate immersed boundary method for fully resolved simulations of particle-laden flows', *Journal of Computational Physics* **231**(13), 4469–4498.

Chi, C., Abdelsamie, A. & Thévenin, D. (2019), 'A directional ghost-cell immersed boundary method for incompressible flows', *Journal of Computational Physics* p. 109122.

Chung, M.-H. (2006), 'Cartesian cut cell approach for simulating incompressible flows with rigid bodies of arbitrary shape', *Computers & Fluids* **35**(6), 607–623.

Fadlun, E., Verzicco, R., Orlandi, P. & Mohd-Yusof, J. (2000), 'Combined immersed-boundary finite-difference methods for three-dimensional complex flow simulations', *Journal of Computational Physics* **161**(1), 35–60.

Fauci, L. J. & McDonald, A. (1995), 'Sperm motility in the presence of boundaries', *Bulletin of Mathematical Biology* **57**(5), 679–699.

Gilmanov, A. & Sotiropoulos, F. (2005), 'A hybrid cartesian/immersed boundary method for simulating flows with 3d, geometrically complex, moving bodies', *Journal of Computational Physics* **207**(2), 457–492.

Gilmanov, A., Sotiropoulos, F. & Balaras, E. (2003), 'A general reconstruction algorithm for simulating flows with complex 3d immersed boundaries on cartesian grids', *Journal of Computational Physics* **191**(2), 660–669.

Iaccarino, G. & Verzicco, R. (2003), 'Immersed boundary technique for turbulent flow simulations', *Applied Mechanics Reviews* **56**(3), 331–347.

Ikeno, T. & Kajishima, T. (2007), 'Finite-difference immersed boundary method consistent with wall conditions for incompressible turbulent flow simulations', *Journal of Computational Physics* **226**(2), 1485–1508.

Kempe, T. & Fröhlich, J. (2012), 'An improved immersed boundary method with direct forcing for the simulation of particle laden flows', *Journal of Computational Physics* **231**(9), 3663–3684.

Kim, J., Kim, D. & Choi, H. (2001), 'An immersed-boundary finite-volume method for simulations of flow in complex geometries', *Journal of Computational Physics* **171**(1), 132–150.

Kirkpatrick, M., Armfield, S. & Kent, J. (2003), 'A representation of curved boundaries for the solution of the navier–stokes equations on a staggered three-dimensional cartesian grid', *Journal of Computational Physics* **184**(1), 1–36.

Lai, M.-C. & Peskin, C. S. (2000), 'An immersed boundary method with formal second-order accuracy and reduced numerical viscosity', *Journal of Computational Physics* **160**(2), 705–719.

Lee, J., Kim, J., Choi, H. & Yang, K.-S. (2011), 'Sources of spurious force oscillations from an immersed boundary method for moving-body problems', *Journal of Computational Physics* **230**(7), 2677–2695.

Lee, J. & You, D. (2013), 'An implicit ghost-cell immersed boundary method for simulations of moving body problems with control of spurious force oscillations', *Journal of Computational Physics* **233**, 295–314.

Luo, K., Wang, Z., Tan, J. & Fan, J. (2019), 'An improved direct-forcing immersed boundary method with inward retraction of lagrangian points for simulation of particle-laden flows', *Journal of Computational Physics* **376**, 210–227.

Majumdar, S., Iaccarino, G. & Durbin, P. (2001), 'Rans solvers with adaptive structured boundary non-conforming grids'.

Meyer, M., Hickel, S. & Adams, N. (2010), 'Assessment of implicit large-eddy simulation with a conservative immersed interface method for turbulent cylinder flow', *International Journal of Heat and Fluid Flow* **31**(3), 368–377.

Mittal, R. & Iaccarino, G. (2005), 'Immersed boundary methods', *Annual Review of Fluid Mechanics* **37**, 239–261.

Mohd-Yusof, J. (1997), 'Combined immersed boundary/b-spline method for simulations of flows in complex geometries in complex geometries ctr annual research briefs, nasa ames', *NASA Ames/Stanford University* .

Muralidharan, B. & Menon, S. (2016), 'A high-order adaptive cartesian cut-cell method for simulation of compressible viscous flow over immersed bodies', *Journal of Computational Physics* **321**, 342–368.

Park, H., Pan, X., Lee, C. & Choi, J.-I. (2016), 'A pre-conditioned implicit direct forcing based immersed boundary method for incompressible viscous flows', *Journal of Computational Physics* **314**, 774–799.

Peller, N., Duc, A. L., Tremblay, F. & Manhart, M. (2006), 'High-order stable interpolations for immersed boundary methods', *International Journal for Numerical Methods in Fluids* **52**(11), 1175–1193.

Peskin, C. S. (1972), 'Flow patterns around heart valves: a numerical method', *Journal of Computational Physics* **10**(2), 252–271.

Peskin, C. S. (1982), 'The fluid dynamics of heart valves: experimental, theoretical, and computational methods', *Annual Review of Fluid Mechanics* **14**(1), 235–259.

Peskin, C. S. (2002), 'The immersed boundary method', *Acta Numerica* **11**, 479–517.

Seo, J. H. & Mittal, R. (2011), 'A sharp-interface immersed boundary method with improved mass conservation and reduced spurious pressure oscillations', *Journal of Computational Physics* **230**(19), 7347–7363.

Silva, A. L. E., Silveira-Neto, A. & Damasceno, J. (2003), 'Numerical simulation of two-dimensional flows over a circular cylinder using the immersed boundary method', *Journal of Computational Physics* **189**(2), 351–370.

Stockie, J. M. & Wetton, B. R. (1999), 'Analysis of stiffness in the immersed boundary method and implications for time-stepping schemes', *Journal of Computational Physics* **154**(1), 41–64.

Tseng, Y.-H. & Ferziger, J. H. (2003), 'A ghost-cell immersed boundary method for flow in complex geometry', *Journal of Computational Physics* **192**(2), 593–623.

Uhlmann, M. (2005), 'An immersed boundary method with direct forcing for the simulation of particulate flows', *Journal of Computational Physics* **209**(2), 448–476.

Unverdi, S. O. & Tryggvason, G. (1992), 'A front-tracking method for viscous, incompressible, multi-fluid flows', *Journal of Computational Physics* **100**(1), 25–37.

Wang, H., Chessa, J., Liu, W. K. & Belytschko, T. (2008), 'The immersed/fictitious element method for fluid–structure interaction: volumetric consistency, compressibility and thin members', *International Journal for Numerical Methods in Engineering* **74**(1), 32–55.

Ye, T., Mittal, R., Udaykumar, H. & Shyy, W. (1999), 'An accurate cartesian grid method for viscous incompressible flows with complex immersed boundaries', *Journal of Computational Physics* **156**(2), 209–240.

Yu, Z. & Shao, X. (2007), 'A direct-forcing fictitious domain method for particulate flows', *Journal of Computational Physics* **227**(1), 292–314.

Zhang, N. & Zheng, Z. C. (2007), 'An improved direct-forcing immersed-boundary method for finite difference applications', *Journal of Computational Physics* **221**(1), 250–268.

Zhu, L. & Peskin, C. S. (2003), 'Interaction of two flapping filaments in a flowing soap film', *Physics of Fluids* **15**(7), 1954–1960.

Chapter 4

Vortex dynamics and flow patterns in a two-dimensional oscillatory lid-driven rectangular cavity

Jianxun Zhu[1], Lars Erik Holmedal[1], Hong Wang[1], Dag Myrhaug[1]

Abstract

The vortex dynamics in a two-dimensional oscillatory lid-driven cavity with depth-to-width ratio 1:2 has been investigated, covering a wide range of Reynolds numbers and Stokes numbers where this flow is known to be two-dimensional regime. Numerical simulations show that the present flow can be divided into four flow patterns based on the vortex dynamics. The regions of these flow patterns are given in the Stokes number and Reynolds number space. For the flow pattern with lowest Reynolds number, there is no transfer of vortices between two successive oscillation half-cycles while for the three other patterns, vortices are carried over from one oscillation half-cycle to the next. For a given Stokes number, the flow pattern appears sequentially as the Reynolds number increases, showing that the transition between the different flow patterns depends strongly on the Reynolds num-

ber. However, if the frequency of oscillation is increased (i.e., the Stokes number is increased) for a given Reynolds number, the extreme of the stream function have less time to grow and the center of the primary vortex has less time to move away from the lid. To compensate these effects, the amplitude has to be increased with increasing frequency to maintain the same flow pattern.

4.1   Introduction

Flow in an oscillatory lid-driven cavity has been studied over the years because of its relevance to industrial flows. Despite the simple geometry involved, this flow contains several complex hydrodynamic flow structures and phenomena, such as vortex merging(Leweke et al. 2016, Josserand & Rossi 2007), flow separation(Sychev 1972, Cheng & Hung 2006), corner singularities(Shankar & Deshpande 2000, Moffatt 2009), boundary layers(Pan & Acrivos 1967, Trowbridge & Lentz 2018) and chaotic mixing(Leong & Ottino 1989, Ottino 1990). Comprehensive reviews of lid-driven cavity flows are given by Shankar & Deshpande (2000) and by Kuhlmann & Romanò (2019). Oscillatory lid-driven cavity flows are characterized by a Stokes layer beneath the horizontally oscillating lid which rolls up at the vertical side walls, forming one clockwise and one anti-clockwise primary vortex which alternate in growing and decaying during the oscillation cycle. Flow separation leads to the formation and evolution of corner vortices which in turn interacts with the primary vortices, thus exhibiting a complicated vortex dynamics, as shown by Soh & Goodrich (1988), Iwatsu et al. (1992) and Mendu & Das (2013) for square cavities.

Ovando et al. (2009) used numerical simulations to investigate the flow in a rectangular cavity driven by a simultaneous oscillatory motion of the vertical walls, relevant to a piston moving inside a circular cylinder in combustion engines. They found two major generation mechanisms for the primary vortex: i) vorticity produced by the shear motion induced by the oscillating walls, and ii) roll-up of vortex sheets as the wall-induced flow changes direction when the fluid meets the vertical walls, as previously observed in experiments by Tabaczynski et al. (1970) and Allen & Chong (2000)

The possible application of an oscillatory lid-driven cavity flow as a viable viscometer (Lopez & Hirsa 2001) spurred further investigations of the stability of the two-dimensional base flow, including the experimental work by Vogel et al. (2003) and Leung et al. (2005) and the stability analysis by Blackburn & Lopez (2003). These works resulted in stability regions as

a function of the Reynolds number Re (based on the height of the cavity and the oscillation velocity amplitude of the lid) and the Stokes number St (based on the height of the cavity and the oscillation frequency of the lid). Three different flow states were found: i) a basic two-dimensional time-periodic flow, ii) a three-dimensional time-periodic flow with a cellular structure in the spanwise direction, iii) a three-dimensional irregular flow.

The vortex dynamics for two-dimensional oscillatory lid-driven cavity flows is more complex than for steady lid-driven cavity flows (Ghia et al. 1982, Cheng & Hung 2006) as it includes the evolution of intermediate primary and secondary vortices through the oscillation cycle, where the location and duration of these intermediate vortices depend strongly on the Reynolds number and the Stokes number. The aim of the present paper is to provide a further detailed investigation of the vortex dynamics for an oscillatory lid-driven cavity with depth-to-width ratio 1:2, covering the wide range of the Reynolds number and the Stokes number where this flow is known to be in the two-dimensional regime (Vogel et al. 2003). Numerical simulations show that this flow regime can be further divided into four different flow patterns based on the vortex dynamics, which is visualized by instantaneous streamline contours through the first half-cycle of oscillation. These flow patterns are mapped out in the Stokes number and Reynolds number space, and a detailed analysis of the vortex dynamics underpinning the flow pattern classification is presented, including the interaction between the primary vortices and the corner and wall vortices, which has not been previously investigated in such detail.

4.2   Governing equations

Incompressible flow with a constant density ρ and kinematic viscosity ν is governed by the two-dimensional Navier-Stokes equations described as follows

$$\frac{\partial u_i}{\partial x_i} = 0 \tag{4.1}$$

$$\frac{St}{Re}\frac{\partial u_i}{\partial t} + \frac{\partial u_i u_j}{\partial x_j} = -\frac{\partial p}{\partial x_i} + \frac{1}{Re}\frac{\partial^2 u_i}{\partial x_j \partial x_j} \tag{4.2}$$

where the Einstein notation using repeated indices is applied. Here $u_i = (u,v)$ and $x_i = (x, y)$ for $i = 1$ and 2, are the velocity and Cartesian coordinates, respectively, whilst t, p, $Re = U_0 H/\nu$ and $St = \omega H^2/\nu$ denote the time, pressure, Reynolds number and Stokes number, respectively, where H, U_0 and ω are the depth of the cavity, the velocity amplitude of the lid motion and the oscillation frequency of the lid, respectively. The velocity,

time, pressure and length are scaled with U_0, T, ρU_0^2 and H, respectively, where T is the period of the lid oscillation. Figure 4.1 shows a sketch of the oscillatory lid-driven cavity. The velocity of the lid is given by $u = cos(2\pi t)$ while no-slip conditions are imposed on the side and bottom walls.
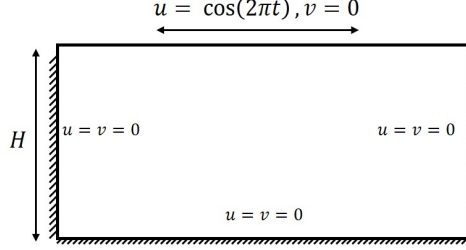
Figure 4.1: Sketch for the oscillatory lid-driven rectangular cavity flow.

4.3 Numerical Method

Eqs.(4.1) and (4.2) have been solved by using a projection method with a semi-implicit time integration using a second-order Adams-Bashforth scheme for the convective terms and a Crank-Nicolson scheme for the diffusive terms. Second-order central differences with a staggered grid arrangement are applied in the spatial discretization. The intermediate velocity u_i^* is obtained as

$$u_i^* = u_i^n + \Delta t[\frac{1}{2}(3H_i^n - H_i^{n-1}) + \frac{1}{2}(F_i^n + F_i^*) - \frac{1}{Re}\frac{\delta}{\delta x_i}(p^{n-1/2})] \quad (4.3)$$

where $\delta/\delta x_i$ represents the numerical spatial gradient operator; the convective and diffusive terms are denoted by $H_i = \delta(u_i u_j)/\delta x_j$ and $F_i = \nu\delta^2(u_i)/(\delta x_j \delta x_j)$, respectively; the superscript n denotes the time step, and $p^{n-1/2}$ indicates the pressure obtained at the previous time-step. The velocity correction is

$$u_i^{n+1} = u_i^* - \Delta t\frac{\delta}{\delta x_j}(\phi^{n+1}) \quad (4.4)$$

where $\phi^{n+1} = p^{n+1/2} - p^{n-1/2}$ is determined such that the resulting velocity field u_i^{n+1} satisfies the continuity condition. Substitution of Eq.(4.4) into the continuity equation $\delta u_i/\delta x_i = 0$ yields a Poisson equation for the pressure correction

$$\frac{\delta^2}{\delta x_j^2}(\phi^{n+1}) = -\frac{1}{\Delta t}\frac{\delta u_i^*}{\delta x_i} \quad (4.5)$$

where Neumann conditions are applied for the pressure corrections on all the walls and on the lid.
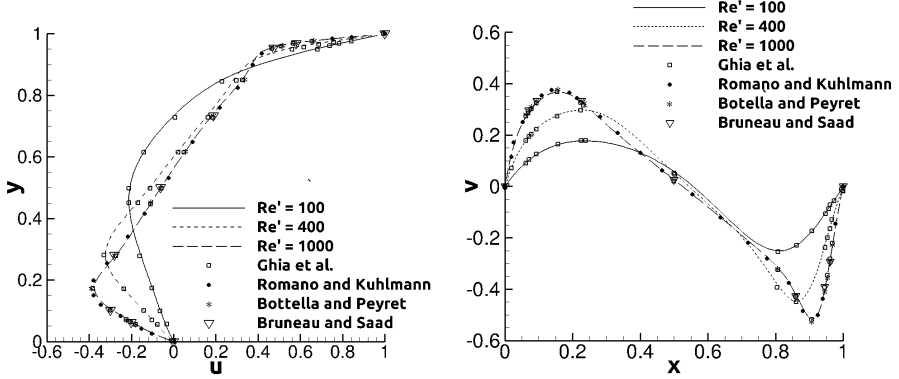
Figure 4.2: Comparisons of $u(0.5, y)$ and $v(x, 0.5)$ between predictions and reference data for the steady lid-driven cavity flow with $Re' = 100, 400$ from Ghia et al. (1982) and $Re' = 1000$ from Ghia et al. (1982), Romano & Kuhlmann (2017), Botella & Peyret (1998) and Bruneau & Saad (2006).

The oscillatory lid-driven cavity flow starts from rest, and after a spin-up time of typically $6-16$ cycles (depending on Re and St), the flow reaches a fully-developed periodic state, i.e. where the velocity and pressure fields at t and $t + T$ are equal within a specified numerical accuracy. The criterion for the flow being fully-developed is given by

$$max|\frac{u_i(x, y, t + T) - u_i(x, y, t)}{u_i(x, y, t + T)}| \leq \epsilon, \quad i = 1, 2 \tag{4.6}$$

where $\epsilon = 1 \times 10^{-6}$.

Based on grid convergence tests, a spatial resolution of 100×100 and 100×200 uniform grid points is sufficient to obtain grid independent results, for the depth-to-width ratios 1:1 and 1:2, respectively.

4.4 Validation against previous numerical and experimental results

4.4.1 Steady lid-driven cavity flow

Figure 4.2 shows the center-line velocities $u(0.5, y)$ and $v(x, 0.5)$ for a steady lid-driven flow in a square cavity for $Re' = UH/\nu = 100, 400$ and 1000,

where U is the constant lid velocity. The velocity gradients near the wall increase as Re' increases, and the thickness of the boundary layers at the wall decreases as Re' increases. A good agreement is obtained with the results by Ghia et al. (1982) for $Re' = 100, 400$ and 1000 and by Romano & Kuhlmann (2017), Botella & Peyret (1998) and Bruneau & Saad (2006) for $Re' = 1000$.
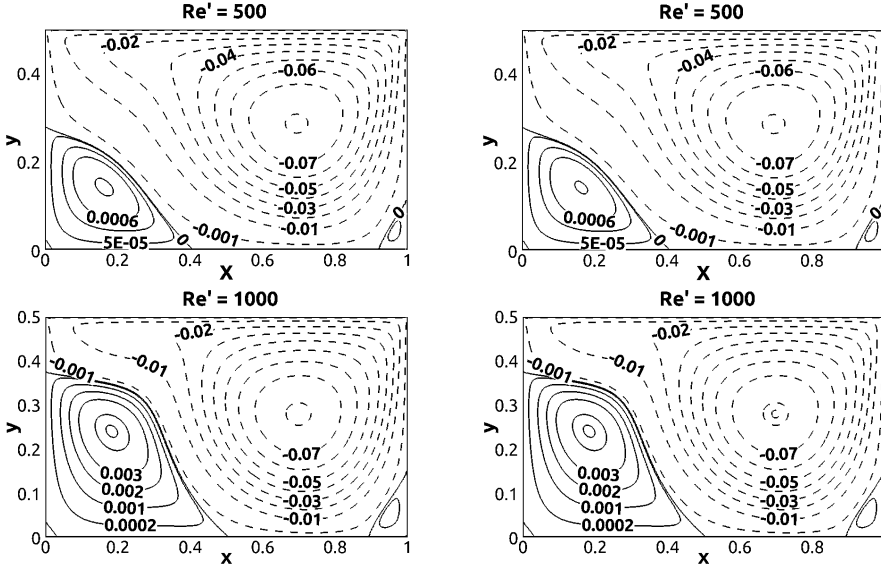
Figure 4.3: Streamline contours for $Re' = 500$ and 1000. Present results (left) and the results by Cheng & Hung (2006) (right) which were digitalized.

Figure 4.3 shows the streamlines for a steady lid-driven flow in a rectangular cavity with depth-to-width ratio 1:2 for $Re' = 500$ and 1000. The size of left bottom corner vortex increases substantially and drifts further off the bottom wall as Re' increases from 500 to 1000, while the positions and strengths of the right bottom corner vortex and the primary vortex are weakly affected by Re'. The present results (left column) are in good agreement with the streamlines (right column) obtained previously by Cheng & Hung (2006).

Figure 4.4 shows contour lines of the stream-function (black lines) and the vortices identified by the λ_2 method (blue lines) proposed by Jeong & Hussain (1995) for steady lid-driven rectangular cavity flow with $Re' = 1000$. The λ_2 method identifies the primary vortex and the bottom corner vortices, which are also visualized by closed streamlines. However, the flow at the upper-left corner is also identified as a vortex by the λ_2 method
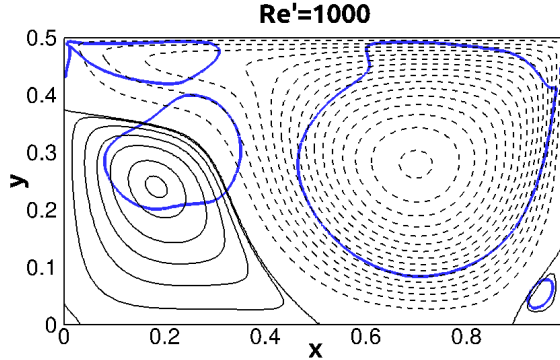
Figure 4.4: Streamlines (positive values for black full lines; negative values for black dashed lines) and $\lambda_2 = -0.1$ (blue lines) contours for steady lid-driven rectangular cavity flow at $Re' = 1000$.

whereas the streamlines are not closed in this case, thus demonstrating the complexity of vortex identification. In this paper, the stream function is applied to identify the flow patterns for both the steady and oscillatory lid-driven cavity flow following the practice of previous works (Gustafson & Halasi 1986, Shankar et al. 2003, Cheng & Hung 2006, Mendu & Das 2013).

4.4.2 Oscillatory lid-driven cavity flow

Simulations of the flow within an oscillatory lid-driven square cavity have been compared with previous numerical results (Iwatsu et al. 1992, Liu 2001, Mendu & Das 2013). Figure 4.5 shows the center-line velocity profiles $u(0.5, y)$ and $v(x, 0.5)$ for $Re = 100$, 400 and 1000 at different times (indicated in the legend) for $\omega' = St/Re = 1$. The present results are in good agreement with those of Iwatsu et al. (1992) while showing some deviation from the results obtained by Liu (2001) especially for $Re = 1000$. The boundary layer thickness beneath the moving lid decreases as the Reynolds number (and consequently the Stokes number) increases. This is consistent with laminar boundary layer theory (i.e. Stokes second problem described in Schlichting et al. 1979) and also with the findings by Duck (1982).

Simulations of the flow within an oscillatory lid-driven rectangular cavity have been compared with the experimental results previously obtained by Vogel et al. (2003). They conducted an experimental investigation of the two-dimensional and three-dimensional flow regimes in an oscillatory lid-driven cavity with depth-to-width ratio 1:2 and spanwise aspect ratio 1:19.4 for a wide range of Re and St. Here the bottom was moving while

the upper lid was fixed. Experimental results for the two-dimensional flow
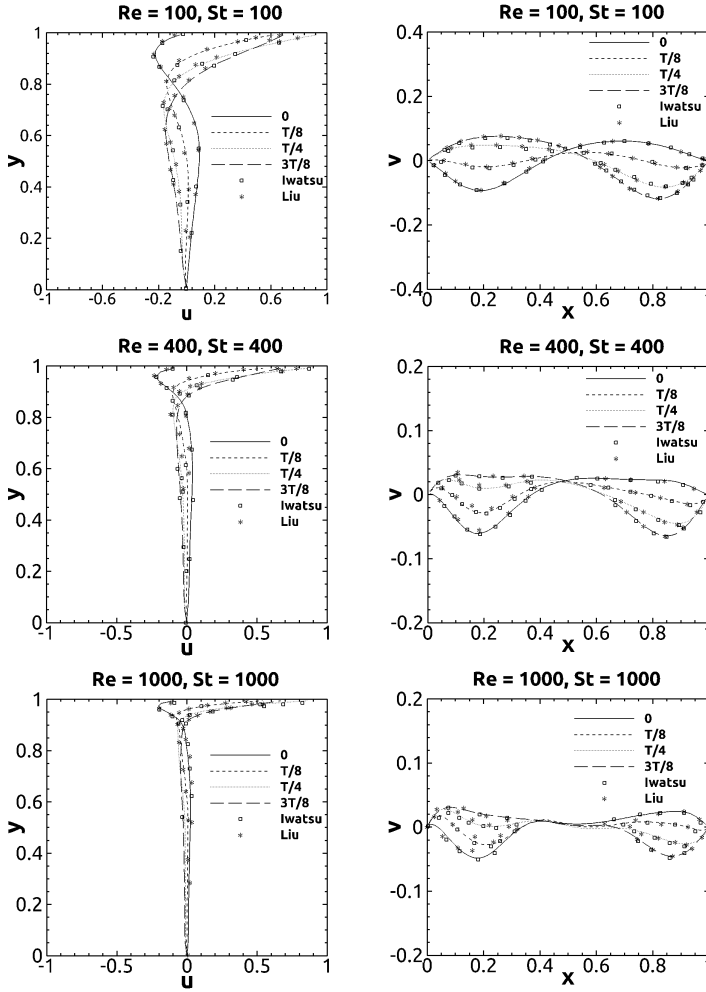
Figure 4.5: Comparisons of $u(0.5, y)$ and $v(x, 0.5)$ between the present results and those obtained by Iwatsu et al. (1992) and Liu (2001) for the oscillatory lid-driven cavity flow.

regime are compared with the present results by contours of the z-component of the vorticity ($\Omega_z = \partial v/\partial x - \partial u/\partial y$) for $Re = 166$, 332, 498 and 747 for a fixed $St = 53$ as shown in Figure 4.6. Here the left column shows Ω_z obtained from the measurements, while the right column shows Ω_z obtained by the present numerical simulations. It should be noted that Vogel et al. (2003) did not present the values of the contours of Ω_z obtained from the

measurements, and thus values of the contours in the numerical simulations have been chosen (as best fit by eye) to match the measurements. Figure 4.6 shows that the qualitative agreement is fair; the experimental measurements may deviate from the numerical simulations due to the uncertainty of the measured vorticity. Moreover, the present contours are similar to the numerical results (not shown here) presented by Vogel et al. (2003).
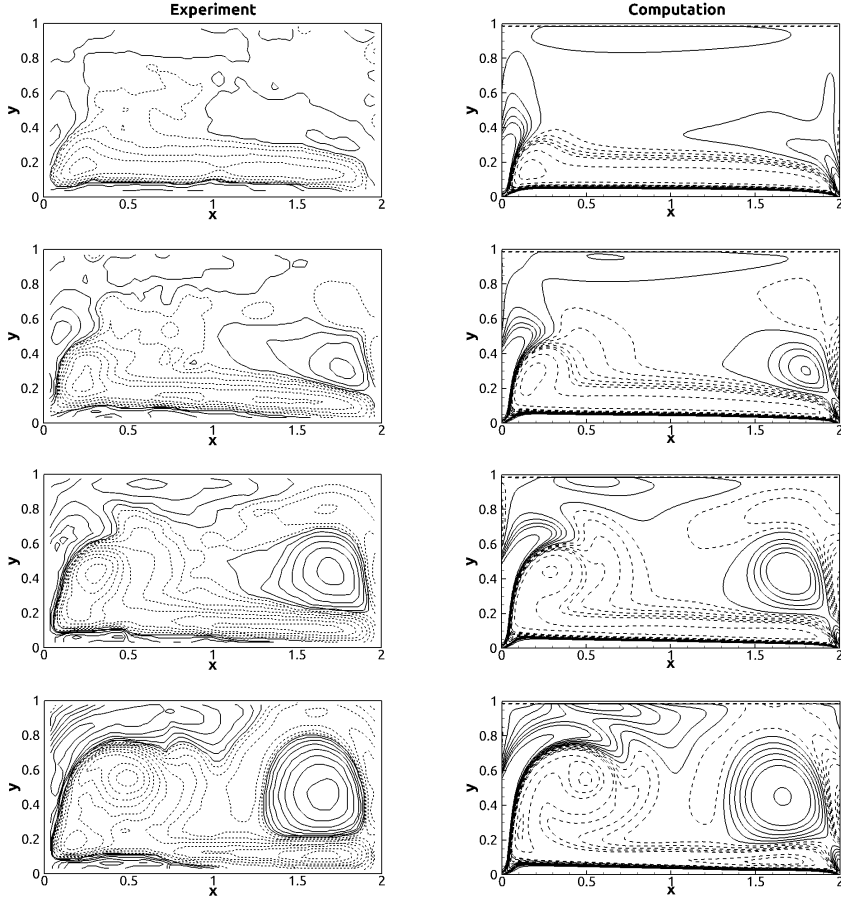
Figure 4.6: Comparisons between predictions (right column) and measurements (left column) by Vogel et al. (2003) for contours of Ω_z at $Re = 166$, 332, 498 and 747 (from top to bottom) and $St = 53$. All the data are for phase $t = 0$. Dashed and solid lines indicate negative values and positive values, respectively.

4.5 Results and discussion

4.5.1 Basic flow patterns

Figure 4.7 shows streamline contours for $Re = 125$ and $St = 23$ for the first half-cycle of oscillation. At $t = 0$, where the lid velocity is at its largest
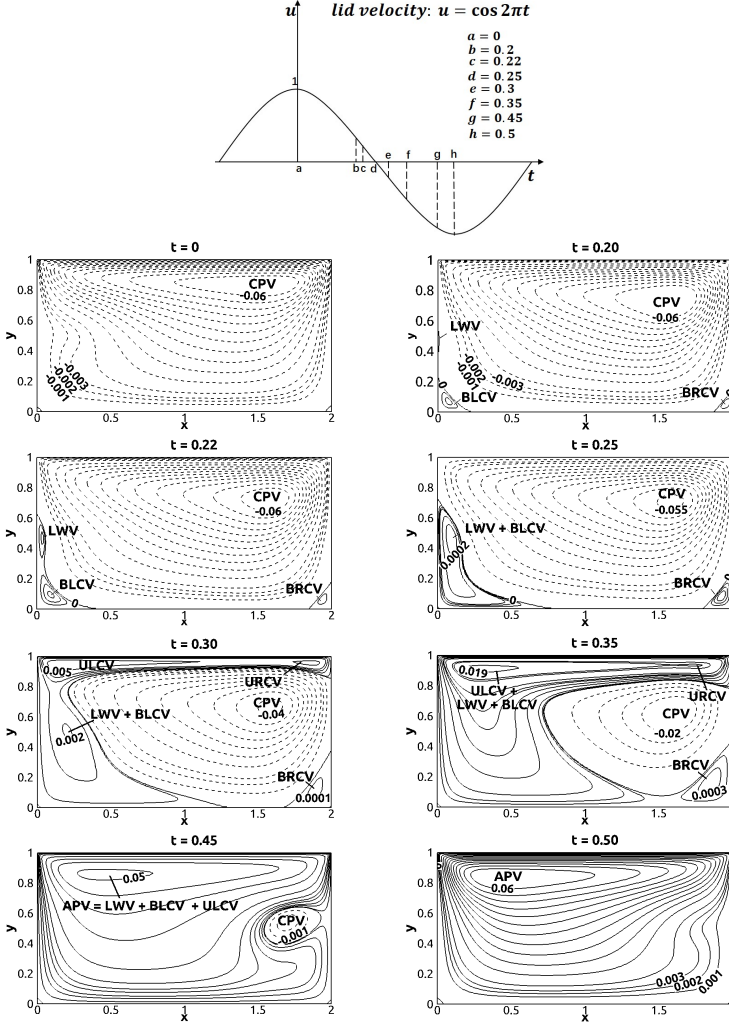
Figure 4.7: Streamline contours for flow pattern A at $Re = 125$ and $St = 23$.

during the oscillation cycle (the lid is moving towards the right), the cavity is almost completely occupied by the clockwise primary vortex (CPV), and

the flow here is qualitatively similar to a steady lid-driven cavity flow. As the lid velocity decreases ($t = 0.2$), flow separation and reattachment cause a bottom left corner vortex ($BLCV$), and a bottom right corner vortex ($BRCV$) as well as a left wall vortex (LWV). These three vortices grow in size and strength and the weaker left wall vortex becomes encircled by the stronger bottom left corner vortex from $t = 0.20$ to 0.22, and then ($t = 0.25$) they merge ($LWV + BLCV$) to an anti-clockwise vortex which grows with time, while the clockwise primary vortex shrinks. As the lid starts
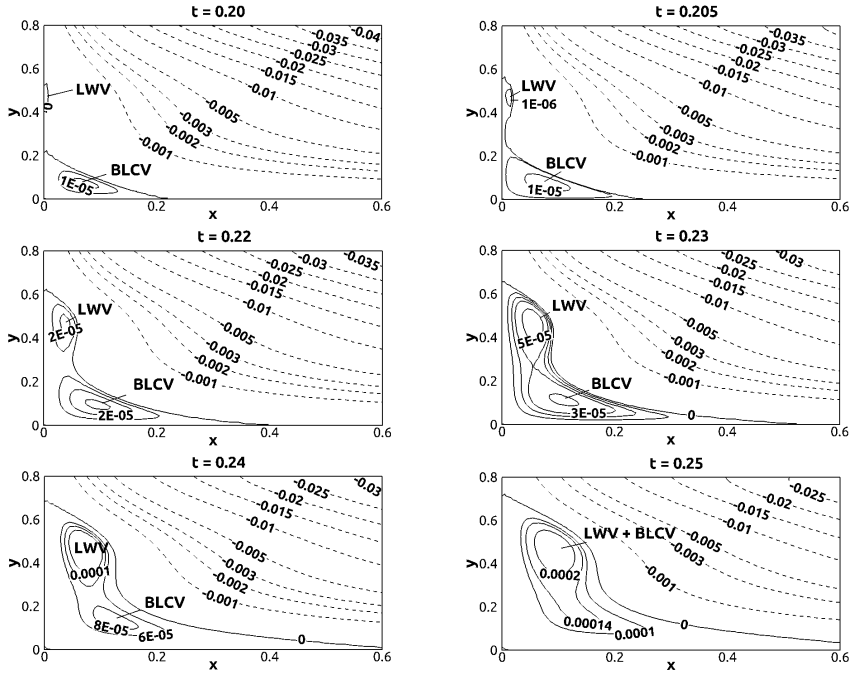
Figure 4.8: The evolution of co-rotating vortex pair of different strengths, i.e. the left wall vortex (LWV) and the bottom left corner vortex (BLCV).

moving towards the left ($t = 0.3$), the flow driven by the lid (rolls down at the upper left corner) forms an anti-clockwise elongated upper left corner vortex ($ULCV$) confined by the clockwise primary vortex and the ($LWV + BLCV$) vortex. Furthermore, an anti-clockwise upper right corner vortex ($URCV$) appears due to the interaction between the flow moving with the lid and the clockwise primary vortex. These two vortices near the lid push the clockwise primary vortex away downwards from the lid, while the ($LWV + BLCV$) vortex pushes the clockwise primary vortex towards the right. As a result, from $t = 0.3$ to $t = 0.45$ the clockwise primary vortex shrinks

gradually, and the $(LWV + BLCV)$ vortex merges with the upper left corner vortex while the vortices at the upper right corner $(URCV)$ and at the bottom right corner $(BRCV)$ erode rapidly. Finally $(t = 0.5)$, the clockwise primary vortex vanishes, and the flow becomes anti-symmetric compared with the flow field at $t = 0$. In the flow shown in figure 4.7 the clockwise primary vortex exists without the simultaneous presence of the anti-clockwise primary vortex (and vice versa) for a small interval of the oscillation cycle where the magnitude of the lid velocity is largest, i.e. at t = n/2 where n is the number of cycles. The flow pattern which fulfills this criterion will hereafter be denoted flow pattern A.
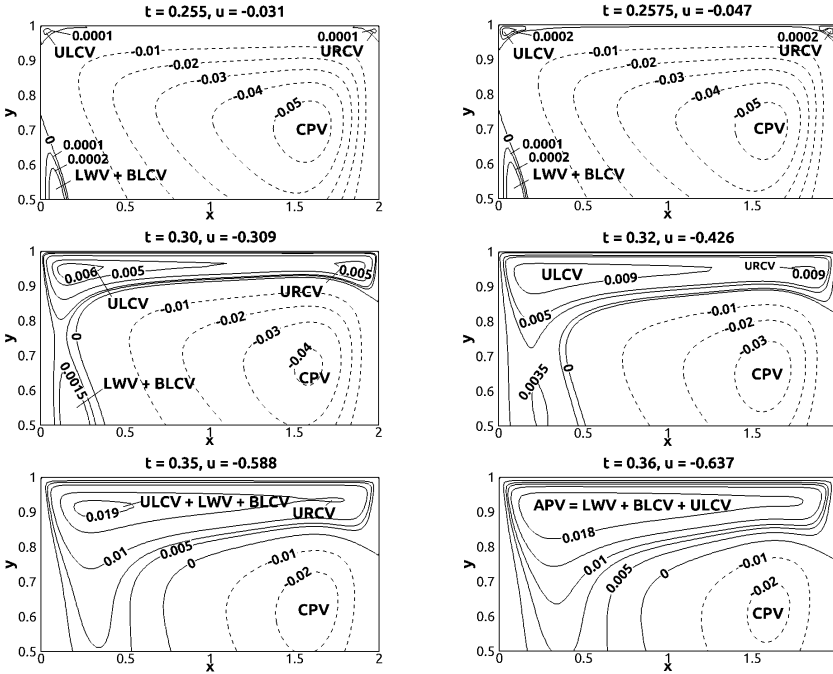
Figure 4.9: The evolution of three co-rotating vortices of different strengths, i.e. the merged vortex $(LWV + BLCV)$, the upper left vortex $(ULCV)$ and the upper right corner vortex $(URCV)$.

Figure 4.8 shows further details (close-up) of the merging of the left wall vortex (LWV) and the bottom left corner vortex $(BLCV)$, previously shown in figure 4.7. At $t = 0.20$, the flow separates at $(x, y) = (0, 0.4)$ and reattaches at $(0, 0.52)$ at the left wall, forming the small left wall vortex. As time increases, the separation point moves downward and meets at $t = 0.205$; the attachment point of the bottom left corner vortex is located at

$(0, 0.3)$. From $t = 0.22$ to $t = 0.23$, these two vortices have nearly equal strength, and grow in size by vorticity diffusion. Additionally, they grow in strength due to the positive vorticity near the walls but they do not
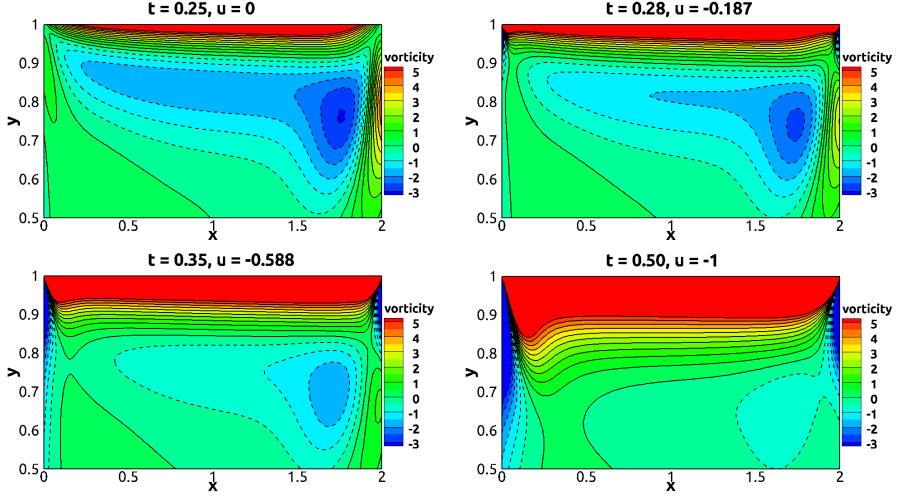
Figure 4.10: Vorticity contours Ω_z from $t = 0.25$ to $t = 0.50$ for $St = 23$ with $Re = 125$.
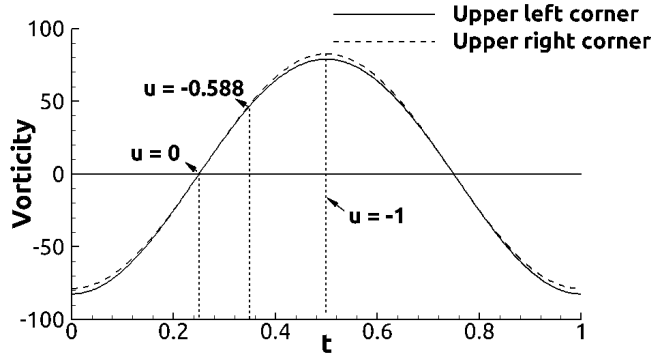
Figure 4.11: Time history of Ω_z monitored at the center of the cells nearest the upper corners through one oscillation cycle for $Re = 125$ and $St = 23$.

rotate about each other due to the presence of the walls. It appears that the left wall vortex grows faster than the bottom left corner vortex, and the merging of them is qualitatively similar to that of an unequal co-rotating vortex pair; the weaker bottom left corner vortex deforms rapidly while the

stronger left wall vortex gradually dominates with core detrainment (from $t = 0.23$ to $t = 0.24$), and finally they merge ($t = 0.25$) to form the ($LWV + BLCV$) vortex .
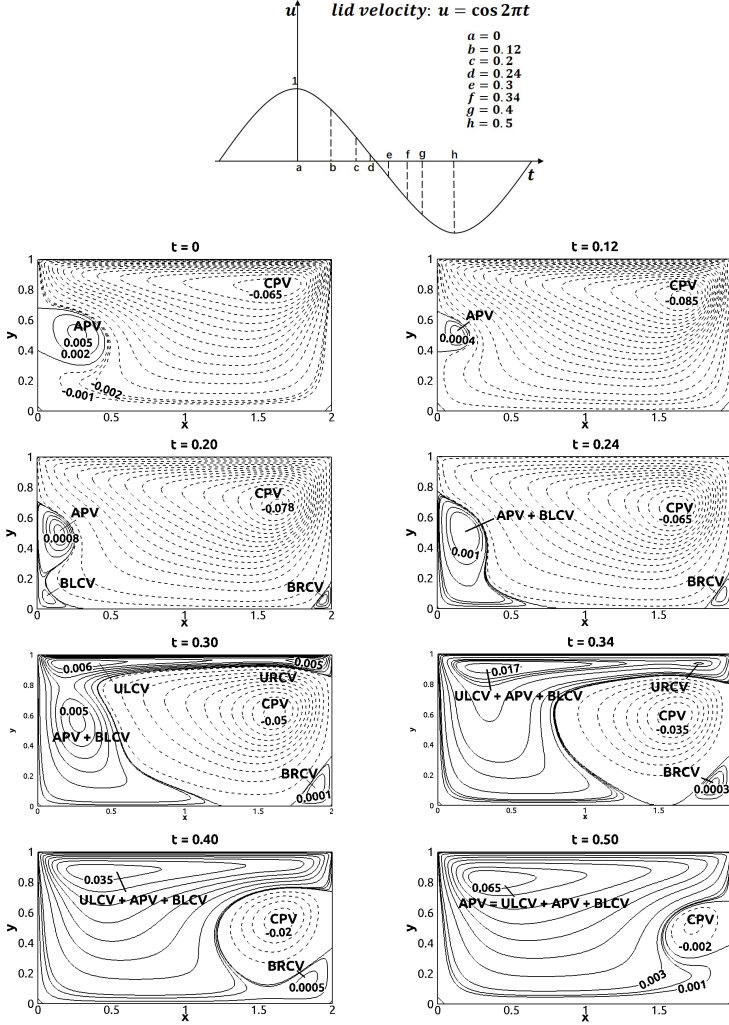
Figure 4.12: Streamline contours for flow pattern B at Re = 200 and St = 23.

Figure 4.9 displays another close-up of figure 4.7, showing the evolution of the two co-rotating vortices at the upper left corner ($ULCV$) and at the upper right corner ($URCV$) as well as the already merged vortex ($LWV + BLCV$). As the lid moves towards the left ($t = 0.255$), two anti-clockwise

vortices are formed at the upper left and right corners, respectively. Then at $t = 0.2575$ they grow and meet beneath the lid. The weaker upper right
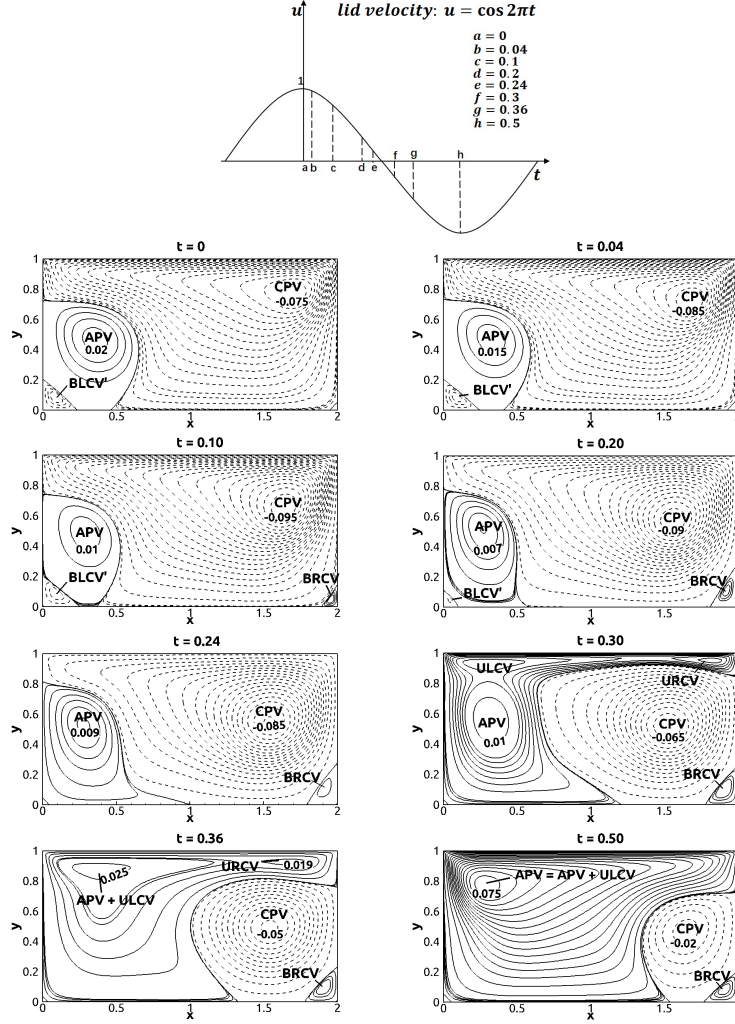
Figure 4.13: Streamline contours for flow pattern C at Re = 350 and St = 23.

corner vortex grows in strength (from $t = 0.30$ to $t = 0.32$) and erodes gradually without the core detrainment of the stronger upper left corner vortex (from $t = 0.35$ to $t = 0.36$), i.e. these two vortices do not merge. However, the merging between the weaker ($LWV + BLCV$) vortex and the stronger ($ULCV$) vortex appears to be present; the core detrainment occurs

in the stronger vortex as the weaker one moves towards it (from $t = 0.30$ to $t = 0.32$), and the merging occurs ($t = 0.35$), forming the anti-clockwise primary vortex ($APV = LWV + BLCV + ULCV$).
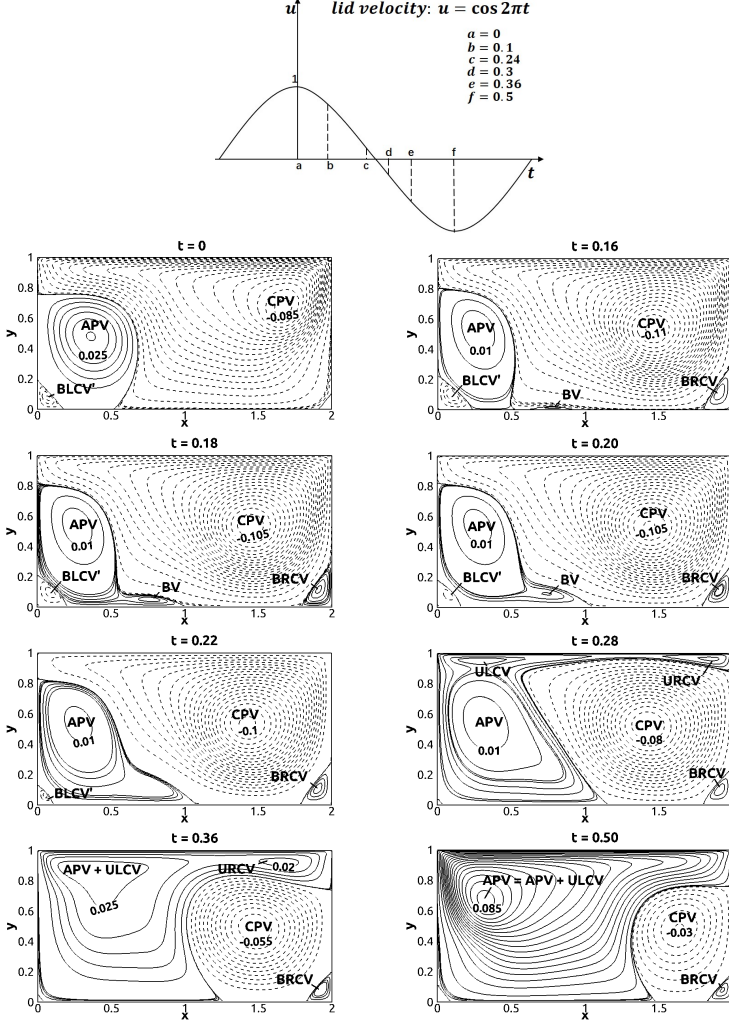
Figure 4.14: Streamline contours for flow pattern D at Re = 550 and St = 23.

The shear layer beneath the moving lid has been further investigated by visualizing the vorticity contours Ω_z in figure 4.10 within the time interval $t = 0.25$ to 0.50 (the corresponding streamlines are shown in figure 4.7). Due to the oscillation cycle, some vorticity remains beneath the lid when

the lid velocity is zero (at $t = 0.25$). As the lid moves from the right towards the left, the thickness of the shear layer beneath the lid increases both with time and along the lid. It is observed that as the shear layer beneath the lid becomes thicker, the corner vorticity singularities shown in figure 4.10 (shown by the contraction of the vorticity contours towards the upper corners) become more visible. This is further visualized in figure 4.11, showing the vorticity evaluated at the center of the cell nearest to the upper left and right corners through the oscillation cycle. The magnitude of the vorticity Ω_z on the bisection of the singular corner and in the immediate vicinity of the corner is small as the lid velocity is zero (at $t = 0.25$ and $t = 0.75$), which is consistent with the observation from figure 4.10 for $t = 0.25$. As the lid moves towards the left in the time interval from $t = 0.25$ (where
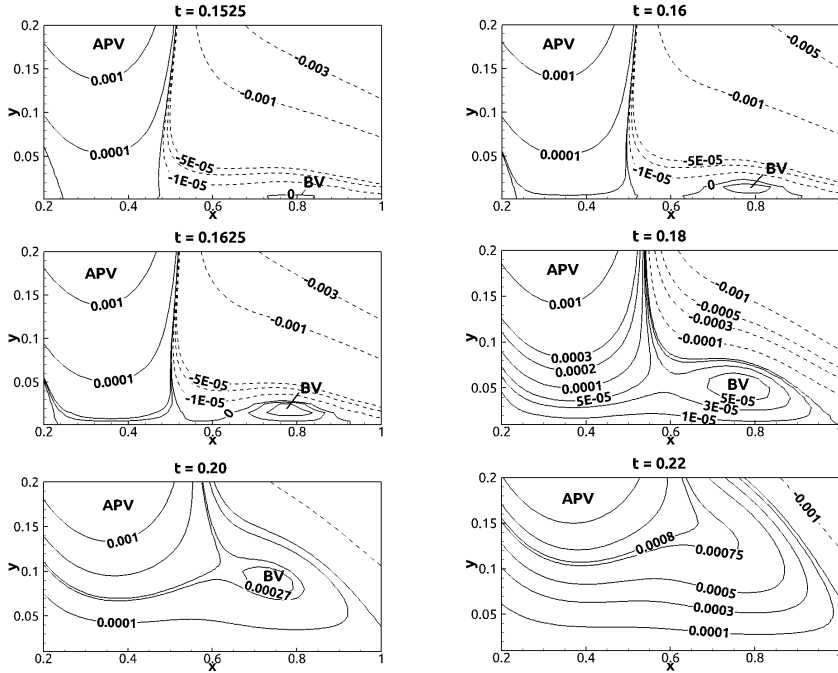
Figure 4.15: The merging process of the asymmetric vortex pair, i.e. the anti-clockwise bottom vortex (BV) and primary vortex (APV).

$u = 0$) to $t = 0.35$ (where $u = $ -0.588), the magnitude of the near-corner vorticities increases. As the lid velocity increases further, the magnitude of the vorticity near the right corner becomes slightly larger than that near the left corner with the maximum deviation observed at $t = 0.50$ (where $u = $ -1). This is consistent with the shear layer beneath the lid being thicker

at the left corner than at the right corner as shown in figure 4.10 for $t = 0.50$. Some further aspects of the upper corner singularities will be discussed below in Section 4.5.2.

Figure 4.12 shows streamline contours for $Re = 200$ and $St = 23$ for the first half-cycle of oscillation. Here, a remaining part of the anti-clockwise primary vortex (APV) from the previous half-cycle of oscillation is present at the left wall; this vortex does not completely vanish at any instance of the oscillation cycle as it does for flow pattern A shown in figure 4.7. Except from this, the vortex dynamics is similar to that of flow pattern A: the remaining part of the anti-clockwise primary vortex merges gradually with the bottom left corner vortex $(t = 0.24)$ in the same manner as the left wall vortex does in flow pattern A; the upper left and right corner vortices are formed beneath the lid $(t = 0.3)$, and from $t = 0.34$ to $t = 0.5$ the upper left corner vortex merge gradually with the $(APV + BLCV)$ vortex, forming the anti-clockwise primary vortex while the upper left corner vortex and the upper right corner vortex erode. However, a small part of the clockwise primary vortex remains as the next half-cycle of oscillation starts. The flow pattern exhibiting this behavior is denoted flow pattern B.

Figure 4.13 shows streamline contours for $Re = 350$ and $St = 23$ for the first half-cycle of oscillation. At $t = 0$, the remaining part of the anti-clockwise primary vortex is so large that it separates the bottom left corner vortex from the clockwise primary vortex, resulting in a bottom left corner vortex $(BLCV')$ with a clockwise rotation instead of the anti-clockwise rotation observed in flow patterns A and B. As the lid velocity decreases, this clockwise bottom vortex $(BLCV')$ decreases gradually in size and strength (from $t = 0.04$ to $t = 0.24$) and finally vanishes $(t = 0.24)$. The merging of $ULCV$ and APV, the erosion of $URCV$ and the decay of the clockwise primary vortex with time are qualitatively similar to those observed in flow patterns A and B, except that the bottom right corner vortex does not erode $(t = 0.5)$. This is because the bottom right corner vortex here is isolated from the anti-clockwise primary vortex by the remaining clockwise primary vortex. Consequently, the flow here carries two vortices (the clockwise primary vortex and the bottom right corner vortex) between the two successive half-cycles of oscillation. The flow exhibiting this behavior is denoted flow pattern C.

Figure 4.14 shows streamline contours for $Re = 550$ and $St = 23$ for the first half-cycle of oscillation. At $t = 0$, the cavity is occupied by the clockwise primary vortex as well as the remaining part of the anti-clockwise primary vortex and the clockwise bottom left corner vortex. As the clockwise primary vortex core approaches the bottom, a closed region of recirculation

appears on the wall, leading to the formation ($t = 0.16$) of an anti-clockwise bottom vortex (BV) which does not appear in flow patterns A-C. This behavior is qualitatively similar to the observations of Walker et al.Walker et al. (1987) who found that as a primary vortex ring approaches a solid wall, a wall eddy with opposite vorticity will be present in the close vicinity of the wall. The interaction between the co-rotating vortex pair (BV and APV) is described in further details in figure 4.15; flow separation and reattachment occur between $(x, y) = (0.725, 0)$ and $(0.84, 0)$ at the bottom for $t = 0.1525$, forming the bottom vortex (BV), which grows gradually ($t = 0.16$) due to the vorticity diffusion and meets ($t = 0.1625$) with the primary vortex (APV), and is eventually ($t = 0.22$) destroyed by the stronger primary vortex (APV) which remains relatively unaffected as shown in figure 4.14 (from $t = 0.2$ to $t = 0.22$). The flow state which includes the bottom vortex is denoted flow pattern D.
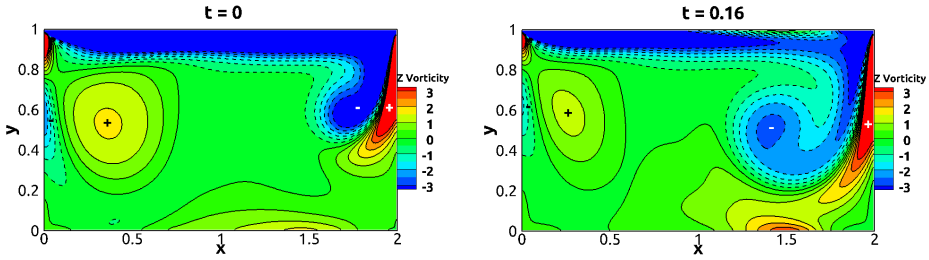
Figure 4.16: Contours of Ω_z for Re = 550 and St = 23; dashed and solid lines indicate negative values and positive values, respectively.

Further details of the vortex generating mechanisms are obtained by contours of Ω_z shown in figure 4.16. Here the vorticity contours for $t = 0$ and $t = 0.16$ corresponds to the streamlines (for $t = 0$ and $t = 0.16$) shown in figure 4.14. The generation of vorticity along the oscillating lid as well as the vorticity which occurs due to the vertical wall are clearly visualized. As pointed out by Ovando et al. (2009), the vortex shedding (figure 4.16, $t = 0.16$) due to the rolling down of the vortex sheets at the right wall follows the qualitative behavior of a vortex approaching a wall perpendicularly, first predicted by Peace & Riley (1983) and observed experimentally by Walker et al. (1987) and Allen & Chong (2000). As the vortex is approaching the wall (figure 4.16, $t = 0$), a region with opposite vorticity sign occurs between the vortex and the wall, causing the vortex to rebound from the wall (figure 4.16, $t = 0.16$); this can also be seen from figure 4.14 ($t = 0$ and $t = 0.16$). These mechanisms are similar to those previously visualized by Ovando et al. (2009) for a rectangular cavity with two simultaneously

oscillating vertical walls.

4.5.2 Effect of upper corner vorticity singularity

Now the flow in the vicinity of the upper left and right corners where the vorticity is singular will be discussed. These singularities cause numerical challenges, making it more difficult to obtain an accurate numerical solution in the close vicinity of the upper corners. For spectral methods, the global nature of the trial function in conjunction with the upper corner singularities leads to spurious oscillations. This is overcome by combining the trial functions with local analytic solutions based on asymptotic series expansions in terms of the local Reynolds number, which is small due to the small flow velocity near the upper corner(Botella & Peyret 1998, Botella et al. 2001). Also for finite difference, finite volume and finite element methods, the upper corner singularities lead to numerical inaccuracies. Bruneau & Saad (2006) applied a finite difference method showing that for a steady lid-driven square cavity flow for $Re = 1000$ and 5000, grid convergence was obtained for the total kinetic energy $E = \frac{1}{2} \oint_S ||U||^2 dS$ (where S is the computation domain, and Ω_z is evaluated at the cell center), whilst grid convergence could not be obtained for neither the enstrophy $Z = \frac{1}{2} \oint_S ||\Omega_z||^2 dS$ nor the palinstrophy $P = \frac{1}{2} \oint_S ||\nabla \Omega_z||^2 dS$. As pointed out by Bruneau & Saad (2006), this is caused by the infinite velocity gradients in the corners, causing the enstrophy and the palinstrophy to approach infinity as the grid cell size approaches zero. Similar results are obtained in the present work for oscillating lid-driven cavities. Figure 4.17 shows the total energy E for $St = 23$ and $Re = 550$ through the oscillation cycle obtained from both a resolution of 200×100 and 400×200 grid cells (in the x and y direction, respectively) with a maximum deviation of 0.8% between the two grid resolutions. However, for the enstrophy (also shown in figure 4.17), the corresponding maximum deviation is 5.9%. This result is qualitatively similar to those by Bruneau & Saad (2006) who obtained corresponding deviations from 4%-8% and from 4%-10% for steady lid-driven flow with $Re = 1000$ and 5000, respectively. Although grid convergence of both the enstrophy and the palinstrophy can be obtained by letting the lid velocity approach zero locally at the corners (Bruneau & Saad 2006), this case is not relevant for comparison with laboratory measurements, as pointed out by Shankar & Deshpande (2000). A close-up of the vorticity contours in the vicinity of the left corner is shown in figure 4.18 for the two different resolutions of 200×100 and 400×200 grid cells; the difference between the contour lines obtained from the two grid resolutions is small. Although the upper corner singularities affect the accuracy of the numerical solution, particularly in

the close vicinity of the corners, the vorticity is adequately resolved in the present simulations, as demonstrated in figure 4.18.
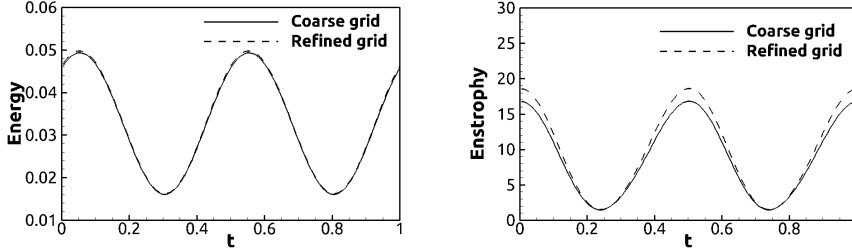
Figure 4.17: Time history of energy (left) and enstrophy (right) over one oscillation cycle for $Re = 550$ and $St = 23$.
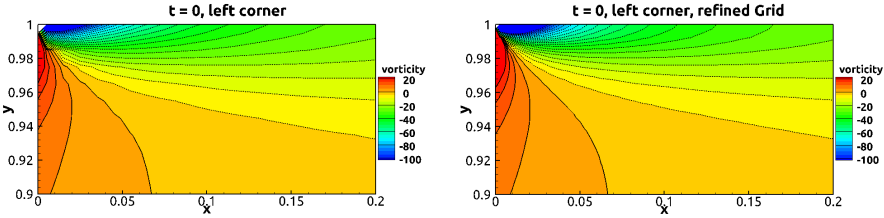
Figure 4.18: Close-up of Ω_z for the upper left corner at grid resolution 200×100 (left) and refined grid resolution 400×200 (right) for $St = 23$ with $Re = 550$.

4.5.3   Distribution of the basic flow patterns in (St, Re)-space

Figure 4.19 shows the distribution of flow patterns A-D in the (St, Re)-space; the full line denotes the transition between $2D$ and $3D$ flow.Vogel et al. (2003) More than 400 numerical simulations with Re from 10 to 875 and with St from 23 to 53 have been conducted to map out the regions in the (St, Re)-space of the flow patterns represented by the dashed lines in figure 4.19. For a given St number, the flow patterns A-D appear sequentially as Re increases, showing that the transition between the different flow patterns strongly depends on Re. Furthermore, as St increases, the Re for the transition between different flow patterns increases. This is because an increase in St for a given Re leads to less time for the extrema of the stream function to grow and for the primary vortex center to move away from the lid. Consequently, a higher Re is required to maintain the same flow pat-

tern. This effect appears to be stronger for the flow pattern D than for the flow pattern A. It appears that the transition between the different flow patterns (i.e. the dashed lines) is given by an approximately linear relation between Re and St.
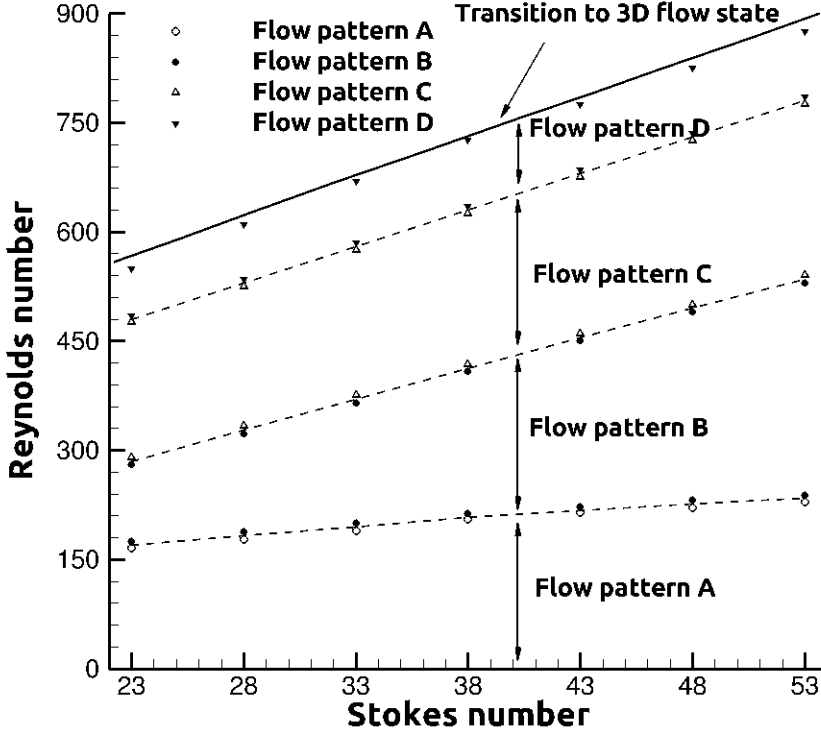
Figure 4.19: Basic flow patterns $A - D$ of the two-dimensional oscillatory lid-driven cavity within (St, Re)-space.

Figure 4.20 shows the scaled drag force (defined as $\int_0^2 \frac{\partial u}{\partial y}|_{y=1}dx$) beneath the moving lid through one oscillation cycle for $St = 23$ and for $Re = 125$, 200, 350 and 550; i.e. for the flow patterns *A-D*. It appears that an increase in Re leads to a moderate growth and phase shift of the drag force. Figure 4.21(a) shows the phase shift between the lid oscillation velocity and the drag force on the lid for $Re = 10$, 125, 250 and 490 and for $St = 23$, 28, 33, 38, 43, 48 and 53. The phase shift increases monotonically as St increases whereas an increase of Re results in lower phase shifts. The maximum phase shift is 30° (for $St = 53$ and $Re = 10$), which is considerably smaller than

the 45° phase shift obtained from the Stokes' classical second problem.
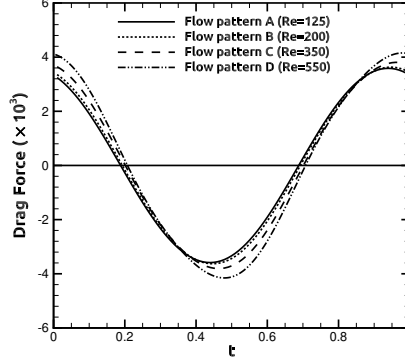
Figure 4.20: The drag force beneath the moving lid at St =23 and for Re = 125, 200, 350 and 550; i.e. for the flow patterns A-D.

Figure 4.21(b) shows the horizontal velocity component along the vertical center-line of the cavity for $t = 0.2$ and 0.6 for $St = 53$ and for $Re = 10$ and 490. The flow driven by an infinite plate (Stokes solution) is given for comparison. As Re decreases, the near-lid velocity becomes more similar to the Stokes solution. This is consistent with the observation in figure 4.21(a) showing that the flow with smallest Re and largest St exhibits the phase shift (30°) between the drag force and the lid velocity, which is closest to that from the Stokes solution (45°). However, farther away from the lid, the velocity component obtained for $Re = 490$ is closer to Stokes solution than that obtained for $Re = 10$.

4.6   Summary and conclusions

This paper provides a detailed investigation of the vortex dynamics in the oscillatory lid-driven cavity with depth-to-width ratio 1:2, covering a wide range of Reynolds numbers and Stokes numbers where this flow is known to be in the two-dimensional flow regime. The predictions have been successfully compared with previous numerical results for steady (Ghia et al. 1982, Romano & Kuhlmann 2017, Botella & Peyret 1998, Bruneau & Saad 2006, Cheng & Hung 2006) and oscillatory (Iwatsu et al. 1992, Liu 2001, Mendu & Das 2013) lid-driven cavity flows as well as with experimental results obtained by Vogel et al. (2003) for oscillatory lid-driven cavity flows. Furthermore, the effect of the upper corner vorticity singularity is discussed:
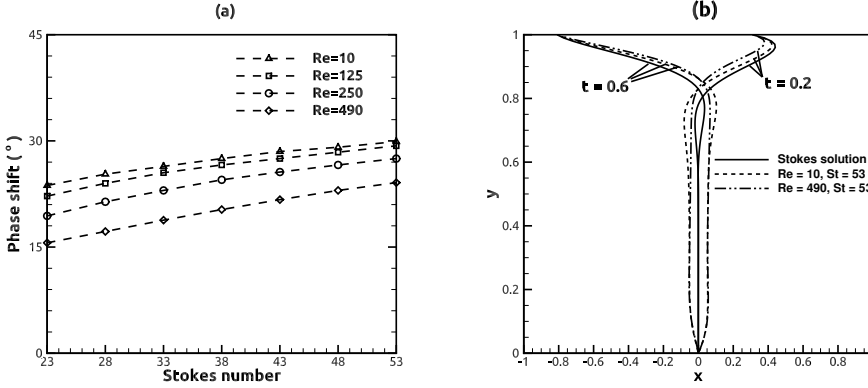
Figure 4.21: (a): phase shift of the drag force on the moving lid at Re = 10, 125, 250 and 490 for St = 23, 28, 33, 38, 43, 48 and 53; (b): the horizontal velocity along the center-line of the cavity at t = 0.2 and 0.6 for St = 53 with Re = 10 and 490.

the total energy exhibits grid convergence while the enstrophy does not; these results are qualitatively similar to those obtained by Bruneau & Saad (2006) for a steady lid-driven flow. Although the upper corner singularities affect the numerical accuracy of the predictions, it is demonstrated that the vorticity is adequately resolved.

It appears that the two-dimensional flow regime can be further divided into four flow patterns based on the vortex dynamics, which is visualized by streamline contours. The classification of these basic flow patterns can be summarized as follows:

- For flow pattern A, there is no transfer of vortices between each successive half-cycle of oscillation; this means that the clockwise primary vortex (generated by the lid moving towards the right) and the anti-clockwise primary vortex (generated by the lid moving towards the left) are not present simultaneously at the end of each half-cycle of oscillation.

- For flow pattern B, a small part of the clockwise primary vortex remains as the next half-cycle of oscillation starts, and thus the flow carries the primary vortex between each successive half-cycle of oscillation when the lid velocity is largest.

- For flow pattern C, the flow carries two vortices between each suc-

cessive half-cycle of oscillation. When the lid is moving towards the right, these two vortices consist of the anti-clockwise primary vortex and the clockwise bottom left corner vortex from the last half-cycle of oscillation.

- Flow pattern D is similar to flow pattern C, except the intermediate appearance of an additional bottom vortex during each half-cycle of oscillation.

These flow structures are unique functions of the Reynolds number and the Stokes number, and the pattern changes with these parameters. The increased forcing quantified by the Reynolds number and the Stokes number leads to finer flow structures and hence different flow patterns. If the frequency of oscillation is increased for a given Reynolds number, the extrema of the stream function have less time to grow and the centre of the primary vortex has less time to move away from the lid. To compensate these effects, the amplitude has to be increased with increasing frequency to maintain the same flow pattern.

Acknowledgements

References

Allen, J. J. & Chong, M. S. (2000), 'Vortex formation in front of a piston moving through a cylinder', *Journal of Fluid Mechanics* **416**, 1–28.

Blackburn, H. M. & Lopez, J. M. (2003), 'The onset of three-dimensional standing and modulated travelling waves in a periodically driven cavity flow', *Journal of Fluid Mechanics* **497**, 289–317.

Botella, O., Forestier, M. Y., Pasquetti, R., Peyret, R. & Sabbah, C. (2001), 'Chebyshev methods for the Navier–Stokes equations: Algorithms and applications', *Nonlinear Analysis: Theory, Methods & Applications* **47**(6), 4157–4168.

Botella, O. & Peyret, R. (1998), 'Benchmark spectral results on the lid-driven cavity flow', *Computers & Fluids* **27**(4), 421–433.

Bruneau, C. H. & Saad, M. (2006), 'The 2D lid-driven cavity problem revisited', *Computers & Fluids* **35**(3), 326–348.

Cheng, M. & Hung, K. C. (2006), 'Vortex structure of steady flow in a rectangular cavity', *Computers & Fluids* **35**(10), 1046–1062.

Duck, P. W. (1982), 'Oscillatory flow inside a square cavity', *Journal of Fluid Mechanics* **122**, 215–234.

Ghia, U., Ghia, K. N. & Shin, C. T. (1982), 'High-Re solutions for incompressible flow using the Navier-Stokes equations and a multigrid method', *Journal of Computational Physics* **48**(3), 387–411.

Gustafson, K. & Halasi, K. (1986), 'Vortex dynamics of cavity flows', *Journal of Computational Physics* **64**(2), 279–319.

Iwatsu, R., Hyun, J. M. & Kuwahara, K. (1992), 'Numerical simulation of flows driven by a torsionally oscillating lid in a square cavity', *Journal of Fluids Engineering* **114**(2).

Jeong, J. & Hussain, F. (1995), 'On the identification of a vortex', *Journal of Fluid Mechanics* **285**, 69–94.

Josserand, C. & Rossi, M. (2007), 'The merging of two co-rotating vortices: a numerical study', *European Journal of Mechanics-B/Fluids* **26**(6), 779–794.

Kuhlmann, H. C. & Romanò, F. (2019), The lid-driven cavity, *in* 'Computational Modelling of Bifurcations and Instabilities in Fluid Dynamics', Springer, pp. 233–309.

Leong, C. W. & Ottino, J. M. (1989), 'Experiments on mixing due to chaotic advection in a cavity', *Journal of Fluid Mechanics* **209**, 463–499.

Leung, J. J. F., Hirsa, A. H., Blackburn, H. M., Marques, F. & Lopez, J. M. (2005), 'Three-dimensional modes in a periodically driven elongated cavity', *Physical Review E* **71**(2), 026305.

Leweke, T., Le Dizes, S. & Williamson, C. H. K. (2016), 'Dynamics and instabilities of vortex pairs', *Annual Review of Fluid Mechanics* **48**, 507–541.

Liu, C. H. (2001), 'Numerical solution of three-dimensional Navier-Stokes equations by a velocity-vorticity method', *International Journal for Numerical Methods in Fluids* **35**(5), 533–557.

Lopez, J. M. & Hirsa, A. H. (2001), 'Oscillatory driven cavity with an air/water interface and an insoluble monolayer: Surface viscosity effects', *Journal of Colloid and Interface Science* **242**(1), 1–5.

Mendu, S. S. & Das, P. K. (2013), 'Fluid flow in a cavity driven by an oscillating lid - a simulation by Lattice Boltzmann method', *European Journal of Mechanics-B/Fluids* **39**, 59–70.

Moffatt, H. K. (2009), Singularities in fluid dynamics and their resolution, *in* 'Lectures on Topological Fluid Mechanics', Springer, pp. 157–166.

Ottino, J. M. (1990), 'Mixing, chaotic advection, and turbulence', *Annual Review of Fluid Mechanics* **22**(1), 207–254.

Ovando, G., Juarez, H., Huelsz, G. & Ramos, E. (2009), 'Vortex formation in a cavity with oscillating walls', *Physics of Fluids* **21**(2), 024101.

Pan, F. & Acrivos, A. (1967), 'Steady flows in rectangular cavities', *Journal of Fluid Mechanics* **28**(4), 643–655.

Peace, A. J. & Riley, N. (1983), 'A viscous vortex pair in ground effect', *Journal of Fluid Mechanics* **129**, 409–426.

Romano, F. & Kuhlmann, H. C. (2017), 'Smoothed-profile method for momentum and heat transfer in particulate flows', *International Journal for Numerical Methods in Fluids* **83**(6), 485–512.

Schlichting, H. et al. (1979), 'Boundary layer theory', *McGraw-Hill Book Company* pp. 135–149.

Shankar, P., Kidambi, R. & Hariharan, J. (2003), 'Oscillatory eddy structure in a container', *Journal of Fluid Mechanics* **494**, 163–185.

Shankar, P. N. & Deshpande, M. D. (2000), 'Fluid mechanics in the driven cavity', *Annual Review of Fluid Mechanics* **32**(1), 93–136.

Soh, W. Y. & Goodrich, J. W. (1988), 'Unsteady solution of incompressible Navier-Stokes equations', *Journal of Computational Physics* **79**(1), 113–134.

Sychev, V. V. (1972), 'Laminar separation', *Fluid Dynamics* **7**(3), 407–417.

Tabaczynski, R. J., Hoult, D. P. & Keck, J. C. (1970), 'High Reynolds number flow in a moving corner', *Journal of Fluid Mechanics* **42**(2), 249–255.

Trowbridge, J. H. & Lentz, S. J. (2018), 'The bottom boundary layer', *Annual Review of Marine Science* **10**, 397–420.

Vogel, M. J., Hirsa, A. H. & Lopez, J. M. (2003), 'Spatio-temporal dynamics of a periodically driven cavity flow', *Journal of Fluid Mechanics* **478**, 197–226.

Walker, J. D. A., Smith, C. R., Cerra, A. W. & Doligalski, T. L. (1987), 'The impact of a vortex ring on a wall', *Journal of Fluid Mechanics* **181**, 99–140.

Chapter 5

Flow patterns in a steady lid-driven rectangular cavity with an embedded circular cylinder

Jianxun Zhu[1], Lars Erik Holmedal[1], Hong Wang[1], Dag Myrhaug[1]

Abstract

A detailed investigation of the flow in a steady lid-driven cavity of depth to width ratio 1:2 containing a circular cylinder is provided. Three different Reynolds numbers (based on the lid velocity and cavity depth) of 100, 500 and 1000 as well as four different cylinder radius to cavity depth ratios (0.1, 0.2, 0.3 and 0.4) located at three different positions along the horizontal centerline of the cavity, are considered. It appears that these flows can be classified into seven different flow patterns. These flow patterns are given for different cylinder radii and positions as well as Reynolds numbers. There is a tendency that for a given cylinder radius, there are more transitions between different flow patterns for a small radius than for a large radius while for a given Reynolds number, the number of transitions is larger for high Reynolds numbers than for low Reynolds numbers. Overall, a larger

---

number of flow patterns tend to emerge as the Reynolds number increases for small radii. The largest variety of flow patterns occur for the left-sided cylinder due to the interaction with the large anti-clockwise circulation flow formed at the bottom left corner.

5.1   Introduction

Steady lid-driven flows containing a solid body have gained considerable attention due to its engineering applications in heat exchangers and electric coolers. The presence of a solid body within the cavity such as a circular (Oztop et al. 2009, Khanafer & Aithal 2013) or square (Islam et al. 2012) cylinder changes the flow patterns substantially, forming strong vortices which are not present in the absence of the solid body. This might strongly affect e.g. mixing or cooling properties of the cavity since these vortices might cause large gaps between isotherms, thus affecting the heat transfer within the cavity. For an incompressible fluid, the effect of moderate temperature gradients on the flow might be small, i.e. the Richardson number is small. In this case the flow is dominated by momentum and the flow structures are nearly independent of the temperature field.

Oztop et al. (2009) and Khanafer & Aithal (2013) investigated mixed convection and heat transfer in a steady lid-driven square cavity containing a circular cylinder by using a finite volume method and a finite element formulation, respectively. Oztop et al. (2009) showed that changing the the cylinder position and radius leads to deformation of both the streamlines and the isotherms in the cavity, although the primary and bottom corner vortices were not investigated in detail. The deformation of the primary vortex caused by the cylinder radius and the temperature field has been investigated numerically by Khanafer & Aithal (2013) who found that for a low Richardson number of 0.01 (forced convection flow), a primary vortex is formed between the moving lid and the centered circular cylinder, and that an increase in the cylinder radius leads to the primary vortex breaking up into two vortices. As the Richardson number increases, these vortices shrink gradually and disappear due to the natural (thermal) convection. Similar results were obtained by Billah et al. (2011).

Galaktionov et al. (1999) developed an analytical method to study creeping flow in a steady-lid driven rectangular cavity with a centered fixed and rotating circular cylinder. As the upper lid moves towards the right for the fixed cylinder, they found that the flow is symmetric about the vertical centerline of the cavity with two clockwise vortices attached to the upper left and the upper right sides of the cylinder.

Khanafer et al. (2017) used a finite element formulation to investigate the mixed convection in a lid-driven square cavity with two circular cylinders. These two cylinders are placed symmetrically about the vertical centerline of the cavity. They found that, for low Richardson numbers, an elongated clockwise vortex was formed between the lid and the two cylinders. As these two cylinders move closer to the bottom, this elongated vortex increases in size. As the two cylinders move closer to the lid, the vortex appears to be split into three clockwise vortices located beneath the mid of the lid as well as at the upper left and right corners, respectively.

The hydro-magnetic mixed convection in a steady lid-driven square cavity with a heat-conducting circular cylinder was investigated by Chatterjee & Gupta (2014) as well as Ray & Chatterjee (2014) who also studied the effect of corner heaters with Joule heating. The mixed convection for nanofluids in a steady lid-driven square cavity with embedded circular cylinders was investigated by Chatterjee et al. (2014), Bansal & Chatterjee (2015) as well as Chatterjee & Halder (2016).

Billah et al. (2011) and Khanafer & Aithal (2013) investigated the effect of the cylinder radius on the primary vortex for flow within a steady lid-driven square cavity with an embedded cylinder. However, a detailed investigation of the flow structures (including the primary vortex, corner and bottom vortices as well as the pressure around the circular cylinder) has not been previously presented. The aim of the present work is to present such detailed results for very low Richardson numbers, where the effect of the temperature field is negligible. Moreover, the effect of increasing the cavity aspect ratio on this flow has not been investigated previously.

Specifically, a detailed investigation of the flow structures within a lid-driven cavity of height to length ratio 1:2 containing a circular cylinder are conducted for a range of Reynolds numbers (based on the lid velocity and the cavity height), cylinder radius to cavity height ratio, for left-, right- and mid-centered cylinders are provided. Numerical simulations show that this flow can be classified into seven different flow patterns which are here visualized by streamlines. These flow patterns are unique functions of the Reynolds number, the ratio between the cylinder radius and the cavity height, as well as the position of the cylinder within the cavity.

5.2   Numerical method

5.2.1   Basic numerical scheme

Incompressible flow with a constant density ρ and kinematic viscosity ν is governed by the two-dimensional Navier-Stokes equations described as follows

$$\frac{\partial u_i}{\partial x_i} = 0 \tag{5.1}$$

$$\frac{\partial u_i}{\partial t} + \frac{\partial u_i u_j}{\partial x_j} = -\frac{\partial p}{\partial x_i} + \frac{1}{Re}\frac{\partial^2 u_i}{\partial x_j \partial x_j} \tag{5.2}$$

where the Einstein notation using repeated indices is applied. Here $u_i = (u,v)$ and $x_i = (x, y)$ for $i = 1$ and 2, are the velocity and Cartesian coordinates, respectively, whilst t, p and $Re = UH/\nu$ denote the dimensionless time, dimensionless pressure and Reynolds number, respectively, where H is the depth of cavity and U is the lid motion velocity. The time, pressure and length are scaled by H/U, ρU^2 and H, respectively.

Eqs.(5.1) and (5.2) are discretized on a staggered mesh arrangement using second-order central differences. A projection method using a second-order Adams-Bashforth scheme for the convective terms and a Crank-Nicolson scheme for the diffusive terms is applied. The intermediate velocity u_i^* is obtained as

$$u_i^* = u_i^n + \Delta t[\frac{1}{2}(3H_i^n - H_i^{n-1}) + \frac{1}{2}(F_i^n + F_i^*) - \frac{\delta}{\delta x_i}(p^{n-1:2})] \tag{5.3}$$

where $\delta/\delta x_i$ represents the numerical spatial gradient operator; the convective and diffusive terms are denoted by $H_i = \delta(u_i u_j)/\delta x_j$ and $F_i = \nu\delta^2(u_i)/(\delta x_j \delta x_j)$, respectively; the superscript n denotes the time step, and $p^{n-1:2}$ is the pressure obtained at the previous time-step. The velocity correction is given as

$$u_i^{n+1} = u_i^* - \Delta t\frac{\delta}{\delta x_j}(\phi^{n+1}) \tag{5.4}$$

where $\phi^{n+1} = p^{n+1:2} - p^{n-1:2}$ is determined such that the resulting velocity field u_i^{n+1} satisfies the continuity condition. Substitution of Eq.(5.4) into the continuity equation $\delta u_i/\delta x_i = 0$ yields a Poisson equation for the pressure correction

$$\frac{\delta^2}{\delta x_j^2}(\phi^{n+1}) = -\frac{1}{\Delta t}\frac{\delta u_i^*}{\delta x_i} \tag{5.5}$$

which is solved using a Jacobi preconditioned bi-conjugate gradient stabilized method.

5.2.2 Implementation of the immersed boundary method
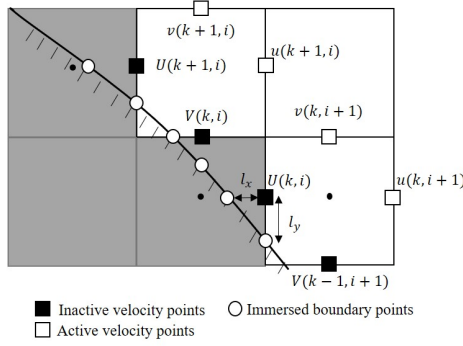
Figure 5.1: Definition of the inactive velocity points (■), immersed boundary points (○), and active velocity points (□).

The immersed boundary technique is based on a direct forcing approach combined with a finite difference method firstly proposed by Fadlun et al. (2000). As shown in figure 5.1, the staggered velocity components nearest the immersed boundary are set as inactive velocity points (■) which are updated by interpolation. Here, a one-dimensional, linear interpolation scheme is applied in each direction according to the following stencil formulation

$$u_i = \frac{x_i - x_\Gamma}{x_{i+1} - x_\Gamma} u_{i+1} + \frac{x_{i+1} - x_i}{x_{i+1} - x_\Gamma} u_\Gamma, \quad i = 1, 2 \tag{5.6}$$

where u_Γ and x_Γ are the velocity and position of the immersed boundary, respectively.

If an inactive velocity point can be interpolated from two directions, each direction is multiplied by a weighting factor as follows (Peller et al. 2006, Berthelsen & Faltinsen 2008)

$$u_i = \lambda_x u_i^x + \lambda_y u_i^y \tag{5.7}$$

where the superscript x and y denotes the interpolation in x and y-directions, respectively, and the weighting factors λ_x and λ_y are given as

$$\lambda_x = \frac{1}{1 + (\frac{l_x}{l_y})^2} \quad and \quad \lambda_y = \frac{1}{1 + (\frac{l_y}{l_x})^2} \tag{5.8}$$

where l_x and l_y is the distance between the inactive velocity point and the immersed boundary in x and y-directions, respectively, as shown in figure 5.1. A Neumann condition is applied for the pressure correction at the inactive velocity points.

5.3   Results and discussion

5.3.1   Uniform flow past a free circular cylinder at $Re' = 40$

Two-dimensional flow past a circular cylinder has been investigated using the present method for a Reynolds number ($Re' = U_0 D/\nu$, where D is the diameter of cylinder and U_0 is free-stream velocity) equal to 40. The dimensionless free-stream velocity $U_0 = 1$ is specified at the inlet boundary while a Neumann condition is imposed on the velocity at the outlet and at the top and bottom of the flow domain. Non-slip conditions are applied on the cylinder. The pressure is set to be zero at the outlet and a Neumann condition for the pressure correction is used at the other boundaries. Figure 5.2 shows the computation domain where the inlet and lateral boundaries are located $8D$ upstream of the cylinder and the outlet is located at $20D$ downstream of the cylinder. A uniform mesh of size $0.02D$ is employed for this domain.
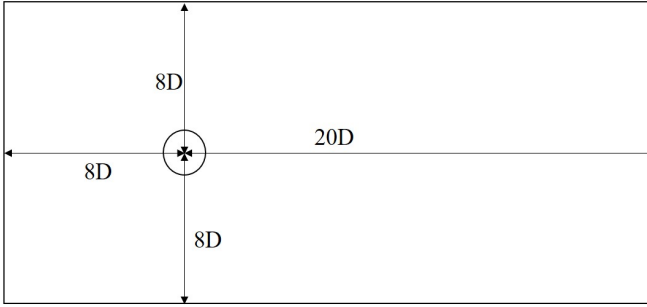
Figure 5.2: Computation domain for flow past a free circular cylinder.

After a spin-up time of $t = t^*U_0/D = 200$ (where t^* is the physical time), the flow reaches a steady and symmetric state where two attached recirculating vortices are formed behind the cylinder. The streamlines for the flow past the cylinder at $Re' = 40$, as well as the separation angle θ, wake length L_w, the horizontal distance a between the rear stagnation point of the cylinder and the recirculation center and vertical distance b between the symmetric recirculation centers, are shown in figure 5.3. Here the characteristic wake dimensions L_w, a and b are scaled by D. The pressure coefficient ($C_p = \frac{p-p_\infty}{0.5\rho U_0^2}$, where p_∞ is the pressure at the outlet) along the bottom half boundary of the cylinder is presented in figure 5.3, showing a good agreement with both experimental (Grove et al. 1964) and numerical (Dennis & Chang 1970, Tseng & Ferziger 2003, Berthelsen & Faltinsen 2008) results. The characteristic wake dimensions L_w, a and b as well as the
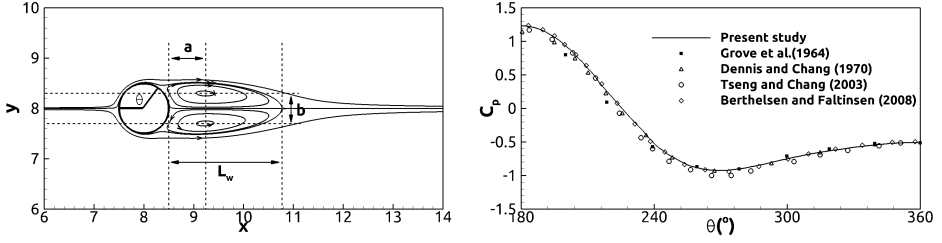
Figure 5.3: Left image: streamlines for the flow over a cylinder at $Re' = 40$ and nomenclature used in Table 5.1; separation angle θ, wake length L_w, horizontal distance a between the rear stagnation point of the cylinder and the recirculation center and vertical distance b between the symmetric recirculation centers; right image: comparison between the present and previous results for the pressure coefficient (C_p) on the bottom half of the cylinder surface at $Re' = 40$. The upstream stagnation point is located at $\theta = 180°$.

drag coefficient (C_D) are given in table 5.1. The predicted separation angle θ and wake length L_w compare well with the experimental results obtained by Coutanceau & Bouard (1977) while the predicted distance a is smaller than their measurements, but in good agreement with the numerical results obtained by Bouchon et al. (2012) and Gautier et al. (2013). Moreover, a good agreement for the drag coefficient is obtained by comparison with previously numerical predictions (Bouchon et al. 2012, Gautier et al. 2013, Fornberg 1980, Tseng & Ferziger 2003, Patil & Lakshmisha 2009) as shown in table 5.1.

Table 5.1: The physical parameters obtained by the present numerical method and previous works for the flow past a circular cylinder at $Re' = 40$.

	C_D	θ	L_w	a	b
Tseng & Ferziger (2003)	1.53		2.21		
Coutanceau & Bouard (1977)		126.2°	2.13	0.76	0.59
Bouchon et al. (2012)	1.50	126.6°	2.26	0.71	0.60
Gautier et al. (2013)	1.49	126.4°	2.24	0.71	0.59
Fornberg (1980)	1.50	124.4°	2.24		
Patil & Lakshmisha (2009)	1.56	127.3°	2.14		
Present study	1.56	126.8°	2.27	0.74	0.60

5.3.2 Flow in a steady lid-driven square cavity with an embedded cylinder

The vortex structures in a steady lid-driven square cavity with a centered cylinder have been investigated for Reynolds numbers ($Re = UH/\nu$) equal to 100, 500 and 1000. Moreover, two cylinders of dimensionless radius $r = r'/H = 0.2$ and 0.3 are considered.
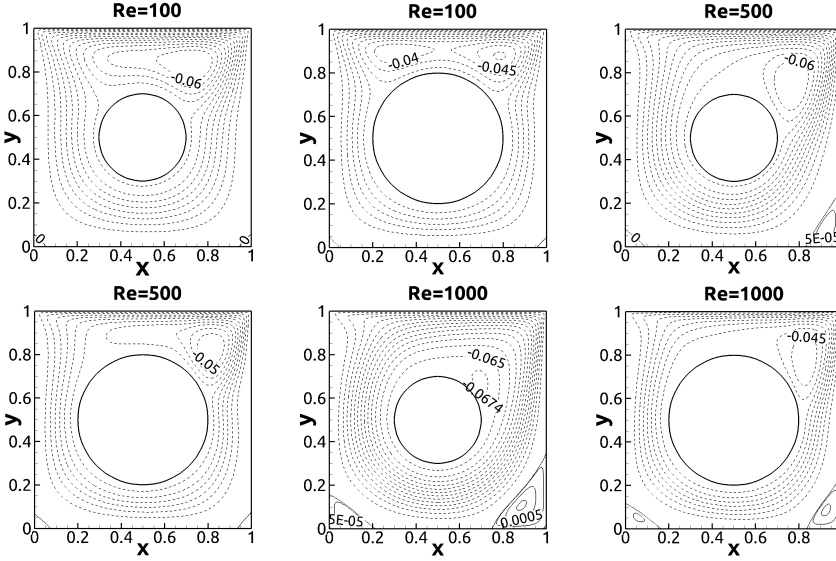
Figure 5.4: Streamline contours for the flow in a steady lid-driven square cavity with a centered cylinder of r = 0.2 (left column) and 0.3 (right column) for Re = 100, 500 and 1000. Solid and dashed lines denote the positive and negative contour values, respectively; for the streamline contours, the equal difference in value of 0.005 between the two unmarked adjacent contour lines is used.

Figure 5.4 shows the velocity components u and v along $x = 0.5$ and $y = 0.5$, respectively, for the steady lid-driven cavity containing a centered cylinder of $r = 0.2$ for $Re = 1000$. A coarse mesh of $\Delta x = \Delta y = 0.01$ and a fine mesh of $\Delta x = \Delta y = 0.005$ are used to obtain the present results, which are in good agreement with those given by Cai et al. (2017) It appears that the coarse mesh is sufficient to obtain grid independent results.

Figure 5.5 shows the streamline contours within a steady lid-driven square cavity with a centered cylinder of $r = 0.2$ (left column) and 0.3 (right column). For the smallest cylinder (left column), the lid-driven flow rolls up at the upper boundary of the cylinder, forming an elongated clockwise primary vortex while flow separation and reattachment at the bottom
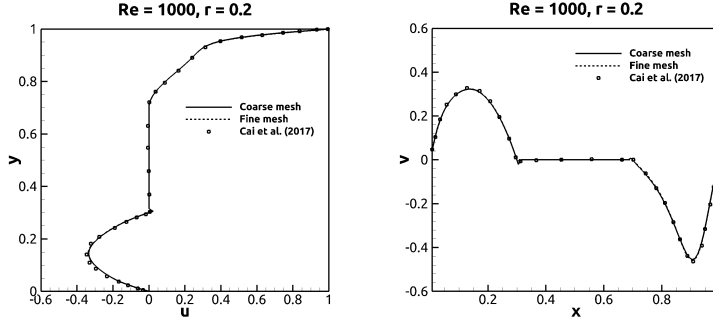
Figure 5.5: Comparison of the velocity profiles for steady lid-driven square cavity flow containing a centered cylinder of $r = 0.2$ for $Re = 1000$ obtained by the present method and by Cai et al. (2017): left image, distribution of the horizontal velocity component u along $x = 0.5$; right image, distribution of the vertical velocity component v along $y = 0.5$.

corner induce two weak anti-clockwise bottom corner vortices which are also present in the absence of the cylinder (Cheng & Hung 2006). As Re increases from 100 to 1000 (left column), the primary vortex decreases in size and moves closer towards the cylinder while the bottom corner vortices grow in size and strength. For the largest cylinder (at $Re = 100$; right column), it appears that the primary vortex breaks up into two clockwise vortices. These patterns were previously predicted by Khanafer & Aithal (2013) for the same Re, size and position of the cylinder for a low Richardson number $R_i = 0.01$, implying that the flow is dominated by momentum instead of temperature gradients and consequently that this prediction is comparable with the present one where the effect of temperature gradients is neglected. Here $R_i = Gr/Re^2$, where $Gr = \frac{g\beta(T_h - T_c)H^3}{\nu^2}$; g is the acceleration due to gravity; β is the thermal expansion coefficient; T_h and T_c are the temperatures of the hot and cold walls, respectively). As Re increases to 1000 (right column), only one primary vortex is present both for $r = 0.2$ and 0.3, indicating that the size of cylinder is a key parameter for the break-up of the primary vortex. Moreover, increasing the cylinder size leads to a weaker primary vortex core as well as weaker bottom corner vortices.

5.3.3 Flow patterns in a steady lid-driven rectangular cavity with an embedded cylinder

A detailed investigation of the flow within the steady lid-driven cavity of height to length ratio $AR = 1:2$ containing a circular cylinder has been

conducted for $Re = 100$, 500 and 1000. Three different locations, i.e. (x, y) = (0.5, 0.5), (1, 0.5) and (1.5, 0.5), as well as four different cylinder radii (r = 0.1, 0.2, 0.3 and 0.4) are considered using a resolution of 200x100 uniform grid cells which is sufficient for obtaining grid independent results. Flow in a steady lid-driven cavity of AR = 1:2 without the cylinder is given as a reference in figure 5.6 for Re = 100, 500 and 1000. These results are in good agreement with previous results by Cheng & Hung (2006), showing that the cavity contains a clockwise primary vortex as well as two anti-clockwise bottom corner vorticies. It is shown that an increase in Re leads to a noticeable growth of the bottom left corner vortex. Further validations for pure lid-driven cavity flows are given in Zhu et al. (2020).
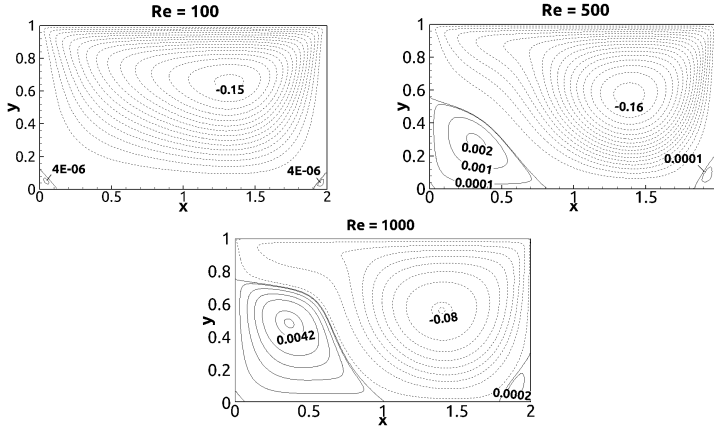
Figure 5.6: Streamline contours for flow in a steady lid-driven cavity of AR = 1:2 without the cylinder for Re = 100, 500 and 1000.

5.3.3.1 Left-centered cylinder

Figure 5.7 shows streamline contours for flow in a steady lid-driven cavity of AR = 1:2 containing a cylinder located at (0.5, 0.5) for r = 0.1, 0.2, 0.3 and 0.4 with Re = 100. For r = 0.1, the cavity contains a clockwise primary vortex to the right of the cylinder and two anti-clockwise bottom corner vortices. This flow denotes the flow pattern I which remains qualitatively the same for r = 0.2. As r increases further to 0.3, a new clockwise vortex is formed at the upper left side of the cylinder; this is also present for r = 0.4. This flow pattern is denoted II. Increasing r from 0.1 to 0.4 leads to a weakening of the primary vortex to the right of the cylinder while the bottom corner vortices are only weakly affected. This is due to the

decreased space between the left wall and the cylinder impeding the growth of the primary vortex.

Figure 5.8 shows streamline contours for the same geometry as in figure 5.7 for $Re = 500$. For $r = 0.1$, there is a large clockwise primary vortex to the right of the cylinder while the flow circulates anti-clockwisely around the cylinder. This is due to the growth of the bottom left corner vortex (as Re increases) which also exists in a steady lid-driven cavity of the same AR without the cylinder as shown in figure 5.6 (see also Cheng & Hung 2006; figure 3). The flow in this circulation region rolls up at the upper left side of the cylinder and down at the lower right side of the cylinder, forming two anti-clockwise vortices. This flow is denoted flow pattern III. As r increases to 0.2, the decreasing gap between the cylinder and the adjacent walls leads to a larger velocity there, destroying the anti-clockwise flow circulation region shown for $r = 0.1$. Instead, a bottom vortex is formed. This flow pattern is denoted IV and remains the same as r increases to 0.3 but with a smaller bottom vortex than for $r = 0.2$. For $r = 0.4$, this bottom vortex vanishes, and the flow here is thus exhibiting flow pattern II.

Figure 5.7: Streamline contours for flow in a steady lid-driven cavity of AR = 1:2 containing a left-centered cylinder with r = 0.1, 0.2, 0.3 and 0.4 for Re = 100

Figure 5.9 shows streamline contours for the same geometry as figures 5.7 and 5.8 for $Re = 1000$. For $r = 0.1$, a larger anti-clockwise circulation region than for $Re = 500$ (figure 5.8) is formed around the cylinder while a large clockwise primary vortex exists to the right of the cylinder. It appears that within the anti-clockwise circulation region, a clockwise vortex is formed at the upper left side of the cylinder. This flow pattern is denoted V. For $r = 0.2$, two anti-clockwise vortices are formed at the upper left and the lower

Figure 5.8: Streamline contours for flow in a steady lid-driven cavity of AR = 1:2 containing a left-centered cylinder with r = 0.1, 0.2, 0.3 and 0.4 for Re = 500.

right side of the cylinder, and the flow is thus exhibiting pattern III. For r = 0.3, the flow exhibits pattern IV but with a larger and stronger bottom vortex than for Re = 500 (figure 5.8). As r increases further to 0.4, the bottom vortex remains and a clockwise vortex, which also appears in flow pattern II (figure 5.8 for r = 0.3 and 0.4), is formed at the upper left side of cylinder. This flow pattern is denoted VI.

Figure 5.9: Streamline contours for flow in a steady lid-driven cavity of AR = 1:2 containing a left-centered cylinder with r = 0.1, 0.2, 0.3 and 0.4 for Re = 1000.

5.3.3.2   Centered cylinder

Figure 5.10 shows streamline contours for the centered cylinder located at (1, 0.5) for $Re = 100$ and $r = 0.1$, 0.2, 0.3 and 0.4. The flow exhibits pattern II for all values of r but the clockwise vortex to the left of the cylinder is larger than for the left-centered cylinder (figure 5.7 for $r = 0.3$ and 0.4). Young et al. (2005) investigated creeping flow for a steady lid-driven rectangular cavity containing a centered rotating and non-rotating cylinder. Two equal clockwise vortices attached to the upper left and right side of the cylinder were formed for the non-rotating cylinder. In the present case, however, the non-linearity of the convective term results in asymmetry of these vortices with the vortex to the right of the cylinder being significantly larger than that to the left of the cylinder. As r increases, the left clockwise vortex grows gradually in size due to more flow rolling down from the lid at the upper left side of the cylinder. Moreover, it appears that the maxima of the stream function for the left and right clockwise vortices decrease as r increases while the bottom corner vortices are only weakly affected by the cylinder size.
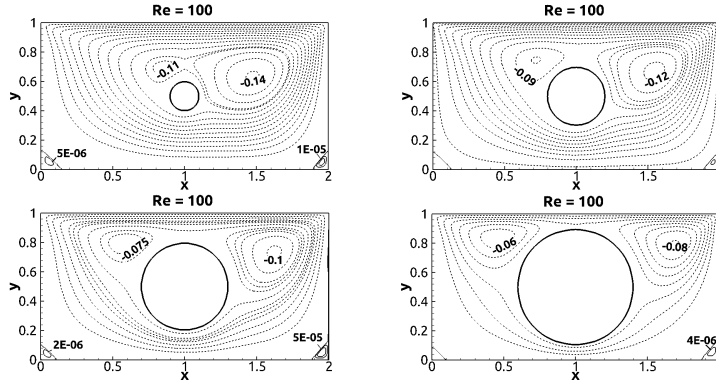
Figure 5.10: Streamline contours for flow in a steady lid-driven cavity of AR = 1:2 containing a centered cylinder with r = 0.1, 0.2, 0.3 and 0.4 for Re = 100.

Figures 5.11 and 5.12 show streamline contours for the same geometry as shown in figure 5.10 but for $Re = 500$ and 1000, respectively. The flow exhibits pattern II for all values of r and Re but with an amplification of the bottom corner vortices due to the higher Reynolds number, which also leads to a weaker clockwise vortex pair attached to the cylinder, as well as the vortex to the left of the cylinder being larger relative to the vortex to the left of the cylinder. As Re increases the vortex to the right of the
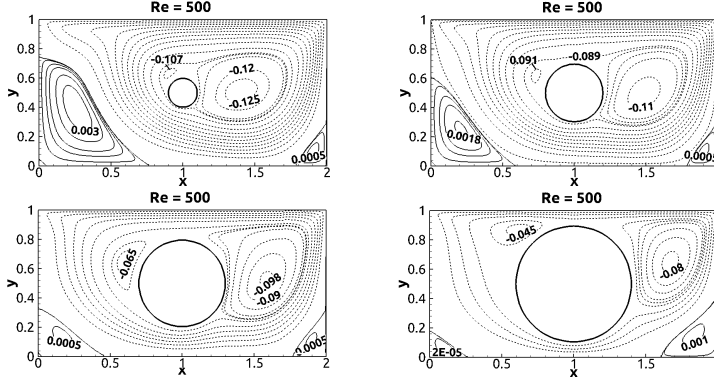
Figure 5.11: Streamline contours for flow in a steady lid-driven cavity of AR = 1:2 containing a centered cylinder with r = 0.1, 0.2, 0.3 and 0.4 for Re = 500.

cylinder moves towards the bottom. Moreover, an increase in r leads to a decay of the bottom left corner vortex while the bottom right vortex is only weakly affected.
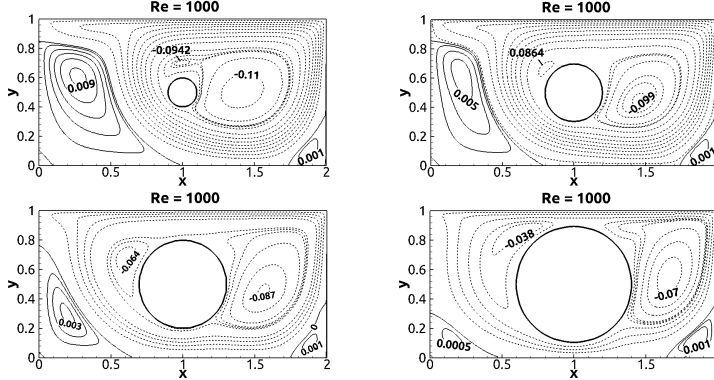
Figure 5.12: Streamline contours for flow in a steady lid-driven cavity of AR = 1:2 containing a centered cylinder with r = 0.1, 0.2, 0.3 and 0.4 for Re = 1000.

5.3.3.3   Right-centered cylinder

Figure 5.13 shows streamline contours for the cylinder located at (1.5, 0.5) with $Re = 100$ and $r = 0.1, 0.2, 0.3$ and 0.4. For $r = 0.1$, the cavity contains one clockwise vortex to the upper left side of the cylinder and two bottom

corner vortices; this flow is denoted flow pattern VII. For $r = 0.2$, 0.3 and 0.4, a clockwise vortex is also formed at the upper right side of the cylinder; here the flow exhibits pattern II.
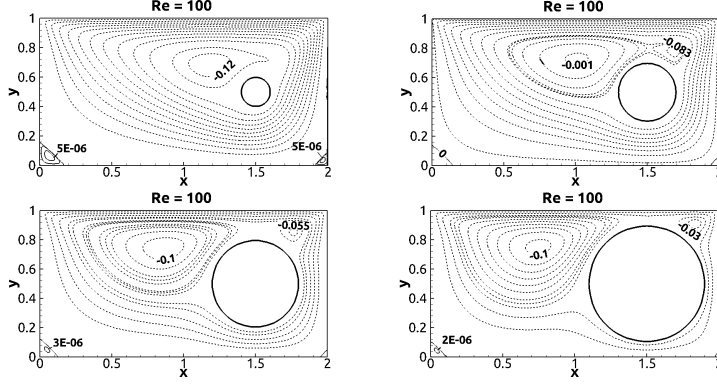
Figure 5.13: Streamline contours for flow in a steady lid-driven cavity of AR = 1:2 containing a right-centered cylinder with r = 0.1, 0.2, 0.3 and 0.4 for Re = 100.
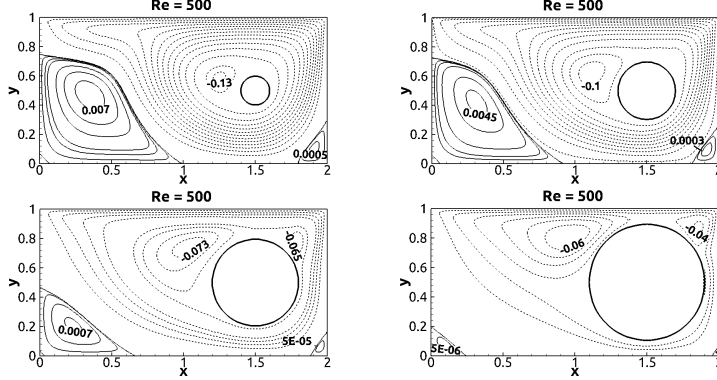
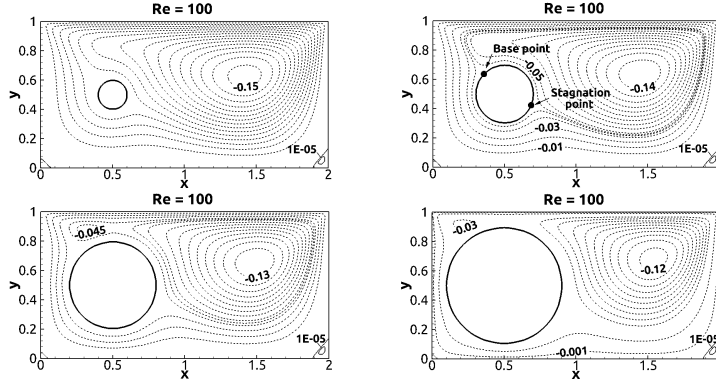*Figure 5.14: Streamline contours for flow in a steady lid-driven cavity of AR = 1:2 containing a right-centered cylinder with r = 0.1, 0.2, 0.3 and 0.4 for Re = 500.*

Figures 5.14 and 5.15 show the streamline contours for $Re = 500$ and 1000, respectively, for the same geometry as in figure 5.13. An increase in Re (for a given r) causes the bottom corner vortices to grow, while an increase of r (for a given Re) leads to a decay of the bottom corner vortices. For $r = 0.1$, the flow exhibits pattern VII both for $Re = 500$ and 1000 but with a smaller clockwise vortex to the left of the cylinder than for $Re = 100$
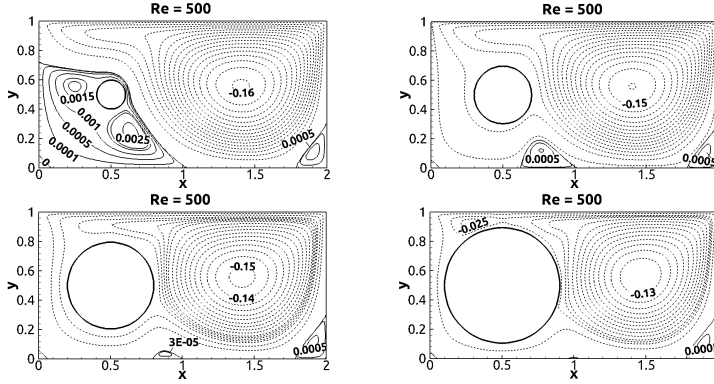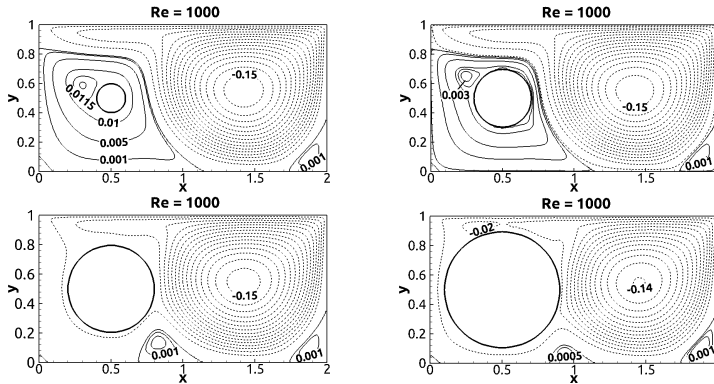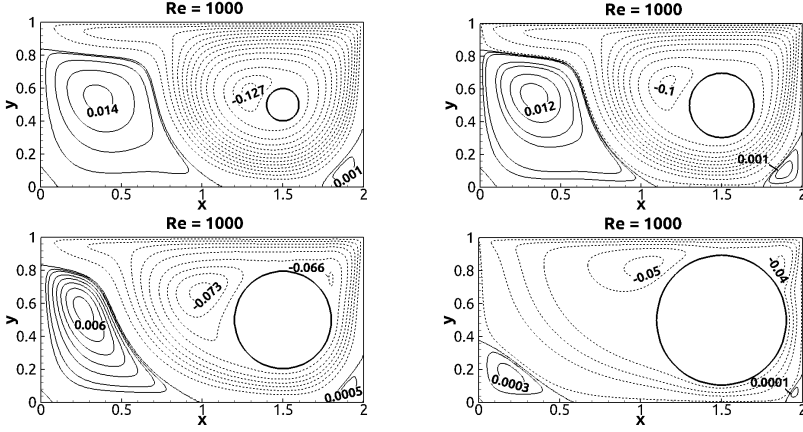
Figure 5.15: Streamline contours for flow in a steady lid-driven cavity of $AR = 1{:}2$ containing a right-centered cylinder with $r = 0.1, 0.2, 0.3$ and 0.4 for $Re = 1000$.

(figure 5.13). For $r = 0.2$, the flow exhibits pattern II for $Re = 500$ with smaller clockwise vortices attached to the cylinder than for $Re = 100$ while for $Re = 1000$ the flow exhibits pattern VII. For $r = 0.3$ and 0.4, the flow exhibits pattern II both for $Re = 500$ and 1000.

5.3.3.4   Distribution of flow patterns

Figure 5.16 shows the distribution of flow patterns within the steady lid-driven cavity of $AR = 1{:}2$ containing a left-centered (top image) and right-centered (bottom image) cylinder. For the centered cylinder, only flow pattern II exists (and hence this distribution is not plotted here). The cavity flow with a left-centered cylinder exhibits all the flow patterns, depending on Re and r, except flow pattern VII. This is due to the large anti-clockwise circulation flow formed at the bottom left corner (which also exists in the absence of the cylinder), which here is strongly affected by r and Re. For a given r, there is a tendency that there are more transitions between different flow patterns for small r than for large r (for Re ranging from 100 to 1000) while for a given Re, the number of transitions is larger for high Re than for low Re (for r ranging from 0.1 to 0.4). Figure 5.16 also shows which transitions are possible. For example, flow pattern V can only have transition to flow pattern III (by either increasing r or decreasing Re), while flow pattern IV can have transition to flow pattern I (by either increasing r or decreasing Re), to flow pattern III (by either decreasing r or increasing Re) and to flow pattern VI (by increasing r). For the right-centered cylinder

Left-centered cylinder

right-centered cylinder
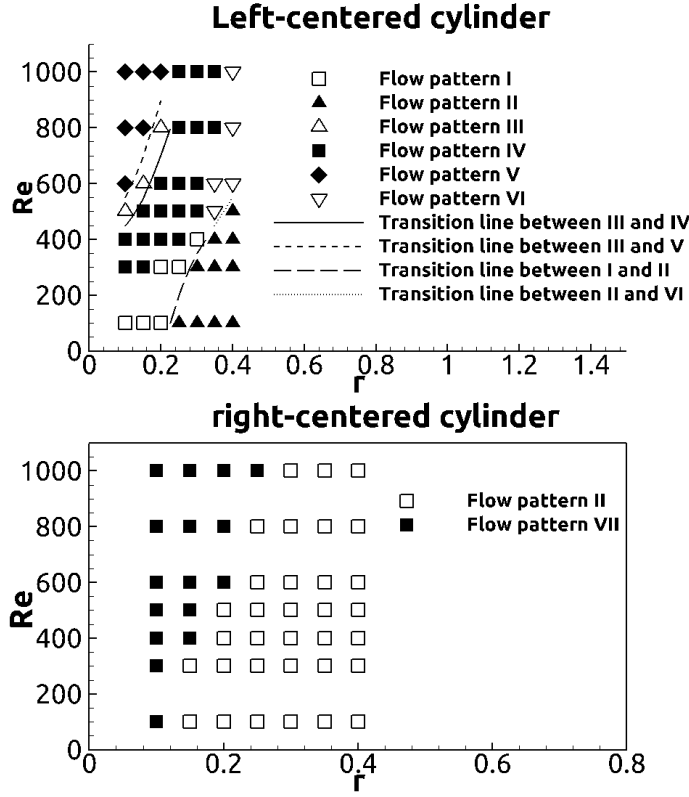
Figure 5.16: Distribution of flow patterns within the steady lid-driven cavity of AR = 1:2 containing a left-centered (top image) and right-centered (bottom image) cylinder.

(bottom image of figure 5.16), only one new flow pattern VII is formed for relatively small r. An increase of r leads to a clockwise vortex to the right of the cylinder (forming flow pattern II). To compensate this effect, a higher Re is required to maintain flow pattern VII.

The solid lines in figure 5.16 denote the transition lines between two different flow patterns. These lines can be given in the form of functional relationships between r and Re as follows:

$$Re = 10955 \times r^2 - 771.36 \times r + 417.96, \qquad \text{III} \leftrightarrow \text{IV}$$

$$Re = 10000 \times r^2 + 500 \times r + 400, \qquad \text{III} \leftrightarrow \text{V}$$

$$Re = -13333 \times r^2 + 10333 \times r - 1550, \qquad \text{I} \leftrightarrow \text{II}$$

$$Re = 2000 \times r - 250, \qquad \text{II} \leftrightarrow \text{VI}$$

5.3.3.5   Pressure distribution around the cylinder

In the present work, the pressure at the bottom left corner (p_0) is taken as a reference point. The pressure coefficient around the cylinder is given by

$$C_p = \frac{p - p_0}{\frac{1}{2}\rho U^2} \tag{5.9}$$

where p is the pressure around the cylinder.

Figure 5.17 (a) shows the pressure coefficient C_p around left-centered cylinders for four different radii ($r = 0.1, 0.2, 0.3$ and 0.4) for $Re = 100$. As r increases, C_p increases. This might be explained by that an increase of r leads to an increase of the gap flow velocity between the cylinder and its adjacent walls (since the gap decreases) as plotted in figure 5.17 (b), which shows $u(0.5, y)$ along the gap G between the cylinder bottom and the bottom wall for $r = 0.1, 0.2, 0.3$ and 0.4 with $Re = 100$.
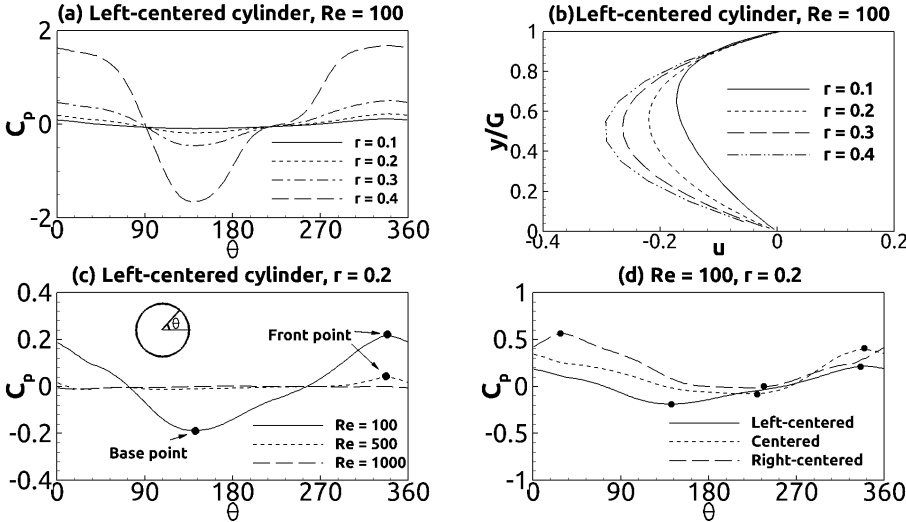
Figure 5.17: (a) pressure coefficient C_p around the left-centered cylinder with $r = 0.1, 0.2, 0.3$ and 0.4 for $Re = 100$; (b) horizontal velocity $u(0.5, y)$ along the gap between the bottom wall and the cylinder bottom for $r = 0.1$ 0.1, 0.2, 0.3 and 0.4 with $Re = 100$; (c) C_p around the left-centered cylinder with $r = 0.2$ for $Re = 100, 500$ and 1000; (d) C_p around the left-centered, centered and right-centered cylinder with $r = 0.2$ for $Re = 100$.

Figure 5.17 (c) shows C_p around the left-centered cylinder with $r = 0.2$ for $Re = 100, 500$ and 1000. For $Re = 100$, the base stagnation pressure (i.e., C_p at the base point) and the front stagnation pressure (i.e., C_p at the

stagnation point) are consistent with the observation elaborated in figure 5.7. As Re increases to 500, C_p decreases significantly since the flow velocity around the cylinder decreases as visualized by the streamline contours in figures 5.7 and 5.8. For $Re = 1000$, C_p decreases further and the front stagnation pressure disappears. This is consistent with the observation that the fluid moves anti-clockwise around the cylinder as shown in figure 5.9.

Figure 5.17 (d) shows C_p around the left-centered, centered and right-centered cylinders with $r = 0.2$ for $Re = 100$. As the cylinder moves towards the right wall, the front and back stagnation points move clock-wise around the cylinder, and the pressure increases since the pressure is larger in the right part of the cavity than in the left part.

5.4 Summary and conclusions

A detailed investigation of the flow patterns in the steady lid-driven cavity of depth to width ratio 1:2 containing a circular cylinder of different radii and positions is provided. Here the Reynolds numbers are 100, 500 and 1000 whilst the radii are 0.1, 0.2, 0.3 and 0.4. The positions of the cylinder are left-centered, centered and right-centered. It appears that this flow can be classified into seven different flow patterns visualized by streamline contours. The flow pattern I is composed of one clockwise vortex to the right side of the cylinder and two bottom corner vortices; flow pattern II is composed by two clockwise vortices attached to the left and right side of the cylinder as well as two bottom corner vortices; flow pattern III contains two anti-clockwise vortices attached to the upper left and bottom right sides of the cylinder, a clockwise vortex at the upper right side of the cylinder as well as a bottom right corner vortex; flow patterns IV and VI are composed by flow patterns I and II, respectively, with an additional bottom vortex; flow pattern V is characterized by the anti-clockwise vortex at the lower right side of the cylinder vanishing from flow pattern III; flow pattern VII is characterized by the clockwise vortex to the right of the cylinder vanishing from flow pattern II.

These flow patterns are given for different cylinder radii and positions as well as Reynolds numbers. There is a tendency that for a given cylinder radius, there are more transitions between different flow patterns for a small radius than for a large radius (for Reynolds numbers ranging from 100 to 1000) while for a given Reynolds number, the number of transitions is larger for high Reynolds numbers than for low Reynolds numbers (for radii ranging from 0.1 to 0.4). Overall, a larger number of flow patterns tend to emerge as the Reynolds number increases for small cylinder radii. The largest variety

of flow patterns occur for the left-centered cylinder due to the interaction with the large anti-clockwise circulation flow formed at the bottom left corner.

Acknowledgements

References

Bansal, S. & Chatterjee, D. (2015), 'Magneto-convective transport of nanofluid in a vertical lid-driven cavity including a heat-conducting rotating circular cylinder', *Numerical Heat Transfer, Part A: Applications* **68**(4), 411–431.

Berthelsen, P. A. & Faltinsen, O. M. (2008), 'A local directional ghost cell approach for incompressible viscous flow problems with irregular boundaries', *Journal of Computational Physics* **227**(9), 4354–4397.

Billah, M. M., Rahman, M. M., Sharif, U. M., Rahim, N. A., Saidur, R. & Hasanuzzaman, M. (2011), 'Numerical analysis of fluid flow due to mixed convection in a lid-driven cavity having a heated circular hollow cylinder', *International Communications in Heat and Mass Transfer* **38**(8), 1093–1103.

Bouchon, F., Dubois, T. & James, N. (2012), 'A second-order cut-cell method for the numerical simulation of 2D flows past obstacles', *Computers & Fluids* **65**, 80–91.

Cai, S.-G., Ouahsine, A., Favier, J. & Hoarau, Y. (2017), 'Moving immersed boundary method', *International Journal for Numerical Methods in Fluids* **85**(5), 288–323.

Chatterjee, D. & Gupta, S. K. (2014), 'Hydromagnetic mixed convective transport in a nonisothermally heated lid-driven square enclosure including a heat-conducting circular cylinder', *Industrial & Engineering Chemistry Research* **53**(51), 19775–19787.

Chatterjee, D., Gupta, S. K. & Mondal, B. (2014), 'Mixed convective transport in a lid-driven cavity containing a nanofluid and a rotating circular cylinder at the center', *International Communications in Heat and Mass Transfer* **56**, 71–78.

Chatterjee, D. & Halder, P. (2016), 'Magnetoconvective transport in a lid-driven square enclosure with two rotating circular cylinders', *Heat Transfer Engineering* **37**(2), 198–209.

Cheng, M. & Hung, K. C. (2006), 'Vortex structure of steady flow in a rectangular cavity', *Computers & Fluids* **35**(10), 1046–1062.

Coutanceau, M. & Bouard, R. (1977), 'Experimental determination of the main features of the viscous flow in the wake of a circular cylinder in

uniform translation. part 1. steady flow', *Journal of Fluid Mechanics* **79**(2), 231–256.

Dennis, S. C. R. & Chang, G. (1970), 'Numerical solutions for steady flow past a circular cylinder at Reynolds numbers up to 100', *Journal of Fluid Mechanics* **42**(3), 471–489.

Fadlun, E. A., Verzicco, R., Orlandi, P. & Mohd-Yusof, J. (2000), 'Combined immersed-boundary finite-difference methods for three-dimensional complex flow simulations', *Journal of Computational Physics* **161**(1), 35–60.

Fornberg, B. (1980), 'A numerical study of steady viscous flow past a circular cylinder', *Journal of Fluid Mechanics* **98**(4), 819–855.

Galaktionov, O. S., Meleshko, V. V., Peters, G. W. M. & Meijer, H. E. H. (1999), 'Stokes flow in a rectangular cavity with a cylinder', *Fluid Dynamics Research* **24**(2), 81.

Gautier, R., Biau, D. & Lamballais, E. (2013), 'A reference solution of the flow over a circular cylinder at Re= 40', *Computers & Fluids* **75**, 103–111.

Grove, A. S., Shair, F. H. & Petersen, E. E. (1964), 'An experimental investigation of the steady separated flow past a circular cylinder', *Journal of Fluid Mechanics* **19**(1), 60–80.

Islam, A. W., Sharif, M. A. R. & Carlson, E. S. (2012), 'Mixed convection in a lid driven square cavity with an isothermally heated square blockage inside', *International Journal of Heat and Mass Transfer* **55**(19-20), 5244–5255.

Khanafer, K., Aithal, S., Assad, M. E. & Pop, I. (2017), 'Flow and heat transfer in a driven cavity with two cylinders', *Journal of Thermophysics and Heat Transfer* **31**(1), 99–108.

Khanafer, K. & Aithal, S. M. (2013), 'Laminar mixed convection flow and heat transfer characteristics in a lid driven cavity with a circular cylinder', *International Journal of Heat and Mass Transfer* **66**, 200–209.

Oztop, H. F., Zhao, Z. & Yu, B. (2009), 'Fluid flow due to combined convection in lid-driven enclosure having a circular body', *International Journal of Heat and Fluid Flow* **30**(5), 886–901.

Patil, D. V. & Lakshmisha, K. N. (2009), 'Finite volume TVD formulation of lattice Boltzmann simulation on unstructured mesh', *Journal of Computational Physics* **228**(14), 5262–5279.

Peller, N., Duc, A. L., Tremblay, F. & Manhart, M. (2006), 'High-order stable interpolations for immersed boundary methods', *International Journal for Numerical Methods in Fluids* **52**(11), 1175–1193.

Ray, S. & Chatterjee, D. (2014), 'Mhd mixed convection in a lid-driven cavity including heat conducting circular solid object and corner heaters with joule heating', *International Communications in Heat and Mass Transfer* **57**, 200–207.

Tseng, Y. H. & Ferziger, J. H. (2003), 'A ghost-cell immersed boundary method for flow in complex geometry', *Journal of Computational Physics* **192**(2), 593–623.

Young, D. L., Chen, C. W., Fan, C. M., Murugesan, K. & Tsai, C. C. (2005), 'The method of fundamental solutions for stokes flow in a rectangular cavity with cylinders', *European Journal of Mechanics-B/Fluids* **24**(6), 703–716.

Zhu, J., Holmedal, L. E., Wang, H. & Myrhaug, D. (2020), 'Vortex dynamics and flow patterns in a two-dimensional oscillatory lid-driven rectangular cavity', *European Journal of Mechanics-B/Fluids* **79**, 255–269.

Chapter 6

Near-wall effect on flow around an elliptic cylinder translating above a plane wall

Jianxun Zhu[1], Lars Erik Holmedal[1], Hong Wang[1], Dag Myrhaug[1]

Abstract

In this work the flow over an elliptic cylinder near a moving wall is investigated for Reynolds numbers less than 150. Here the ratio between the gap (i.e., the distance between the cylinder and the wall) and the length of the semi-major axis of the elliptic cylinder varies from 0.1 to 5. This ratio is hereafter denoted the gap ratio. The resulting Kármán vortex street, the two-layered wake and the secondary vortex street have been investigated and visualized. Numerical simulations show that for steady flow, the wake is composed of two asymmetric recirculation vortices while a decrease in the gap ratio suppresses the vortex shed from the lower part of the cylinder. For the unsteady flow, the wake can be classified into four different patterns based on the wake structures (the Kármán vortex street, the two-layered wake and the secondary vortex street). The regions of these wake pattern

[1]Department of Marine Technology, Norwegian University of Science and Technology, NO-7491 Trondheim, Norway

are given in the gap ratio and Reynolds number space, showing that the critical Reynolds number for the transition between different patterns increases as the gap ratio decreases. An overall increase of the mean drag coefficient with increasing gap ratios is observed except for a sudden drop which occurs within a small gap ratio range. Moreover, as the gap ratio increases, the onset location of the two-layered wake firstly decreases due to a decrease in flow velocity in the gap, and then increases due to the weakening of the wall suppression effect.

6.1   Introduction

The wake behind an isolated circular cylinder has been studied extensively because of its vital importance in understanding vortex shedding in engineering applications such as marine risers and bridges. At low Reynolds numbers (based on the cylinder diameter and the free-stream velocity), the flow is symmetrical around the cylinder without flow separation. As the Reynolds number increases to about 7, laminar separation occurs, forming a pair of counter-rotating vortices which are symmetrical about the centerline of the wake (Dennis & Chang 1970, Sen et al. 2009), and as the Reynolds number increases further, the well-known Kármán vortex street is formed (Le Gal et al. 2001, Kumar & Mittal 2006). This vortex street exhibits a transition to a two-layered wake farther downstream, followed by a second transition (even farther downstream) to a secondary vortex street with larger spatial scales than the primary ones (Cimbala et al. 1988). The physical mechanism underpinning the formation of the two-layered wake was investigated experimentally by, e.g. Durgin & Karlsson (1971) and Karasudani & Funakoshi (1994). They measured the vertical distance (h) between the upper and lower wake vortices and the horizontal distance (l) between two successive co-rotating vortices along the wake, and found that the ratio (h/l) between these vertical and horizontal distances increases downstream. At a given downstream location, this ratio reaches a critical value where two successive vortices shed from the upper part of the cylinder impose convection of vorticity within the vortex shed from the lower part of the cylinder. This vortex is located horizontally in between the two upper vortices (and vice versa if the two successive vortices shed from the lower part of the cylinder). As a result, this vortex starts to distort and rotate to align with the stream-wise direction, forming the two-layered wake.

Experiments conducted by Cimbala et al. (1988) showed a broad-band time frequency spectra of the vertical velocity fluctuation in the far wake. For Reynolds numbers between 100 and 160, the broad-band spectra con-

tains several prominent frequencies considerably lower than the Kármán shedding frequency. It appears to be a strong correlation between these low frequencies and the secondary vortex street, which contains vortices with spatial scales larger than the Kármán vortices. In the view of this, Cimbala et al. (1988) attributed the formation for the secondary vortex street to the hydrodynamic instability of the mean wake. This hypothesis was supported by Kumar & Mittal (2012) who conducted two-dimensional numerical simulations of flow around an isolated circular cylinder for a Reynolds number of 150. Here packets of fluctuating vortices (i.e. based on the fluctuating velocity field) with a range of spatial scales were formed in the far wake, and these vortex packets grew stronger (i.e. contained larger vorticity) through convection. On this basis, Kumar & Mittal (2012) argued that the transition from the two-layered wake to the secondary vortex street is due to the convective instability of the mean wake flow. Matsui & Okude (1983) conducted experimental measurements for flow around an isolated circular cylinder for Reynolds numbers less than 160 and explained the formation of the secondary vortex street in terms of merging of Kármán vortices. They also found that when the wake was forced acoustically by one-half and one-third of the Kármán shedding frequency, two and three of vortices merged into a large secondary vortex, respectively. The explanation of this behavior, as demonstrated by Williamson & Prasad (1993) in their experiments for Reynolds numbers less than 170, is that the far wake flow is sensitive to the perturbation of the free-stream velocity. A very small perturbation of the free-stream velocity can lead to visible spectral peaks with the perturbation frequency and with the frequency difference between the Kármán shedding and the perturbation. Recently, Jiang & Cheng (2019) investigated unforced (uniform inlet velocity without perturbations) cylinder wakes using two-dimensional numerical simulations and found two formation mechanisms for the secondary vortex street; i) the merging of two co-rotating vortices for Reynolds numbers ranging from 200 to 300; ii) the pairing of two counter-rotating vortices, followed by the merging of these paired vortices for Reynolds numbers ranging from 400 to 1000.

Wakes behind other bluff bodies such as square (Arif & Hasan 2019a,b) and elliptic cylinders have been investigated due to the practical impact on, e.g., submarines (Mittal & Balachandar 1996) and heat exchangers (Khan et al. 2005). For elliptic cylinders, the flow depends both on the aspect ratio of the elliptic cylinder (defined by the ratio of the semi-minor to semi-major axis length) and the incident angle (defined by the angle between the inlet flow direction and the semi-minor axis) in addition to the Reynolds number based on the free-stream velocity and the semi-major axis length. Johnson

et al. (2001) used two-dimensional numerical simulations to investigate flow around an isolated elliptic cylinder of aspect ratios ranging from 0.01 to 1 (i.e. from a flat plat to a circular cylinder) for Reynolds numbers up to 200 at zero incident angle. They found that for an aspect ratio of 0.5, the flow is steady for a Reynolds number of 40 while Kármán vortex shedding exists for a Reynolds number of 75. As the Reynolds number increases further to 125, the Kármán vortex street is followed by a two-layered wake (farther downstream); as the Reynolds number increases even further to 150, the secondary vortex street is formed in the far wake. This secondary vortex street moves upstream and becomes more irregular as the Reynolds number increases up to 200. The critical Reynolds number for the onset of the Kármán vortex street, the two-layered wake and the secondary vortex street in the wake increases as the aspect ratio increases. Johnson et al. (2004) investigated the power spectrum numerically of the vertical velocity along the horizontal centerline downstream of the cylinder, revealing the presence of secondary and tertiary frequencies in the far wake. These frequencies are lower than the Kármán shedding frequency. The peaks of the power spectrum at these low frequencies become larger farther downstream, triggering the transition from the two-layered wake to the secondary vortex street. Raman et al. (2013) conducted two-dimensional simulations for the flow around an elliptic cylinder with aspect ratios from 1 to 10 for Reynolds numbers from 50 to 500. They found that the vortex shedding can be suppressed by increasing the aspect ratio for a given Reynolds number. Yoon et al. (2016) and Paul et al. (2014) found that the critical Reynolds number for the vortex shedding suppression decreases as the angle of attack increases from 0° to 90°. Subburaj et al. (2018) used the immersed boundary method and the level set method to investigate the two-dimensional flow around the elliptic cylinder with aspect ratios of 0.25 and 0.5 near a free surface for a Reynolds number of 180 with different angles of attack, showing that for a submergence depth of 0.096, the vortex shedding is suppressed at the angle of attack of 45° while metastable states appear at -45°; at 90° vortex shedding is partially suppressed.

Transitional movements of bluff bodies near a stationary plane wall are both important in academic research and engineering applications such as e.g. submarines or AUV (Autonomous Underwater Vehicle) moving near a seabed. The latter is of great importance for inspections of subsea structures as well as for mapping of the ocean bathymetry and collection of both physical data (e.g. of wave-induced velocities, current velocities and sediment concentration) and biological data (e.g. fish larvae, plankton and contamination). Taneda (1965) and Zdravkovich (1985) towed a circular cylinder

along a plane wall in a water tank for Reynolds numbers of 170 and 3550, respectively, and found alternating vorticies shed from the upper and lower parts of the cylinder with a gap-to-diameter ratio of 0.6. When the same experiment was conducted for a gap-to-diameter ratio of 0.1, only a single row of vortices were shed from the upper part of the cylinder. Huang & Sung (2007) conducted two-dimensional numerical simulations, finding that for a Reynolds number of 300 the flow exhibits: i) a Kármán-like vortex shedding at a gap-to-diameter ratio of 0.6; ii) a pair-wise vortex shedding, where the lift and drag forces fluctuate with the same frequency at a gap-to-diameter ratio of 0.2; iii) a single row of vortex shedding from the upper part of the cylinder at a gap-to-diameter ratio of 0.1. The drag force increases as the gap-to-diameter ratio increases (for a given Reynolds number) up to a critical value (i.e., at the onset of the Kármán-like vortex shedding) where the drag force reaches its maximum value. As the gap-to-diameter ratio increases further the drag force decreases. It appears that the drag force is closely correlated to the base pressure (Sumer et al. 2006), i.e., the lowest pressure located at the downstream side of the cylinder. As the gap-to-diameter ratio increases up to the critical value, the vortices behind the cylinder become stronger due to the weakening of the wall suppression effect, thus drawing in fluid at a higher rate (Bearman & Trueman 1972) resulting in a lower base pressure and a larger drag force. As the gap-to-diameter ratio increases beyond this critical value, stronger vortices are shed from the bottom of the cylinder, resulting in an enhanced interaction with the vortices shed from the top of the cylinder, causing a higher vortex shedding frequency. This implies a shorter time interval for the vortices to grow before they move downstream, resulting in weaker vortices, which again cause a larger base pressure and a smaller drag force (Sumer et al. 2006). Moreover, as the gap-to-diameter ratio decreases (for a given Reynolds number), the stagnation point at the front of the cylinder moves downwards along the cylinder, causing a more asymmetric flow distribution around the cylinder, resulting in a larger lift force (Sumer et al. 2006). Jiang et al. (2017) conducted a comprehensive set of numerical investigations of the two- and three-dimensional wake transitions for Reynolds numbers up to 300 at gap-to-diameter ratios between 0.1 to 19.5. They found that for flow in the two-dimensional regime, the critical Reynolds number for the onset of the vortex shedding increases as the gap-to-diameter ratio decreases. This behavior further confirms that the presence of the wall weakens the interaction between the vortices shed from the top and bottom part of the cylinder, thus delaying the vortex shedding.

The development of the Kármán vortex street, the two-layered wake and

the secondary vortex street behind isolated cylinders have been investigated previously for a wide range of Reynolds numbers and aspect ratios. Paul et al. (2014) showed that the critical Reynolds number for the onset of the flow separation and the Kármán vortex shedding decreases with decreasing aspect ratios. Johnson et al. (2001) found that the critical Reynolds number for the onset of the two-layered wake and the secondary vortex street decreases with decreasing gap ratio. Thompson et al. (2014) found that an increase in Reynolds number for a given gap ratio or a decrease in gap ratios for a given Reynolds numbers results in the onset location of the two-layered wake and the secondary vortex street (which becomes more irregular) being closer to the cylinder. Moreover, Jiang et al. (2017) showed that the presence of a moving wall have a significant effect on the flow around a near-wall circular cylinder, e.g., suppressing the Kármán vortex shedding, changing the lift and drag coefficients by varying the gap ratio. However, the effect of a moving wall on the two-layered wake and the secondary vortex street behind a near-wall elliptic cylinder with an aspect ratio less than 1 has not been investigated previously. This is presented in the present work, together with the resulting forces on the elliptic cylinder itself.

Specifically, the flow over an elliptic cylinder with the aspect ratio of 0.4 near a moving wall is investigated for Reynolds numbers less than 150. Here the ratio between the gap (i.e., the distance between the cylinder and the wall) and the length of the semi-major axis of the elliptic cylinder varies from 0.1 to 5. The resulting Kármán vortex street, the two-layered wake and the secondary vortex street have been investigated and visualized. Numerical simulations show that for the steady flow, the wake is composed either of two asymmetric recirculation vortices or one recirculation vortex behind the cylinder; for the unsteady flow, the wake can be classified into four different patterns based on the wake structures. These wake patterns are mapped out in the gap ratio and Reynolds number space, and a detailed analysis of the near-wall effect (i.e., the effect of the gap ratios) on the lift and drag coefficients as well as on the onset location of the two-layered wake are presented.

6.2   Problem definition and governing equations

The current paper addresses the flow around an elliptic cylinder moving parallel to a wall with a constant velocity. It is convenient for numerical simulations to use a uniformly translating frame of reference fixed on the cylinder, such that the cylinder is stationary whilst the wall and the fluid move towards the right at a uniform speed as shown in figure 6.1. The

aspect ratio (AR) of the cylinder is defined by the semi-minor (a) to semi-major (D) axis length ratio, i.e. $AR = a/D$. The gap ratio is given by G/D where G is the gap between the moving wall and the cylinder, and the Reynolds number is based on the major axis, i.e. $Re = UD/\nu$ where ν is the kinematic viscosity. Here the incompressible flow with a constant density ρ is governed by the dimensionless two-dimensional Navier-Stokes equations given as

$$\frac{\partial u_i}{\partial x_i} = 0 \tag{6.1}$$

$$\frac{\partial u_i}{\partial t} + \frac{\partial u_i u_j}{\partial x_j} = -\frac{\partial p}{\partial x_i} + \frac{1}{Re}\frac{\partial^2 u_i}{\partial x_j \partial x_j} \tag{6.2}$$

where the Einstein notation using repeated indices is applied. Here $u_i = (u,v)$ and $x_i = (x, y)$ for $i = 1$ and 2, indicate the velocity and Cartesian coordinates, respectively, whilst t and p denote the time and pressure, respectively. The velocity, time, pressure and length are scaled by U, D/U, ρU^2 and D, respectively.
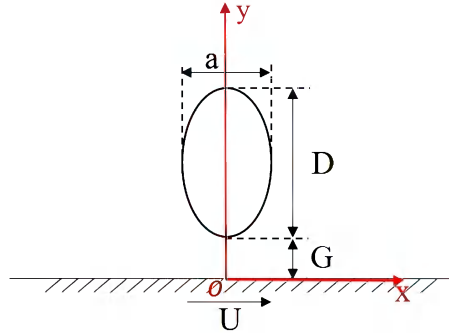
Figure 6.1: Definition of relevant dimensions

6.3   Numerical methods

A projection method is used for solving Eqs.(6.1) and (6.2). The convective terms and the diffusive terms are discretized by Adams–Bashforth and Crank-Nicolson schemes, respectively. The spatial derivatives are discretized with a second-order centred finite difference scheme on a staggered grid arrangement. The Poisson equation for pressure correction is solved using a biconjugate gradient stabilized method (Van der Vorst 1992) with a Jacobi preconditioner.

The cylinder geometry is taken into account by a direct-forcing immersed boundary method (Peller et al. 2006). Figure 6.2 shows the treatment of the Cartesian grid and the immersed boundary. A grid cell is blocked out of the simulation if its corresponding variable (velocity or pressure) lies within the immersed boundary. Then, the velocity point at the cell face between a blocked cell and an unblocked cell is set as an inactive velocity (■), which are updated by interpolation using the physical boundary condition at the immersed boundary point (○) and the active velocity point (□) within the fluid. Here, weighted one-dimensional, cubic Lagrange interpolation schemes are applied as follows:
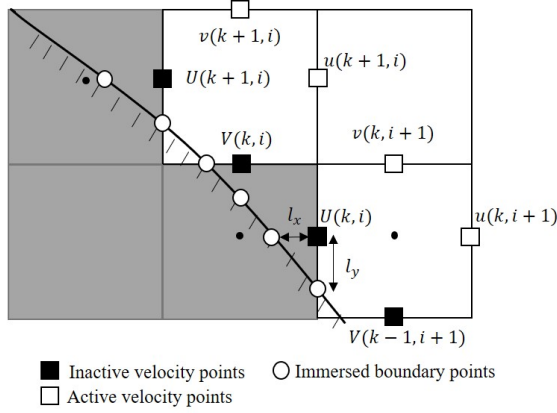
Figure 6.2: Definition of the inactive velocity points (■), immersed boundary points (○), and active velocity points (□).

$$f(x) = \sum_{k=1}^{3} \beta_k(x) f_k + \beta(x_\Gamma) f_\Gamma \tag{6.3}$$

where x and x_Γ denote the locations of the inactive point and the immersed boundary, respectively, whilst $f(x)$, f_k and f_Γ represent the velocity values at the inactive points, the active velocity points and the immersed boundary, respectively. Here the Lagrange coefficients $\beta_k(x)$ and $\beta(x_\Gamma)$ can be obtained by

$$\beta_k(x) = \left(\prod_{j=1, j \neq k}^{3} \frac{(x - x_j)}{(x_k - x_j)} \right) \frac{x - x_\Gamma}{x_k - x_\Gamma} \tag{6.4}$$

$$\beta(x_\Gamma) = \left(\prod_{j=1}^{3} \frac{(x - x_j)}{(x_\Gamma - x_j)} \right) \qquad (6.5)$$

where x_j denote the location of the jth active point.

If an inactive velocity point can be interpolated from two directions, each direction is multiplied by a weighting factor as follows:

$$f(x) = \lambda_x f^x + \lambda_y f^y \qquad (6.6)$$

where the superscript x and y denotes interpolation in the x and y-directions, respectively, and the weighting factors λ_x and λ_y are given as

$$\lambda_x = \frac{1}{1 + (\frac{l_x}{l_y})^2} \quad \text{and} \quad \lambda_y = \frac{1}{1 + (\frac{l_y}{l_x})^2} \qquad (6.7)$$

where l_x and l_y is the distance between the inactive point and the immersed boundary in the x and y-direction, respectively, as shown in figure 6.2. Moreover, a Neumann condition for the pressure correction is applied at the inactive velocity points.
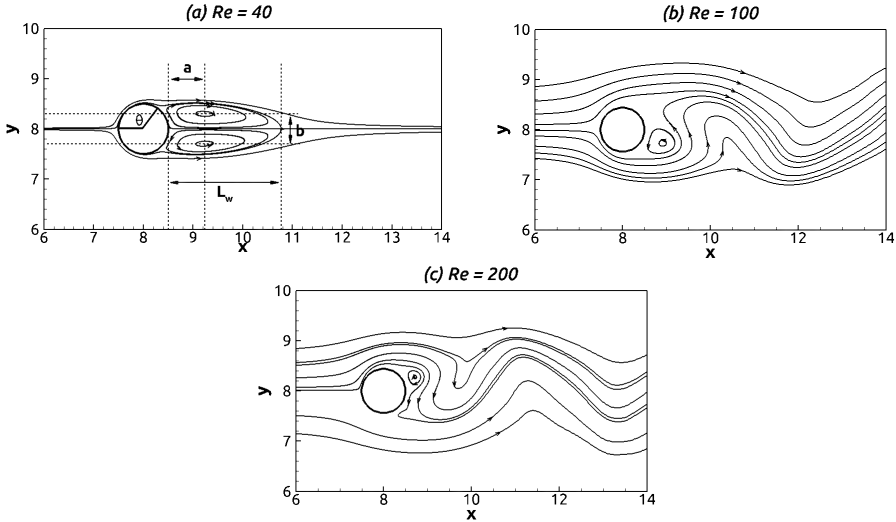
Figure 6.3: Streamlines for the flow over a cylinder at Re = (a) 40, (b) 100 and (c) 200 as well as the nomenclature used in Table 6.1; separation angle θ, wake length L_w, horizontal distance a between the rear stagnation point of the cylinder and the recirculation center and vertical distance b between the symmetric recirculation centers

6.4 Validation against previous numerical and experimental results

Numerical investigations of the two-dimensional flow around an isolated circular cylinder are conducted for $Re = 40$, 100 and 200. A dimensionless free-stream velocity $U = 1$ is specified at the inlet boundary while a Neumann condition is imposed for the velocity at the outlet and lateral boundaries. A no-slip condition is applied at the cylinder. The pressure is set to be zero at the outlet and a Neumann condition for the pressure correction is imposed at the other boundaries. A spin-up time of $t = t^*U/D = 200$ (where t^* is the physical time) was found to be sufficient to obtain a fully developed flow for all the cases. For $Re = 40$, the flow reaches a steady state where two counter-rotating vortices which are symmetrical about the centerline of the wake are formed (see figure 6.3a); for $Re = 100$ and 200, the flow exhibits an unsteady state where periodic alternating vortex shedding (Kármán vortices) occurs as visualized by the streamlines in figure 6.3(b) and 6.3(c).

*Table 6.1: The physical parameters obtained by the present numerical method and previous works for the flow around a circular cylinder at Re = 40; the superscript * denotes that the results were obtained by experiments. The front stagnation point is located at θ = 180°.*

	C_D	θ	L_w	a	b
*Coutanceau & Bouard (1977)		53.8°	2.13	0.76	0.59
Linnick & Fasel (2005)	1.54	53.6°	2.28	0.72	0.60
Fornberg (1980)	1.50	55.6°	2.24		
Patil & Lakshmisha (2009)	1.56	52.7°	2.14		
Taira & Colonius (2007)	1.54	53.7°	2.30	0.73	0.60
Berthelsen & Faltinsen (2008)	1.59	53.9°	2.29	0.72	0.60
Coarse mesh (0.02)	1.57	52.5°	2.26	0.72	0.60
Fine mesh (0.01)	1.59	53.1°	2.26	0.72	0.60

The inlet is located 10 cylinder diameters upstream of the cylinder center; the outlet is located 20 diameters downstream of the cylinder center, while the top and bottom boundaries are located 10 diameters away from the cylinder center. A fine uniform grid ($\Delta x = \Delta y = 0.01$) is applied in a small square region around the cylinder (i.e. $-0.7 \leq x \leq 0.7$, $-0.7 \leq y \leq 0.7$). From the edges of this region, the grid is stretched (using geometric series) in both the horizontal and vertical directions, using stretch ratios less than

1.05.

*Table 6.2: Comparisons between present results and previous numerical and experimental results: Strouhal number St, lift coefficient amplitude $C_{L,a}$, drag coefficient C_D and amplitude $C_{D,a}$ for uniform flow around a circular cylinder at Re = 100 and 200; the superscript * denotes that the results were obtained by experiments.*

Re = 100	$\bar{C}_D$	St	$C_{L,a}$	$C_{D,a}$
*Williamson (1989)	-	0.164	-	-
Calhoun (2002)	1.33	0.175	0.298	0.014
Russell & Wang (2003)	1.38	0.169	0.300	0.007
Xu & Wang (2006)	1.42	0.171	0.340	0.013
Berthelsen & Faltinsen (2008)	1.38	0.169	0.340	0.010
Wang et al. (2009)	1.38	0.170	0.357	-
Coarse mesh (0.02)	1.36	0.170	0.323	0.010
Fine mesh (0.01)	1.37	0.171	0.337	0.012
Re = 200	$\bar{C}_D$	St	$C_{L,a}$	$C_{D,a}$
*Williamson (1989)	-	0.197	-	-
Calhoun (2002)	1.17	0.202	0.668	0.058
Russell & Wang (2003)	1.29	0.195	0.500	0.022
Xu & Wang (2006)	1.42	0.202	0.660	0.040
Berthelsen & Faltinsen (2008)	1.37	0.200	0.700	0.046
Wang et al. (2009)	1.26	0.195	0.708	-
Coarse mesh (0.02)	1.35	0.200	0.707	0.047
Fine mesh (0.01)	1.36	0.200	0.706	0.048

Table 6.1 shows comparisons between the results obtained in the present work and available results obtained from experiments (Coutanceau & Bouard 1977) and numerical simulations for $Re = 40$ (Linnick & Fasel 2005, Fornberg 1980, Patil & Lakshmisha 2009, Taira & Colonius 2007, Berthelsen & Faltinsen 2008). Here C_D is the drag coefficient; θ, L_w, a and b (as shown in figure 6.3) denote the separation angle, wake length, the horizontal distance between the rear stagnation point of the cylinder and the recirculation center as well as the vertical distance between the symmetric recirculation centers, respectively. The drag coefficient C_D is defined as $C_D = 2F_d/(\rho U^2 D)$, where F_d is the drag force acting on the cylinder in the x-direction. The wake parameters L_w, a and b are scaled by the diameter of the cylinder. Table 6.1 shows that a good agreement is obtained with previous experimental (Coutanceau & Bouard 1977) and numerical (Linnick

& Fasel 2005, Fornberg 1980, Patil & Lakshmisha 2009, Taira & Colonius 2007, Berthelsen & Faltinsen 2008) results.
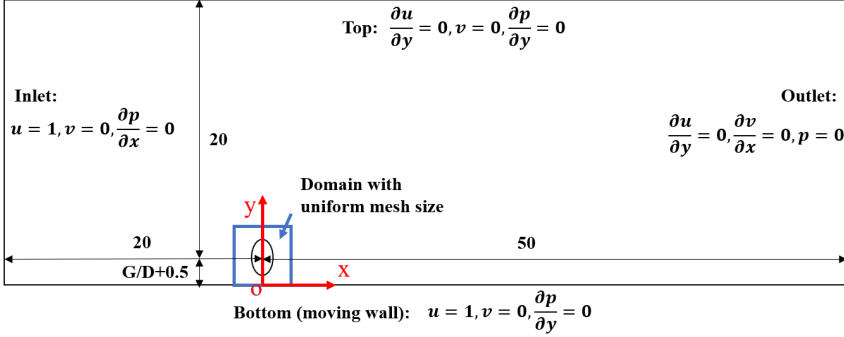
Figure 6.4: Sketch of the computational domain and the boundary conditions for the flow around an elliptic cylinder near a moving wall.

Table 6.2 shows comparisons between the present results and available results obtained from experiments (Williamson 1989) and the numerical simulations (Calhoun 2002, Russell & Wang 2003, Xu & Wang 2006, Berthelsen & Faltinsen 2008, Wang et al. 2009) for $Re = 100$ and 200. The quantities which are compared are the time-averaged drag coefficient ($\bar{C}_D$), the Stroudhal number $St = Df/U$(where f represents the vortex shedding frequency), the lift coefficient amplitude ($C_{L,a}$) and the drag coefficient amplitude ($C_{D,a}$). The present results are in good agreement with those obtained by Berthelsen & Faltinsen (2008) who used an immersed boundary method similar as the present method. Overall, the present results are in fair to good agreement with those presented in Table 6.2.

A grid refinement test was conducted using a coarse grid ($\Delta x = \Delta y = 0.02$) in the small rectangular domain around the cylinder, and then stretching the grid vertically and horizontally from the edges of this domain. The deviation from the results obtained with the fine grid was less than 1.2 % for the quantities given in Tables 6.1 and 6.2.

6.5   Results and discussion

Numerical investigations of the flow around an elliptic cylinder with an aspect ratio $AR = 0.4$ near a moving wall have been conducted for Re ranging from 30 to 150 for gap ratios G/D ranging from 0.1 to 5. Figure 6.4 shows the computational domain, the location of the cylinder and the boundary conditions. The inlet and top boundaries are located $20D$ away from the
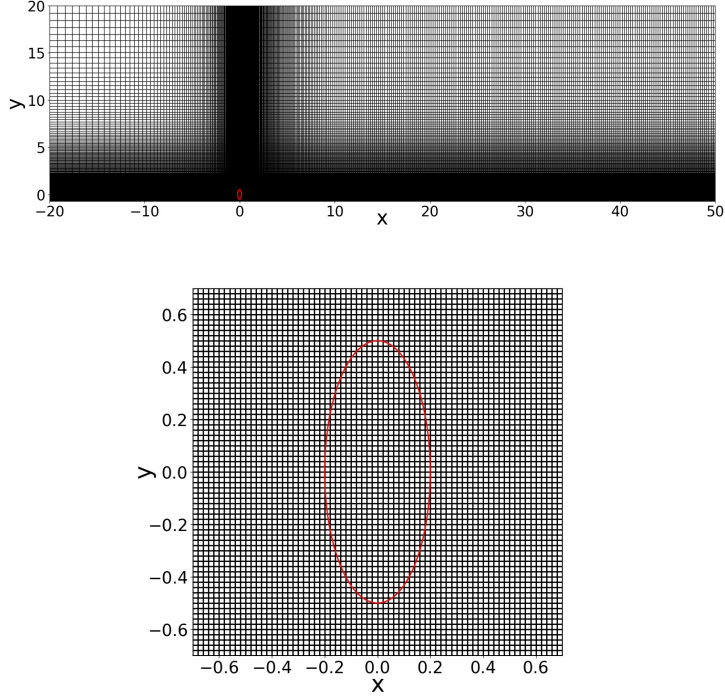
Figure 6.5: Grid for the whole computational domain and a close-up of the uniform grid around the cylinder at $G/D = 0.2$.

cylinder center; the outlet is located $50D$ downstream of the cylinder center, and the bottom boundary is located $(G/D+0.5)D$ from the cylinder center. A dimensionless velocity $u = 1$ is set at the inlet, and a Neumann condition is imposed for the velocity at the top and outlet boundaries. A no-slip condition is applied at the cylinder and the bottom wall which moves towards the right at $u = 1$. The pressure equals to zero at outlet and a Neumann condition for the pressure correction is imposed at other boundaries.

A uniform grid ($\Delta x = \Delta y = 0.02$) is applied to a region (marked by a blue rectangle) around the cylinder. The edges of this region is located 0.7 semi-major axis lengths away from the cylinder center. The grid is stretched from the top and left edges of this edge, using constant stretch ratios less than 1.02. From the right edge, the grid is stretched over the next 10 semi-major axis lengths downstream (using a stretch ratio of 1.01) until $\Delta x = 0.1$ which is held constant over the rest of the downstream region. For gap ratios less than 1, the grids between the cylinder bottom and the bottom wall have the same vertical size, i.e. $\Delta y = 0.02$. For gap ratios larger than 1, the
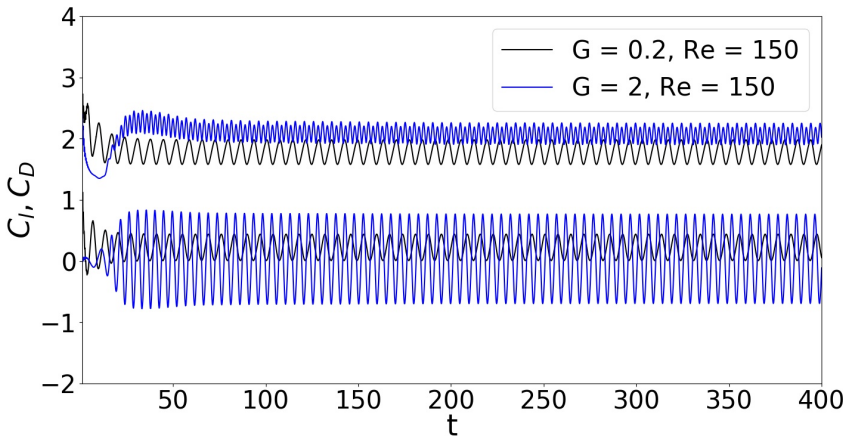
Figure 6.6: Time history of C_D (upper two curves) and C_l (lower two curves) for $Re = 150$ with $G/D = 0.2$ and 2.

Table 6.3: Comparisons of the St, $\bar{C}_D$ and $\bar{C}_l$ obtained by the computation domain 2 with the uniform mesh sizes $\Delta x = \Delta y = 0.02$ and 0.01 for $Re = 150$ and $G/D = 0.1$.

Mesh size	St	$\bar{C}_D$	$\bar{C}_l$
Coarse ($\Delta x = \Delta y = 0.02$)	0.105	1.66	0.36
Fine ($\Delta x = \Delta y = 0.01$)	0.106	1.67	0.35

grid is stretched symmetrically from the bottom wall and from the cylinder bottom to the center position between them, using a stretching ratio less than 1.01. Figure 6.5 shows the complete grid for the whole computational domain and a close-up of the uniform grid around the cylinder for $G/D = 0.2$. For all the simulations conducted in this study, a spin-up time of $t = 400$ was found to be sufficient to obtain a fully developed flow where the fluctuation amplitude and period of C_D and C_l are fully developed, as exemplified in figure 6.6 showing the time history of C_D and C_l for $Re = 150$ with $G/D = 0.2$ and 2. This was checked for each simulation.

To test grid independence, numerical simulations were conducted using the coarse grid resolution and the fine grid resolution as given in Table 6.3 for the largest Reynolds number $Re = 150$ and the smallest gap ratio $G/D = 0.1$. Table 6.3 shows St, $\bar{C}_D$ and $\bar{C}_l$ obtained by the two grid resolutions, showing deviations of 0.9%, 0.6% and 2.7%, respectively, from

those obtained with the coarse grid. Thus, the coarse grid is remaining sufficient to obtain the grid independent results.

6.5.1 Steady state

Flow around an isolated elliptic cylinder with $AR = 0.4$ is in the steady regime for $Re = 30$ while vortex shedding occurs for $Re = 40$ as visualized by vorticity and streamline contours in figures 6.7(a) and 6.7(b), respectively. Here the critical Reynolds number Re_c for the onset of the vortex shedding is 35±5 which is smaller than the critical Reynolds number for a circular cylinder ($AR = 1$) which ranges from 45 to 49 (Jackson 1987, Le Gal et al. 2001, Kumar & Mittal 2006); a decrease in AR leads to a decrease of Re_c. The effect of the aspect ratio on the critical Reynolds number has been investigated numerically by Thompson et al. (2014) and Paul et al. (2014), finding that Re_c decreases from 47.2 to 31.6 and from 48.5±0.5 to 23.5±0.5, respectively, as AR decreases from 1 to 0.1. Thompson et al. obtained a larger Re_c for $AR = 0.1$ than Paul et al.. This is mainly because the blockage ratio of the grid system used by Thompson et al. is 1%, which is much smaller than 6.25% used by Paul et al..
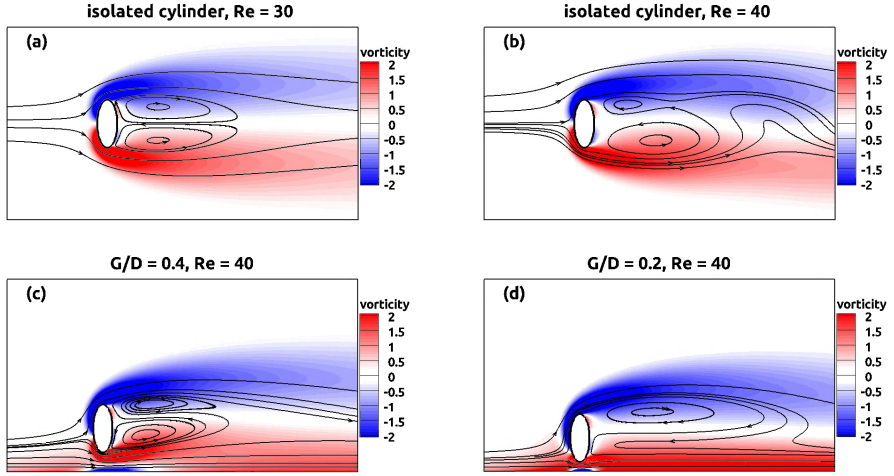
Figure 6.7: Vorticity contours and streamlines (black solid lines) for flow around an isolated elliptic cylinder of $AR = 0.4$ for (a) $Re = 30$ and (b) $Re = 40$; for flow around an elliptic cylinder of $AR = 0.4$ for $Re = 40$ at (c) $G/D = 0.4$ and (d) $G/D = 0.2$.

Figures 6.7(c) and 6.7(d) show the vorticity and streamline contours for

$Re = 40$ at $G/D = 0.4$ and 0.2, respectively. The flow reaches a steady state (i.e. no vortex shedding) at $G/D = 0.4$ (figure 6.7c) while at the same Re the flow exhibits vortex shedding for the isolated cylinder (figure 6.7b). This is because the shear layer (negative vorticity) generated near the moving wall weakens the shear layer beneath the bottom of the cylinder (positive vorticity), thus delaying the onset of vortex shedding. This is the same mechanism as has been previously observed for a circular cylinder near a moving wall (Rao et al. 2013, 2015, Jiang et al. 2017). As G/D decreases further to 0.2, the lower recirculation vortex as observed in figure 6.7(c) vanishes. The impact of G/D on the front stagnation point for a circular cylinder near a moving wall was investigated by Jiang et al. (2017) using two-dimensional numerical simulations, showing that the front stagnation point moves downwards along the cylinder as G/D decreases. This behavior is also observed in the present studies and is visualized by the streamlines in figures 6.7(c) and 6.7(d). It appears that more fluid move upwards along the cylinder due to the enhanced blockage effect in the gap (as can be seen by the downward movement of the front stagnation point in figure 6.7c and 6.7d) caused by decreasing G/D, forming a larger recirculation vortex for $G/D = 0.2$ than for $G/D = 0.4$. This behavior is qualitatively similar to the observation by Jiang et al. (2017) for the flow around a circular cylinder near a moving wall.

Figure 6.8(a) shows the recirculation vortex centers for Re ranging from 30 to 70 at $G/D = 0.2$ and 0.4, i.e. in the parameter range where the flow is steady. The upper recirculation vortex is formed for all the values of Re and G/D considered here while the lower recirculation vortex disappears for $Re \leq 40$ at $G/D = 0.2$. It appears that the lower recirculation vortex center is located closer to the cylinder than the upper recirculation vortex center, and this difference is larger for $G/D = 0.2$ than for $G/D = 0.4$ due to stronger wall suppression effect on the lower recirculation vortex. For $G/D = 0.4$, an increase of Re leads to a smaller difference since thinner shear layers are formed, resulting in a weaker interaction between the shear layers beneath the cylinder bottom and near the wall. For $G/D = 0.2$, however, an increase of Re does not affect the bottom vortex much due to the wall suppression effect.

Figure 6.8(b) shows C_D and C_l against Re in the steady flow regime, i.e., for $Re \in [30$, $100]$ at $G/D = 0.2$ and 0.4. For a given Re, C_D and C_l are larger for $G/D = 0.2$ than for $G/D = 0.4$. For a given G/D, C_D and C_l decrease almost linearly as Re increases in log-log scale. This is in qualitative agreement with results observed previously by Rao et al. (2013, 2015) (for the steady flow regime, i.e., no vortex shedding) for a fixed and
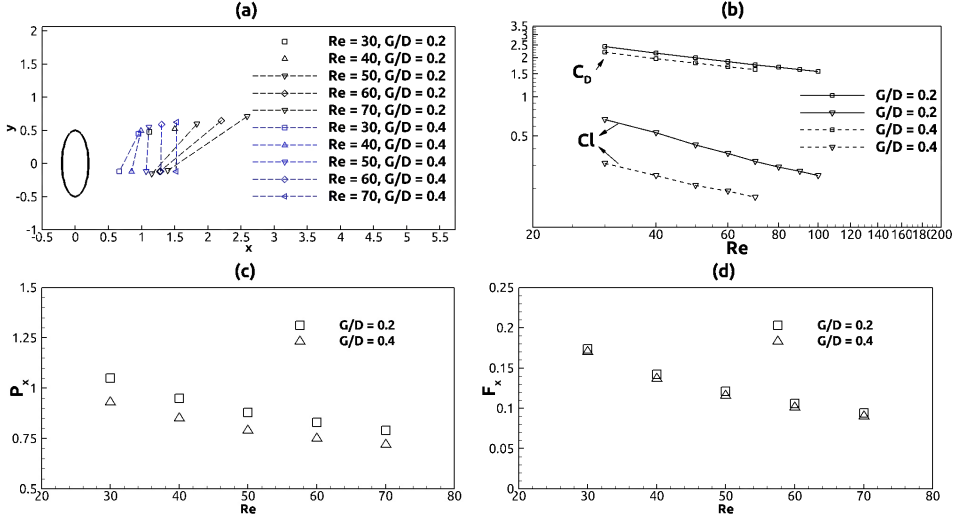
Figure 6.8: (a) Locations of the vortex center behind the cylinder; (b) the drag (C_D) and lift (C_l) coefficient for Re from 30 to 70 and for $G/D = 0.2$ and 0.4; (c) and (d) show the pressure (P_x) and viscous (F_x) drag coefficients, respectively, for Re from 30 to 70 and for $G/D = 0.2$ and 0.4.

a rotating circular cylinder near a moving wall for G/D ranging from 0.05 to 4. Figures 6.8 (c) and (d) show the drag force due to the pressure (P_x) and due to the cylinder friction (F_x) against Re for $G/D = 0.2$ and 0.4, respectively. It appears that G/D has a weaker effect on F_x than on P_x, implying that the G/D affects the cylinder friction less than the pressure distribution around the cylinder as previously demonstrated by Sumer et al. (2006) for a circular cylinder.

6.5.2 Unsteady state

6.5.2.1 Wake patterns

Figure 6.9 shows vorticity contours of the flow around an isolated elliptic cylinder with $AR = 0.4$ for $Re = 130$. The three different wake structures (separated by vertical dashed lines) can be classified into three different flow regimes (Thompson et al. 2014, Jiang & Cheng 2019); *i*) the near wake where clockwise and anti-clockwise vortices are alternately shed from the upper and lower parts of the cylinder, forming the Kármán vortex street; *ii*) further downstream the Kármán vortex street breaks down and develops into a two-layered wake (Durgin & Karlsson 1971, Karasudani & Funakoshi
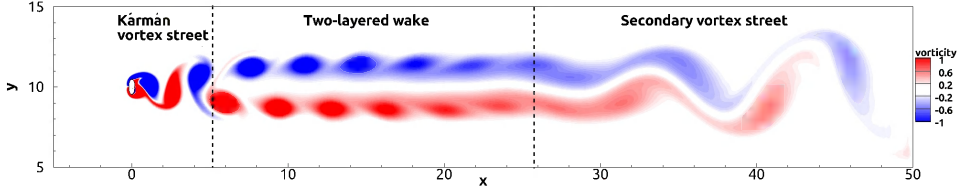
Figure 6.9: Instantaneous vorticity contours for flow around an isolated elliptic cylinder of AR = 0.4 with Re = 130.

1994, Thompson et al. 2014); *iii*) the far wake where the hydrodynamic instability of the two-layered wake (Johnson et al. 2004, Kumar & Mittal 2012) leads to a secondary vortex street characterized by larger scales and lower frequencies than the Kármán vortex street.

Figure 6.10 shows instantaneous vorticity contours for the flow around an elliptic cylinder near a moving wall for $Re = 130$ and for $G/D = 2$, 0.8, 0.2 and 0.1. For $G/D = 2$ (figure 6.10a), the wake structure is composed of the Kármán vortex street, the two-layered wake and the secondary vortex street. This flow structure is qualitatively similar to that for an isolated elliptic cylinder (figure 6.9). Moreover, it is worth noting that the onset location of the two layered wake is nearly the same (this will be further discussed in section 6.5.2.3), while the secondary vortex occurs farther downstream for $G/D = 2$ than for the isolated cylinder. The bottom wall shear layer is a result of the vortex (with positive vorticity) shed from the cylinder bottom; a region with negative vorticity occurs between the vortex and the wall. This result is valid for a vortex in the vicinity of a wall as first predicted by Peace & Riley (1983), observed experimentally by Walker et al. (1987) and Allen & Chong (2000), and shown by Ovando et al. (2009) and Zhu et al. (2020) using numerical simulations. This flow is denoted wake pattern *A*. Figure 6.11 shows the amplitude v_a of the vertical velocity fluctuation along the downstream cylinder centerline for the isolated cylinder and for $G/D = 2$ and 0.8. In the near-wake region, v_a decreases downstream (which is consistent with the decay of the Kármán vortex street and the transition to the two-layered wake where a calm region is formed between the two vortex layers; see figure 6.9 and figure 6.10a-6.10b). Then, v_a grows farther downstream for the isolated cylinder and for $G/D = 2$, which coincides with the transition from the two-layered wake to the secondary vortex street (see figure 6.9 and figure 6.10a). Furthermore, figure 6.11 shows that the presence of the moving wall leads to a significant reduction of v_a in the far-wake region, consistent with the delayed onset of the secondary vortex
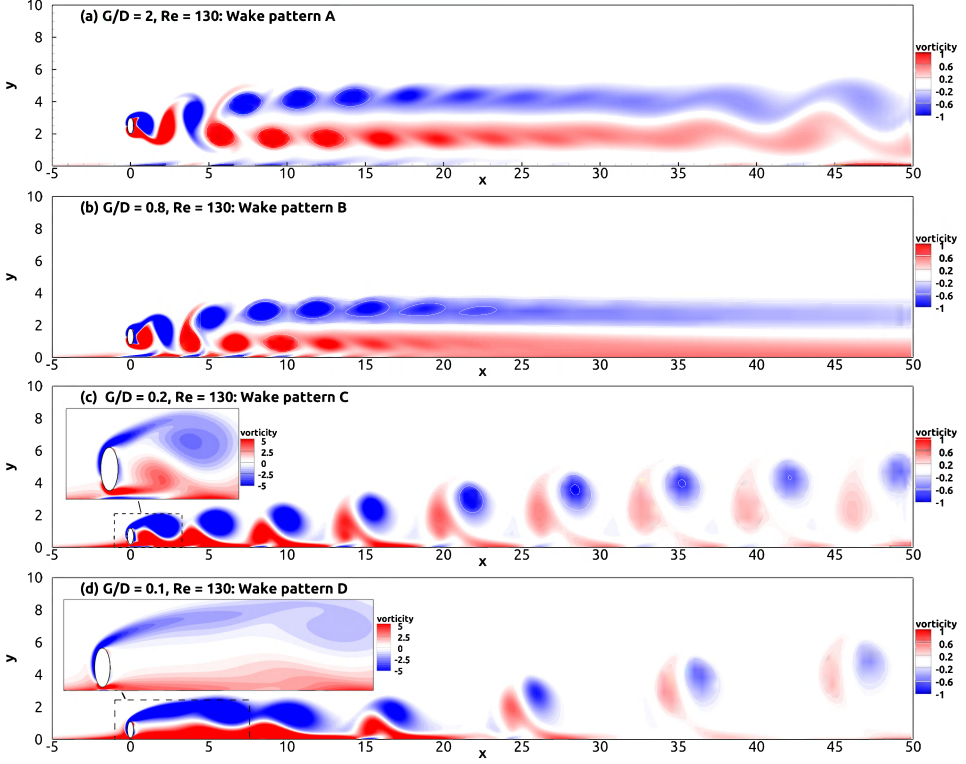
Figure 6.10: Instantaneous vorticity contours for flow around an elliptic cylinder of AR = 0.4 near a moving wall with Re = 130 and G/D = 2, 0.8, 0.2 and 0.1.

street for $G/D = 2$; the secondary vortex street appears farther downstream for $G/D = 2$ (figure 6.10a) than for the isolated cylinder (figure 6.9).

As G/D decreases to 0.8 (figure 6.10b), the secondary vortex street disappears in the far wake region, which is present for $G/D = 2$ (figure 6.10a) and for the isolated cylinder (figure 6.9). This is consistent with the observation that v_a remains almost zero in the far wake region (figure 6.11); i.e., the vertical fluctuations are further suppressed as the wall is approached. Thus the wake structure here is composed of the Kármán vortex street and the two-layered wake; this flow is denoted the wake pattern B. Here the onset location of the two-layered wake for $G/D = 0.8$ is closer to the cylinder than for $G/D = 2$. The transition location from the Kármán vortex street to the two-layered wake is closer to the cylinder for $G/D = 0.8$ than that for $G/D = 2$. This will be further discussed and quantified in section 6.5.2.3.
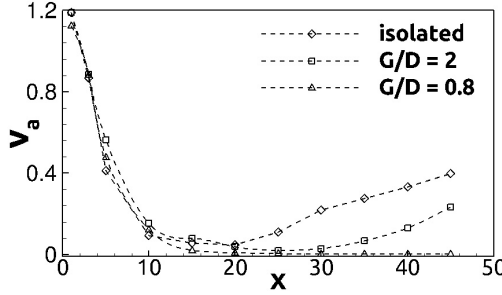
Figure 6.11: Amplitude of the vertical velocity fluctuation along the wake centerline for the isolated cylinder and for $G/D = 0.8$ and 2 at $Re = 130$.
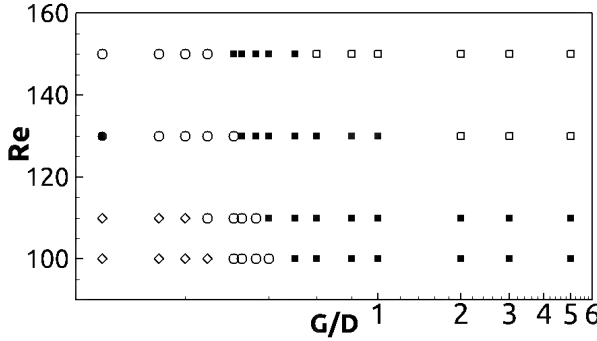
Figure 6.12: Distribution of wake patterns, i.e. wake pattern A ($\square$), wake pattern B ($\blacksquare$), wake pattern C ($\bigcirc$), wake pattern D ($\bullet$) and the steady state ($\diamond$) within (G/D, Re)-space;

As G/D decreases further to 0.2 (figure 6.10c), the lower vortex (behind the bottom of the cylinder) is shed immediately following the upper one (behind the top of the cylinder), forming a vortex pair moving downstream and deflecting away from the wall. This pair-wise vortex shedding destroys the geometric arrangement of the vortices required for the transition to the two-layered wake. Thus the Kármán vortex street and the two-layered wake break down simultaneously; this flow is denoted wake pattern C.

For $G/D = 0.1$ (figure 6.10 d), the upper shear layer (behind the top of the cylinder) becomes more elongated than for $G/D = 0.2$, and rolls down at a downstream location of $x \approx 5$. The shear layer near the wall rolls up when meeting the rolled-down shear layer at $x \approx 15$, forming a new vortex pair moving downstream and deflecting away from the wall. This

behavior is qualitatively similar to that observed for $G/D = 0.2$ except for the existence of a quasi-steady near-wake region ($x < 5$), where the drag and lift coefficients are almost constant as will be discussed later in section 6.5.2.2); this flow is denoted the wake pattern D.
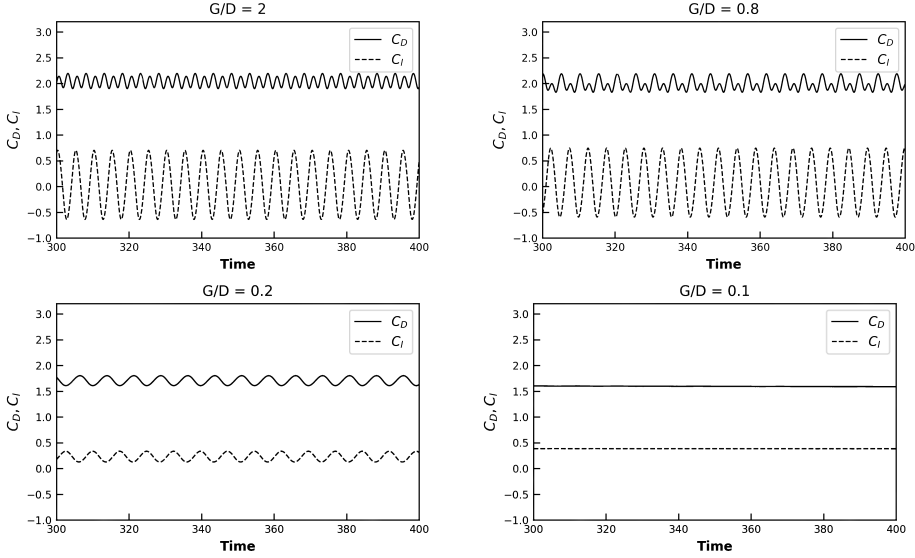
Figure 6.13: Time history of C_D and C_l for flow around an elliptic cylinder of AR = 0.4 near a moving wall with Re = 130 and G/D = 2, 0.8, 0.2 and 0.1.

Figure 6.12 shows the distribution of the wake patterns A, B, C and D as well as the steady state flow (i.e., no vortex shedding occurs) in the $(G/D, Re)$-space. Wake pattern D only exists at $G/D = 0.1$ for $Re = 130$. For $Re \leq 110$, the wake pattern A does not exist (i.e., the secondary vortex street does not appear) and the steady state flow appears only at small values of G/D and Re. Overall, it appears that as G/D decreases (for a given Re), the flow undergoes a transition sequence from wake pattern $A \rightarrow$ wake pattern $B \rightarrow$ wake pattern C. Moreover, as Re increases (for a given G/D), the critical gap ratio for the transition between two wake patterns (except wake pattern D) decreases. This critical gap ratio G/D_c denotes a threshold value where one wake pattern exists and below which another wake pattern appears. For example, the transition between wake patterns B and C occurs for $G/D \in [0.36, 0.4]$ (where $G/D_c = 0.38 \pm 0.02$) for $Re = 110$ and for $G/D \in [0.3, 0.32]$ (where $G/D_c = 0.31 \pm 0.01$) for $Re = 130$. This might be explained by that an increase of Re leads to an

enhanced growth of the secondary instability (i.e., the transition of wake pattern B to A) as well as the vortex shedding behind the bottom of the cylinder (i.e., the transition from the steady state flow to wake pattern C). Conversely, a decrease in G/D suppresses the growth of v_a (i.e., the secondary instability) in the far-wake region (figure 6.11) and the Kármán vortex shedding. Therefore, a smaller G/D is required for a higher Re to maintain the same wake pattern.
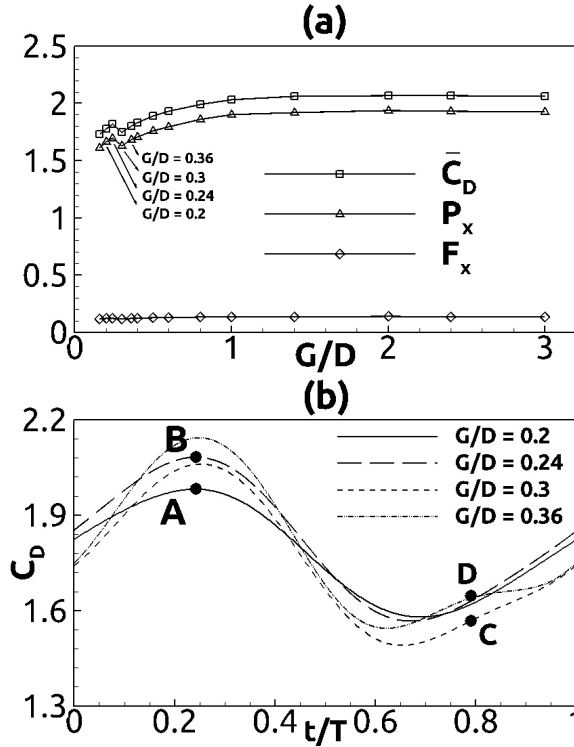
Figure 6.14: (a): variations of the time-averaged drag coefficient ($\overline{C}_D$), viscous (F_x) and pressure (P_x) drag coefficient at various G/D for $Re = 150$; (b): time history of the C_D for $Re = 150$ and for $G/D = 0.2$, 0.24, 0.3 and 0.36. Here T is the vortex shedding period, which is different for different G/D.

6.5.2.2 Hydrodynamic forces

Figure 6.13 shows the time history of the drag coefficient C_D and the lift coefficient C_l for flow around the elliptic cylinder near a moving wall for $Re = 130$ at $G/D = 2$, 0.8, 0.2 and 0.1, i.e., corresponding to the flow shown

in figure 6.10. For both $G/D = 2$ and $G/D = 0.8$, it is observed that every second crest value of C_D is larger than the crest values in between; this effect is strongest for $G/D = 0.8$. The smaller crest values are caused by the vortex shed from the bottom part of the cylinder, whilst the larger crest values are caused by the vortex shed from the top of the cylinder (Huang & Sung 2007, Wang et al. 2018). It is observed that the lift coefficient C_l oscillates with half the frequency of C_D both for $G/D = 2$ and $G/D = 0.8$ since two vortices with opposite sign are shed from the top and bottom of the cylinder within each oscillation period and C_D is not sensitive to the sign of the vortex (Norberg 2003). For $G/D = 0.2$, the upper and lower vortices are not shed alternately; the lower vortex is shed and follows the upper vortex immediately, forming a vortex pair moving downstream (as previously shown in figure 6.10c). Consequently, the small crest caused by
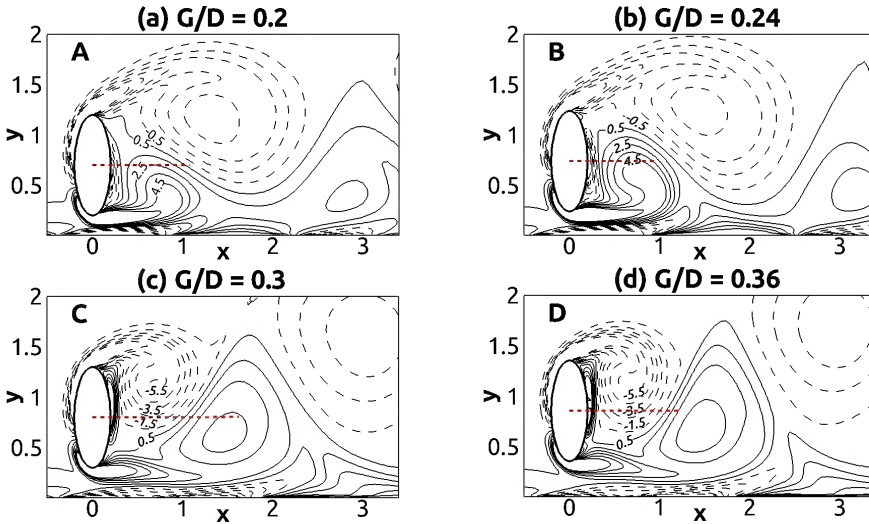
Figure 6.15: Vorticity contours for flow around an elliptic cylinder near a moving wall with $G/D = 0.2$, 0.24, 0.3 and 0.36 at instants A, B, C and D, respectively, marked in figure 6.14; for contours with values from -5.5 to 5.5, the difference in value between two adjacent contour lines is 1. Dashed and solid line indicate the negative and positive values, respectively.

the alternately shedding lower vortex (see, e.g., figure 6.10*b* and figure 6.13 for $G/D = 0.8$) disappears, resulting in a constant crest value of C_D and the same oscillating frequency but with different phases for C_D and C_l. A similar explanation was also found by Huang & Sung (2007) for the flow around a circular cylinder near a moving wall with G/D = 0.2 and Re = 300. As G/D decreases further to 0.1, the oscillations of C_D and C_l vanish

since the vortex shedding near the cylinder is suppressed as shown in figure 6.10(d).

Figure 6.14(a) shows the time-averaged drag coefficient ($\overline{C}_D$), the time-averaged drag coefficients due to the pressure (P_x) and due to the skin friction (F_x) against G/D for $Re = 150$. Here $\overline{C}_D = P_x + F_x$. The value of $\overline{C}_D$ increases gradually for $G/D \in [0.1 , 1.4]$ except for a sudden drop at $G/D \in [0.24 , 0.3]$, which will be further explained below. For G/D larger than 1.4, $\overline{C}_D$ remains nearly constant. A similar behavior is observed for P_x while F_x is hardly affected by G/D at all. The overall increase of $\overline{C}_D$ as G/D increases is mainly due to the time-averaged pressure difference over the cylinder, which is closely related to the growth of the vortex attached to backside of the cylinder as shown in figure 6.15; a stronger attached vortex draws in fluid more rapidly from the base region behind the cylinder during its growth, leading to a smaller pressure behind the cylinder and thus a larger pressure difference over the cylinder, leading to larger values of P_x and thus of $\overline{C}_D$.
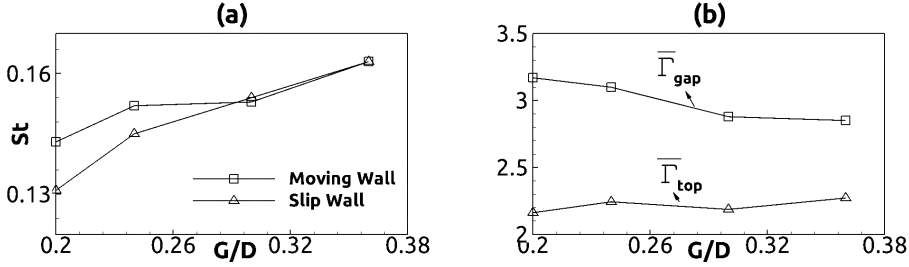
Figure 6.16: (a) the Strouhal number St, (b) the injection rate $\overline{\Gamma}_{top}$ of the circulation into the upper vortex over the top of the cylinder and the injection rate $\overline{\Gamma}_{gap}$ of the circulation into the lower vortex through the gap for $Re = 150$ with $G/D = 0.2, 0.24, 0.3$ and 0.36.

Here the increase of $\overline{C}_D$ for $G/D \in [0.2, 0.24]$ and $G/D \in [0.3, 0.36]$ observed in figure 6.14(a) is investigated; the decay of $\overline{C}_D$ for $G/D \in [0.24, 0.3]$ will be discussed in the paragraph below. The time-history of C_D at $G/D = 0.2, 0.24, 0.3$ and 0.36 for $Re = 150$ during one dimensionless vortex shedding cycle is shown in figure 6.14(b). Here the largest value of C_D is smaller for $G/D = 0.2$ than for $G/D = 0.24$ (marked as A and B, respectively). This coincides with the occurrence of the lower vortex behind the bottom of the cylinder shown in figures 6.15(a) and (b), which show the lower vortex becomes stronger (i.e., the vorticity increases) as G/D increases from 0.2 to 0.24. This is because an increase in G/D weakens the effect of the bottom-wall shear layer on the vortex shedding, thus contributing to

the formation of the stronger lower vortex (Jiang et al. 2017), i.e., the wall suppression effect on the lower vortex shedding becomes weaker. Thus an increase in G/D enhances the dimensionless vortex shedding frequency here represented by the Strouhal number St as shown in figure 6.16(a) for the moving wall (the case of applying the slip wall condition will be discussed below). Figure 6.14(b) shows that C_D is smaller for $G/D = 0.3$ than for $G/D = 0.36$ at the instants C and D, coinciding with the occurrence of the upper vortex which is weaker for $G/D = 0.3$ than for $G/D = 0.36$ as shown in figure 6.15(c) and (d), respectively. This is because the circulation generated at the front of the cylinder is injected into the upper vortex over the cylinder top with lower frequency for $G/D = 0.3$ than for $G/D = 0.36$ (consistent with the variation of St as shown in figure 6.16a for a moving wall). This behavior can be quantified by the cycle-averaged circulation $\overline{\Gamma}_{top}(= -\frac{1}{T}\int_0^T(\int_{G/D+1}^2 u\omega_z dy)dt)$ and $\overline{\Gamma}_{gap}(= \frac{1}{T}\int_0^T(\int_0^{G/D} u\omega_z dy)dt)$ (will be discussed below), which represent the rate of the circulation generated at the front of the cylinder injected into the upper and lower vortices shed from the cylinder, respectively. Figure 6.16(b) shows a smaller $\overline{\Gamma}_{top}$ for $G/D = 0.3$ than for $G/D = 0.36$, leading to a weaker upper vortex for $G/D = 0.3$ than for $G/D = 0.36$, thus resulting in a smaller C_D for $G/D = 0.3$ than for $G/D = 0.36$. This behavior is also observed as G/D increases from 0.2 to 0.24 (figure 6.16b), which is consistent with a slightly larger C_D for $G/D = 0.24$ than for $G/D = 0.2$ during the growth phases of the upper vortex (i.e., at instants C and D) shown in figure 6.14(b). Overall, it appears that for $G/D \in [0.2, 0.24]$ and $G/D \in [0.3, 0.36]$ an increase of G/D weakens the wall suppression effect on the vortex shedding behind the cylinder, thus forming a stronger lower vortex behind the cylinder while the circulation is injected over the top of the cylinder with higher frequency, contributing to a stronger upper vortex.

Now the sudden drop of $\overline{C}_D$ for $G/D \in [0.24, 0.3]$ observed in figure 6.14(a) is discussed. As shown in figure 6.14(b), the value of C_D is smaller for $G/D = 0.3$ than for $G/D = 0.24$ during the entire shedding cycle. This implies that both the upper and lower vortices are weaker for $G/D = 0.3$ than for $G/D = 0.24$. The formation of the weaker upper and lower vortices for $G/D = 0.3$ relative to $G/D = 0.24$ is consistent with the decrease of $\overline{\Gamma}_{top}$ and $\overline{\Gamma}_{gap}$ as G/D increases from 0.24 to 0.3 as shown in figure 6.16(b). It should be noted that the vortex shedding frequency ($\frac{1}{T}$) is almost the same for $G/D = 0.24$ and 0.3 (which will be further explained in the following paragraph) shown in figure 6.16(b). Hence, the decrease of both $\overline{\Gamma}_{top}$ and $\overline{\Gamma}_{gap}$ is determined by the total circulation convecting into the vortices from the top of the cylinder ($\Gamma_{top} = -\int_0^T(\int_{G/D+1}^2 u\omega_z dy)dt$) and through the gap

$(\Gamma_{gap} = \int_0^T (\int_0^{G/D} u\omega_z dy)dt)$ during one vortex shedding cycle. The decrease of Γ_{top} as G/D increases from 0.24 to 0.3 is due to less fluid moving upwards along the cylinder since the front stagnation point moves upwards along the cylinder as G/D increases as depicted in figure 6.7(c) and (d); the decrease of Γ_{gap} is due to the decrease of the gap velocity as G/D increases. However, the wall suppression effect is weaker for $G/D = 0.3$ than for $G/D = 0.24$, which (as an isolated effect) would lead to an increase of $\overline{C}_D$ from G/D = 0.24 to $G/D = 0.3$. It appears that for $G/D \in [0.24, 0.3]$, the total vortex strength (i.e., from the upper and lower vortices) is stronger affected by the circulation injection rate than by the wall suppression effect. This is contrary to the case of $G/D \in [0.2, 0.24]$, where $\overline{\Gamma}_{gap}$ decreases whilst $\overline{\Gamma}_{top}$ increases, resulting in that $\overline{C}_D$ increases, indicating that the lower vortex strength here is stronger affected by the wall suppression than by the circulation generated at the front of the cylinder. Moreover, it is worth to note that $\overline{\Gamma}_{gap}(= \Gamma_{gap}/T)$ also keeps decreasing as G/D increases, which is different from $\overline{\Gamma}_{top}$ and $\overline{C}_D$ as shown in figure 6.16(b) and figure 6.14(a), respectively. It appears that the decrease of T induced by increasing G/D does not compensate the simultaneous decrease of Γ_{gap} due to the decrease of flow velocity in the gap caused by increasing G/D.
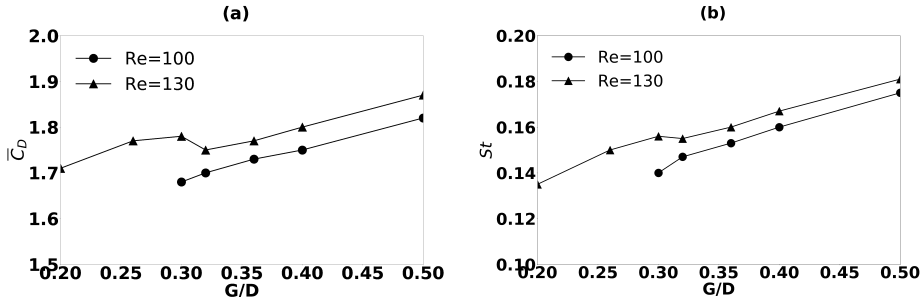
Figure 6.17: (a) the time-averaged drag coefficient $\overline{C}_D$ and (b) the Strouhal number St for the flow around an elliptic cylinder near a moving wall for Re = 100 and 130 with G/D from 0.2 to 0.5.

Now the nearly constant value of St for $G/D \in [0.24, 0.3]$ for $Re = 150$ (figure 6.16a, moving wall where the no-slip conditions $u = 1$ and $v = 0$ are imposed) is discussed. For a given Re, the vortex shedding frequency is mainly affected by the wall suppression effect and the bottom-wall shear layer. The effect of these shear layers can be eliminated by conducting simulations with a slip condition ($\frac{\partial u}{\partial y} = 0$, $v = 0$) imposed on the bottom wall. At large gap ratios, e.g., for $G/D > 0.3$ (figure 6.16a), St is almost equal for the two boundary conditions because the shedding vortices are

weakly affected by the bottom-wall shear layers. Here St increases as G/D increases due to the weakening of the wall suppression effect. For $G/D \in$ [0.2, 0.24] the vortex suppression effect is larger than for $G/D > 0.3$ but in this gap ratio range, the bottom-wall shear layers cause the vortex shed from the cylinder bottom to roll up such that it is located closer to the vortex shed from the cylinder top. This results in an enhancement of the vortex shedding frequency (St) for $G/D \in$ [0.2, 0.24] which compensates the decrease of St induced by the strengthening of the wall suppression effect (as G/D decreases from 0.3 to 0.24), thus resulting in the nearly equal St for $G/D \in$ [0.24, 0.3]. Moreover, for $G/D \in$ [0.2, 0.24], St increases as G/D increases but is larger than for the case of applying the slip condition as shown in figure 6.16(a).

Figure 6.17(a) shows the time-averaged drag coefficient $\overline{C}_D$ (a) and the Strouhal number St (b) for $Re = 100$ and 130. For $Re = 130$ $\overline{C}_D$ exhibits a qualitatively similar behavior as for $Re = 150$ (shown in figure 6.14a), showing an overall increase of $\overline{C}_D$ as G/D increases from 0.2 to 0.3 with a sudden drop for $G/D \in$ [0.3, 0.32]. However, the sudden drop of $\overline{C}_D$ does not occur for $Re = 100$. This is because here the bottom-wall shear layer becomes weaker, thus reducing its effect on the vortex shedding frequency at small G/D, i.e., as G/D increases the vortex shedding frequency increases smoothly as shown in figure 6.17(b) without a nearly constant region similar to that for $Re = 130$. Hence the circulation is injected into the vortex with higher frequency as G/D increases, contributing to a stronger vortex shedding, i.e., a smooth growth of $\overline{C}_D$.
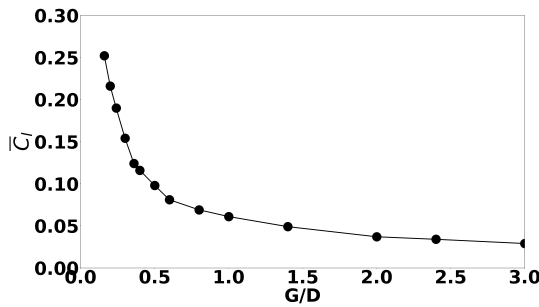
Figure 6.18: The mean lift coefficient $\overline{C}_l$ against G/D for $Re = 150$.

Figure 6.18 shows the time-averaged lift coefficient ($\overline{C}_l$) against G/D for $Re = 150$. The non-zero $\overline{C}_l$ is caused by the asymmetric flow distribution around the stream-wise centerline of the cylinder due to the presence of the moving wall. As G/D increases, the flow tends to be less asymmetric,

leading to a decrease of $\overline{C}_l$. A qualitatively similar behavior was also found for flow around a circular cylinder near a moving wall for $Re < 500$ (Huang & Sung 2007, Rao et al. 2013, Jiang et al. 2017).
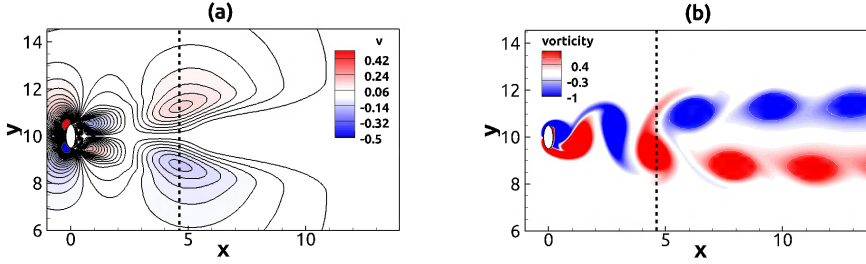
Figure 6.19: (a) time-averaged vertical velocity field and (b) instantaneous vorticity contours for flow around an isolated cylinder for Re = 130. The dashed black line denotes the transition location for the two-layered wake.

6.5.2.3   The onset location of the two-layered wake

As previously proposed by Jiang & Cheng (2019), the onset location of the two-layered wake behind the isolated elliptic cylinder (for $AR = 0.4$ and for $Re = 130$), can be identified by the location of the positive and negative local maxima of the time-averaged vertical velocity contours (i.e., the vertical dashed line in figure 6.19a). A snapshot of the instantaneous vorticity contours are shown in figure 6.19(b) depicting the Kármán vortex and the two-layered wake farther downstream.

Figure 6.20 shows the time-averaged vertical velocity contours (left column) and the instantaneous vorticity contours (right column) for $Re = 130$ at $G/D = 2$ and 0.8. Here the distribution of the time-averaged velocity becomes asymmetric about the horizontal center-line of the cylinder; the positive local maximum is slightly farther away from the cylinder than the negative maximum. Thus the transition to the two-layered wake occurs farther downstream for the upper part than for the lower part of the cylinder. This is because the lower vortex behind the cylinder is weaker than the upper vortex due to wall suppression effect, and thus the upper vortex induces a stronger vorticity convection within the lower vortex (Durgin & Karlsson 1971, Karasudani & Funakoshi 1994). Consequently, the lower vortex distorts and rotates to align with the stream-wise direction at a location closer to the cylinder than the horizontal upper vortex. Here the negative maximum is used to identify the onset location of the two-layered flow for $G/D = 2$ and 0.8 (figure 6.20a and c, respectively). As G/D de-
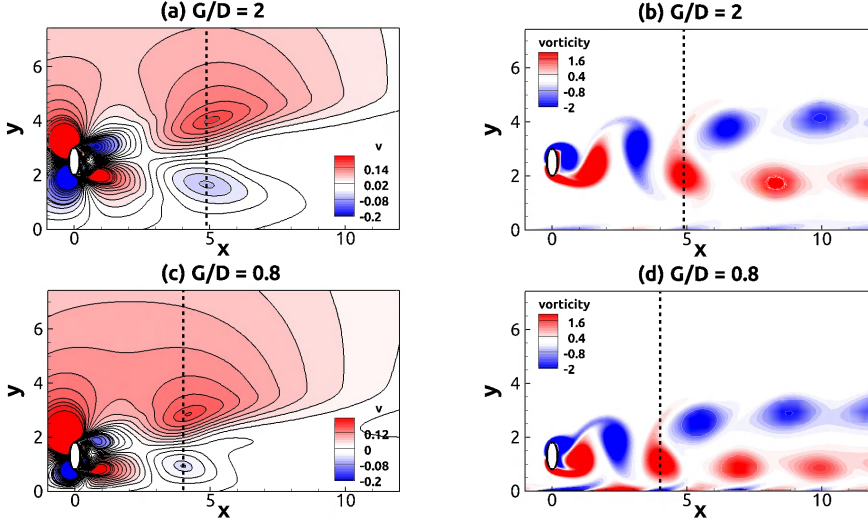
Figure 6.20: *Time-averaged vertical velocity field (left column) and instan-taneous vorticity contours (right column) for flow around an elliptic cylinder near a moving wall for Re = 130 with G/D = 2 and 0.8.*

creases from 2 to 0.8, the distance (x_{loc}) between the onset location of the two-layered wake and the cylinder center decreases. This behavior can be further explained by the spacing ratio h/l of the Kármán vortices (Durgin & Karlsson 1971, Karasudani & Funakoshi 1994) (figure 6.21a), where l denotes the distance between two same-sign (here negative) vortices ($V1$ and $V2$) while h represents the distance between the vortex ($V3$) with opposite sign (here positive) and the line connecting $V1$ and $V2$. This spacing ratio h/l increases as the Kármán vortices move downstream, and then reaches a threshold value at x_{loc}, where the transition of the two-layered wake occurs.

The threshold value of h/l, for the transition to the two-layered wake, is here determined by the center of the $V3$ vortex being located at the dashed line (determined by the time-averaged vertical velocity; figure 6.20a). Here the threshold values are 0.453, 0.45 and 0.449 for the isolated elliptic cylinder with $AR = 0.4$ and $Re = 100$, 130 and 150, respectively. This is in qualitative agreement with the results obtained by Durgin & Karlsson (1971) and Karasudani & Funakoshi (1994) for an isolated circular cylinder, reporting threshold values in the range 0.45-0.5 for Re ranging from 80 to 150. It appears that the threshold value does not vary much with AR and Re in the absence of the wall; the threshold value is dominated by the wall. The wall suppression effect leads to the $V1$ and $V2$ vortices being stronger
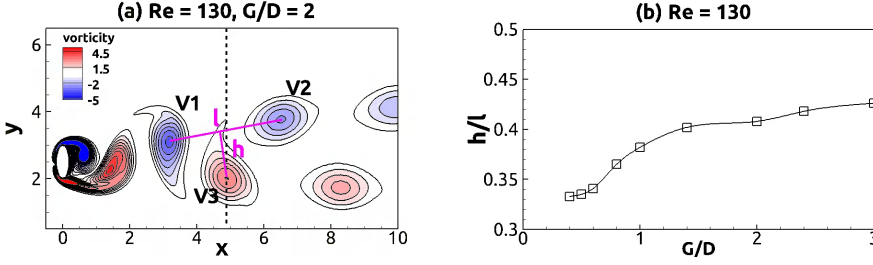
Figure 6.21: (a): definition of the spacing ratio h/l of the Kármán vortices, where l denotes the distance between two same sign vortices (V1 and V2) while h represents the distance between the positive vortex (V3) and the line connecting V1 and V2; (b): variations of the threshold value of the spacing ratio h/l against G/D for Re = 130.

than the $V3$ vortex, thus causing a stronger vorticity convection within the $V3$ vortex than that for the isolated cylinder where these three vortices are of almost equal strength (Durgin & Karlsson 1971). Consequently, the $V3$ vortex distorts and rotates closer to the cylinder as G/D decreases (i.e., as the wall suppression effect becomes stronger), forming the two-layered wake; i.e., x_{loc} decreases as G/D decreases as shown in figure 6.22. This coincides with the behavior for the threshold value of h/l, which decreases with decreasing G/D as shown in figure 6.21(b) for $Re = 130$. In contrast, x_{loc} increases as G/D decreases from 0.6 to 0.5 for $Re = 100$ and from 0.5 to 0.4 for $Re = 130$. It appears that an increase of the low velocity in the gap with decreasing G/D leads to the lower shear layer beneath the cylinder rolling up slightly farther downstream for $G/D = 0.4$ (figure 6.23a) than for $G/D = 0.5$ (figure 6.23b), thus resulting in a larger x_{loc}.

Thompson et al. (2014) investigated the effect of Re on x_{loc} for the flow around an isolated elliptic cylinder for $AR \in [0.25, 1]$, and found that x_{loc} decreases as Re increases from 100 to 150. This is because an increase in Re leads to a stronger increase of h/l downstream, resulting in the threshold value of h/l being achieved closer to the cylinder. This behavior is qualitatively similar to that observed in figure 6.22 for a given G/D. Moreover, x_{loc} is less sensitive to G/D when $G/D > 1.4$ for $Re = 100$ and $G/D > 1$ for $Re = 130$ and 150. This can be explained by that a decrease in Re forms a thicker shear layer on the bottom of the cylinder, which starts to interact with the bottom-wall shear layer at relatively large G/D for low Re (Lei et al. 2000).
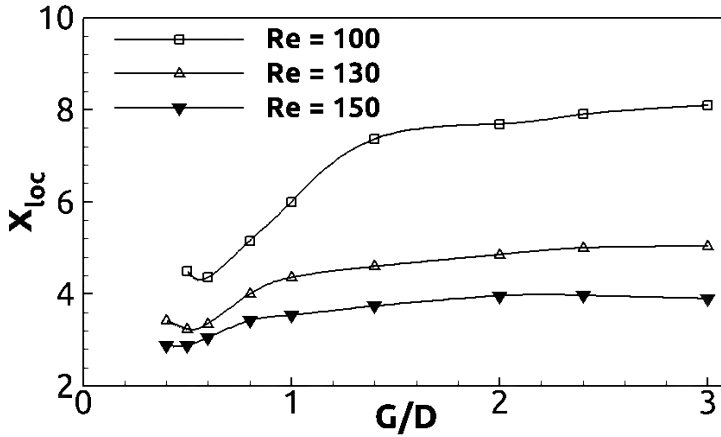
Figure 6.22: The distance (x_{loc}) between the onset location of of the two-layered wake and the cylinder center for G/D from 3 to 0.2 and for $Re = 100$, 130 and 150.

6.6 Summary and conclusions

This paper provides a detailed numerical investigation for the flow around an elliptic cylinder with an aspect ratio of 0.4 translating above a plane wall in still water, where the Reynolds number is in the range from 30 to 150 and the gap ratio (i.e., the ratio between the distance of the cylinder from the wall and the length of the semi-major axis of the cylinder) ranging from 0.1 to 3.

In the steady flow regime, the wake contains two asymmetric counter-rotating recirculation vortices attached to the cylinder. Here the lower vortex center is located closer to the cylinder than the upper vortex center. This difference increases as the gap ratio decreases (for a given Reynolds number) due to stronger wall suppression effect on the lower vortex for lower gap ratios. As the Reynolds number increases (for a given gap ratio), this difference decreases since thinner shear layers are formed,resulting in a weaker interaction between the shear layers beneath the cylinder bottom and above the wall. Moreover, as the gap ratio decreases (for a given Reynolds number) the time-averaged drag coefficient decreases while the time-averaged lift coefficient increases; as the Reynolds number increases (for a given gap ratio), the drag and lift coefficients decrease almost linearly in log-log scale.

In the unsteady flow regime, four different wake patterns have been

Figure 6.23: The vorticity contours for the flow around an elliptic cylinder near a moving wall for Re = 130 with G/D = 0.4 and 0.5; for contours with values from -5.5 to 5.5, the difference in value between two adjacent contour lines is 1. Black dashed and solid lines indicate the negative and positive values, respectively, while the red and blue dashed lines denote a reference line at x = 1.4 and the onset location of the two-layered wake, respectively.

classified; i) at relatively large gap ratios, the flow, which is denoted wake pattern A, contains the Kármán vortex street, the two-layered wake and the secondary vortex street; ii) a decrease in the gap ratio leads to the suppression of the vertical fluctuations in the far-wake region, resulting in the disappearance of the secondary vortex street; this represents wake pattern B; iii) a further decrease in the gap ratio leads to the break-down of the Kármán vortex, resulting in a pair-wise vortex shedding (denoted wake pattern C) or iv) forming a quasi-steady near-wake region (with constant lift and drag coefficients) and a pair-wise vortex shedding farther downstream, which is denoted wake pattern D. Moreover, an increase in the Reynolds number (for a given gap ratio) enhances the vortex shedding behind the cylinder, thus triggering the transition between two different wake patterns. Therefore, a smaller gap ratio is required for a higher Reynolds number to maintain the same wake pattern, i.e., a smaller critical gap ratio is required for the transition between two different wake patterns (except wake pattern D).

The time-averaged drag coefficient increases gradually as the gap ratio increases (for a given Reynolds number) due to the decay of the wall suppression effect. A sudden drop of the time-averaged drag coefficient is observed as the gap ratio increases from 0.3 to 0.32 as well as from 0.24 to 0.3 for the Reynolds number of 130 and 150, respectively, where the vortex shedding frequency remains nearly constant. It appears that the vortex strength here is determined by the total circulation injected into the wake from the top and the bottom of the cylinder. This total circulation decreases as the gap ratio increases due to less fluid moving upwards along the cylinder and a

decrease of the gap flow velocity. Consequently, the weaker upper and lower vortices are formed for the larger gap ratio, resulting in the sudden drop of the time-averaged drag coefficient. Moreover, the time-averaged lift co-efficient increases as the gap ratio decreases (for a given Reynolds number) due to more asymmetric flow distribution around the cylinder.

Stronger wall suppression effect for smaller gap ratios leads to the upper vortex being stronger than the lower vortices, thus enhancing the convection of the vorticity within the lower vortex. Consequently, the lower vortex distorts and rotates to align with the stream-wise direction at a location closer to the cylinder than the horizontal upper vortex, showing that the onset location of the two-layered wake moves closer to the cylinder as the gap ratio decreases (for a given Reynolds number).

Overall, the present work gives some insight into the physical process of transitional movements of bluff bodies near a stationary plane wall (including the far-wake dynamics) which is relevant for engineering and geophysical applications such as e.g. an AUV moving over the seabed. In future studies the effects of the aspect ratio and the angle of attack, as well as the effect of turbulence on this physical process (i.e., on wake patterns, drag and lift coefficients) should be addressed.

Acknowledgements

References

Allen, J. & Chong, M. (2000), 'Vortex formation in front of a piston moving through a cylinder', *Journal of Fluid Mechanics* **416**, 1–28.

Arif, M. R. & Hasan, N. (2019*a*), 'Performance of characteristic numerical boundary conditions for mixed convective flows past a heated square cylinder using a non-boussinesq approach', *Numerical Heat Transfer, Part A: Applications* **76**(4), 254–280.

Arif, M. R. & Hasan, N. (2019*b*), 'Vortex shedding suppression in mixed convective flow past a square cylinder subjected to large-scale heating using a non-boussinesq model', *Physics of Fluids* **31**(2), 023602.

Bearman, P. W. & Trueman, D. M. (1972), 'An investigation of the flow around rectangular cylinders', *The Aeronautical Quarterly* **23**(3), 229–237.

Berthelsen, P. A. & Faltinsen, O. M. (2008), 'A local directional ghost cell approach for incompressible viscous flow problems with irregular boundaries', *Journal of Computational Physics* **227**(9), 4354–4397.

Calhoun, D. (2002), 'A cartesian grid method for solving the two-dimensional streamfunction-vorticity equations in irregular regions', *Journal of Computational Physics* **176**(2), 231–275.

Cimbala, J. M., Nagib, H. M. & Roshko, A. (1988), 'Large structure in the far wakes of two-dimensional bluff bodies', *Journal of Fluid Mechanics* **190**, 265–298.

Coutanceau, M. & Bouard, R. (1977), 'Experimental determination of the main features of the viscous flow in the wake of a circular cylinder in uniform translation. part 1. steady flow', *Journal of Fluid Mechanics* **79**(2), 231–256.

Dennis, S. C. R. & Chang, G.-Z. (1970), 'Numerical solutions for steady flow past a circular cylinder at Reynolds numbers up to 100', *Journal of Fluid Mechanics* **42**(3), 471–489.

Durgin, W. W. & Karlsson, S. K. (1971), 'On the phenomenon of vortex street breakdown', *journal of Fluid Mechanics* **48**(3), 507–527.

Fornberg, B. (1980), 'A numerical study of steady viscous flow past a circular cylinder', *Journal of Fluid Mechanics* **98**(4), 819–855.

Huang, W.-X. & Sung, H. J. (2007), 'Vortex shedding from a circular cylinder near a moving wall', *Journal of Fluids and Structures* **23**(7), 1064–1076.

Jackson, C. P. (1987), 'A finite-element study of the onset of vortex shedding in flow past variously shaped bodies', *Journal of Fluid Mechanics* **182**, 23–45.

Jiang, H. & Cheng, L. (2019), 'Transition to the secondary vortex street in the wake of a circular cylinder', *Journal of Fluid Mechanics* **867**, 691–722.

Jiang, H., Cheng, L., Draper, S. & An, H. (2017), 'Two-and three-dimensional instabilities in the wake of a circular cylinder near a moving wall', *Journal of Fluid Mechanics* **812**, 435–462.

Johnson, S. A., Thompson, M. C. & Hourigan, K. (2001), Flow past elliptical cylinders at low reynolds numbers.

Johnson, S. A., Thompson, M. C. & Hourigan, K. (2004), 'Predicted low frequency structures in the wake of elliptical cylinders', *European Journal of Mechanics-B/Fluids* **23**(1), 229–239.

Karasudani, T. & Funakoshi, M. (1994), 'Evolution of a vortex street in the far wake of a cylinder', *Fluid Dynamics Research* **14**(6), 331.

Khan, W. A., Culham, R. J. & Yovanovich, M. M. (2005), 'Fluid flow around and heat transfer from elliptical cylinders: analytical approach', *Journal of Thermophysics and Heat Transfer* **19**(2), 178–185.

Kumar, B. & Mittal, S. (2006), 'Effect of blockage on critical parameters for flow past a circular cylinder', *International Journal for Numerical Methods in Fluids* **50**(8), 987–1001.

Kumar, B. & Mittal, S. (2012), 'On the origin of the secondary vortex street', *Journal of Fluid Mechanics* **711**, 641–666.

Le Gal, P., Nadim, A. & Thompson, M. (2001), 'Hysteresis in the forced stuart–landau equation: application to vortex shedding from an oscillating cylinder', *Journal of Fluids and Structures* **15**(3-4), 445–457.

Lei, C., Cheng, L., Armfield, S. & Kavanagh, K. (2000), 'Vortex shedding suppression for flow over a circular cylinder near a plane boundary', *Ocean Engineering* **27**(10), 1109–1127.

Linnick, M. N. & Fasel, H. F. (2005), 'A high-order immersed interface method for simulating unsteady incompressible flows on irregular domains', *Journal of Computational Physics* **204**(1), 157–192.

Matsui, T. & Okude, M. (1983), Formation of the secondary vortex street in the wake of a circular cylinder, *in* 'Structure of Complex Turbulent Shear Flow', Springer, pp. 156–164.

Mittal, R. & Balachandar, S. (1996), 'Direct numerical simulation of flow past elliptic cylinders', *Journal of Computational Physics* **124**(2), 351–367.

Norberg, C. (2003), 'Fluctuating lift on a circular cylinder: review and new measurements', *Journal of Fluids and Structures* **17**(1), 57–96.

Ovando, G., Juarez, H., Huelsz, G. & Ramos, E. (2009), 'Vortex formation in a cavity with oscillating walls', *Physics of Fluids* **21**(2), 024101.

Patil, D. V. & Lakshmisha, K. (2009), 'Finite volume tvd formulation of lattice boltzmann simulation on unstructured mesh', *Journal of Computational Physics* **228**(14), 5262–5279.

Paul, I., Prakash, K. A. & Vengadesan, S. (2014), 'Onset of laminar separation and vortex shedding in flow past unconfined elliptic cylinders', *Physics of Fluids* **26**(2), 023601.

Peace, A. J. & Riley, N. (1983), 'A viscous vortex pair in ground effect', *Journal of Fluid Mechanics* **129**, 409–426.

Peller, N., Duc, A. L., Tremblay, F. & Manhart, M. (2006), 'High-order stable interpolations for immersed boundary methods', *International Journal for Numerical Methods in Fluids* **52**(11), 1175–1193.

Raman, S. K., Arul Prakash, K. & Vengadesan, S. (2013), 'Effect of axis ratio on fluid flow around an elliptic cylinder—a numerical study', *Journal of Fluids Engineering* **135**(11).

Rao, A., Thompson, M. C., Leweke, T. & Hourigan, K. (2013), 'The flow past a circular cylinder translating at different heights above a wall', *Journal of Fluids and Structures* **41**, 9–21.

Rao, A., Thompson, M., Leweke, T. & Hourigan, K. (2015), 'Flow past a rotating cylinder translating at different gap heights along a wall', *Journal of Fluids and Structures* **57**, 314–330.

Russell, D. & Wang, Z. J. (2003), 'A cartesian grid method for modeling multiple moving objects in 2d incompressible viscous flow', *Journal of Computational Physics* **191**(1), 177–205.

Sen, S., Mittal, S. & Biswas, G. (2009), 'Steady separated flow past a circular cylinder at low reynolds numbers', *Journal of Fluid Mechanics* **620**, 89–119.

Subburaj, R., Khandelwal, P. & Vengadesan, S. (2018), 'Numerical study of flow past an elliptic cylinder near a free surface', *Physics of Fluids* **30**(10), 103603.

Sumer, B. M. et al. (2006), *Hydrodynamics around cylindrical strucures*, Vol. 26, World Scientific.

Taira, K. & Colonius, T. (2007), 'The immersed boundary method: a projection approach', *Journal of Computational Physics* **225**(2), 2118–2137.

Taneda, S. (1965), 'Experimental investigation of vortex streets', *Journal of the Physical Society of Japan* **20**(9), 1714–1721.

Thompson, M. C., Radi, A., Rao, A., Sheridan, J. & Hourigan, K. (2014), 'Low-reynolds-number wakes of elliptical cylinders: from the circular cylinder to the normal flat plate', *Journal of Fluid Mechanics* **751**, 570–600.

Van der Vorst, H. A. (1992), 'Bi-CGSTAB: A fast and smoothly converging variant of bi-cg for the solution of nonsymmetric linear systems', *SIAM Journal on scientific and Statistical Computing* **13**(2), 631–644.

Walker, J. D. A., Smith, C. R., Cerra, A. W. & Doligalski, T. L. (1987), 'The impact of a vortex ring on a wall', *Journal of Fluid Mechanics* **181**, 99–140.

Wang, L., Guo, C. & Su, Y. (2018), 'Numerical analysis of flow past an elliptic cylinder near a moving wall', *Ocean Engineering* **169**, 253–269.

Wang, Z., Fan, J. & Cen, K. (2009), 'Immersed boundary method for the simulation of 2d viscous flow based on vorticity–velocity formulations', *Journal of Computational Physics* **228**(5), 1504–1520.

Williamson, C. H. K. (1989), 'Oblique and parallel modes of vortex shedding in the wake of a circular cylinder at low Reynolds numbers', *Journal of Fluid Mechanics* **206**, 579–627.

Williamson, C. & Prasad, A. (1993), 'Acoustic forcing of oblique wave resonance in the far wake', *Journal of Fluid Mechanics* **256**, 315–341.

Xu, S. & Wang, Z. J. (2006), 'An immersed interface method for simulating the interaction of a fluid with moving boundaries', *Journal of Computational Physics* **216**(2), 454–493.

Yoon, H. S., Yin, J., Choi, C., Balachandar, S. & Ha, M. Y. (2016), 'Bifurcation of laminar flow around an elliptic cylinder at incidence for low reynolds numbers', *Progress in Computational Fluid Dynamics, an International Journal* **16**(3), 163–178.

Zdravkovich, M. M. (1985), Observation of vortex shedding behind a towed circular cylinder near a wall, *in* 'Flow Visualization III', pp. 423–427.

Zhu, J., Holmedal, L. E., Wang, H. & Myrhaug, D. (2020), 'Vortex dynamics and flow patterns in a two-dimensional oscillatory lid-driven rectangular cavity', *European Journal of Mechanics-B/Fluids* **79**, 255–269.

Chapter 7

Numerical simulation of oscillatory boundary layer

Jianxun Zhu[1], Lars Erik Holmedal[1]

7.1 Introduction

Oscillatory flow generated by an unsteady pressure gradient near a flat wall is relevant to a bottom boundary layer under surface gravity waves. This flow depends on the Reynolds number defined by $u_0^* \delta^* / \nu^*$, where u_0^* denotes the amplitude of the velocity oscillations in the irrotational region, and $\delta^* = \sqrt{2\nu^*/\omega^*}$ is the conventional boundary layer thickness. Here ω^* and ν^* are the angular frequency of fluid oscillations and the kinematic viscosity, respectively. A star is used to denote dimensional quantities.

The oscillatory boundary layer can be classified into four flow regimes: i) for low Reynolds numbers the flow is laminar and unidirectional and can be described by the Stokes solution (Stokes 1851); ii) for Reynolds numbers larger than about 100, the disturbed laminar regime occurs, where small perturbations appear but do not lead to significant modification of the laminar velocity profile (Vittori & Verzicco 1998); iii) when the Reynolds number becomes larger than about 550 the flow is in the intermittently turbulent regime where turbulent bursts appear during the decelerating phase of the cycle (Vittori & Verzicco 1998); iv) for Reynolds numbers larger than about 3500 the fully developed turbulent regime is observed, where the flow remains turbulent during the whole cycle (Jensen et al. 1989).

---

[1]Department of Marine Technology, Norwegian University of Science and Technology, NO-7491 Trondheim, Norway

7.2   Numerical method

The oscillatory flow is considered to be incompressible and generated by an oscillating pressure gradient $\partial p^*/\partial x^*$ defined as follows

$$\frac{\partial p^*}{\partial x^*} = -\rho^* u_0^* \omega^* sin(\omega^* t^*), \quad \frac{\partial P^*}{\partial y^*} = 0, \quad \frac{\partial P^*}{\partial z^*} = 0 \tag{7.1}$$

where ρ^* denotes the density; x^*, y^* and z^* indicate the stream-wise, span-wise and cross-stream coordinates, respectively; t^*, u_0^* and ω^* are the time, the amplitude and angular frequency of the velocity oscillation, respectively. The following dimensionless variables are introduced:

$$t = \omega^* t^*, \quad (x, y, z) = \frac{(x^*, y^*, z^*)}{\delta^*}, \quad (u, v, w) = \frac{(u^*, v^*, w^*)}{U_0^*}, \quad p = \frac{p^*}{\rho^* U_0^{*2}} \tag{7.2}$$

Hence, the incompressible Navier-Stokes equations in dimensionless form with Cartesian coordinates $(x_1, x_2, x_3) = (x, y, z)$ can be written as follows:

$$\frac{\partial u_i}{\partial x_i} = 0 \tag{7.3}$$

$$\frac{\partial u_i}{\partial t} + \frac{Re_\delta}{2} \frac{\partial u_i u_j}{\partial x_j} = -\frac{Re_\delta}{2} \frac{\partial p}{\partial x_i} + \delta_{1,i} sin(t) + \frac{1}{2} \frac{\partial^2 u_i}{\partial x_j \partial x_j} \tag{7.4}$$

where $(u_1, u_2, u_3) = (u, v, w)$ are the Cartesian velocity components and $\delta_{1,i}$ is the Kronecker delta function.

Eqs. (7.3) and (7.4) are solved by using a projection method with a semi-implicit time integration using a second-order Adams-Bashforth scheme for the convective terms and a Crank-Nicolson scheme for the diffusive terms. The spatial discretization employs the centered second-order finite differences on a staggered grid.

7.3   Validation against previous results

In order to validate the correctness of the numerical code, numerical simulations of the oscillating boundary layer for $Re_\delta = 500$ and 1120 have been conducted and compared with the numerical and experimental results obtained by Vittori & Verzicco (1998) and Jensen et al. (1989), respectively. These simulations were conducted in the same computational domain (L_x, L_y, L_z) = $(25.13\delta^*, 12.57\delta^*, 25.13\delta^*)$, and numerical grids $64 \times 32 \times 64$, $97 \times 49 \times 97$ and $100 \times 60 \times 100$ were used for $Re_\delta = 500$, 1000 and 1120, respectively. The grid size is uniform in the x and y-directions, while the grid is stretched with

a constant ratio in the z-direction (i.e., from the bottom wall to the top of the computational domain). The imperfection conditions adopted by, e.g. Vittori & Verzicco (1998) and Scandura (2007) are imposed on the bottom wall to trigger the turbulence. After the turbulence has been developed (about two oscillation cycles), the wall imperfection condition is removed and the simulation is continued on a smooth flat wall.
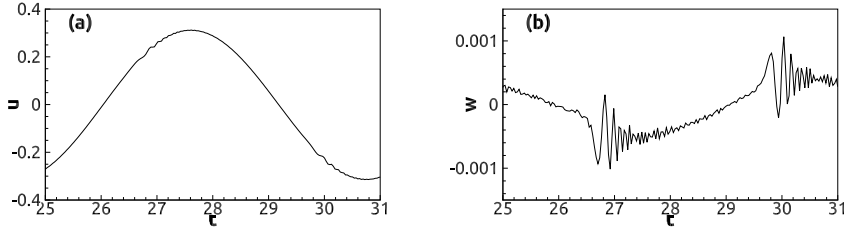
Figure 7.1: Temporal development of stream-wise (a) and cross-stream (b) velocity components at $x = 3.93$, $y = 3.93$, $z = 0.25$ for $Re_\delta = 500$.
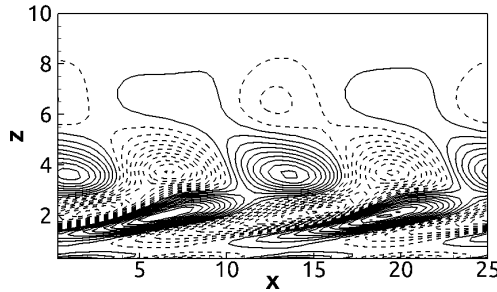
Figure 7.2: Contour plot of the span-wise vorticity Ω_y for $Re_\delta = 500$ at $t = 21.99$ in the plane $y = 5.69$. Contour values are from -0.021 to 0.021 with $\Delta\Omega_y = 0.002$; continues lines denote the positive vorticity, while dashed lines represent the negative vorticity.

The flow for $Re_\delta = 500$ is categorized as the disturbed laminar regime, where disturbances of the flow velocities are present during the end of the acceleration phase as shown in figure 7.1. From figure 7.1(a), the disturbances of the stream-wise velocity u appear before u reaches the maximum value, i.e., during the end of the deceleration phase. Meanwhile, the fluctuation of the cross-stream velocity (w) grows significantly as shown in figure 7.1(b). A good agreement is obtained with the figures 3 (a) and (b) of Vittori & Verzicco (1998). Figure 7.2 shows the span-wise vorticity contours

for $Re_\delta = 500$ at $t = 21.99$ in a vertical plane $y = 5.69$. The vorticity was calculated after the average in the x-direction of the velocity field was removed. The results are in a good agreement with the results shown in figure 5(c) of Vittori & Verzicco (1998) and figure 1 of Scandura (2007).
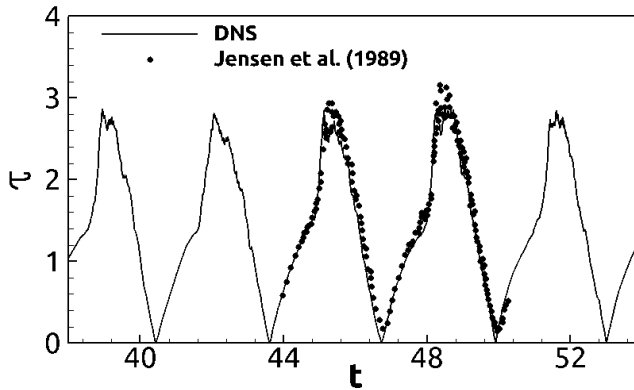
Figure 7.3: Time development of wall shear stress for oscillating turbulent boundary layer at $Re_\delta = 1120$; continuous line: present numerical results; dots: experimental results of Jensen et al. (1989).

A further check of the numerical code has been conducted for $Re_\delta = 1120$, where the flow is in the intermittently turbulent regime. Figure 7.3 shows the time-history of the dimensionless wall shear stress $\tau = \tau^*/(\rho U_0^{*2})$ averaged in x- and y-directions for $Re_\delta = 1120$. A good agreement is obtained with the experimental results (dots) obtained by Jensen et al. (1989). A sudden increase of the wall shear stress (i.e., the occurrence of turbulence) is present at the end of the accelerating and early decelerating phase.

References

Jensen, B. L., Sumer, B. M. & Fredsøe, J. (1989), 'Turbulent oscillatory boundary layers at high Reynolds numbers', *Journal of Fluid Mechanics* **206**, 265–297.

Scandura, P. (2007), 'Steady streaming in a turbulent oscillating boundary layer', *Journal of Fluid Mechanics* **571**, 265–280.

Stokes, G. G. (1851), *On the effect of the internal friction of fluids on the motion of pendulums*, Vol. 9, Pitt Press Cambridge.

Vittori, G. & Verzicco, R. (1998), 'Direct simulation of transition in an oscillatory boundary layer', *Journal of Fluid Mechanics* **371**, 207–232.

Chapter 8

Conclusions and future works

8.1   Conclusions

The present numerical method was successfully validated against the previous numerical and experimental results for the lid-driven cavity flows, flow past an isolated circular cylinder and the oscillatory turbulent boundary layer. Numerical investigations were conducted for steady and oscillatory lid-driven cavity flows, the flow in a steady lid-driven cavity with an embedded circular cylinder and the flow over an elliptic cylinder near a moving wall. The main conclusions are as follows:

A detailed investigation of the flow patterns in an oscillatory lid-driven cavity with depth-to-width ratio 1:2, covering a wide range of Reynolds numbers and Stokes numbers where this flow is known to be in the two-dimensional flow regime, was conducted using two-dimensional numerical simulations. Four distinct flow patterns are classified based on the vortex dynamics, which is visualized by streamline contours. These flow structures are unique functions of the Reynolds number and the Stokes number, and the pattern changes with these parameters. An increase of the driven force quantified by the two parameters results in finer flow structures and hence different flow patterns. If the oscillation frequency increases for a given Reynolds number, the extrema of the stream function have less time to grow and the primary vortex center has less time to move away from the lid. To compensate these effects, a larger oscillation amplitude is required for an increased frequency to maintain the same flow pattern.

A detailed investigation of the flow patterns in the steady lid-driven cavity of depth to width ratio 1:2 containing a circular cylinder of differ-

ent radii and positions was conducted for Reynolds numbers of 100, 500 and 1000 and the cylinder radii of 0.1, 0.2, 0.3 and 0.4. The positions of the cylinder are left-centered, centered and right-centered in the cavity. It appears that this flow can be classified into seven different flow patterns visualized by streamline contours. For a given cylinder position, the distribution of these flow patterns was given as a function of the cylinder radius and the Reynolds number. More transitions between different flow patterns exist for a small radius than for a larger radius. For a given cylinder radius, there are more transitions for high Reynolds numbers than for low Reynolds numbers. Overall, a larger number of flow patterns tend to emerge as the Reynolds number increases for small cylinder radii. The largest variety of flow patterns occur for the left-centered cylinder due to the interaction with the large anti-clockwise circulation flow formed at the bottom left corner.

A detailed numerical investigation for the flow around an elliptic cylinder with an aspect ratio of 0.4 translating above a plane wall in still water has been conducted for Reynolds numbers in the range from 30 to 150 and the gap ratios (i.e., the ratio between the distance of the cylinder from the wall and the length of the semi-major axis of the cylinder) ranging from 0.1 to 5.

In the steady flow regime, the wake contains two asymmetric counter-rotating recirculation vortices attached to the cylinder. Here the lower vortex center is located closer to the cylinder than the upper vortex center. This difference increases as the gap ratio decreases (for a given Reynolds number) due to stronger wall suppression effect on the lower vortex for lower gap ratios. As the Reynolds number increases (for a given gap ratio), this difference decreases since thinner shear layers are formed,resulting in a weaker interaction between the shear layers beneath the cylinder bottom and above the wall. Moreover, as the gap ratio decreases (for a given Reynolds number) the time-averaged drag coefficient decreases while the time-averaged lift coefficient increases; as the Reynolds number increases (for a given gap ratio), the drag and lift coefficients decrease almost linearly in log-log scale.

In the unsteady flow regime, four different wake patterns have been classified; i) at relatively large gap ratios, the flow, which is denoted wake pattern A, contains the Kármán vortex street, the two-layered wake and the secondary vortex street; ii) a decrease in the gap ratio leads to the suppression of the vertical fluctuations in the far-wake region, resulting in the disappearance of the secondary vortex street; this represents wake pattern B; iii) a further decrease in the gap ratio leads to the break-down of the Kármán vortex, resulting in a pair-wise vortex shedding (denoted wake pat-

tern C) or iv) forming a quasi-steady near-wake region (with constant lift and drag coefficients) and a pair-wise vortex shedding farther downstream, which is denoted wake pattern D. Moreover, an increase in the Reynolds number (for a given gap ratio) enhances the vortex shedding behind the cylinder, thus triggering the transition between two different wake patterns. Therefore, a smaller gap ratio is required for a higher Reynolds number to maintain the same wake pattern, i.e., a smaller critical gap ratio is required for the transition between two different wake patterns (except wake pattern D).

The time-averaged drag coefficient increases gradually as the gap ratio increases (for a given Reynolds number) due to the decay of the wall suppression effect. A sudden drop of the time-averaged drag coefficient is observed as the gap ratio increases from 0.3 to 0.32 as well as from 0.24 to 0.3 for the Reynolds number of 130 and 150, respectively, where the vortex shedding frequency remains nearly constant. It appears that the vortex strength here is determined by the total circulation injected into the wake from the top and the bottom of the cylinder. This total circulation decreases as the gap ratio increases due to less fluid moving upwards along the cylinder and a decrease of the gap flow velocity. Consequently, the weaker upper and lower vortices are formed for the larger gap ratio, resulting in the sudden drop of the time-averaged drag coefficient. Moreover, the time-averaged lift coefficient increases as the gap ratio decreases (for a given Reynolds number) due to more asymmetric flow distribution around the cylinder.

Stronger wall suppression effect for smaller gap ratios leads to the upper vortex being stronger than the lower vortices, thus enhancing the convection of the vorticity within the lower vortex. Consequently, the lower vortex distorts and rotates to align with the stream-wise direction at a location closer to the cylinder than the horizontal upper vortex, showing that the onset location of the two-layered wake moves closer to the cylinder as the gap ratio decreases (for a given Reynolds number).

8.2   Future works

The near future work is the implementation of the three-dimensional Navier-Stokes solver in conjunction with the immersed boundary method with parallel computing. The code can be validated by comparison with previous results of, e.g., the turbulent channel flow, the oscillatory turbulent boundary layer and the steady flow around an isolated or near-wall cylinder. Some recommendations for future works are given as follows:

- Three-dimensional vortex dynamics and turbulent flow in the oscillatory lid-driven cavity. This thesis focuses on the two-dimensional vortex dynamics and the laminar flow. Only few investigations have been conducted on the oscillatory lid-driven three-dimensional cavity flow, which is of vital importance to understand the three-dimensional vortex interaction, the three-dimensional instability and the turbulent characteristics for vortex flows.

- Three-dimensional wake transition behind the elliptic cylinder translating above a plane. This thesis focuses on the two-dimensional flow features. It was found that the two-layered wake formed near the elliptic cylinder has a significant effect on the three-dimensional wake transition in the near-wake region. The mechanism underlying this effect is still not well-known. Moreover, the effects of the Reynolds number, the aspect ratio of the elliptic cylinder and the gap ratio on this flow are worth to be investigated.

- Oscillatory flow around a small-diameter cylinder near a seabed. The current design method is overly conservative for small-diameter pipelines because the pipeline is experienced a velocity reduction in the wave-induced boundary layers, which has not been accounted for in estimating hydrodynamic forces on pipelines. Most previous studies focus on the oscillatory flow around the cylinder for low KC numbers (based on the amplitude of the oscillatory velocity, the oscillation period and the cylinder diameter). The KC number are usually large for small-diameter cylinders. The numerical investigations here can be of great interest for both academic researches and industrial applications.

Appendix A

Appended papers

A.1   Paper 1

Fluid flow in steady and oscillatory lid-driven square cavities

[a]J Zhu, [a]L E Holmedal, [a]D Myrhaug, [a]H Wang

[a]*Dept. of Marine Technology, Norwegian University of Science and Technology*, Trondheim, Norway

E-mail: `jianxun.zhu@ntnu.no`

Abstract. This paper presents numerical simulations of steady and oscillatory lid-driven cavity flow at different Reynolds numbers with a fixed aspect ratio of 1:1. A projection method (P2 pressure correction method) is applied to solve the incompressible Navier-Stokes equations. The code is validated by comparison with published works of steady lid-driven flow at Re = 100, 400 and 1000. Oscillatory lid-driven cavity flow at different Reynolds numbers (100, 400 and 1000) at a fixed oscillation frequency has been investigated. It is observed that the oscillatory lid-driven cavity flow is substantially affected by the Reynolds number.

1. Introduction

Steady lid-driven cavity flow is one important benchmark for Navier-Stokes solvers due to its simple geometry and can also serve as a simplified model for industrial applications like e.g. wave-induced flow in sandpits (see e.g. [1]). Flow phenomena such as corner vortices and longitudinal vortices exist within the cavity. Flow structures in the cavity vary significantly at different Reynolds numbers $Re = Uh/\nu$ and aspect ratios $D = h/l$ (where ν, U, h and l are the kinematic viscosity of the fluid, the steady lid motion velocity, the depth and width of the cavity, respectively). Flow in a square cavity was investigated extensively by [2]. The predictions, limited up to $Re = 400$, show that there are three vortices existing in the cavity (one primary vortex occupying the central core and two other relatively small vortices located at the bottom corners of the cavity). Steady square lid-driven cavity flow at $Re \leq 10000$ was presented by [3] and [4]. The primary vortex and two corner vortices grow in strength as the Reynolds number increases while an upper left wall vortex is observed when the Reynolds number increases to 3200.

A few studies have been carried out for flow in a square cavity driven by an oscillating wall. The vortex dynamics have been investigated by [5] at different Reynolds numbers and Stokes numbers (here, the Stokes number is $St = \omega A^2/\nu$, where ω and A are the frequency and amplitude of the lid motion) for equal values ($Re = St$) ranging from 0 to 600. It is observed that one counter-rotating vortex pair and two corner vortices occur within the cavity during one cycle. Similar results have also been presented by [6], [7] and [8].

In the present paper, the steady lid-driven cavity flow at different Reynolds numbers has been investigated and compared with corresponding results obtained from [4]. Simulations of the oscillatory lid-driven cavity flow at a fixed oscillation frequency have been conducted at different Reynolds numbers. The results show good agreement with the previous data presented

by [8]. This approach facilitates a detailed study of the oscillatory lid-driven cavity flow covering a wide range of physical parameters in terms of Stokes numbers and Reynolds numbers.

2. Problem formation

A definition sketch of the flow in a square lid-driven cavity is shown in Figure. 1. The flow is considered to be incompressible and homogeneous. The continuity equation and Navier-Stokes equations are given as:

$$\nabla \cdot \vec{U} = 0 \tag{1}$$

$$\frac{\partial \vec{U}}{\partial t} + \vec{U} \cdot \nabla \vec{U} = -\frac{1}{\rho}\nabla p + \nu\Delta\vec{U} \tag{2}$$

where $\vec{U}$ is the velocity vector with the horizontal velocity component u and vertical component w; $Re = U_{lid}h/\nu$ for steady lid-driven cavity flow and $Re = U_{max}h/\nu$ for oscillatory lid-driven cavity flow (where U_{lid} is the steady velocity and U_{max} is the velocity amplitude, respectively). Moreover, the velocity presented in this paper is scaled by U_{lid} and U_{max} for the steady and the oscillatory lid-driven flow, respectively. No-slip velocity and Neumann pressure conditions are imposed on all the walls.
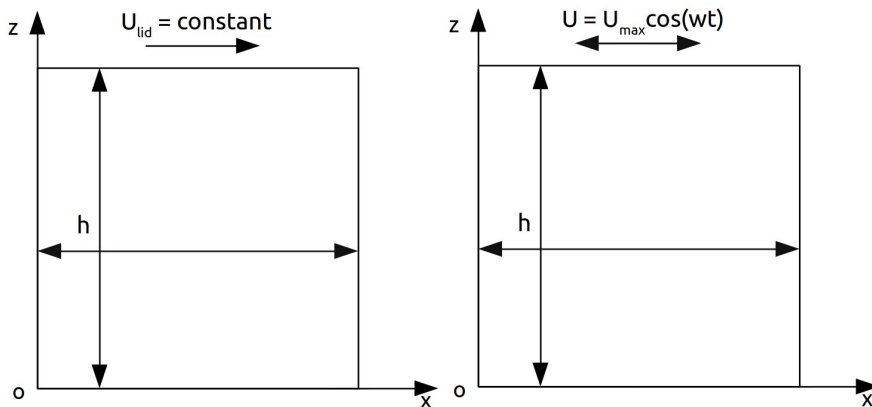
Figure 1. Schematic of the steady and oscillatory lid-driven cavity flow.

3. Numerical method

Equations (1) and (2) are discretized by second order central differences in space with a staggered grid arrangement. The impulse equations have been integrated in time using a semi-implicit second order scheme in conjunction with a projection method, where Adams-Bashforth and Crank-Nicolson are applied to the convective terms and diffusive terms, respectively.

A P2 projection method has been applied in a standard manner to solve the Navier-Stokes equations. Here an intermediate velocity field (which does not satisfy the continuity equation) is obtained by using the pressure gradient from the last time step (P2 method). A Poisson equation for the pressure is solved in such a way that the resulting pressure gradients are applied to correct the intermediate velocity field such that the resulting velocity satisfies the continuity equation.

4. Results of test cases and examples

4.1. Grid convergence test

The grid convergence test is carried out by using the predictions of the steady lid-driven flow in a square cavity at $Re = 100$, 400 and 1000. Five different uniform grid resolutions have

been applied for each Reynolds number. The minimum values of the velocities $u(0.5, z/h)$ and $w(x/h, 0.5)$ and the maximum values of $w(x/h, 0.5)$ are shown in Table 1. At $Re = 100$, these values obtained from 64×64 grid cells deviate less than 0.1% from those obtained from 48×48 grid cells. As the Reynolds number increases to 400, the deviation between the values from 96×96 and 128×128 grid cells is less than 0.1% while for $Re = 1000$, this deviation is obtained between 128×128 and 160×160 grid cells.

Table 1. Results of cases with different grid resolutions

Test Cases	Velocity at the central line		
	$min_z u(0, z/h)$	$min_x w(0, x/h)$	$max_x w(0, x/h)$
32	-0.2072	-0.2461	0.1734
48	-0.2099	-0.2488	0.1757
64	-0.2111	-0.2499	0.1765
96[a]	-0.2117	-0.2506	0.1771
128	-0.2120	-0.2508	0.1773
	Re = 100		
48	-0.3118	-0.4352	0.0.2871
64	-0.3179	-0.4417	0.2933
96	-0.3225	-0.4472	0.2976
128[a]	-0.3242	-0.4493	0.2991
160	-0.3250	-0.4498	0.2998
	Re = 400		
64	-0.3634	-0.4970	0.3524
96	-0.3753	-0.5117	0.3636
128	-0.3797	-0.5172	0.3679
160[a]	-0.3818	-0.5197	0.3699
192	-0.3825	-0.5207	0.3703
	Re = 1000		

[a]The case for investigation.

4.2. Two-dimensional steady lid-driven flow in a square cavity
The steady flow predictions with $Re = 100$, 400 and 1000 are presented in this section. Figure. 2 depicts the velocity profiles on the center-line of the cavity showing good agreement with the corresponding results obtained from [4]. The slope of the velocity profiles $u(0.5, z/h)$ and $w(x/h, 0.5)$ is nearly constant in the core region (i.e. away from the wall) for a Reynolds number of 1000. Moreover, the region with near uniform vorticity grows with increasing Reynolds number as shown in Figure. 3. It is demonstrated that the thickness of the boundary layers at the walls decreases as the Reynolds number increases.

Figure. 4 shows streamlines for the primary vortex and corner vortices at Re = 100, 400 and 1000. The primary vortex core moves towards the centre of the cavity and increases in strength while the corner vortices grow both in size and strength as the Reynolds number increases. The right corner vortex is smaller and weaker than the left vortex. Moreover, the stream-function and the vorticity contours are in good agreement with the results in [4].

4.3. Two-dimensional oscillatory lid-driven flow in a square cavity
Here results for the periodic solutions on the oscillatory lid-driven cavity flow at $Re = 100$, 400 and 1000 with a fixed oscillation frequency parameter $\omega' = \pi/3$ (here, $\omega' = h\omega/U_{max} = h/A$)

are given. The results are presented for 10 intervals of each oscillation cycle.

The oscillatory lid-driven cavity flow is expected to give a time-periodic flow. The criterion for the flow being fully developed is:

$$\frac{max|\vec{U}^n(x,z,t+T) - \vec{U}^{n-1}(x,z,t)|}{max|\vec{U}^n(x,z,t)|} \leq \epsilon \tag{3}$$

where n denotes the time step number; $\epsilon = 1 \times 10^{-6}$ and T is the period of the lid motion.
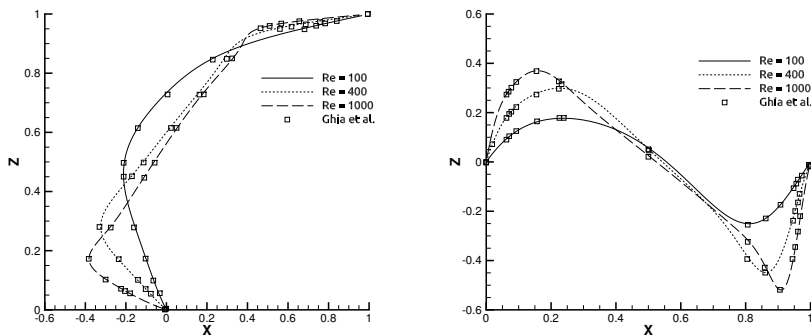
Figure 2. Comparisons of $u(0.5, z/h)$ and $w(x/h, 0.5)$ between predictions of the steady lid-driven cavity flow and reference data from Ghia et al. [4] at various Reynolds numbers

Figures 5 and 6 show the velocity profiles $u(0.5, z/h)$ and $w(x/h, 0.5)$, respectively. It is observed that the velocity profiles at t and $t+T/2$ are mirror images of each other. Comparison with the results in Fig. 2 reveals that the velocity profiles for the oscillatory lid-driven cavity flow are more complex than those for the steady lid-driven cavity flow. For instance, the velocity $u(0.5, z/h)$ at $t = 0.3T$ changes from a negative value to a positive maximum, and then decreases again to a negative value. Thereafter, it increases gradually to zero as it approaches the bottom wall. In other words, the direction of the velocity changes twice along the center-line indicating that at least one counter-rotating vortex pair emerge in the central region of the cavity. The boundary layer thickness beneath the moving lid decreases as the Reynolds number and consequently the Stokes number increase. This is consistent with laminar boundary layer theory (i.e. Stokes second problem described in [9]); the boundary layer thickness increases as the oscillation period (i.e. Stokes number) increases. Furthermore, the number of local extrema of $w(x/h, 0.5)$ increases as the Reynolds number increases. This indicates, as shown in Figure. 7 that the number of vortices near the central plane of the cavity increases.

Figure. 7 shows streamlines for different Reynolds numbers at $t = 0.4T$. The location and number of vortices within the cavity change for different Reynolds numbers. At $Re = 100$, two counter-rotating vortices occur in the cavity (one primary counterclockwise vortex and one small clockwise vortex are formed during the initial phase of the lid motion). As the Reynolds number increases from 100 to 400, an additional counterclockwise vortex appears beneath the clockwise vortex, and the size of the clockwise vortex increases. At $Re = 1000$, four vortices appear in the cavity, comprising two counter-rotating vortex pairs. Thus it appears that the flow structures in the cavity become more complex as the Reynolds number increases. The results for $Re = 100, 400$ and 1000 with $\omega' = \pi/3$ are in good agreement with results obtained by [8].
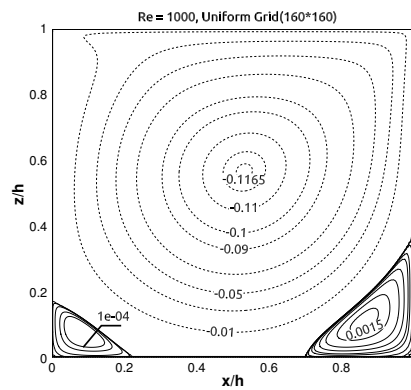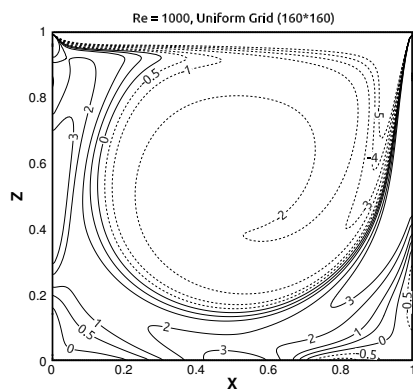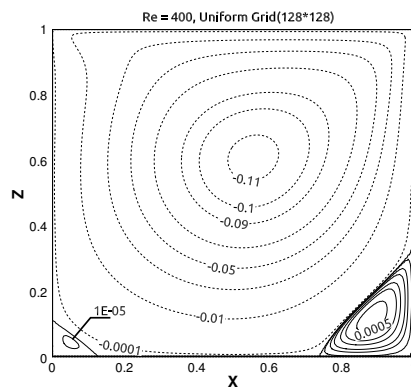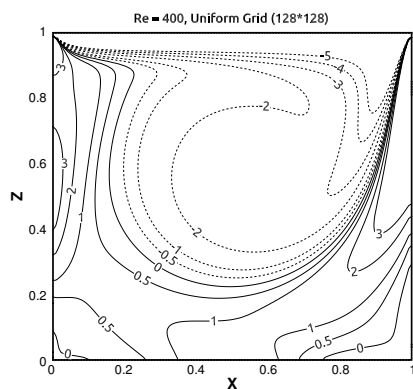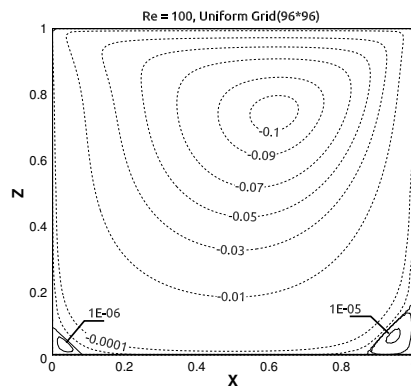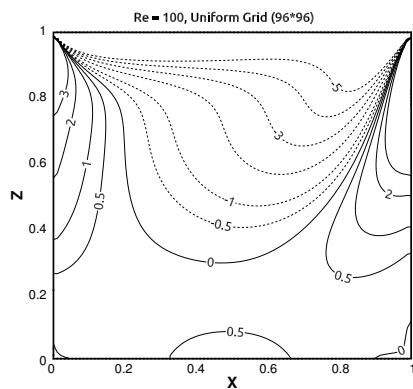
Figure 3. Contours of y-vorticity for the steady lid-driven cavity flow at different Reynolds numbers

Figure 4. Contours of stream-function for the steady lid-driven cavity flow at different Reynolds numbers
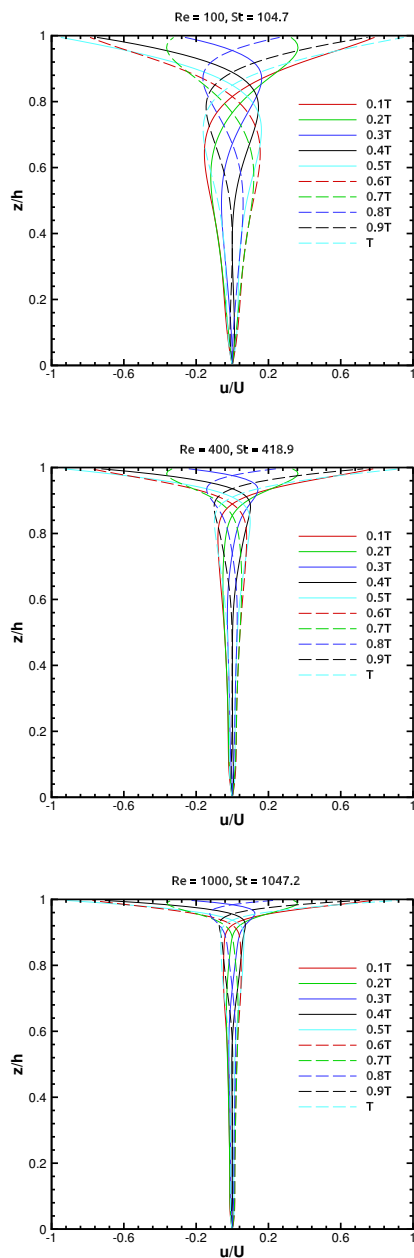
Figure 5. Profiles of $u(0.5, z/h)$ for the oscillatory lid-driven cavity flow at different Reynolds numbers with a fixed $\omega' = \pi/3$
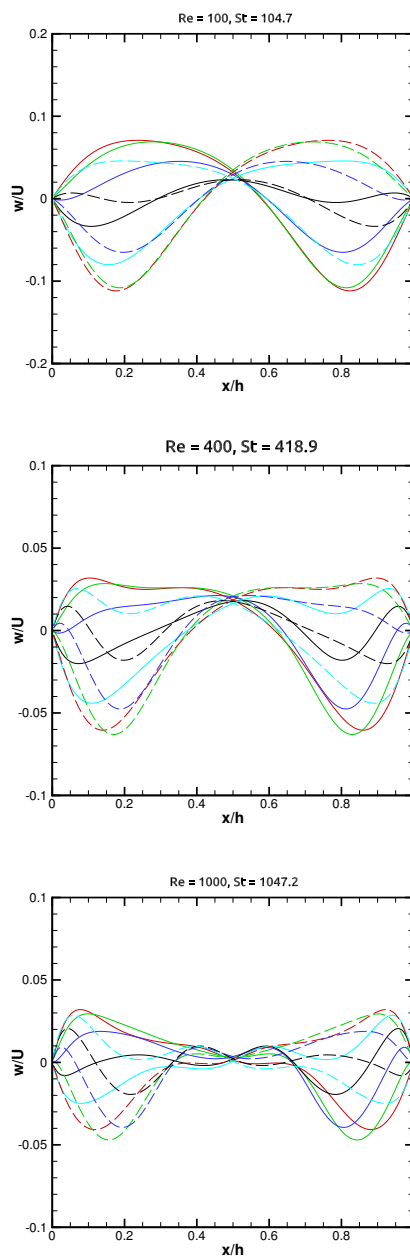
Figure 6. Profiles of $w(x/h, 0.5)$ for the oscillatory lid-driven cavity flow at different Reynolds numbers with a fixed $\omega' = \pi/3$. Velocities at different time instants are marked by the same color as in Figure. 5.

5. Summary and Conclusions

The flow features in the steady and oscillatory lid-driven cavity have been investigated. It appears that the oscillatory lid-driven flow exhibits more complex fluid dynamical behaviors than the steady lid-driven flow. For the chosen oscillation frequency, the boundary layer thickness at the top lid decreases as the Reynolds number increases. Finally, the number of vortices appearing in the central part of the cavity increases with increasing Reynolds number.
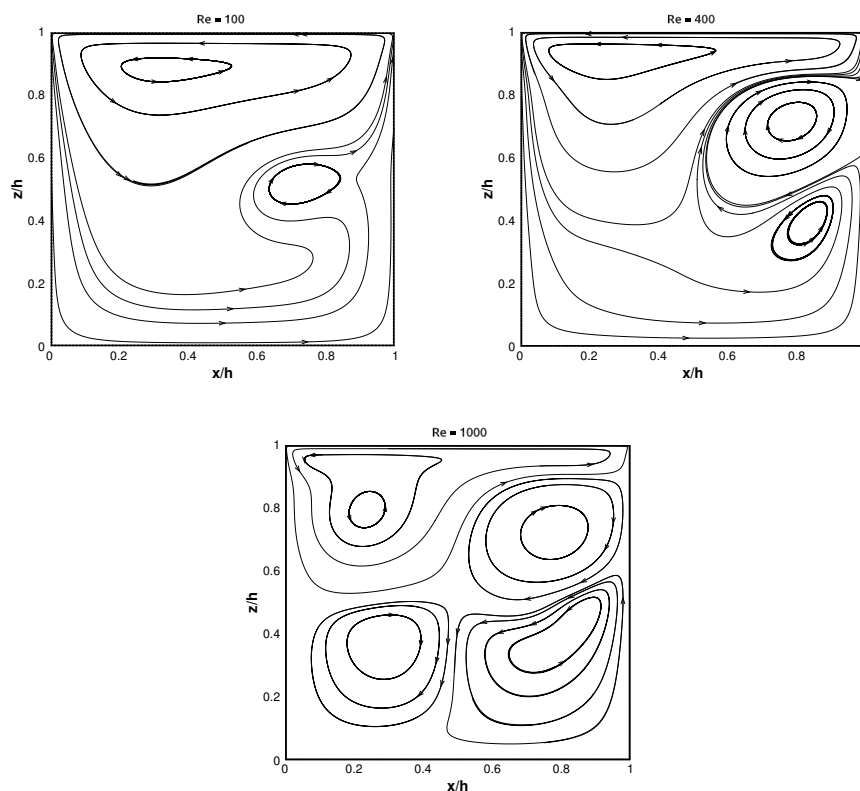
Figure 7. Streamline patterns of the oscillatory lid-driven flow with different Reynolds numbers at $t = 0.4T$.

References

[1] Van Rijn L, Soulsby R, Hoekstra P and Davies A 2005 *SANDPIT, Sand Transport and Morphology of Offshore Mining Pits.*
[2] Burggraf O R 1966 *J. Fluid Mech.* **24(1)** 113–151
[3] Benjamin A and Denny V 1979 *J. Comput. Phys.* **33(3)** 340–358
[4] Ghia U, Ghia K N and Shin C 1982 *J. Comput. Phys.* **48(3)** 387–411

[5] Duck P 1982 *J. Fluid Mech.* **122** 215–234
[6] Liu C H 2001 *Int. J. Numer. Methods Fluids* **35(5)** 533–557
[7] Iwatsu R, Hyun J M and Kuwahara K 1992 *J. Fluids Eng.* **114(2)**
[8] Mendu S S and Das P 2013 *Eur. J. Mech. B. Fluids* **39** 59–70
[9] Hermann S *et al.* 1979 *McGarw-Hill Book Company* 135–149

A.2   Paper 2

Paper 2:
Effects of an inserted circular cylinder on a steady lid-driven rectangular cavity flow.
Authors: Jianxun Zhu, Lars Erik Holmedal, Dag Myrhaug
This is an extended work for Chapter 5 published in Proceedings of
Second Conference of Computational Methods in Offshore Technology,
Stavanger, Norway, 2019

Effects of an inserted circular cylinder on a steady lid-driven rectangular cavity flow

J Zhu, L E Holmedal and D Myrhaug

Dept. of Marine Technology, Norwegian University of Science and Technology, Trondheim, Norway

E-mail: `jianxun.zhu@ntnu.no`

Abstract. This paper provides numerical investigations of flow in a steady lid-driven cavity of depth to width ratio 1/3 containing a circular cylinder. The inner cylinder is treated using a direct-forcing immersed boundary method, and a project method is applied to solve the incompressible Navier-Stokes equations. Three different Reynolds numbers and positions of the cylinder are considered; for a lower Reynolds number, flow structures are weakly affected by the cylinder near the left wall while two clockwise vortices attached to the cylinder are formed as the cylinder moves rightwards; for a moderate Reynolds number, an anticlockwise bottom vortex is formed for the cylinder near the left wall, and it disappears as the cylinder is shifted rightwards; for the largest Reynolds number, two anti-clockwise vortices attached the cylinder are formed for the cylinder close to the left wall, and as the cylinder moves gradually closer to the left wall a bottom vortex is formed and disappears together with the clockwise vortex to the right side of the cylinder.

1. Introduction

Vortex structures, e.g. elongated primary vortices and corner vortices, within a steady lid-driven cavity are controlled by two parameters; i) Reynolds number based on the lid motion velocity and the depth of the cavity; ii) the aspect ratio of cavity. These flow structures will change due to an inserted square or circular cylinder within the cavity. Understanding the influence of the inserted cylinder on the flow structures is of fundamental importance in engineering applications like heat exchangers and electronic coolers.

Oztop et al.[1] and Khanafer and Aithal[2] numerically investigated mixed convection and heat transfer in a steady lid-driven square cavity containing a circular cylinder by using a finite volume method and a finite element formulation, respectively. They found that for the forced convection flow an increase in the cylinder's size leads to the primary vortex breaking up into two vortices, and various locations of the cylinder result in the movement of the vortex cores. Moreover, a large gap between isotherms which affects the heat transfer was present due to strong flow circulation (i.e. the vortex formed in the cavity).

The lid-driven cavity flow with multiple embedded obstacles were also investigated and applied to test the accuracy of some numerical methods, e.g. the immersed boundary method by Su et al.[3] and the immersed interface method by Ito et al.[4] due to its low computational cost. Moreover, in the absence of the lid motion, many investigations were conducted for the natural convection (dominated by the temperature gradient) in a cavity containing obstacles with different locations and geometries (see e.g. [5, 6, 7]).

A thorough investigation of the vortex structures for steady lid-driven cavity flow containing a cylinder has, to the limit of author's knowledge, not been conducted in detail for purely forced convection flow. The present paper provides a detailed investigation of vortex structures in a two-dimensional steady lid-driven cavity of depth to width ratio 1/3 with an embedded circular cylinder with a dimensionless radius of 0.2 (i.e. the ratio between the cylinder radius and the cavity depth). Three different Reynolds numbers (100, 500 and 1000) based on the depth of the cavity and three different locations of the cylinder have been considered. A direct forcing immersed boundary method combined with the finite difference method proposed by e.g. Fadlun et al. [8] and improved by Peller et al.[9] is applied due to its easy meshing and efficiency of solving the Navier-Stokes equations in Cartesian grids.

2. Problem formation and numerical method

The flow with a constant density ρ and kinematic viscosity ν is governed by the two-dimensional Navier-Stokes equations described as follows:

$$\frac{\partial u_i}{\partial x_i} = 0 \tag{1}$$

$$\frac{\partial u_i}{\partial t} + \frac{\partial u_i u_j}{\partial x_j} = -\frac{\partial p}{\partial x_i} + \frac{1}{Re}\frac{\partial^2 u_i}{\partial x_j \partial x_j} \tag{2}$$

where the Einstein notation using repeated indices is applied. Here $u_i = (u, v)$ and $x_i = (x, y)$ for $i = 1$ and 2, are the velocity and Cartesian coordinates, respectively, whilst t, p and $Re = UH/\nu$ denote the dimensionless time, dimensionless pressure and Reynolds number, respectively, where H is the depth of cavity and U is the lid motion velocity. The time scale, pressure scale and length scale is H/U, $0.5\rho U^2$ and H, respectively.

Equations (1) and (2) are solved using a semi-implicit second order scheme in conjunction with a projection method, where Adams-Bashforth and Crank-Nicolson are applied to the convective terms and diffusive terms, respectively. A second-order central difference scheme is applied on a staggered mesh arrangement.
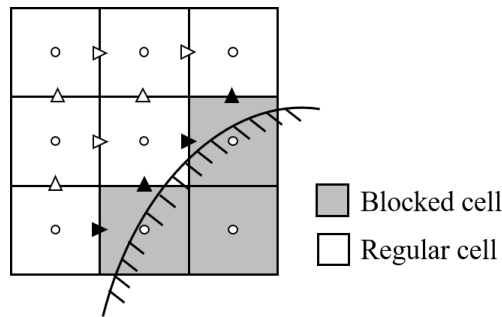
Figure 1. Definition of the blocked cell (grey square), the regular cell (white square), the active (white arrows) and inactive (black arrows) velocity points.

The immersed boundary method is based on a direct forcing approach combined with finite difference method. The relationship between the grid and the immersed boundary is shown in figure 1. A cell with the pressure point inside the solid is defined as a blocked cell while the rest cells inside the fluid are denoted by the regular cells. The velocity components at the connection face between the blocked and regular cells are set as inactive velocity points (▶ and
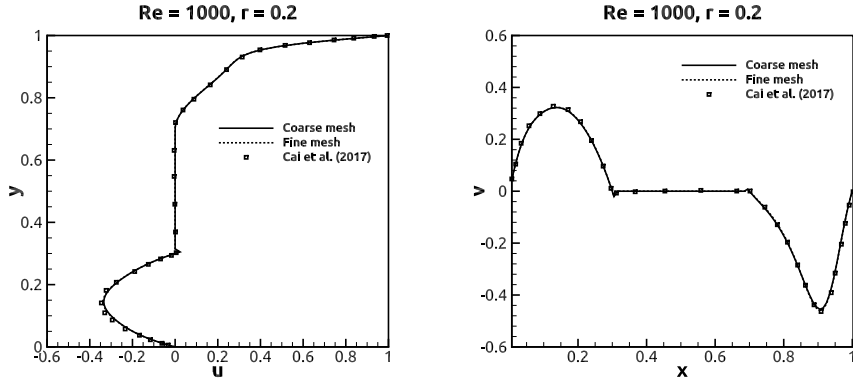
Figure 2. Comparison of the velocity profiles of the steady lid-driven cavity flow containing a centered cylinder of $r = 0.2$ for $Re = 1000$ obtained by the present method and by Cai et al.[11]: left image, distribution of velocity component u along $x = 0.5$; right image, distribution of velocity component v along $y = 0.5$.

$\blacktriangle$), and those connecting two regular cells are considered as active velocity points ($\triangleright$ and $\triangle$). The inactive velocity points is updated by interpolation of its adjacent active velocity points. A linear interpolation applied in directions is given as follows

$$u_i = \frac{x_i - x_\Gamma}{x_{i+1} - x_\Gamma} u_{i+1} + \frac{x_{i+1} - x_i}{x_{i+1} - x_\Gamma} u_\Gamma, \quad i = 1, 2 \tag{3}$$

where u_Γ and x_Γ denote the velocity components and the position of the solid surface, respectively.

A weighting factor λ is introduced in Eq.(2) for the inactive velocity components which are interpolated from two directions[9, 10].

$$u_i = \lambda_x u_i^x + \lambda_y u_i^y \tag{4}$$

where the superscripts x and y denote the interpolation in x and y-directions, respectively. Moreover, a Neumann condition is applied for the pressure correction at the inactive velocity points.

3. Results and discussion
3.1. Verification against previous numerical results
A numerical simulation for flow in a steady lid-driven square cavity containing a centered circular cylinder has been conducted for $Re = 1000$. The velocity of the lid is given by $u = 1$, and no-slip conditions are imposed on the side and bottom walls as well as the cylinder. The dimensionless cylinder radius r equals to 0.2 ($= r'/H$). Two grid resolutions of 100×100 and 200×200 uniform cells are considered for the grid convergence test. Figure 2 shows the velocity profiles for u (left) and v (right) along $x = 0.5$ and $y = 0.5$, respectively. Previous numerical results obtained by Cai et al.[11] using an immersed boundary method which takes the body force as a Lagrange multiplier were included for comparison. A good agreement is obtained using both the coarse and fine meshes. It appears that the coarse mesh is sufficient to obtain the grid independent results.
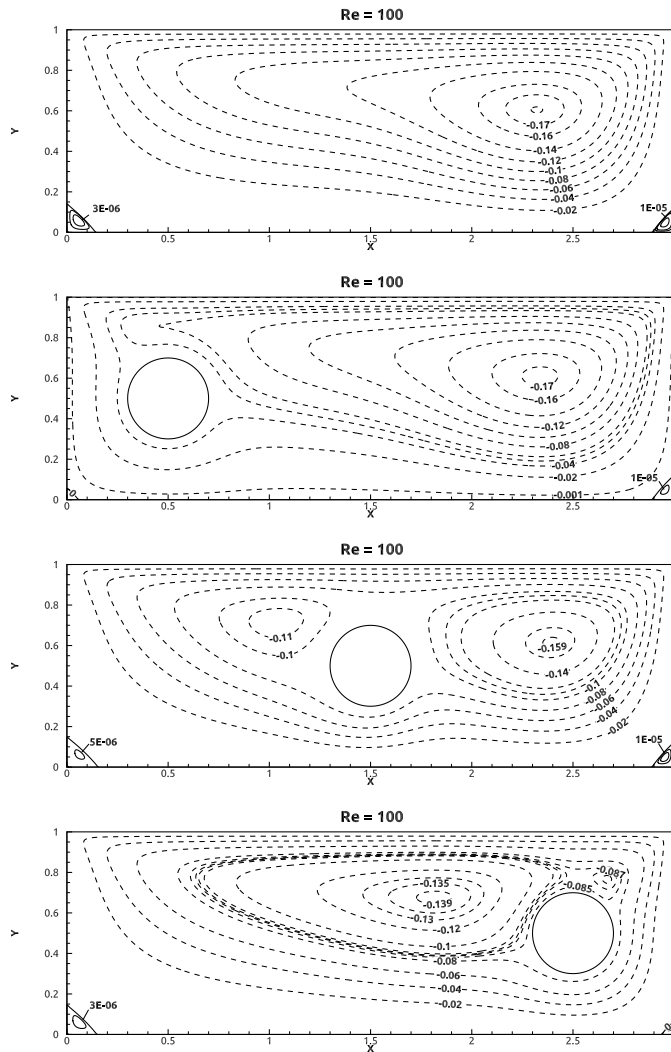
Figure 3. Streamfunctions within a steady lid-driven cavity of AR = 1/3 with and without a circular cylinder for Re = 100. The cylinder is positioned at $(x, y) = (0.5, 0.5)$, $(1.5, 0.5)$ and $(2.5, 0.5)$.

3.2. Flow in a steady lid-driven rectangular cavity containing a circular cylinder
Predictions for flow in a steady lid-driven rectangular cavity containing a circular cylinder are presented for $Re = 100$, 500 and 1000 in this section. The depth to width ratios (AR) of the cavity is 1/3, and three different locations of the cylinder with $r = 0.2$ are considered to investigate their effects on flow structures. Moreover, the steady lid-driven cavity flows at respective Re are predicted for comparison purpose.

Figure 3 shows the streamfunctions within a steady lid-driven cavity of $AR = 1/3$ containing
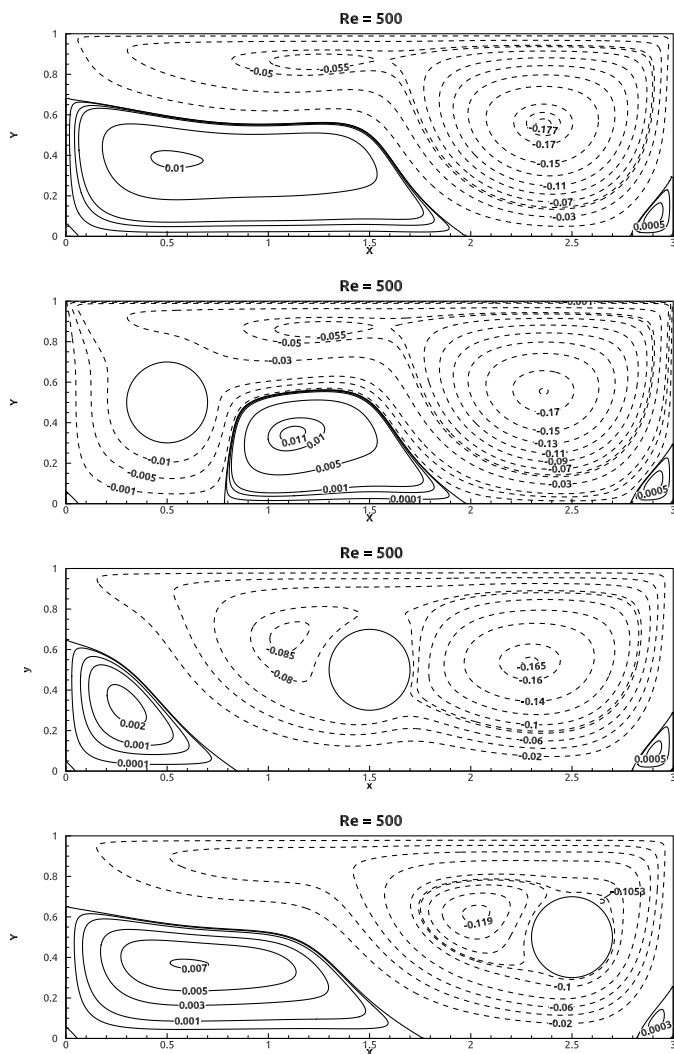
Figure 4. Streamfunctions within a steady lid-driven cavity of AR = 1/3 with and without a circular cylinder for Re = 500. The cylinder is positioned at $(x, y) = (0.5, 0.5)$, $(1.5, 0.5)$ and $(2.5, 0.5)$.

a circular cylinder for $Re = 100$. The cylinder is located at $(x, y) = (0.5, 0.5)$, $(1.5, 0.5)$ and $(2.5, 0.5)$. The cavity without the cylinder contains a clockwise primary vortex and two small anti-clockwise bottom corner vortices. These vortex structures qualitatively remain for the cylinder positioned at $(0.5, 0.5)$ but with a slightly weaker primary vortex core and the nearly vanishing bottom left corner vortex. The bottom right corner vortex are weakly affected since it is far away from the cylinder. As the cylinder is positioned at $(1.5, 0.5)$, the primary vortex present in the cavity without a cylinder appears to break into two clockwise vortices due to the presence of
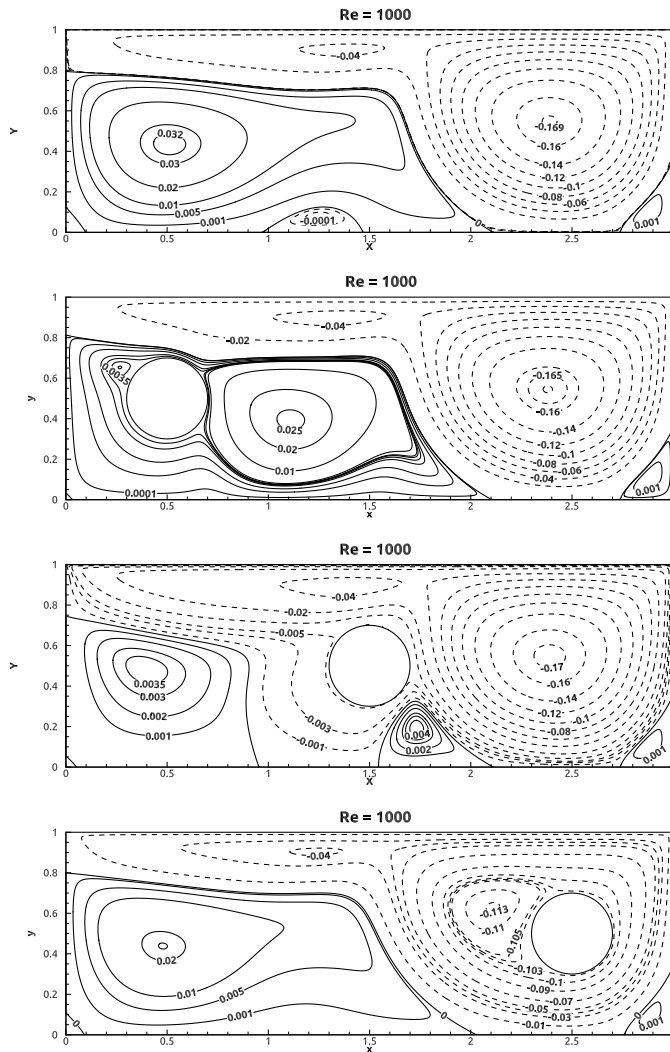
Figure 5. Streamfunctions within a steady lid-driven cavity of AR = 1/3 with and without a circular cylinder for Re = 1000. The cylinder is positioned at $(x, y) = (0.5, 0.5)$, $(1.5, 0.5)$ and $(2.5, 0.5)$.

the cylinder at the right side of which the flow driven by the lid rolls down. Similar qualitatively vortex structures were previously investigated by Young et al.[12] for creeping flow within a steady lid-driven rectangular cavity with a centered cylinder. They found two equal clockwise vortices attached to the upper left and right side of the cylinder, respectively. In present cases, the non-linear effect from the convective terms attributes to the asymmetry of the attached vortices where the left one is smaller and weaker than the right one. As the cylinder is shifted to (2.5, 0.5), a decrease in space between the cylinder and the right wall suppresses the growth

of the right vortex, causing the left vortex becoming larger than the right one. This behavior qualitatively remains the same for $Re = 500$ as the cylinder moves rightwards from (1.5, 0.5) to (2.5, 0.5) shown in figure 4.

Figure 4 shows the streamfunctions for the same geometry shown in figure 3 but for $Re = 500$. In the cavity without the cylinder, a new clockwise vortex is formed beneath the lid, and flow separation occurs at $x = 2$, forming a larger bottom corner than that for $Re = 100$ (figure 3). As the cylinder is inserted at (0.5, 0.5), flow separation remains at $x = 2$ while the presence of the cylinder leads to the flow rolling down at the lower right side of the cylinder and reattaching the bottom wall, thus forming a large bottom vortex. For the cylinder located at (1.5, 0.5) and (2.5, 0.5), the clockwise vortex beneath the lid disappears, forming qualitatively similar vortex structures present for $Re = 100$ (figure 3) but with stronger vortex cores. Moreover, the attached vortices for $Re = 100$ (figure 3) is larger than those for 500 (figure 4) with the cylinder located at (2.5, 0.5). It appears that an increase in Re leads to a higher flow velocity around the cylinder, thus impeding the growth of the attached vortices.

Figure 5 shows the streamfunctions for the same geometry shown in figure 3 but for $Re = 1000$. In the cavity without the cylinder, an increase in Re forms a larger bottom left corner vortex and a small clockwise bottom vortex. This small bottom vortex disappears as the cylinder is inserted in the cavity. For the cylinder positioned at (0.5, 0.5), the cylinder is surrounded by a stronger anti-clockwise flow circulation due to a larger Re, such that the flow rolls down at the right side of the cylinder and up at the upper left side of the cylinder, forming two anti-clockwise attached vortices. The right one is much larger than the left one. As the cylinder is positioned at (1.5, 0.5), the bottom left corner vortex present in the cavity without the cylinder appears to break up into a large bottom left corner vortex and a bottom vortex. As the cylinder moves to (2.5, 0.5), the primary vortex in the cavity without the cylinder disappears (due to a higher Re) while the flow rolls up at the upper left side of the cylinder, forming the left attached vortex.

4. Summary and conclusion

The present paper provides a detailed investigation for flow in a steady lid-driven cavity of depth to width aspect ratio 1/3 containing a circular cylinder with a radius equals to 0.2. Three different Reynolds numbers and three different locations are considered. For a lower Reynolds number ($Re = 100$), the cylinder causes the flow rolling up and down, forming two clockwise vortices. As the cylinder moves rightwards, the left one grows while the right one decays. For a moderate Reynolds number ($Re = 500$), a large bottom vortex is formed for cylinder located near the left wall, and it disappears as the cylinder moves rightwards. For the largest Reynolds number ($Re = 1000$), two attached anti-clockwise vortices are formed around the cylinder located near the left wall. As the cylinder moves gradually closer the left wall, a large bottom vortex is formed and disappears together with the clockwise vortex to the right side of the cylinder.

References

[1] Oztop H F, Zhao Z and Yu B 2009 *International Journal of Heat and Fluid Flow* **30** 886–901
[2] Khanafer K and Aithal S 2013 *International Journal of Heat and Mass Transfer* **66** 200–209
[3] Su S W, Lai M C and Lin C A 2007 *Computers & Fluids* **36** 313–324
[4] Ito K, Lai M C and Li Z 2009 *Journal of Computational Physics* **228** 2616–2628
[5] Ghaddar N K 1992 *International journal of Heat and Mass Transfer* **35** 2327–2334
[6] De A K and Dalal A 2006 *International Journal of Heat and Mass Transfer* **49** 4608–4623
[7] Lee J, Ha M and Yoon H 2010 *International Journal of Heat and Mass Transfer* **53** 5905–5919

[8] Fadlun E, Verzicco R, Orlandi P and Mohd-Yusof J 2000 *Journal of Computational Physics* **161** 35–60
[9] Peller N, Duc A L, Tremblay F and Manhart M 2006 *International Journal for Numerical Methods in Fluids* **52** 1175–1193
[10] Berthelsen P A and Faltinsen O M 2008 *Journal of Computational Physics* **227** 4354–4397
[11] Cai S G, Ouahsine A, Favier J and Hoarau Y 2017 *International Journal for Numerical Methods in Fluids* **85** 288–323
[12] Young D, Chen C, Fan C, Murugesan K and Tsai C 2005 *European Journal of Mechanics-B/Fluids* **24** 703–716

Previous PhD theses published at the Department of Marine Technology
(earlier: Faculty of Marine Technology)
NORWEGIAN UNIVERSITY OF SCIENCE AND TECHNOLOGY

Report No.	Author	Title
	Kavlie, Dag	Optimization of Plane Elastic Grillages, 1967
	Hansen, Hans R.	Man-Machine Communication and Data-Storage Methods in Ship Structural Design, 1971
	Gisvold, Kaare M.	A Method for non-linear mixed -integer programming and its Application to Design Problems, 1971
	Lund, Sverre	Tanker Frame Optimalization by means of SUMT-Transformation and Behaviour Models, 1971
	Vinje, Tor	On Vibration of Spherical Shells Interacting with Fluid, 1972
	Lorentz, Jan D.	Tank Arrangement for Crude Oil Carriers in Accordance with the new Anti-Pollution Regulations, 1975
	Carlsen, Carl A.	Computer-Aided Design of Tanker Structures, 1975
	Larsen, Carl M.	Static and Dynamic Analysis of Offshore Pipelines during Installation, 1976
UR-79-01	Brigt Hatlestad, MK	The finite element method used in a fatigue evaluation of fixed offshore platforms. (Dr.Ing. Thesis)
UR-79-02	Erik Pettersen, MK	Analysis and design of cellular structures. (Dr.Ing. Thesis)
UR-79-03	Sverre Valsgård, MK	Finite difference and finite element methods applied to nonlinear analysis of plated structures. (Dr.Ing. Thesis)
UR-79-04	Nils T. Nordsve, MK	Finite element collapse analysis of structural members considering imperfections and stresses due to fabrication. (Dr.Ing. Thesis)
UR-79-05	Ivar J. Fylling, MK	Analysis of towline forces in ocean towing systems. (Dr.Ing. Thesis)
UR-80-06	Nils Sandsmark, MM	Analysis of Stationary and Transient Heat Conduction by the Use of the Finite Element Method. (Dr.Ing. Thesis)
UR-80-09	Sverre Haver, MK	Analysis of uncertainties related to the stochastic modeling of ocean waves. (Dr.Ing. Thesis)
UR-81-15	Odland, Jonas	On the Strength of welded Ring stiffened cylindrical Shells primarily subjected to axial Compression
UR-82-17	Engesvik, Knut	Analysis of Uncertainties in the fatigue Capacity of

Welded Joints

UR-82-18	Rye, Henrik	Ocean wave groups
UR-83-30	Eide, Oddvar Inge	On Cumulative Fatigue Damage in Steel Welded Joints
UR-83-33	Mo, Olav	Stochastic Time Domain Analysis of Slender Offshore Structures
UR-83-34	Amdahl, Jørgen	Energy absorption in Ship-platform impacts
UR-84-37	Mørch, Morten	Motions and mooring forces of semi submersibles as determined by full-scale measurements and theoretical analysis
UR-84-38	Soares, C. Guedes	Probabilistic models for load effects in ship structures
UR-84-39	Aarsnes, Jan V.	Current forces on ships
UR-84-40	Czujko, Jerzy	Collapse Analysis of Plates subjected to Biaxial Compression and Lateral Load
UR-85-46	Alf G. Engseth, MK	Finite element collapse analysis of tubular steel offshore structures. (Dr.Ing. Thesis)
UR-86-47	Dengody Sheshappa, MP	A Computer Design Model for Optimizing Fishing Vessel Designs Based on Techno-Economic Analysis. (Dr.Ing. Thesis)
UR-86-48	Vidar Aanesland, MH	A Theoretical and Numerical Study of Ship Wave Resistance. (Dr.Ing. Thesis)
UR-86-49	Heinz-Joachim Wessel, MK	Fracture Mechanics Analysis of Crack Growth in Plate Girders. (Dr.Ing. Thesis)
UR-86-50	Jon Taby, MK	Ultimate and Post-ultimate Strength of Dented Tubular Members. (Dr.Ing. Thesis)
UR-86-51	Walter Lian, MH	A Numerical Study of Two-Dimensional Separated Flow Past Bluff Bodies at Moderate KC-Numbers. (Dr.Ing. Thesis)
UR-86-52	Bjørn Sortland, MH	Force Measurements in Oscillating Flow on Ship Sections and Circular Cylinders in a U-Tube Water Tank. (Dr.Ing. Thesis)
UR-86-53	Kurt Strand, MM	A System Dynamic Approach to One-dimensional Fluid Flow. (Dr.Ing. Thesis)
UR-86-54	Arne Edvin Løken, MH	Three Dimensional Second Order Hydrodynamic Effects on Ocean Structures in Waves. (Dr.Ing. Thesis)
UR-86-55	Sigurd Falch, MH	A Numerical Study of Slamming of Two-Dimensional Bodies. (Dr.Ing. Thesis)
UR-87-56	Arne Braathen, MH	Application of a Vortex Tracking Method to the Prediction of Roll Damping of a Two-Dimension Floating Body. (Dr.Ing. Thesis)

UR-87-57	Bernt Leira, MK	Gaussian Vector Processes for Reliability Analysis involving Wave-Induced Load Effects. (Dr.Ing. Thesis)
UR-87-58	Magnus Småvik, MM	Thermal Load and Process Characteristics in a Two-Stroke Diesel Engine with Thermal Barriers (in Norwegian). (Dr.Ing. Thesis)
MTA-88-59	Bernt Arild Bremdal, MP	An Investigation of Marine Installation Processes – A Knowledge - Based Planning Approach. (Dr.Ing. Thesis)
MTA-88-60	Xu Jun, MK	Non-linear Dynamic Analysis of Space-framed Offshore Structures. (Dr.Ing. Thesis)
MTA-89-61	Gang Miao, MH	Hydrodynamic Forces and Dynamic Responses of Circular Cylinders in Wave Zones. (Dr.Ing. Thesis)
MTA-89-62	Martin Greenhow, MH	Linear and Non-Linear Studies of Waves and Floating Bodies. Part I and Part II. (Dr.Techn. Thesis)
MTA-89-63	Chang Li, MH	Force Coefficients of Spheres and Cubes in Oscillatory Flow with and without Current. (Dr.Ing. Thesis
MTA-89-64	Hu Ying, MP	A Study of Marketing and Design in Development of Marine Transport Systems. (Dr.Ing. Thesis)
MTA-89-65	Arild Jæger, MH	Seakeeping, Dynamic Stability and Performance of a Wedge Shaped Planing Hull. (Dr.Ing. Thesis)
MTA-89-66	Chan Siu Hung, MM	The dynamic characteristics of tilting-pad bearings
MTA-89-67	Kim Wikstrøm, MP	Analysis av projekteringen for ett offshore projekt. (Licenciat-avhandling)
MTA-89-68	Jiao Guoyang, MK	Reliability Analysis of Crack Growth under Random Loading, considering Model Updating. (Dr.Ing. Thesis)
MTA-89-69	Arnt Olufsen, MK	Uncertainty and Reliability Analysis of Fixed Offshore Structures. (Dr.Ing. Thesis)
MTA-89-70	Wu Yu-Lin, MR	System Reliability Analyses of Offshore Structures using improved Truss and Beam Models. (Dr.Ing. Thesis)
MTA-90-71	Jan Roger Hoff, MH	Three-dimensional Green function of a vessel with forward speed in waves. (Dr.Ing. Thesis)
MTA-90-72	Rong Zhao, MH	Slow-Drift Motions of a Moored Two-Dimensional Body in Irregular Waves. (Dr.Ing. Thesis)
MTA-90-73	Atle Minsaas, MP	Economical Risk Analysis. (Dr.Ing. Thesis)
MTA-90-74	Knut-Aril Farnes, MK	Long-term Statistics of Response in Non-linear Marine Structures. (Dr.Ing. Thesis)
MTA-90-75	Torbjørn Sotberg, MK	Application of Reliability Methods for Safety Assessment of Submarine Pipelines. (Dr.Ing.

Thesis)

MTA-90-76	Zeuthen, Steffen, MP	SEAMAID. A computational model of the design process in a constraint-based logic programming environment. An example from the offshore domain. (Dr.Ing. Thesis)
MTA-91-77	Haagensen, Sven, MM	Fuel Dependant Cyclic Variability in a Spark Ignition Engine - An Optical Approach. (Dr.Ing. Thesis)
MTA-91-78	Løland, Geir, MH	Current forces on and flow through fish farms. (Dr.Ing. Thesis)
MTA-91-79	Hoen, Christopher, MK	System Identification of Structures Excited by Stochastic Load Processes. (Dr.Ing. Thesis)
MTA-91-80	Haugen, Stein, MK	Probabilistic Evaluation of Frequency of Collision between Ships and Offshore Platforms. (Dr.Ing. Thesis)
MTA-91-81	Sødahl, Nils, MK	Methods for Design and Analysis of Flexible Risers. (Dr.Ing. Thesis)
MTA-91-82	Ormberg, Harald, MK	Non-linear Response Analysis of Floating Fish Farm Systems. (Dr.Ing. Thesis)
MTA-91-83	Marley, Mark J., MK	Time Variant Reliability under Fatigue Degradation. (Dr.Ing. Thesis)
MTA-91-84	Krokstad, Jørgen R., MH	Second-order Loads in Multidirectional Seas. (Dr.Ing. Thesis)
MTA-91-85	Molteberg, Gunnar A., MM	The Application of System Identification Techniques to Performance Monitoring of Four Stroke Turbocharged Diesel Engines. (Dr.Ing. Thesis)
MTA-92-86	Mørch, Hans Jørgen Bjelke, MH	Aspects of Hydrofoil Design: with Emphasis on Hydrofoil Interaction in Calm Water. (Dr.Ing. Thesis)
MTA-92-87	Chan Siu Hung, MM	Nonlinear Analysis of Rotordynamic Instabilities in Highspeed Turbomachinery. (Dr.Ing. Thesis)
MTA-92-88	Bessason, Bjarni, MK	Assessment of Earthquake Loading and Response of Seismically Isolated Bridges. (Dr.Ing. Thesis)
MTA-92-89	Langli, Geir, MP	Improving Operational Safety through exploitation of Design Knowledge - an investigation of offshore platform safety. (Dr.Ing. Thesis)
MTA-92-90	Sævik, Svein, MK	On Stresses and Fatigue in Flexible Pipes. (Dr.Ing. Thesis)
MTA-92-91	Ask, Tor Ø., MM	Ignition and Flame Growth in Lean Gas-Air Mixtures. An Experimental Study with a Schlieren System. (Dr.Ing. Thesis)
MTA-86-92	Hessen, Gunnar, MK	Fracture Mechanics Analysis of Stiffened Tubular Members. (Dr.Ing. Thesis)

MTA-93-93	Steinebach, Christian, MM	Knowledge Based Systems for Diagnosis of Rotating Machinery. (Dr.Ing. Thesis)
MTA-93-94	Dalane, Jan Inge, MK	System Reliability in Design and Maintenance of Fixed Offshore Structures. (Dr.Ing. Thesis)
MTA-93-95	Steen, Sverre, MH	Cobblestone Effect on SES. (Dr.Ing. Thesis)
MTA-93-96	Karunakaran, Daniel, MK	Nonlinear Dynamic Response and Reliability Analysis of Drag-dominated Offshore Platforms. (Dr.Ing. Thesis)
MTA-93-97	Hagen, Arnulf, MP	The Framework of a Design Process Language. (Dr.Ing. Thesis)
MTA-93-98	Nordrik, Rune, MM	Investigation of Spark Ignition and Autoignition in Methane and Air Using Computational Fluid Dynamics and Chemical Reaction Kinetics. A Numerical Study of Ignition Processes in Internal Combustion Engines. (Dr.Ing. Thesis)
MTA-94-99	Passano, Elizabeth, MK	Efficient Analysis of Nonlinear Slender Marine Structures. (Dr.Ing. Thesis)
MTA-94-100	Kvålsvold, Jan, MH	Hydroelastic Modelling of Wetdeck Slamming on Multihull Vessels. (Dr.Ing. Thesis)
MTA-94-102	Bech, Sidsel M., MK	Experimental and Numerical Determination of Stiffness and Strength of GRP/PVC Sandwich Structures. (Dr.Ing. Thesis)
MTA-95-103	Paulsen, Hallvard, MM	A Study of Transient Jet and Spray using a Schlieren Method and Digital Image Processing. (Dr.Ing. Thesis)
MTA-95-104	Hovde, Geir Olav, MK	Fatigue and Overload Reliability of Offshore Structural Systems, Considering the Effect of Inspection and Repair. (Dr.Ing. Thesis)
MTA-95-105	Wang, Xiaozhi, MK	Reliability Analysis of Production Ships with Emphasis on Load Combination and Ultimate Strength. (Dr.Ing. Thesis)
MTA-95-106	Ulstein, Tore, MH	Nonlinear Effects of a Flexible Stern Seal Bag on Cobblestone Oscillations of an SES. (Dr.Ing. Thesis)
MTA-95-107	Solaas, Frøydis, MH	Analytical and Numerical Studies of Sloshing in Tanks. (Dr.Ing. Thesis)
MTA-95-108	Hellan, Øyvind, MK	Nonlinear Pushover and Cyclic Analyses in Ultimate Limit State Design and Reassessment of Tubular Steel Offshore Structures. (Dr.Ing. Thesis)
MTA-95-109	Hermundstad, Ole A., MK	Theoretical and Experimental Hydroelastic Analysis of High Speed Vessels. (Dr.Ing. Thesis)
MTA-96-110	Bratland, Anne K., MH	Wave-Current Interaction Effects on Large-Volume Bodies in Water of Finite Depth. (Dr.Ing. Thesis)
MTA-96-111	Herfjord, Kjell, MH	A Study of Two-dimensional Separated Flow by a Combination of the Finite Element Method and

Navier-Stokes Equations. (Dr.Ing. Thesis)

MTA-96-112	Æsøy, Vilmar, MM	Hot Surface Assisted Compression Ignition in a Direct Injection Natural Gas Engine. (Dr.Ing. Thesis)
MTA-96-113	Eknes, Monika L., MK	Escalation Scenarios Initiated by Gas Explosions on Offshore Installations. (Dr.Ing. Thesis)
MTA-96-114	Erikstad, Stein O., MP	A Decision Support Model for Preliminary Ship Design. (Dr.Ing. Thesis)
MTA-96-115	Pedersen, Egil, MH	A Nautical Study of Towed Marine Seismic Streamer Cable Configurations. (Dr.Ing. Thesis)
MTA-97-116	Moksnes, Paul O., MM	Modelling Two-Phase Thermo-Fluid Systems Using Bond Graphs. (Dr.Ing. Thesis)
MTA-97-117	Halse, Karl H., MK	On Vortex Shedding and Prediction of Vortex-Induced Vibrations of Circular Cylinders. (Dr.Ing. Thesis)
MTA-97-118	Igland, Ragnar T., MK	Reliability Analysis of Pipelines during Laying, considering Ultimate Strength under Combined Loads. (Dr.Ing. Thesis)
MTA-97-119	Pedersen, Hans-P., MP	Levendefiskteknologi for fiskefartøy. (Dr.Ing. Thesis)
MTA-98-120	Vikestad, Kyrre, MK	Multi-Frequency Response of a Cylinder Subjected to Vortex Shedding and Support Motions. (Dr.Ing. Thesis)
MTA-98-121	Azadi, Mohammad R. E., MK	Analysis of Static and Dynamic Pile-Soil-Jacket Behaviour. (Dr.Ing. Thesis)
MTA-98-122	Ulltang, Terje, MP	A Communication Model for Product Information. (Dr.Ing. Thesis)
MTA-98-123	Torbergsen, Erik, MM	Impeller/Diffuser Interaction Forces in Centrifugal Pumps. (Dr.Ing. Thesis)
MTA-98-124	Hansen, Edmond, MH	A Discrete Element Model to Study Marginal Ice Zone Dynamics and the Behaviour of Vessels Moored in Broken Ice. (Dr.Ing. Thesis)
MTA-98-125	Videiro, Paulo M., MK	Reliability Based Design of Marine Structures. (Dr.Ing. Thesis)
MTA-99-126	Mainçon, Philippe, MK	Fatigue Reliability of Long Welds Application to Titanium Risers. (Dr.Ing. Thesis)
MTA-99-127	Haugen, Elin M., MH	Hydroelastic Analysis of Slamming on Stiffened Plates with Application to Catamaran Wetdecks. (Dr.Ing. Thesis)
MTA-99-128	Langhelle, Nina K., MK	Experimental Validation and Calibration of Nonlinear Finite Element Models for Use in Design of Aluminium Structures Exposed to Fire. (Dr.Ing. Thesis)
MTA-99-	Berstad, Are J., MK	Calculation of Fatigue Damage in Ship Structures.

129		(Dr.Ing. Thesis)
MTA-99-130	Andersen, Trond M., MM	Short Term Maintenance Planning. (Dr.Ing. Thesis)
MTA-99-131	Tveiten, Bård Wathne, MK	Fatigue Assessment of Welded Aluminium Ship Details. (Dr.Ing. Thesis)
MTA-99-132	Søreide, Fredrik, MP	Applications of underwater technology in deep water archaeology. Principles and practice. (Dr.Ing. Thesis)
MTA-99-133	Tønnessen, Rune, MH	A Finite Element Method Applied to Unsteady Viscous Flow Around 2D Blunt Bodies With Sharp Corners. (Dr.Ing. Thesis)
MTA-99-134	Elvekrok, Dag R., MP	Engineering Integration in Field Development Projects in the Norwegian Oil and Gas Industry. The Supplier Management of Norne. (Dr.Ing. Thesis)
MTA-99-135	Fagerholt, Kjetil, MP	Optimeringsbaserte Metoder for Ruteplanlegging innen skipsfart. (Dr.Ing. Thesis)
MTA-99-136	Bysveen, Marie, MM	Visualization in Two Directions on a Dynamic Combustion Rig for Studies of Fuel Quality. (Dr.Ing. Thesis)
MTA-2000-137	Storteig, Eskild, MM	Dynamic characteristics and leakage performance of liquid annular seals in centrifugal pumps. (Dr.Ing. Thesis)
MTA-2000-138	Sagli, Gro, MK	Model uncertainty and simplified estimates of long term extremes of hull girder loads in ships. (Dr.Ing. Thesis)
MTA-2000-139	Tronstad, Harald, MK	Nonlinear analysis and design of cable net structures like fishing gear based on the finite element method. (Dr.Ing. Thesis)
MTA-2000-140	Kroneberg, André, MP	Innovation in shipping by using scenarios. (Dr.Ing. Thesis)
MTA-2000-141	Haslum, Herbjørn Alf, MH	Simplified methods applied to nonlinear motion of spar platforms. (Dr.Ing. Thesis)
MTA-2001-142	Samdal, Ole Johan, MM	Modelling of Degradation Mechanisms and Stressor Interaction on Static Mechanical Equipment Residual Lifetime. (Dr.Ing. Thesis)
MTA-2001-143	Baarholm, Rolf Jarle, MH	Theoretical and experimental studies of wave impact underneath decks of offshore platforms. (Dr.Ing. Thesis)
MTA-2001-144	Wang, Lihua, MK	Probabilistic Analysis of Nonlinear Wave-induced Loads on Ships. (Dr.Ing. Thesis)
MTA-2001-145	Kristensen, Odd H. Holt, MK	Ultimate Capacity of Aluminium Plates under Multiple Loads, Considering HAZ Properties. (Dr.Ing. Thesis)
MTA-2001-146	Greco, Marilena, MH	A Two-Dimensional Study of Green-Water

Loading. (Dr.Ing. Thesis)

MTA-2001-147	Heggelund, Svein E., MK	Calculation of Global Design Loads and Load Effects in Large High Speed Catamarans. (Dr.Ing. Thesis)
MTA-2001-148	Babalola, Olusegun T., MK	Fatigue Strength of Titanium Risers – Defect Sensitivity. (Dr.Ing. Thesis)
MTA-2001-149	Mohammed, Abuu K., MK	Nonlinear Shell Finite Elements for Ultimate Strength and Collapse Analysis of Ship Structures. (Dr.Ing. Thesis)
MTA-2002-150	Holmedal, Lars E., MH	Wave-current interactions in the vicinity of the sea bed. (Dr.Ing. Thesis)
MTA-2002-151	Rognebakke, Olav F., MH	Sloshing in rectangular tanks and interaction with ship motions. (Dr.Ing. Thesis)
MTA-2002-152	Lader, Pål Furset, MH	Geometry and Kinematics of Breaking Waves. (Dr.Ing. Thesis)
MTA-2002-153	Yang, Qinzheng, MH	Wash and wave resistance of ships in finite water depth. (Dr.Ing. Thesis)
MTA-2002-154	Melhus, Øyvin, MM	Utilization of VOC in Diesel Engines. Ignition and combustion of VOC released by crude oil tankers. (Dr.Ing. Thesis)
MTA-2002-155	Ronæss, Marit, MH	Wave Induced Motions of Two Ships Advancing on Parallel Course. (Dr.Ing. Thesis)
MTA-2002-156	Økland, Ole D., MK	Numerical and experimental investigation of whipping in twin hull vessels exposed to severe wet deck slamming. (Dr.Ing. Thesis)
MTA-2002-157	Ge, Chunhua, MK	Global Hydroelastic Response of Catamarans due to Wet Deck Slamming. (Dr.Ing. Thesis)
MTA-2002-158	Byklum, Eirik, MK	Nonlinear Shell Finite Elements for Ultimate Strength and Collapse Analysis of Ship Structures. (Dr.Ing. Thesis)
IMT-2003-1	Chen, Haibo, MK	Probabilistic Evaluation of FPSO-Tanker Collision in Tandem Offloading Operation. (Dr.Ing. Thesis)
IMT-2003-2	Skaugset, Kjetil Bjørn, MK	On the Suppression of Vortex Induced Vibrations of Circular Cylinders by Radial Water Jets. (Dr.Ing. Thesis)
IMT-2003-3	Chezhian, Muthu	Three-Dimensional Analysis of Slamming. (Dr.Ing. Thesis)
IMT-2003-4	Buhaug, Øyvind	Deposit Formation on Cylinder Liner Surfaces in Medium Speed Engines. (Dr.Ing. Thesis)
IMT-2003-5	Tregde, Vidar	Aspects of Ship Design: Optimization of Aft Hull with Inverse Geometry Design. (Dr.Ing. Thesis)
IMT-	Wist, Hanne Therese	Statistical Properties of Successive Ocean Wave

2003-6		Parameters. (Dr.Ing. Thesis)
IMT-2004-7	Ransau, Samuel	Numerical Methods for Flows with Evolving Interfaces. (Dr.Ing. Thesis)
IMT-2004-8	Soma, Torkel	Blue-Chip or Sub-Standard. A data interrogation approach of identity safety characteristics of shipping organization. (Dr.Ing. Thesis)
IMT-2004-9	Ersdal, Svein	An experimental study of hydrodynamic forces on cylinders and cables in near axial flow. (Dr.Ing. Thesis)
IMT-2005-10	Brodtkorb, Per Andreas	The Probability of Occurrence of Dangerous Wave Situations at Sea. (Dr.Ing. Thesis)
IMT-2005-11	Yttervik, Rune	Ocean current variability in relation to offshore engineering. (Dr.Ing. Thesis)
IMT-2005-12	Fredheim, Arne	Current Forces on Net-Structures. (Dr.Ing. Thesis)
IMT-2005-13	Heggernes, Kjetil	Flow around marine structures. (Dr.Ing. Thesis
IMT-2005-14	Fouques, Sebastien	Lagrangian Modelling of Ocean Surface Waves and Synthetic Aperture Radar Wave Measurements. (Dr.Ing. Thesis)
IMT-2006-15	Holm, Håvard	Numerical calculation of viscous free surface flow around marine structures. (Dr.Ing. Thesis)
IMT-2006-16	Bjørheim, Lars G.	Failure Assessment of Long Through Thickness Fatigue Cracks in Ship Hulls. (Dr.Ing. Thesis)
IMT-2006-17	Hansson, Lisbeth	Safety Management for Prevention of Occupational Accidents. (Dr.Ing. Thesis)
IMT-2006-18	Zhu, Xinying	Application of the CIP Method to Strongly Nonlinear Wave-Body Interaction Problems. (Dr.Ing. Thesis)
IMT-2006-19	Reite, Karl Johan	Modelling and Control of Trawl Systems. (Dr.Ing. Thesis)
IMT-2006-20	Smogeli, Øyvind Notland	Control of Marine Propellers. From Normal to Extreme Conditions. (Dr.Ing. Thesis)
IMT-2007-21	Storhaug, Gaute	Experimental Investigation of Wave Induced Vibrations and Their Effect on the Fatigue Loading of Ships. (Dr.Ing. Thesis)
IMT-2007-22	Sun, Hui	A Boundary Element Method Applied to Strongly Nonlinear Wave-Body Interaction Problems. (PhD Thesis, CeSOS)
IMT-2007-23	Rustad, Anne Marthine	Modelling and Control of Top Tensioned Risers. (PhD Thesis, CeSOS)
IMT-2007-24	Johansen, Vegar	Modelling flexible slender system for real-time simulations and control applications
IMT-2007-25	Wroldsen, Anders Sunde	Modelling and control of tensegrity structures.

(PhD Thesis, CeSOS)

IMT-2007-26	Aronsen, Kristoffer Høye	An experimental investigation of in-line and combined inline and cross flow vortex induced vibrations. (Dr. avhandling, IMT)
IMT-2007-27	Gao, Zhen	Stochastic Response Analysis of Mooring Systems with Emphasis on Frequency-domain Analysis of Fatigue due to Wide-band Response Processes (PhD Thesis, CeSOS)
IMT-2007-28	Thorstensen, Tom Anders	Lifetime Profit Modelling of Ageing Systems Utilizing Information about Technical Condition. (Dr.ing. thesis, IMT)
IMT-2008-29	Refsnes, Jon Erling Gorset	Nonlinear Model-Based Control of Slender Body AUVs (PhD Thesis, IMT)
IMT-2008-30	Berntsen, Per Ivar B.	Structural Reliability Based Position Mooring. (PhD-Thesis, IMT)
IMT-2008-31	Ye, Naiquan	Fatigue Assessment of Aluminium Welded Box-stiffener Joints in Ships (Dr.ing. thesis, IMT)
IMT-2008-32	Radan, Damir	Integrated Control of Marine Electrical Power Systems. (PhD-Thesis, IMT)
IMT-2008-33	Thomassen, Paul	Methods for Dynamic Response Analysis and Fatigue Life Estimation of Floating Fish Cages. (Dr.ing. thesis, IMT)
IMT-2008-34	Pákozdi, Csaba	A Smoothed Particle Hydrodynamics Study of Two-dimensional Nonlinear Sloshing in Rectangular Tanks. (Dr.ing.thesis, IMT/ CeSOS)
IMT-2007-35	Grytøyr, Guttorm	A Higher-Order Boundary Element Method and Applications to Marine Hydrodynamics. (Dr.ing.thesis, IMT)
IMT-2008-36	Drummen, Ingo	Experimental and Numerical Investigation of Nonlinear Wave-Induced Load Effects in Containerships considering Hydroelasticity. (PhD thesis, CeSOS)
IMT-2008-37	Skejic, Renato	Maneuvering and Seakeeping of a Singel Ship and of Two Ships in Interaction. (PhD-Thesis, CeSOS)
IMT-2008-38	Harlem, Alf	An Age-Based Replacement Model for Repairable Systems with Attention to High-Speed Marine Diesel Engines. (PhD-Thesis, IMT)
IMT-2008-39	Alsos, Hagbart S.	Ship Grounding. Analysis of Ductile Fracture, Bottom Damage and Hull Girder Response. (PhD-thesis, IMT)
IMT-2008-40	Graczyk, Mateusz	Experimental Investigation of Sloshing Loading and Load Effects in Membrane LNG Tanks Subjected to Random Excitation. (PhD-thesis, CeSOS)
IMT-2008-41	Taghipour, Reza	Efficient Prediction of Dynamic Response for Flexible amd Multi-body Marine Structures. (PhD-

thesis, CeSOS)

IMT-2008-42	Ruth, Eivind	Propulsion control and thrust allocation on marine vessels. (PhD thesis, CeSOS)
IMT-2008-43	Nystad, Bent Helge	Technical Condition Indexes and Remaining Useful Life of Aggregated Systems. PhD thesis, IMT
IMT-2008-44	Soni, Prashant Kumar	Hydrodynamic Coefficients for Vortex Induced Vibrations of Flexible Beams, PhD thesis, CeSOS
IMT-2009-45	Amlashi, Hadi K.K.	Ultimate Strength and Reliability-based Design of Ship Hulls with Emphasis on Combined Global and Local Loads. PhD Thesis, IMT
IMT-2009-46	Pedersen, Tom Arne	Bond Graph Modelling of Marine Power Systems. PhD Thesis, IMT
IMT-2009-47	Kristiansen, Trygve	Two-Dimensional Numerical and Experimental Studies of Piston-Mode Resonance. PhD-Thesis, CeSOS
IMT-2009-48	Ong, Muk Chen	Applications of a Standard High Reynolds Number Model and a Stochastic Scour Prediction Model for Marine Structures. PhD-thesis, IMT
IMT-2009-49	Hong, Lin	Simplified Analysis and Design of Ships subjected to Collision and Grounding. PhD-thesis, IMT
IMT-2009-50	Koushan, Kamran	Vortex Induced Vibrations of Free Span Pipelines, PhD thesis, IMT
IMT-2009-51	Korsvik, Jarl Eirik	Heuristic Methods for Ship Routing and Scheduling. PhD-thesis, IMT
IMT-2009-52	Lee, Jihoon	Experimental Investigation and Numerical in Analyzing the Ocean Current Displacement of Longlines. Ph.d.-Thesis, IMT.
IMT-2009-53	Vestbøstad, Tone Gran	A Numerical Study of Wave-in-Deck Impact usin a Two-Dimensional Constrained Interpolation Profile Method, Ph.d.thesis, CeSOS.
IMT-2009-54	Bruun, Kristine	Bond Graph Modelling of Fuel Cells for Marine Power Plants. Ph.d.-thesis, IMT
IMT 2009-55	Holstad, Anders	Numerical Investigation of Turbulence in a Sekwed Three-Dimensional Channel Flow, Ph.d.-thesis, IMT.
IMT 2009-56	Ayala-Uraga, Efren	Reliability-Based Assessment of Deteriorating Ship-shaped Offshore Structures, Ph.d.-thesis, IMT
IMT 2009-57	Kong, Xiangjun	A Numerical Study of a Damaged Ship in Beam Sea Waves. Ph.d.-thesis, IMT/CeSOS.
IMT 2010-58	Kristiansen, David	Wave Induced Effects on Floaters of Aquaculture Plants, Ph.d.-thesis, CeSOS.

IMT 2010-59	Ludvigsen, Martin	An ROV-Toolbox for Optical and Acoustic Scientific Seabed Investigation. Ph.d.-thesis IMT.
IMT 2010-60	Hals, Jørgen	Modelling and Phase Control of Wave-Energy Converters. Ph.d.thesis, CeSOS.
IMT 2010- 61	Shu, Zhi	Uncertainty Assessment of Wave Loads and Ultimate Strength of Tankers and Bulk Carriers in a Reliability Framework. Ph.d. Thesis, IMT/ CeSOS
IMT 2010-62	Shao, Yanlin	Numerical Potential-Flow Studies on Weakly-Nonlinear Wave-Body Interactions with/without Small Forward Speed, Ph.d.thesis,CeSOS.
IMT 2010-63	Califano, Andrea	Dynamic Loads on Marine Propellers due to Intermittent Ventilation. Ph.d.thesis, IMT.
IMT 2010-64	El Khoury, George	Numerical Simulations of Massively Separated Turbulent Flows, Ph.d.-thesis, IMT
IMT 2010-65	Seim, Knut Sponheim	Mixing Process in Dense Overflows with Emphasis on the Faroe Bank Channel Overflow. Ph.d.thesis, IMT
IMT 2010-66	Jia, Huirong	Structural Analysis of Intect and Damaged Ships in a Collission Risk Analysis Perspective. Ph.d.thesis CeSoS.
IMT 2010-67	Jiao, Linlin	Wave-Induced Effects on a Pontoon-type Very Large Floating Structures (VLFS). Ph.D.-thesis, CeSOS.
IMT 2010-68	Abrahamsen, Bjørn Christian	Sloshing Induced Tank Roof with Entrapped Air Pocket. Ph.d.thesis, CeSOS.
IMT 2011-69	Karimirad, Madjid	Stochastic Dynamic Response Analysis of Spar-Type Wind Turbines with Catenary or Taut Mooring Systems. Ph.d.-thesis, CeSOS.
IMT - 2011-70	Erlend Meland	Condition Monitoring of Safety Critical Valves. Ph.d.-thesis, IMT.
IMT – 2011-71	Yang, Limin	Stochastic Dynamic System Analysis of Wave Energy Converter with Hydraulic Power Take-Off, with Particular Reference to Wear Damage Analysis, Ph.d. Thesis, CeSOS.
IMT – 2011-72	Visscher, Jan	Application of Particla Image Velocimetry on Turbulent Marine Flows, Ph.d.Thesis, IMT.
IMT – 2011-73	Su, Biao	Numerical Predictions of Global and Local Ice Loads on Ships. Ph.d.Thesis, CeSOS.
IMT – 2011-74	Liu, Zhenhui	Analytical and Numerical Analysis of Iceberg Collision with Ship Structures. Ph.d.Thesis, IMT.
IMT – 2011-75	Aarsæther, Karl Gunnar	Modeling and Analysis of Ship Traffic by Observation and Numerical Simulation. Ph.d.Thesis, IMT.

Imt – 2011-76	Wu, Jie	Hydrodynamic Force Identification from Stochastic Vortex Induced Vibration Experiments with Slender Beams. Ph.d.Thesis, IMT.
Imt – 2011-77	Amini, Hamid	Azimuth Propulsors in Off-design Conditions. Ph.d.Thesis, IMT.
IMT – 2011-78	Nguyen, Tan-Hoi	Toward a System of Real-Time Prediction and Monitoring of Bottom Damage Conditions During Ship Grounding. Ph.d.thesis, IMT.
IMT- 2011-79	Tavakoli, Mohammad T.	Assessment of Oil Spill in Ship Collision and Grounding, Ph.d.thesis, IMT.
IMT- 2011-80	Guo, Bingjie	Numerical and Experimental Investigation of Added Resistance in Waves. Ph.d.Thesis, IMT.
IMT- 2011-81	Chen, Qiaofeng	Ultimate Strength of Aluminium Panels, considering HAZ Effects, IMT
IMT- 2012-82	Kota, Ravikiran S.	Wave Loads on Decks of Offshore Structures in Random Seas, CeSOS.
IMT- 2012-83	Sten, Ronny	Dynamic Simulation of Deep Water Drilling Risers with Heave Compensating System, IMT.
IMT- 2012-84	Berle, Øyvind	Risk and resilience in global maritime supply chains, IMT.
IMT- 2012-85	Fang, Shaoji	Fault Tolerant Position Mooring Control Based on Structural Reliability, CeSOS.
IMT- 2012-86	You, Jikun	Numerical studies on wave forces and moored ship motions in intermediate and shallow water, CeSOS.
IMT- 2012-87	Xiang ,Xu	Maneuvering of two interacting ships in waves, CeSOS
IMT- 2012-88	Dong, Wenbin	Time-domain fatigue response and reliability analysis of offshore wind turbines with emphasis on welded tubular joints and gear components, CeSOS
IMT- 2012-89	Zhu, Suji	Investigation of Wave-Induced Nonlinear Load Effects in Open Ships considering Hull Girder Vibrations in Bending and Torsion, CeSOS
IMT- 2012-90	Zhou, Li	Numerical and Experimental Investigation of Station-keeping in Level Ice, CeSOS
IMT- 2012-91	Ushakov, Sergey	Particulate matter emission characteristics from diesel enignes operating on conventional and alternative marine fuels, IMT
IMT- 2013-1	Yin, Decao	Experimental and Numerical Analysis of Combined In-line and Cross-flow Vortex Induced Vibrations, CeSOS

IMT-2013-2	Kurniawan, Adi	Modelling and geometry optimisation of wave energy converters, CeSOS
IMT-2013-3	Al Ryati, Nabil	Technical condition indexes doe auxiliary marine diesel engines, IMT
IMT-2013-4	Firoozkoohi, Reza	Experimental, numerical and analytical investigation of the effect of screens on sloshing, CeSOS
IMT-2013-5	Ommani, Babak	Potential-Flow Predictions of a Semi-Displacement Vessel Including Applications to Calm Water Broaching, CeSOS
IMT-2013-6	Xing, Yihan	Modelling and analysis of the gearbox in a floating spar-type wind turbine, CeSOS
IMT-7-2013	Balland, Océane	Optimization models for reducing air emissions from ships, IMT
IMT-8-2013	Yang, Dan	Transitional wake flow behind an inclined flat plate-----Computation and analysis, IMT
IMT-9-2013	Abdillah, Suyuthi	Prediction of Extreme Loads and Fatigue Damage for a Ship Hull due to Ice Action, IMT
IMT-10-2013	Ramìrez, Pedro Agustìn Pèrez	Ageing management and life extension of technical systems- Concepts and methods applied to oil and gas facilities, IMT
IMT-11-2013	Chuang, Zhenju	Experimental and Numerical Investigation of Speed Loss due to Seakeeping and Maneuvering. IMT
IMT-12-2013	Etemaddar, Mahmoud	Load and Response Analysis of Wind Turbines under Atmospheric Icing and Controller System Faults with Emphasis on Spar Type Floating Wind Turbines, IMT
IMT-13-2013	Lindstad, Haakon	Strategies and measures for reducing maritime CO_2 emissons, IMT
IMT-14-2013	Haris, Sabril	Damage interaction analysis of ship collisions, IMT
IMT-15-2013	Shainee, Mohamed	Conceptual Design, Numerical and Experimental Investigation of a SPM Cage Concept for Offshore Mariculture, IMT
IMT-16-2013	Gansel, Lars	Flow past porous cylinders and effects of biofouling and fish behavior on the flow in and around Atlantic salmon net cages, IMT
IMT-17-2013	Gaspar, Henrique	Handling Aspects of Complexity in Conceptual Ship Design, IMT
IMT-18-2013	Thys, Maxime	Theoretical and Experimental Investigation of a Free Running Fishing Vessel at Small Frequency of Encounter, CeSOS
IMT-19-2013	Aglen, Ida	VIV in Free Spanning Pipelines, CeSOS

IMT-1-2014	Song, An	Theoretical and experimental studies of wave diffraction and radiation loads on a horizontally submerged perforated plate, CeSOS
IMT-2-2014	Rogne, Øyvind Ygre	Numerical and Experimental Investigation of a Hinged 5-body Wave Energy Converter, CeSOS
IMT-3-2014	Dai, Lijuan	Safe and efficient operation and maintenance of offshore wind farms ,IMT
IMT-4-2014	Bachynski, Erin Elizabeth	Design and Dynamic Analysis of Tension Leg Platform Wind Turbines, CeSOS
IMT-5-2014	Wang, Jingbo	Water Entry of Freefall Wedged – Wedge motions and Cavity Dynamics, CeSOS
IMT-6-2014	Kim, Ekaterina	Experimental and numerical studies related to the coupled behavior of ice mass and steel structures during accidental collisions, IMT
IMT-7-2014	Tan, Xiang	Numerical investigation of ship's continuous- mode icebreaking in leverl ice, CeSOS
IMT-8-2014	Muliawan, Made Jaya	Design and Analysis of Combined Floating Wave and Wind Power Facilities, with Emphasis on Extreme Load Effects of the Mooring System, CeSOS
IMT-9-2014	Jiang, Zhiyu	Long-term response analysis of wind turbines with an emphasis on fault and shutdown conditions, IMT
IMT-10-2014	Dukan, Fredrik	ROV Motion Control Systems, IMT
IMT-11-2014	Grimsmo, Nils I.	Dynamic simulations of hydraulic cylinder for heave compensation of deep water drilling risers, IMT
IMT-12-2014	Kvittem, Marit I.	Modelling and response analysis for fatigue design of a semisubmersible wind turbine, CeSOS
IMT-13-2014	Akhtar, Juned	The Effects of Human Fatigue on Risk at Sea, IMT
IMT-14-2014	Syahroni, Nur	Fatigue Assessment of Welded Joints Taking into Account Effects of Residual Stress, IMT
IMT-1-2015	Bøckmann, Eirik	Wave Propulsion of ships, IMT
IMT-2-2015	Wang, Kai	Modelling and dynamic analysis of a semi-submersible floating vertical axis wind turbine, CeSOS
IMT-3-2015	Fredriksen, Arnt Gunvald	A numerical and experimental study of a two-dimensional body with moonpool in waves and current, CeSOS
IMT-4-2015	Jose Patricio Gallardo Canabes	Numerical studies of viscous flow around bluff bodies, IMT

IMT-5-2015	Vegard Longva	Formulation and application of finite element techniques for slender marine structures subjected to contact interactions, IMT
IMT-6-2015	Jacobus De Vaal	Aerodynamic modelling of floating wind turbines, CeSOS
IMT-7-2015	Fachri Nasution	Fatigue Performance of Copper Power Conductors, IMT
IMT-8-2015	Oleh I Karpa	Development of bivariate extreme value distributions for applications in marine technology,CeSOS
IMT-9-2015	Daniel de Almeida Fernandes	An output feedback motion control system for ROVs, AMOS
IMT-10-2015	Bo Zhao	Particle Filter for Fault Diagnosis: Application to Dynamic Positioning Vessel and Underwater Robotics, CeSOS
IMT-11-2015	Wenting Zhu	Impact of emission allocation in maritime transportation, IMT
IMT-12-2015	Amir Rasekhi Nejad	Dynamic Analysis and Design of Gearboxes in Offshore Wind Turbines in a Structural Reliability Perspective, CeSOS
IMT-13-2015	Arturo Jesùs Ortega Malca	Dynamic Response of Flexibles Risers due to Unsteady Slug Flow, CeSOS
IMT-14-2015	Dagfinn Husjord	Guidance and decision-support system for safe navigation of ships operating in close proximity, IMT
IMT-15-2015	Anirban Bhattacharyya	Ducted Propellers: Behaviour in Waves and Scale Effects, IMT
IMT-16-2015	Qin Zhang	Image Processing for Ice Parameter Identification in Ice Management, IMT
IMT-1-2016	Vincentius Rumawas	Human Factors in Ship Design and Operation: An Experiential Learning, IMT
IMT-2-2016	Martin Storheim	Structural response in ship-platform and ship-ice collisions, IMT
IMT-3-2016	Mia Abrahamsen Prsic	Numerical Simulations of the Flow around single and Tandem Circular Cylinders Close to a Plane Wall, IMT
IMT-4-2016	Tufan Arslan	Large-eddy simulations of cross-flow around ship sections, IMT

IMT-5-2016	Pierre Yves-Henry	Parametrisation of aquatic vegetation in hydraulic and coastal research,IMT
IMT-6-2016	Lin Li	Dynamic Analysis of the Instalation of Monopiles for Offshore Wind Turbines, CeSOS
IMT-7-2016	Øivind Kåre Kjerstad	Dynamic Positioning of Marine Vessels in Ice, IMT
IMT-8-2016	Xiaopeng Wu	Numerical Analysis of Anchor Handling and Fish Trawling Operations in a Safety Perspective, CeSOS
IMT-9-2016	Zhengshun Cheng	Integrated Dynamic Analysis of Floating Vertical Axis Wind Turbines, CeSOS
IMT-10-2016	Ling Wan	Experimental and Numerical Study of a Combined Offshore Wind and Wave Energy Converter Concept
IMT-11-2016	Wei Chai	Stochastic dynamic analysis and reliability evaluation of the roll motion for ships in random seas, CeSOS
IMT-12-2016	Øyvind Selnes Patricksson	Decision support for conceptual ship design with focus on a changing life cycle and future uncertainty, IMT
IMT-13-2016	Mats Jørgen Thorsen	Time domain analysis of vortex-induced vibrations, IMT
IMT-14-2016	Edgar McGuinness	Safety in the Norwegian Fishing Fleet – Analysis and measures for improvement, IMT
IMT-15-2016	Sepideh Jafarzadeh	Energy effiency and emission abatement in the fishing fleet, IMT
IMT-16-2016	Wilson Ivan Guachamin Acero	Assessment of marine operations for offshore wind turbine installation with emphasis on response-based operational limits, IMT
IMT-17-2016	Mauro Candeloro	Tools and Methods for Autonomous Operations on Seabed and Water Coumn using Underwater Vehicles, IMT
IMT-18-2016	Valentin Chabaud	Real-Time Hybrid Model Testing of Floating Wind Tubines, IMT
IMT-1-2017	Mohammad Saud Afzal	Three-dimensional streaming in a sea bed boundary layer
IMT-2-2017	Peng Li	A Theoretical and Experimental Study of Wave-induced Hydroelastic Response of a Circular Floating Collar
IMT-3-2017	Martin Bergström	A simulation-based design method for arctic maritime transport systems

IMT-4-2017	Bhushan Taskar	The effect of waves on marine propellers and propulsion
IMT-5-2017	Mohsen Bardestani	A two-dimensional numerical and experimental study of a floater with net and sinker tube in waves and current
IMT-6-2017	Fatemeh Hoseini Dadmarzi	Direct Numerical Simualtion of turbulent wakes behind different plate configurations
IMT-7-2017	Michel R. Miyazaki	Modeling and control of hybrid marine power plants
IMT-8-2017	Giri Rajasekhar Gunnu	Safety and effiency enhancement of anchor handling operations with particular emphasis on the stability of anchor handling vessels
IMT-9-2017	Kevin Koosup Yum	Transient Performance and Emissions of a Turbocharged Diesel Engine for Marine Power Plants
IMT-10-2017	Zhaolong Yu	Hydrodynamic and structural aspects of ship collisions
IMT-11-2017	Martin Hassel	Risk Analysis and Modelling of Allisions between Passing Vessels and Offshore Installations
IMT-12-2017	Astrid H. Brodtkorb	Hybrid Control of Marine Vessels – Dynamic Positioning in Varying Conditions
IMT-13-2017	Kjersti Bruserud	Simultaneous stochastic model of waves and current for prediction of structural design loads
IMT-14-2017	Finn-Idar Grøtta Giske	Long-Term Extreme Response Analysis of Marine Structures Using Inverse Reliability Methods
IMT-15-2017	Stian Skjong	Modeling and Simulation of Maritime Systems and Operations for Virtual Prototyping using co-Simulations
IMT-1-2018	Yingguang Chu	Virtual Prototyping for Marine Crane Design and Operations
IMT-2-2018	Sergey Gavrilin	Validation of ship manoeuvring simulation models
IMT-3-2018	Jeevith Hegde	Tools and methods to manage risk in autonomous subsea inspection,maintenance and repair operations
IMT-4-2018	Ida M. Strand	Sea Loads on Closed Flexible Fish Cages
IMT-5-2018	Erlend Kvinge Jørgensen	Navigation and Control of Underwater Robotic Vehicles

IMT-6-2018	Bård Stovner	Aided Intertial Navigation of Underwater Vehicles
IMT-7-2018	Erlend Liavåg Grotle	Thermodynamic Response Enhanced by Sloshing in Marine LNG Fuel Tanks
IMT-8-2018	Børge Rokseth	Safety and Verification of Advanced Maritime Vessels
IMT-9-2018	Jan Vidar Ulveseter	Advances in Semi-Empirical Time Domain Modelling of Vortex-Induced Vibrations
IMT-10-2018	Chenyu Luan	Design and analysis for a steel braceless semi-submersible hull for supporting a 5-MW horizontal axis wind turbine
IMT-11-2018	Carl Fredrik Rehn	Ship Design under Uncertainty
IMT-12-2018	Øyvind Ødegård	Towards Autonomous Operations and Systems in Marine Archaeology
IMT-13-2018	Stein Melvær Nornes	Guidance and Control of Marine Robotics for Ocean Mapping and Monitoring
IMT-14-2018	Petter Norgren	Autonomous Underwater Vehicles in Arctic Marine Operations: Arctic marine research and ice monitoring
IMT-15-2018	Minjoo Choi	Modular Adaptable Ship Design for Handling Uncertainty in the Future Operating Context
MT-16-2018	Ole Alexander Eidsvik	Dynamics of Remotely Operated Underwater Vehicle Systems
IMT-17-2018	Mahdi Ghane	Fault Diagnosis of Floating Wind Turbine Drivetrain- Methodologies and Applications
IMT-18-2018	Christoph Alexander Thieme	Risk Analysis and Modelling of Autonomous Marine Systems
IMT-19-2018	Yugao Shen	Operational limits for floating-collar fish farms in waves and current, without and with well-boat presence
IMT-20-2018	Tianjiao Dai	Investigations of Shear Interaction and Stresses in Flexible Pipes and Umbilicals
IMT-21-2018	Sigurd Solheim Pettersen	Resilience by Latent Capabilities in Marine Systems
IMT-22-2018	Thomas Sauder	Fidelity of Cyber-physical Empirical Methods. Application to the Active Truncation of Slender Marine Structures
IMT-23-2018	Jan-Tore Horn	Statistical and Modelling Uncertainties in the Design of Offshore Wind Turbines

IMT-24-2018	Anna Swider	Data Mining Methods for the Analysis of Power Systems of Vessels
IMT-1-2019	Zhao He	Hydrodynamic study of a moored fish farming cage with fish influence
IMT-2-2019	Isar Ghamari	Numerical and Experimental Study on the Ship Parametric Roll Resonance and the Effect of Anti-Roll Tank
IMT-3-2019	Håkon Strandenes	Turbulent Flow Simulations at Higher Reynolds Numbers
IMT-4-2019	Siri Mariane Holen	Safety in Norwegian Fish Farming – Concepts and Methods for Improvement
IMT-5-2019	Ping Fu	Reliability Analysis of Wake-Induced Riser Collision
IMT-6-2019	Vladimir Krivopolianskii	Experimental Investigation of Injection and Combustion Processes in Marine Gas Engines using Constant Volume Rig
IMT-7-2019	Anna Maria Kozlowska	Hydrodynamic Loads on Marine Propellers Subject to Ventilation and out of Water Condition.
IMT-8-2019	Hans-Martin Heyn	Motion Sensing on Vessels Operating in Sea Ice: A Local Ice Monitoring System for Transit and Stationkeeping Operations under the Influence of Sea Ice
IMT-9-2019|	Stefan Vilsen	Method for Real-Time Hybrid Model Testing of Ocean Structures – Case on Slender Marine Systems
IMT-10-2019	Finn-Christian W. Hanssen	Non-Linear Wave-Body Interaction in Severe Waves
IMT-11-2019	Trygve Olav Fossum	Adaptive Sampling for Marine Robotics
IMT-12-2019	Jørgen Bremnes Nielsen	Modeling and Simulation for Design Evaluation
IMT-13-2019	Yuna Zhao	Numerical modelling and dyncamic analysis of offshore wind turbine blade installation
IMT-14-2019	Daniela Myland	Experimental and Theoretical Investigations on the Ship Resistance in Level Ice
IMT-15-2019	Zhengru Ren	Advanced control algorithms to support automated offshore wind turbine installation
IMT-16-2019	Drazen Polic	Ice-propeller impact analysis using an inverse propulsion machinery simulation approach
IMT-17-2019	Endre Sandvik	Sea passage scenario simulation for ship system performance evaluation

IMT-18-2019	Loup Suja-Thauvin	Response of Monopile Wind Turbines to Higher Order Wave Loads
IMT-19-2019	Emil Smilden	Structural control of offshore wind turbines – Increasing the role of control design in offshore wind farm development
IMT-20-2019	Aleksandar-Sasa Milakovic	On equivalent ice thickness and machine learning in ship ice transit simulations
IMT-1-2020	Amrit Shankar Verma	Modelling, Analysis and Response-based Operability Assessment of Offshore Wind Turbine Blade Installation with Emphasis on Impact Damages
IMT-2-2020	Bent Oddvar Arnesen Haugaløkken	Autonomous Technology for Inspection, Maintenance and Repair Operations in the Norwegian Aquaculture
IMT-3-2020	Seongpil Cho	Model-based fault detection and diagnosis of a blade pitch system in floating wind turbines
IMT-4-2020	Jose Jorge Garcia Agis	Effectiveness in Decision-Making in Ship Design under Uncertainty
IMT-5-2020	Thomas H. Viuff	Uncertainty Assessment of Wave-and Current-induced Global Response of Floating Bridges
IMT-6-2020	Fredrik Mentzoni	Hydrodynamic Loads on Complex Structures in the Wave Zone
IMT-7-2020	Senthuran Ravinthrakumar	Numerical and Experimental Studies of Resonant Flow in Moonpools in Operational Conditions
IMT-8-2020	Stian Skaalvik Sandøy	Acoustic-based Probabilistic Localization and Mapping using Unmanned Underwater Vehicles for Aquaculture Operations
IMT-9-2020	Kun Xu	Design and Analysis of Mooring System for Semi-submersible Floating Wind Turbine in Shallow Water
IMT-10-2020	Jianxun Zhu	Cavity Flows and Wake Behind an Elliptic Cylinder Translating Above the Wall